# Targeting the actin polymerisation pathway for improved treatment of glioblastoma

**Sophie Elizabeth Ketchen**

Submitted in accordance with the requirements for the degree of
Doctor of Philosophy

The University of Leeds
School of Medicine
September 2019

The candidate confirms that the work submitted is her own, except where work which has formed part of jointly authored publications has been included. The contribution of the candidate and the other authors to this work has been explicitly indicated below. The candidate confirms that appropriate credit has been given within the thesis where reference has been made to the work of others.

The work in Chapter 4 of this thesis has been used in publication as follows:

Ketchen S, Rohwedder A, Knipp S, Esteves F, Struve N, Peckham M, Ladbury JE, Curd A, Short SC, Brüning-Richardson A. A novel workflow for 3D analysis of tumour cell migration. *Interface Focus.*

All assays in this publication were planned and carried out by S Ketchen with supervision from A Brüning-Richardson, J E Ladbury and S C Short. The manuscript was written by S Ketchen and reviewed by all co-authors.

# Preface

## Acknowledgements

I would like to thank my supervisors Dr Anke Brüning-Richardson, Professor John Ladbury and Professor Susan Short for all their laboratory support and advice during my PhD. I would also like to express my ongoing gratitude to Dr Anke Brüning-Richardson and Professor John Ladbury for their continued mentorship and guidance. Anke, I don't know what I would have done without you. You have been the most incredible supervisor and I owe you so much. Thank you doesn't seem enough.

I would also like to thank Dr Sabine Knipp for all of her mentoring and advice in the Ladbury lab. Additionally, I am very grateful for all of the help of Dr Arndt Rohwedder and Dr Alistair Curd on the iSIM studies, Dr Filomena Esteves for her immunohistochemistry expertise and advice and Ruth Morton for her continued help and support in the lab. Furthermore, I would like to thank Dr Sean Lawler for giving me the incredible opportunity of being a member of his lab group at Harvard Medical School. A special thank you to Dr Michal Oskar Nowicki for his mentorship and to all of the Lawler group.

This project was kindly funded by The PPR Foundation, to whom I am incredibly grateful for the opportunity. I would also like to thank The Musella Foundation and The North American Foundation for the University of Leeds without whom, my placement at Harvard would not have happened.

I would like to thank my family for their incredible support throughout my PhD, especially my Mum and Les, without whom I would not have been able to achieve this.

Finally, I would like to dedicate the work within this thesis to my husband, George Ketchen, whose support, love and encouragement has been the reason for my successes. Thank you for always believing in me.

**Abstract**

One of the most devastating hallmarks of cancer is invasion, a prerequisite for tumour metastasis. Recently, the concept of migrastatics, a term used for drugs that interfere with cancer cell invasion/migration, has championed the development of drugs targeting the actin polymerisation pathway, as a main driver of cell migration. Targeting this cellular phenomenon offers an opportunity to improve the treatment of invasive and highly migratory tumours such as glioblastoma (GBM) and to better understand the mechanisms controlling glioma cell migration.

In this study, a small molecule inhibitor, CCG-1423, was identified that distinctively failed to halt migration. These observations suggest that cells continue to migrate via mesenchymal-amoeboid transition (MAT). Immunofluorescence studies and western blotting supported this novel MAT switch by demonstrating the loss of nuclear MKL1, a regulator of CCN1; a key adhesion and secretory protein in mesenchymal cell migration.

MAT induction was confirmed at high resolution by Instant Structured Illumination Microscopy (iSIM) and a newly developed ImageJ plugin allowing identification and quantification of MAT associated features such as lamellipodia or filopodia. This approach allowed for the first time, the detailed characterisation of CCG-1423 effects on MAT in gliomas.

Clinical relevance of CCN1 was established by an association with tumour grade including increases in CCN1 concentration detected in matched patient blood

samples. CCN1 levels were significantly increased in recurrent patient blood samples in comparison to their primary blood samples, suggesting that CCN1 is a key player in GBM invasion and progression.

The presented findings support pharmacological intervention with migrastatics through the development of combination treatments to target both mesenchymal and amoeboid cell migration in GBM management to fully inhibit invasion. In addition, this work has generated compelling evidence that CCN1 is a potential blood biomarker to monitor and potentially predict GBM recurrence earlier, therefore increasing survival rates of this devastating disease.

# Table of Contents

**List of Figures**

## List of Tables

**Abbreviations**

| | |
|---|---|
| 2D | Two-dimensional |
| 3D | Three-dimensional |
| ADP | Adenosine diphosphate |
| AMT | Amoeboid-mesenchymal transition |
| ATP | Adenosine triphosphate |
| BBB | Blood brain barrier |
| BIO | 6-bromoindirubin-oxime |
| CCN1 | CYR61 CTGF NOV family member 1 |
| Cdc42 | Cell division control protein 42 |
| CHCA | α-cyano-4-hydroxycinnamic acid |
| $CO_2$ | Carbon dioxide |
| CYR61 | Cysteine-rich angiogenic inducer 6 |
| DAPI | 4',6-diamidino-2-phenylindole |
| DHB | 2,5-dihydroxybenzoic acid |
| DLC2 | Deleted in liver cancer 2 |
| DMEM | Dulbecco's Modified Eagle Medium |
| DMSO | Dimethylsulfoxide |
| DNA | Deoxyribonucleic acid |
| E-cadherin | Epithelial-cadherin |
| ECM | Extracellular matrix |
| EGFR | Epidermal growth factor receptor |
| ELISA | Enzyme-linked immunosorbent assay |
| EMT | Epithelial-mesenchymal transition |
| F-actin | Filamentous-actin |
| g | Gram |
| G-actin | Globular-actin |

| | |
|---|---|
| GBM | Glioblastoma |
| GDI | Guanine nucleotide dissociation inhibitor |
| GDP | Guanosine diphosphate |
| GEF | Guanine nucleotide exchange factors |
| GFAP | Glial fibrillary acidic protein |
| GFP | Guanosine triphosphate |
| GPCR | G-protein-coupled receptors |
| GSC | Glioblastoma stem cell |
| GSK | Glycogen synthase kinase |
| GTP | Guanosine triphosphate |
| $H_2O$ | Water |
| HGF | Hepatocyte growth factor |
| HI-FCS | Heat-inactivated foetal calf serum |
| HRP | Horseradish peroxidase |
| IF | immunofluorescence |
| IHC | Immunohistochemistry |
| iSIM | Instant Structured Illumination Microscopy |
| ITO | Indium-Tin-Oxide |
| kDa | Kilodalton |
| kg | Kilogram |
| LatA | Latrunculin A |
| LESA | Liquid extraction surface analysis |
| LICAP | Leeds Institute of Cancer and Pathology |
| LiCl | Lithium chloride |
| M | Molar |
| MAL | Megakaryocytic acute leukeamia |
| MALDI | Matrix-assisted laser desorption/ionisation |
| MAT | Mesenchymal-amoeboid transition |
| mg | Milligram |
| MI | Migration index |
| MKL1 | Megakaryoblastic leukaemia 1 |
| ml | Microlitre |
| mM | Millimolar |

| | |
|---|---|
| MMP | Matrix metalloproteinases |
| MPRL | 1:4 1-methyl-2-pyrrolidinone |
| MRTF-A | Myocardin related transcription factor A |
| MSI | Mass spectrometry imaging |
| MTT | 3-(4,5-dimethylthiazol-2-yl)-2,5-diphenyltetrazolium bromide |
| NaOH | Sodium |
| nM | Nanomolar |
| OCT | optimal cutting temperate |
| PBS | Phosphate buffered saline |
| PFA | Paraformaldehyde |
| PVDF | Polyvinylidene difluoride |
| Rac1 | Ras-related C3 botulinum toxin substrate 1 |
| REMBRANDT | Repository for Molecular Brain Neoplasia Data |
| Rhoda | Ras homolog gene family member A |
| RhoGAP | Rho GTPase activating protein |
| ROCK | Rho-associated protein kinase |
| SDS-PAGE | Sodium dodecyl sulphate polyacrylamide gel electrophoresis |
| SRE | Serum response element |
| SRF | Serum response factor |
| TBS | Tris-Buffered Saline |
| TBST | Tris-Buffered Saline and Tween®20 |
| TCGA | The Cancer Genome Atlas |
| TFA | Trifluoroacetic acid |
| THAP | 2,4,6-trihydroxyacetophenone monohydrate |
| TMA | Tissue microarray |
| µg | Microgram |
| µl | Microlitre |
| µM | Micromolar |
| µm | Micrometre |

# Chapter 1: Background

## 1.1 The hallmarks of cancer

Cancer research has rapidly progressed over the past decades and with it our knowledge of this disease. For example, we now know that cancer is characterised by active changes to the genome. The foundations of these changes are established from mutations that produce the recessive loss of tumour suppressor gene function and the dominant gain of oncogenes (1). Both types of mutations have been extensively researched and confirmed in experimental human clinical trials and animal cancer models. As a result, a selection of fundamental underlying principles (Figure 1) shared by all cancer types has been proposed as being the hallmarks of cancer, simplifying how we look at cancer as a whole (2).

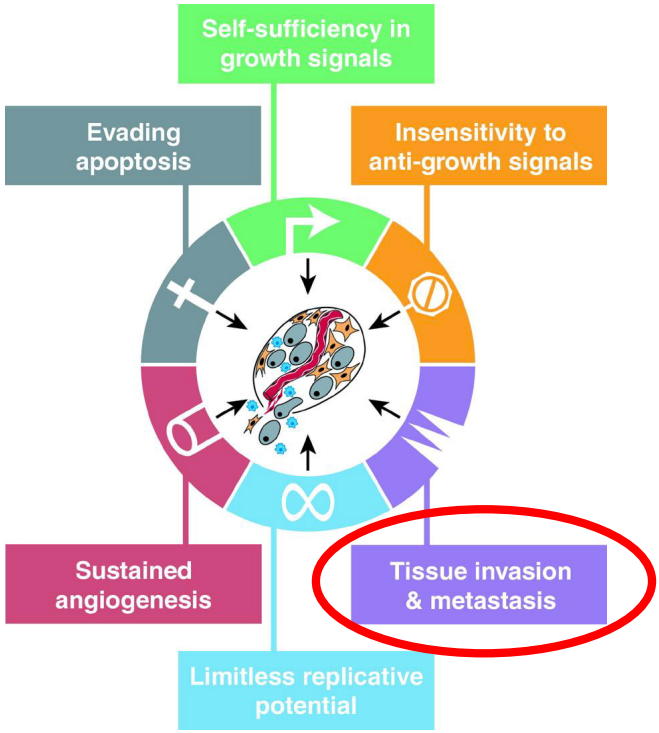


Figure 1. The first hallmarks of cancer to be identified. It is suggested that most, if not all, cancers share these traits during development through various mechanistic processes (Hanahan and Weinberg, 2000).

### 1.1.1 Tissue invasion and metastasis

One of the hallmarks of cancer is tissue invasion and metastasis. Ninety percent of all cancer mortalities are caused by tissue invasion and metastasis highlighting the importance of cancer cell transition to invasiveness (3). During the development of most cancers it is inevitable that a primary tumour will produce cells that possess the ability to move away from their original tumour site and migrate to healthy tissue where they will invade and create new tumours. It is this process of invasion and seeding of new tumours (metastases) that are the biggest cause of deaths due to cancer (4). Cell migration and invasion enables new tumours to establish themselves avoiding competition for nutrients and space within the original tumour, leading to a tumour blend of cancer cells and normal cells, recruited to support tumour growth. Processes involved in metastasis and invasion remain poorly understood due to their exceptionally complex mechanisms. They are closely linked processes illustrated by their paired association in the hallmarks of cancer. They both share functional characteristics, allowing them to manipulate their environment and activate extracellular processes to their advantage (5).

## 1.2 Cell migration

The underlying basis for invasion and metastasis is the mobility of cancer cells. Common treatment regimens targeting the removal or destruction of primary tumours include surgery, radiotherapy and chemotherapy depending on cancer type. In some cancers, this approach has been shown to be successful in promoting cancer remission (6). However, when cancer cells start to spread via cell migration and invade surrounding tissues, treatment becomes more difficult.

The potential of a malignant tumour to induce a metastatic cascade highlights the importance of treating cancer as early as possible or targeting migratory activity at late diagnosis.

Cell migration is a vital cellular process; the orchestrated movement of cells to a specific site, in a directed manner, allowing for a number of biological processes including the developmental formation of organs, wound healing and immune responses (7). Cell migration, regardless of cell type, occurs by similar molecular mechanisms that have been evolutionally protected. However, deviations in the migratory process can be detrimental to health and have devastating consequences resulting in disease, organ failure and in many cases death (8).

In order for cells to migrate, a dynamic interaction between cell and substratum must occur. It also requires an orchestrated interaction between the cell actin cytoskeleton (cell motility), the microtubules (cell polarity) and focal adhesions (cell attachment). These interactions can create very distinct modes of migration leading to a diverse range of cell movement. For motility of a single cell, two main types of migration ‘mesenchymal’ or ‘amoeboid’, are recognised (9).

### 1.2.1 Mesenchymal migration

Mesenchymal cell migration is characterised by a leading-edge protrusion caused by actin extensions (lamellipodia) through cell polarisation. This protrusion leads to adhesion formation, cell body translocation, de-adhesion and retraction of cell rear (10). This process requires the interaction of multiple members of the Rho family, in particular the Rho GTPases Rac1, active Rho and

Cdc42, which work collectively to control the actin cytoskeleton (11). Rho GTPases, a sub-group of the Ras superfamily, are a small family of signalling G proteins that are expressed across all species. They are involved in a wide spectrum of cellular functions and like all members of the Ras superfamily, Rho GTPases are a collection of molecular switches within the signal transduction pathways in eukaryotic cells. This means they have an ability to switch between active and inactive states allowing fast cellular responses to extracellular stimuli, resulting in precise coordination of intracellular activities for cell migration.

The regulation of membrane protrusions and actin polymerisation requires Rac1 at the front of the cell, which is spatially restricted (12). Rac1 activation leads to cell polarisation, which subsequently coordinates actin polymerisation and protrusion of lamellipodia. Cdc42 also has a role in encouraging actin polymerisation by maintaining cell directionality through attachment and alignment of microtubules. These events form an actin-rich protrusion (13). Rho regulates the formation of actin stress fibres and drives translocation of the cell body (14). This activity is reduced during protrusion extension and promoted during retraction.

The extracellular matrix (ECM) is a three-dimensional (3D) structure that is present in all tissues. The ECM is composed of water, proteins and polysaccharides; however, each tissue has a specific ECM composition and topology established during development. It provides an essential physical framework for the cellular components and initiates vital biomechanical and biochemical signals (15). It regulates cell adhesion, migration, proliferation and

differentiation by transmitting signals via cell-surface receptors (16). Cell differentiation is regulated by ECM remodelling. This important and controlled process involves quantitative and qualitative changes in the ECM and is mediated by specific enzymes that regulate ECM degradation (17). ECM remodelling plays a crucial role in governing structural integrity and regulating cell motility, growth and shape (18).

### 1.2.2 Amoeboid migration

In contrast, amoeboid cell migration is characterised by a rapid mode of motility with weak substratum adhesion (Table 1). It is driven by actin-rich pseudopods; elongated narrow structures that are as thick as the non-nuclear cytoplasm (in contrast to lamellipodia). More than one pseudopod extension is common in migrating cells along with secondary pseudopodia branching, resulting in a round or irregular morphology (19). Rho and Cdc42 signalling are the key players in amoeboid movement as they drive actomyosin contractility. However, the mode of cell movement is dependent on the activation of Rho/ROCK signalling (20). This signalling pathway is believed to induce blebbing through stimulation of actomyosin contraction. The enhancement of contractility enables amoeboid migrating cells to distort their shape in order to push themselves into gaps of free space in the ECM or to produce a significant amount of force to instead distort the surrounding ECM. Such intense invasiveness makes amoeboid migration, arguably, the most effective mode of cell movement (21). The differences between mesenchymal and amoeboid cell migration are summarised in Table 1.

| **Table 1. Phenotypic characteristics of mesenchymal and amoeboid modes of migration** | | |
|---|---|---|
| | **Mesenchymal** | **Amoeboid** |
| **Morphology** | Elongated | Rounded |
| **Attachment** | Integrin clusters creating focal adhesions | Weak, integrins diffused in membrane |
| **Migration** | ECM degradation and remodelling | Pushing through ECM |
| **Organisation** | Actin framework and stress fibres | Contractile actin cortex |
| **Speed/ Velocity** | Low (0.1-0.4μm/min) | High (0.4-5μm/min) |
| **Extensions** | Filopodia and lamellipodia | Blebbing and pseudopodia |

Table 1. A comparison between the phenotypic characteristics of mesenchymal migration and amoeboid migration in ECM.

### 1.2.3 Collective cell migration

A third main mode of migration is called collective cell motility. In this form, cells sustain their cell-cell interactions and migrate in sheets, clusters or strands (Figure 2). This can occur as an independent migrating cluster or remaining in connection with the tissue of origin (13). Collective migrating cells respond in coordination with the environment and promote otherwise immobile or directionally contrasting cells to adhere to the overall movement. This profound feature increases migration efficiency compared to single cell movements (22). The number of cells in a collective migration movement can vary from as few as 10 cells to thousands of cells, as can the distance they travel. Guidance signals take the form of chemical diffusion gradients (23). These guidance signals usually involve leader and follower cells, within the collective, to be in coordination. At

the front of the group are leader cells that receive the guidance signals and instruct the follower cells to conform to the collective movement, via cell-cell junctions (7).

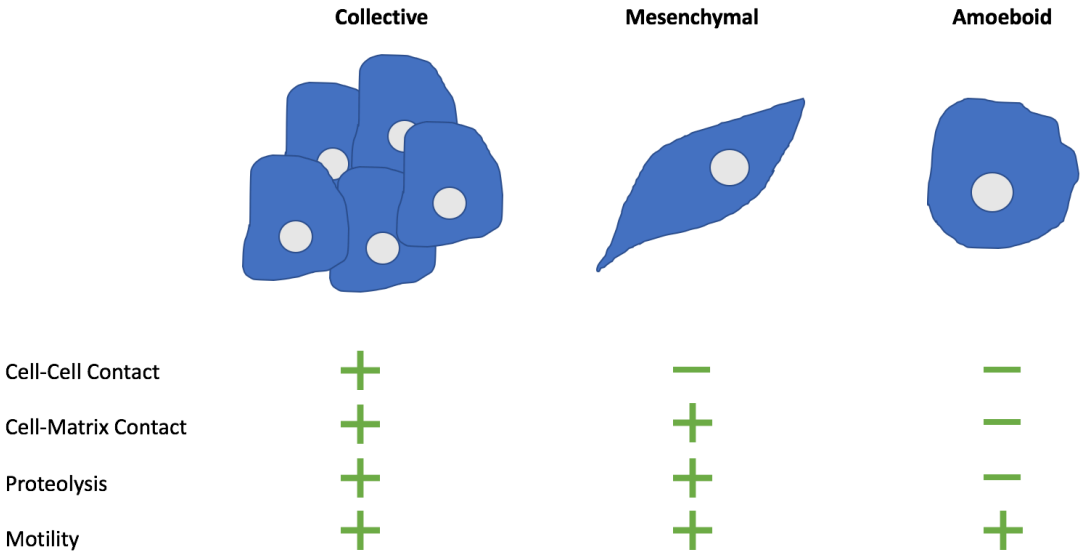


Figure 2. A diagram illustrating the different types of migration, collective, mesenchymal and amoeboid, and their properties.

### 1.3 Cancer cell invasion

As previously stated, cell migration is the directed translocation of cells from one site to another and occurs in the early stages of invasion, however it does not involve cell-cell interactions with neighbouring cells. Invasion is a separate, highly dynamic process that implicates cell-cell adhesion and proteolysis of the ECM (24). The process of invasion promotes the dissemination of tumour cells in the primary tumour to navigate through the ECM within a tissue or to infiltrate neighbouring tissues. Cancer cells that become invasive may infiltrate the circulatory and lymphatic systems, cross endothelial walls and basement membranes to colonise distant organs forming metastases. Amoeboid migrating cells undergo invasion by different means as their mechanisms do not involve ECM proteolysis but the process of expansion and retraction to squeeze through

gaps in the ECM (25).

### 1.3.1 Cell adhesion molecules

Changes to cell-cell adhesion occur via fluctuations in the levels of adhesion molecules that promote this linkage. When adhesion between cells is lost, tumour cells can dissociate themselves from the original tumour mass and initiate cellular events that lead to metastasis. Typically, cell adhesion molecules can be grouped into four families; the cadherins, the selectins, the integrins and the immunoglobulin superfamily (26).

Cadherins are transmembrane cell-cell adhesion molecules that are present in both simple and complex organisms. In addition to adhesion between cells, cadherins are responsible for a number of different processes in tissue morphogenesis including boundary formation, cell sorting and the induction and maintenance of cell polarity (27). During cell-cell communication, cadherins from one cell form trans-bonds at the position of contact. Once the cells are connected in trans-bonds, the cadherins control the development of cell-cell contact via three different mechanisms: using adhesion tension to directly reduce the local interfacial tension, signalling to the actomyosin cytoskeleton to indirectly reduce interfacial tension and determining the mechanical coupling of communicating cells (28).

One of the most well-characterised and important cadherins in cancer cell invasion is epithelial-cadherin (E-cadherin). As well as being involved in cell-cell adhesion, E-cadherin is responsible for the formation of epithelial cell sheets (29).

The *E-cadherin* gene has been extensively studied in the field of cancer progression and has been found to play a major role in malignant cell transformation. It is known as the 'suppressor of invasion' gene, due to the fact that *E-cadherin* gene suppression is recognised as one of the key events accountable for the dysregulation of cell-cell adhesion. Most tumours that have a loss of this gene present with abnormal cell morphology and reduced tissue stability leading to invasion. The loss of E-cadherin function directly correlates with metastasis and invasiveness (30). Interestingly, although this is true for most cancers, in gliomas E-cadherin has little value as a prognostic marker. A study into the prognostic significance of E-cadherin expression in gliomas showed that identification was rare in both low and high grade gliomas, which is to be expected due to glioma being a non-epithelial malignancy (31).

Selectins are calcium-dependent transmembrane lectins that initiate the first step in leukocyte extravasation during an inflammatory response; the binding of leukocytes to the activated endothelium of blood vessel walls (32). Cancer cells take advantage of this cellular process and use their own surface selectins to bind to blood vessel walls and get extravasated in order to invade other tissues in the metastatic cascade. This mechanism is the most researched and most evident function of selectins in cancer progression (33).

Integrins are large, complex heterodimeric glycoproteins that contain an $\alpha$ chain and a $\beta$ chain. Integrins facilitate cell-cell adhesion, directly bind ECM components and function as an anchorage system for cell migration and invasion (34). As well as these processes, integrins also activate growth factor receptors

and promote proliferation and cell survival. They also enable bidirectional signalling promoting changes in cell structure. Many human tumours arise from malignant transformation of epithelial cells, therefore as integrins are expressed on epithelial cells, they are also expressed on the transformed cancer cells and expression is correlated with metastasis and patient survival (5).

Epithelial-mesenchymal transition (EMT) is a dynamic mechanism by which polarised epithelial cells undergo a number of conformational and biochemical changes which enable them to become motile by adopting a mesenchymal phenotype and invasive properties (5). Epithelial cells are highly polarised and are closely linked by a number of different cell-cell junctions including gap junctions, tight junctions, adherens junctions and desmosomes. A key step in EMT is the loss of these intimately connected junctions between neighbouring cells, allowing the dissociation of cells from the primary tumour. Therefore, EMT is typified by a loss of these junctions and their proteins, including E-cadherin, and a gain of mesenchymal markers including neural-cadherin (N-cadherin), vimentin and fibronectin (35). EMT also presents with reorganisation of the actin cytoskeleton and a loss of polarity resulting in the cells taking on an elongated migratory phenotype. This ‘cadherin switch’ is also a key characteristic of EMT and appears to be a necessity in the gain of invasive properties for tumour cells (36).

### 1.3.2 Proteolysis of the ECM

The ECM is a dynamic environment providing growth factors and matrix proteins to control cellular functions including remodelling and structural support. In order

to create a favourable environment for tumour cell proliferation and invasion, proteases remodel and degrade the ECM allowing room for these neoplastic processes (15). There are 5 groups of proteases that are known to remodel and degrade the ECM including serine, cysteine, aspartate, threonine and matrix metalloproteinases (MMPs) (18).

A third of all proteolytic enzymes are the serine proteases. They are involved in a vast number of different biological processes including development, fertilisation, digestion and blood coagulation (37). The well-known digestive serine protease trypsin has been implemented in various cancers to promote proliferation, invasion and metastasis. In colorectal cancer, expression of trypsin is correlated with poor prognosis and survival (38). Another serine protease, urokinase-type plasminogen activator (uPA), has a membrane-bound receptor (uPAR), which induces the degradation of two ECM proteins, fibronectin and laminin, causing structural changes to the ECM resulting in channels for invading cells (39).

Cysteine proteases are characterised by an active site cysteine residue. These proteases are involved in intracellular protein catabolism and signalling molecule activation (including interleukins and protein kinase C), as well as the degradation of the extracellular proteins laminins and collagen (38). A unique feature of cathepsin cysteine proteases is the ability to degrade both extracellular and intracellular matrix proteins. Their extracellular activity permits cancer cells to invade surrounding tissues and thus are said to be promising anti-cancer targets (40).

Aspartate proteases possess a catalytic site consisting of two aspartate residues. Cathepsin-D (Cath-D), an aspartic endo-protease, is found universally in all lysosomes and works to degrade them (40). It is overexpressed and over-secreted in breast cancer and has been used as a marker for poor prognosis due to its role in promoting cancer cell proliferation, angiogenesis and metastasis. It was shown that Cath-D is a rate limiting factor in tumorigenicity, outgrowth and lung colonisation in breast cancer cell lines (38).

Threonine proteases play an important role in the degradation of cellular proteins. They are catalysts in a complex mechanism called polyubiquitinisation, whereby a series of ubiquitin molecules bind to the same target protein. This is a trigger signal that leads to the degradation of proteins in the proteosome. This mechanism has been linked to cancer invasion and studies into threonine protease inhibitors have been suggested as a cancer therapy (38). Inhibition of threonine proteases have been shown to induce accumulation of pro-apoptotic proteins in tumour cells, but not in normal cells, leading to programmed cell death to be induced in cancer cells. The first US FDA-approved inhibitor drug of this kind, Bortezomib, was used for the treatment of multiple myeloma, relapsed/refractory multiple myeloma and mantle cell lymphoma (41).

Matrix metalloproteinases (MMPs) are enzymes which have the capability to degrade all types of ECM protein. Because of their action, they can create tracks for cancer cells to migrate along, therefore promoting invasion and progression (18). Studies have shown a direct correlation between MMP expression and

tumour invasiveness. In addition to this role, MMPs also promote cell proliferation, differentiation and angiogenesis (42).

### 1.4 Actin polymerisation

The driving force that propels cell migration is built from the actin cytoskeleton; the largest cell organelle. By assembly and disassembly, the actin cytoskeleton can completely change the morphology of a cell with ease and flexibility. Differing from other large protein complexes, the actin filaments that make up the cytoskeleton vary in length, abundance and organisation (43). The ability to create networks and bundles of cross-linked filaments in a flexible and rapid manner underlines the importance of actin in cell migration and explains its well established place in this field of research.

In terms of mass, actin is the most abundant protein in the majority of cell types, partaking in more protein-protein interactions than any other known protein. Its ability to shift between two states, globular and filamentous, makes actin an important player in many cellular functions apart from motility including cell shape and polarity (44). When globular actin (G-actin) polymerises into filamentous actin (F-actin) it can result in a range of different organisational arrangements including branched, cross-linked bundles and contractile structures. It is these mechanical assemblies that drive shape changes within the cell and promote cell motility (45).

When the concentration of actin monomers (G-actin) reaches a certain level, polymerisation into F-actin occurs. These F-actin strands link each other in a double-helical structure and form distinct ends to the polymer; a barbed end and

a pointed end (46). Because the subunits of the polymer all have the same orientation and directionality, actin filaments are polar. The monomers are preferentially added onto the barbed end and lost at the pointed end. However, as actin polymerisation is an equilibrium process, either activity can occur at both the barbed or pointed end of the polymer. It is the kinetics of the polymerisation process that differ, i.e., a more rapid growth of the barbed end of the filament than the pointed end (10). Within an internal cleft of monomeric actin, ATP is bound to stabilise the globular structure. Shortly after filament assembly, the actin-bound ATP gradually releases the terminal phosphate from the bound ATP through hydrolysis (47). This process does not regulate actin polymerisation but acts as an internal clock that is keeping track of the filament's age. It activates the disassembly of actin filaments within the cell when the filament's lifespan is at an end (48).

When an actin polymer is not in the process of shortening or lengthening, it is said to be in equilibrium. When it is in this state it is constantly dissociating actin monomers at the pointed end and associating monomers at the barbed end. As a result of this, an actin monomer added at the barbed end will ultimately move along the filament until it is dissociated at the pointed end. This continuous progression is known as treadmilling (49). Treadmilling is made possible by the free energy created by the hydrolysis of ATP. It may seem that this energy is being lost to a process that has little advantage to the cell, however, treadmilling provides the cell with a way in which to control the cytoskeletal organisation (50). This means if there is a requirement for filaments in a different region of the cell, disassembly of existing actin filaments is instantaneous as is the re-assembly of

the new actin filaments due to the rapidly diffusing actin monomers. This spatial and flexible arrangement allows cellular control over actin filament location and overall cellular structure (43).

### 1.4.1 Actin polymerisation activators

Recent evidence linking Rho GTPases to a range of diseases has raised interest in the signalling pathways and downstream processes, including actin polymerisation, as potential targets for pharmacological intervention. Continuing studies into the identification and functions of vital players involved in actin polymerisation is key to developing new therapeutic treatments for cancer progression and many other diseases (51).

Potential key players in this process are members of a large family of over 30 genes called the *ARHGAP*s. *ARHGAP* genes have been described in scientific literature as being associated with a number of diseases; the main one being cancer. However, the detail on this is minimal. The *ARHGAP* genes encode a group of proteins called Rho GTPase activating proteins (RhoGAPs), which interact with Rho GTPases. They are primarily known for their role in regulating the actin cytoskeleton and, therefore, are involved in cell migration (52).

### 1.4.2 RhoA transcriptional signalling pathway

Rho GTPases make up one of five distinctive families in the Ras superfamily. Included in the 23 members of the Rho family subgroup are Rho, Rac and Cdc42; three of the best characterised Rho GTPases. Rho-like proteins are highly conserved and act as molecular switches, regulating signal transduction

pathways by cycling between an inactive (GDP-bound) and an active (GTP-bound) state (11). Rho GTPases are activated via stimulation of cell surface receptors known as G-protein coupled receptors (GPCRs). This family of receptors produces a multitude of cellular functions when activated by extracellular stimuli, such as hormones, cytokines, lipids, proteases and neurotransmitters (53). The G-proteins consist of the protein subunits Gα, Gβ and Gγ to form a heterodimer. When activated, the Gα subunit exchanges GDP for GTP, whilst the Gβ and Gγ disassociate. The now activated GTP-bound Gα and Gβγ can interact with their corresponding effectors and generate various downstream effects such as cytoskeletal changes, cell motility, cell growth and gene transcription (54). The Rho family of GTPases is best known for its involvement in cytoskeletal changes, which promote cell motility. The three main subgroups (Rho, Rac and Cdc42) are responsible for this through their control of focal adhesions, stress fibres and cell protrusions (lamellipodia and filopodia).

The activation of Rho GTPases is regulated by a number of other protein families. Guanine nucleotide exchange factors (GEFs) catalyse the exchange of GTP for GDP thus activating Rho GTPases and promoting the downstream effects. The RhoGAPs do the opposite, thus inactivating Rho GTPases by hydrolysing GTP (Figure 3). Guanine nucleotide dissociation inhibitors (GDIs) extract Rho GTPases from membranes and solubilise them in the cytosol, preventing their activation and membrane localisation (55).

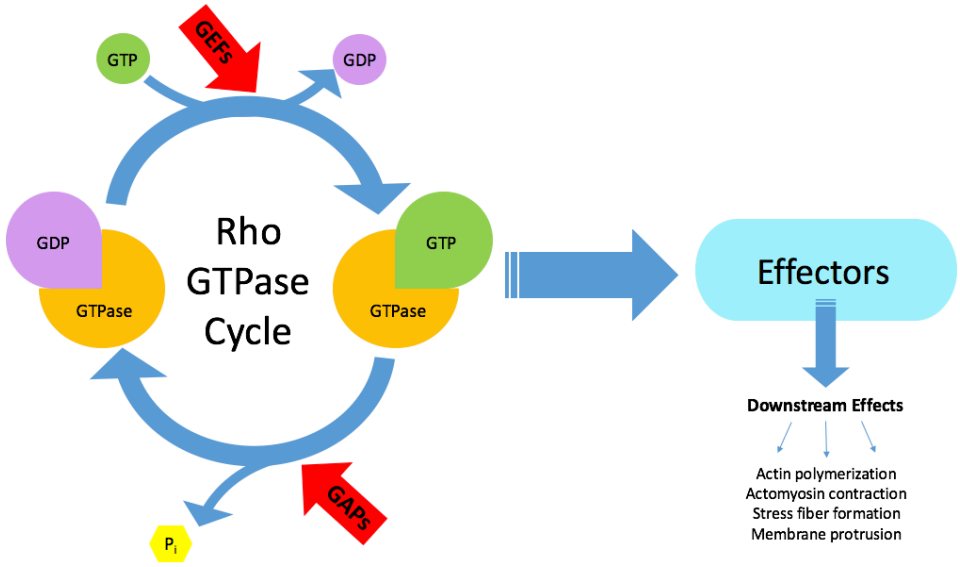


Figure 3. The Rho GTPase Cycle. Rho GTPases cycle between an inactive GDP-bound state and an active GTP-bound state. They are regulated by RhoGEFs and RhoGAPs. Active GTPases then interact with an effector protein to initiate a response and promote downstream effects.

RhoGEFs are activated by $G_{12/13}$ signalling of GPCRs. There are four mammalian RhoGEFs that are known to be regulated by $G_{12/13}$ and link the activation of GPCRs to the small Rho GTPase, RhoA. These are p115-RhoGEF, PSD-95/Disc-large/ZO-1 homology-RhoGEF, leukaemia-associated RhoGEF and lymphoid blast crisis-RhoGEF (56). RhoA promotes reorganisation of the actin cytoskeleton and regulates cell shape, attachment and motility. It mediates the activation of Rho Kinases (ROCK1/2) which leads to the phosphorylation of focal adhesion kinase (FAK). FAK induces the formation of actin stress fibres and the activation of serum response factor (SRF); a widely expressed and highly conserved, single copy transcription factor (57). In the nucleus, SRF binds to serum response element (SRE) sequences in the promotor of specific genes, regulating their transcription. SRF has a crucial role in cell migration and the actin cytoskeleton. Genomic studies have revealed that out of the 200+ SRF target

genes, over half of them encode proteins with functions that relate to actin dynamics, contraction, lamellipodia/filopodia formation and integrin-cytoskeleton coupling. It is therefore an essential part of the actin cytoskeleton and contractile homeostasis (57).

SRF interacts with a number of transcriptional coactivators in order to stimulate gene expression. In the RhoA signalling pathway, a key SRF interactant is megakaryoblastic leukaemia 1 (MKL1) (58). MKL1 (also known as megakaryocytic acute leukaemia [MAL] and myocardin-related transcription factor A [MRTF-A]) was originally identified in acute megakaryoblastic leukaemias of infants and children through its fusion to RBM15 (RNA binding motif protein 15); a unique interaction found in leukaemias. More recently, MKL1, along with its other family members MKL2 and myocardin, have been shown to be coactivators to SRF and have a vital role in the activation of SRF target genes (59). Within the cell, MKL1 is bound to monomeric G-actin. When actin polymerisation is induced, MKL1 is released from G-actin and is imported from the cytoplasm into the nucleus by an importin $\alpha/\beta$ heterodimer where it forms a complex with SRF and activates the target genes (60).

### 1.4.3 RhoA transcriptional signalling pathway and cancer

The link between Rho proteins and cancer was not discovered for some time due to lack of evidence of activating mutations within the coding sequences of these proteins. Now it is well known that Rho GTPases play a fundamental role in many aspects of tumorigenesis such as cell migration, invasion and metastasis. Rho proteins are found to be overexpressed in numerous tumour types (43). For

example, overexpression of RhoA was found in breast, colon and lung, Rac1 is overexpressed in breast, lung and testicular and Cdc42 is also overexpressed in breast and testicular cancers (61).

As well as overexpression of the Rho GTPase itself, the mis-regulation of these proteins can also occur in cancer through irregular changes in RhoGEFs, RhoGAPs and GDIs. For example, MyoGEF, a RhoGEF, has been shown to drive invasive breast cancer through its activation of RhoA and RhoC (62). Another GEF, known as Tiam1 (Rac specific), was identified as a promotor of T lymphoma invasion as well as being overexpressed in breast cancer (63). Deleted in liver cancer 2 (DLC2) is a GAP that is found to be under-expressed in many types of hepatocellular cancers and also in fibrosarcoma of bone. ARHGAP35 is a well-known tumour suppressor in gliomas and has been found to be deleted in 50-80% of oligodendrogliomas. When overexpressed in these cancers, ARHGAP35 reduced proliferation and expression of nestin; a neural precursor marker (64). With RhoGDIs, there are conflicting data on their alterations in cancer with studies showing both increased and decreased expression in a number of different cancer types (61). An imbalance of Rho and RhoGDIs has been shown in breast cancer with an excessive level of Rho and a reduced level of RhoGDIs. This results in the inability to switch off Rho, leading to increased invasion. This correlates with the fact the RhoGDI-2 mRNA was found to be expressed in low-invasive breast cancers but not high-invasive (65). In contrast, the same RhoGDI-2 is upregulated in ovarian cancer, showing the contradictory action of RhoGDIs in cancer (66).

Arguably, one of the most prominent Rho effectors that has a role in cancer progression is the Rho-associated protein kinase (ROCK). ROCK, like its activators, RhoA and RhoC, is overexpressed in a number of different cancer types (67) including pancreatic cancer, oesophageal squamous cell carcinoma and hepatocellular carcinoma (68–70). ROCK has been shown, both *in vitro* and *in vivo*, to be associated with metastasis in the B16 melanoma models, HT1080 lung cancer and MDA-MB-231 breast cancer cell lines (71,72). Through the use of 3D-Matrigel matrix assays, ROCK has been shown to be a key player for *in vitro* cell invasion in rounded blebbing cells (amoeboid) vs elongated cells (mesenchymal) (73). In addition, ROCK has been implicated in the regulation of MMPs in hepatocellular carcinoma and colon cancer cells. This means that ROCK has the ability to regulate MMP-dependent types of cell migration in certain cancer types and could therefore function as a successful therapeutic target for cancer treatment (74).

### 1.4.4 Targeting the RhoA transcriptional pathway

The RhoA transcriptional signalling pathway has been thoroughly studied in cancer progression, however, very few inhibitors have been developed to target it. The inhibition of carboxy-terminal isoprenylation of active Rho GTPases has been the focus of most inhibitor studies of this pathway. Carboxy-terminal isoprenylation is a modification of lipids and is vital for the membrane localisation of Rho GTPases and their functions (75). However, the drugs used to inhibit this lipid modification, including inhibitors of farnesyl transferase and geranylgeranyl transferase as well as statins, are not selective for the Rho family or GTPases or the RhoA transcriptional signalling pathway (76).

ROCK has also been the subject of many inhibitor studies for this pathway. Compounds, including Y-27632, fasudil and WF-536, have achieved promising results in both *in vitro* and *in vivo* anti-invasion experiments (69,70). However, one of the drawbacks of these drugs is their limited inhibitory effects targeting only one branch of the RhoA signalling pathway (Figure 4). As a consequence, these inhibitors may be ineffective against tumours that rely upon the transcriptional branch (branch II) of the same pathway (77).

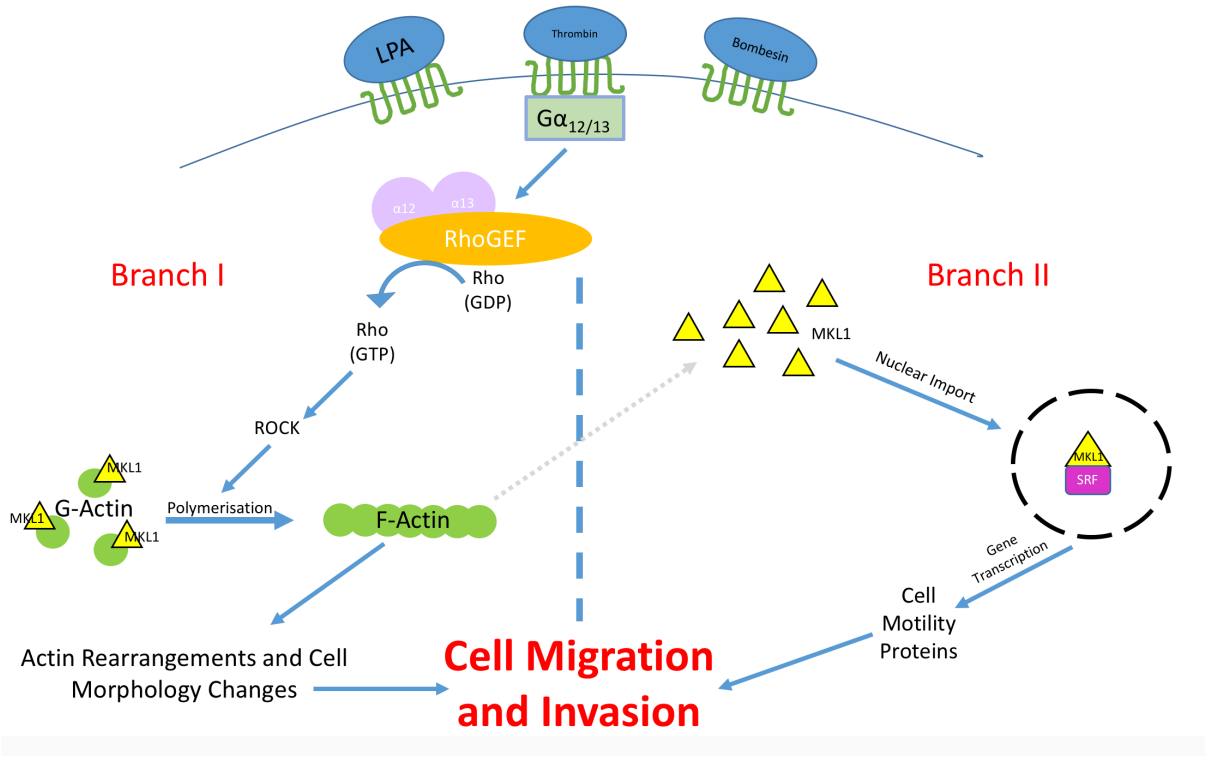


Figure 4. A simplified schematic diagram of the RhoA signalling pathway. Branch I shows the RhoA pathway that results in morphological changes to promote migration. Branch II shows the transcriptional pathway of RhoA whereby MKL1 is imported into the nucleus to form a complex with SRF. This promotes cancer cell migration and invasion by gene production of motility proteins following gene transcription.

In addition to the ROCK inhibitors, two specific inhibitors of the Rho GTPase signalling pathway (NSC23766 and EHT-1864) have been shown to directly

inhibit the Rho GTPase, Rac1 (78) (79). As with the other inhibitors, these drugs do not target the RhoA transcriptional signalling pathway and so would become ineffective. The need for inhibitors that target specific regulators and effectors of the RhoA transcriptional pathway is still evident in order to target the progression of cancer and stop invasion and metastasis.

### 1.4.5 Anti-invasion and anti-metastatic treatments

In solid tumours, invasion and metastasis account for 90% of the fatalities in cancers, yet there is a lack of anti-invasion and anti-metastatic drugs in treatment regimens (80). Candidate drugs for anti-cancer treatments are still mainly evaluated on their efficacy to reduce tumour size by their cytotoxic effect on cancer cells. This approach is understandable, however, tumour shrinkage is rarely sustainable and is not a predictor of an anti-invasive effect (81).

Another difficulty in anti-cancer treatments is drug resistance. This is a recognised problem as a result of a disease becoming tolerant to a pharmacological intervention. Drug resistance was first studied in bacteria with antibiotic resistance but is also now documented in other diseases including cancer. Some processes of drug resistance can be specific to certain diseases but others are evolutionally conserved, such as drug efflux in drug-resistant human cancers. A family of proteins known as ATP-binding cassette (ABC) transporters facilitate efflux and are important biological regulators at plasma membranes in healthy cells. ABC transporters push toxins out of cells in order to prevent toxin accumulation. Although this is a normal process in healthy cells, in

cancer cells this is a recognised mechanism of drug resistance and results in protection against chemotherapy (82).

Recently there has been an increase in the number of studies on anti-invasion drugs in order to address the high cancer mortality rate associated with cancer invasion and metastasis. First attempts to target cancer invasion by using synthetic MMP inhibitors showed promising results *in vitro*. Following *in vivo* studies also produced effective inhibition of growth and invasion and increased survival in treated mice compared to control mice (83). However, when taken forward to clinical trials no benefits with MMP inhibitors were observed in a variety of cancers, including pancreatic, glioblastoma, lung, ovarian and renal, and toxicity was also associated with this type of treatment (84). It is now acknowledged that pharmacological inhibition of MMP activity or integrin function is associated with a cellular motility shift, i.e., switching from one mode of migration to the other. Mesenchymal-amoeboid transition (MAT) or amoeboid-mesenchymal transition (AMT) can be promoted by environmental or epigenetic factors (85). These changes create an advantageous state for cancer cells to metastasise (86). It is also important to note that non-migrating cells, for example epithelial cells, can undergo EMT to become mesenchymal migratory cells (87). From here the cells can then undergo transition again via MAT (25).

L-type calcium channels have been identified as regulators of filopodia; cytoplasmic projections extending at the leading edge of a migrating cell. Studies in p53 mutation breast cancers have demonstrated that L-type calcium channels are present and functional in cancer cells, uncovering a novel role for these

channels in tumour progression. Blocking the channels with FDA-approved calcium channel blockers has proved to have an anti-migratory effect in cancer cells by inhibiting the formation of filopodia (88).

Studies using *in silico* screens have uncovered that cell migration can be reduced by using drugs that affect the fluidity of the cell membrane. Over-expression of ABCA-1, a regulator of membrane fluidity and cholesterol, in breast cancers has been associated with cancer metastasis (89). Drugs targeting this cholesterol efflux regulatory protein, through either pharmacological or genetic inducers, allow the manipulation of metastatic processes. *In vivo* mouse models showed that reducing the fluidity of the cell membrane prevents metastasis and inhibits and/or reverses epithelial-mesenchymal transition (EMT) which is commonly associated with cancer invasion and metastasis (90).

An increasing number of experimental techniques have been developed recently that aim to screen and identify anti-invasion drugs for improved cancer patient survival. One such technique is a high-throughput three-dimensional invasion assay, involving the embedding of a tumour spheroid in collagen, which provides a 3D environment for the cells to migrate and invade into (91). By using a 3D matrix, the natural 3D tumour environment can be mimicked rather than using a 2D assay before validation in *in vivo* studies. Drug development based on testing drugs on 2D cell monolayers has been shown to not effectively translate to clinical trials resulting in a high rate of trial failure due to limited drug efficacy (92). Live cell imaging of tumour cell generated spheroids allows insights into cell dynamics

of migrating cells, modes of migration by different cell types and the effects of drugs on cell morphology.

Immunocytochemistry can also be employed on the collagen-embedded spheroids adding another level of assessment of drug efficacy (93). Large scale screening of such 3D-based assays will enhance accuracy of research findings and increase the chance of identifying drugs to progress towards trial phases.

A new trend in cancer invasion research has been introduced known as migrastatics; a term used to describe drugs that interfere with cancer cell migratory mechanics and their ability to metastasise. Migrastatics have been proposed to specifically focus on inhibiting metastasis and invasion and to distinguish between drugs of a cytostatic nature that target proliferation and those that are specifically for anti-invasion purposes. For a successful launch of migrastatics, regulations for the approval of anti-cancer drugs targeting invasion need to be modified so that, in the absence of tumour shrinkage, candidate drugs can still be clinically evaluated. There is also an urgent need for large-scale testing of drug archives as well as testing new drugs that interfere with cell migration and invasion (81).

### 1.5 Brain tumours - World Health Organisation classification of tumours of the central nervous system

There are over 120 different types of brain and central nervous system tumours, all with different histological patterns, cell phenotypes, behaviours and mechanisms of progression and survival. This poses a great problem for neuro-oncologists, neuro-pathologists and research scientists, alike, for diagnosis,

treatment and development of new treatments, as variances between the types of brain cancer can be slight but can have an important impact on tumour progression (94). In 2016, the World Health Organisation (WHO) published a reclassification of tumours of the central nervous system to introduce a more precise classification system in neuro-oncology and to reflect the heterogeneity of these tumours. The 2016 WHO classification of tumours of the central nervous system classifies brain tumours by cell origin, cell behaviour and least aggressive (benign) to most aggressive (malignant). Invasive tumour types are given a grade based on their rate of growth from least aggressive (Grade I) to most aggressive (Grade IV). By grading and classifying an individual tumour, predictions can be made on how the tumour is likely to behave (95). The information gathered and formed into the new classification combines histology with molecular biology, providing a tool that enables clinicians to deliver more accurate diagnoses, prognoses and treatment plans for patients. The new classification will also improve research and contribute to the development of novel treatments for this set of tumours as it allows scientists to be more selective and target particular tumour types. Eventually this will ensure that patients are matched to clinical trials according to the molecular make-up of their tumour and will receive targeted therapeutic intervention that will have the most advantageous effect. Another benefit of the updated classification is the effect on basic research. It will provide a platform for more accurate analysis and interpretation of experimental results, allowing for the identification of causes of tumour progression (96). By incorporating the integrated classification of molecular characteristics and histopathology, the brain tumour field will be able to progress to the same level

as other well-researched cancers, resulting in the development of highly targeted treatments for personalised care plans for brain tumour patients.

### 1.6 Gliomas

The 120 different types of brain tumour are generally named after the type of cell from which they originate. Gliomas develop from glial cells and account for 30% of all brain and central nervous system tumours (97). Gliomas can develop in the spine or the brain, the latter being the most common accounting for 80% of all malignant brain tumours. In 2013, 10624 new brain tumour cases were diagnosed in the UK with just 19% of patients surviving 5 years or more (98). Worldwide, 256 000 people were diagnosed with a primary brain tumour in 2012 (99). There are three types of glioma; ependymomas, oligodendroglioma and astrocytoma. Astrocytomas account for 50% of all brain tumours and are graded from I to IV, IV being the most severe and known as glioblastoma (GBM) (100). These cancers are especially prevalent among children and the young adult, accounting for the biggest loss in life due to a cancer among all cancer types. In addition, personality changes frequently observed in glioma patients place a big strain on relatives and carers.

### 1.7 Glioblastoma

The location and infiltrative nature of GBM means surgery alone cannot cure it as it cannot be completely resected, unlike other cancers that can be completely cured by surgery such as non-melanoma skin cancer and testicular cancer. In addition, the characteristic of GBM resistance to therapeutic intervention stems from the complex disposition of the tumour itself (101). One of the main

contributors to the poor prognosis of GBM is its cellular heterogeneity. Phenotypical heterogeneity is evident in GBMs as they are composed of cell populations that express markers of both differentiated and undifferentiated cells. The level of differentiation and cell type varies between tumours, which exposes a fundamental difference in the progenitor cells of individual tumours (102). Sottoriva et al. (2013) demonstrated that GBM exhibits a multitude of heterogeneous mutations across the whole genome, backing the concept that individually tailored treatments need to be developed based on a range of biopsies from the same GBM (103).

This heterogeneity has been associated with glioblastoma stem cells (GSCs), which in themselves, are a distinct subpopulation in GBM that are responsible for hierarchal cellular organisation. GSCs can be functionally defined by their self-renewal properties and ability to give rise to a mass of heterogeneous tumour cell progeny (104). Whilst GSCs have been found to have a high tumorigenic potential, their proliferation rate remains low, presenting a similar phenotype to normal stem cells, including *CD133* gene expression and other commonly expressed genes in neural stem cells. GSCs coordinate a number of other biological aspects of GBM including therapy resistance, cellular invasion and recurrence of tumour. Due to the failures of therapies to completely eliminate GBM tumours, the remaining cancer cells will greatly consist of those in a stem cell state, leading to tumour recurrence and regrowth. This underlines the need for stem cell specific targeting within therapies to prevent the regrowth of cancer cell populations (105).

The heterogeneous GBM cell populations take advantage of their surroundings by detecting and responding to external signals from the environment. Direct interactions of tumour-associated parenchymal cells and GBM cells control the progression of the disease and make up the tumour micro-environment that has a pathological impact on malignant brain tumours (106). Microglia are the most prevalent inflammatory cells that are able to penetrate GBMs by degrading the ECM. By doing so, these tumour-associated macrophages enhance the invasion of GBM cells into the surrounding brain. This infiltration of microglia is conducted by the tumour itself via the release of chemo-attractive cytokines, in order for it to take advantage of degradation carried out by the macrophages (107).

Angiogenesis is a physiological process whereby new blood vessels form from pre-existing ones (108). It is a key factor in the progression and growth of GBM with microvasculature proliferation being linked to tumour aggression and recurrence. Microvessel density can be used as a postoperative prognostic marker. Through the use of the immunohistochemical stain Von Willebrand Factor on paraffin embedded samples of GBM, a direct correlation has been shown between microvessel density and patient survival (105). The strong vasculature network of neurogenic niches has been shown as the site for stem cell production for both malignant and normal brain tissue (109). Malignant gliomas are one of the most vascularised tumour types. They inhabit perivascular niches and depend on these to control the balance between self-renewal and differentiation. These niches support the tumours by providing nutrients and removing metabolic by-products (110).

The treatment of GBM is difficult and there are no curative approaches. Research leading to a better understanding of the molecular mechanisms and genetic mutations of GBM, as well as clinical trials, is pointing towards more tailored therapeutic approaches. However, an array of challenges still remains, including tumour location, relapse and as previously mentioned, tumour heterogeneity. The current standard of care consists of surgical resection followed by radiotherapy and adjuvant chemotherapy with temozolomide (111). Nearly all patients will develop a recurrent tumour, despite therapy, and treatment options are limited to palliative care. For some, a second resection may be beneficial but for the majority of patients, chemotherapy remains the treatment of choice for recurrence. For patients with a decreased performance status (criteria used by clinicians to assess the progression of the disease) solely palliative care options could be more appropriate (112).

### 1.7.1 GBM subtypes

The Cancer Genome Atlas Network compiled recurrent genomic aberrations in GBM and classified them based on gene expression. This molecular classification forms four GBM subtypes; Proneural, Classical, Mesenchymal and Neural. Multidimensional genomic information was integrated into this classification to determine patterns of somatic mutations (113). By classifying GBM into subtypes, a foundation for improved molecular knowledge of GBM signalling pathways has been established that will potentially lead to personalised treatment plans for patients suffering from this devastating disease and improve survival rates.

Proneural GBM is characterised by *IDH/TP53* mutations, normal *EGFR/PTEN*/Notch signalling and is positive for the glioma-CpG island methylator phenotype (G-CIMP). The G-CIMP phenotype seems to be a common trait in low grade gliomas and provides a molecular classification for secondary GBMs, much like IDH mutation. Proneural GBM has neuronal differentiation and is commonly seen in young adults. This subtype of GBM is related to a better prognosis (114).

The mesenchymal subtype of GBM is characterised by aberrant *EGFR* amplification, *PTEN* loss, *NF1* and *TP53* tumour suppressor gene mutations and Akt signalling. It has mesenchymal differentiation and is common in older adults with an association with worse prognosis, however with very aggressive treatment regimens, significant increases in survival are seen in patients with this type of GBM (115).

Classical GBM tumour types are characterised by aberrantly high levels of EGFR, the highest of all the subtypes. In contrast, the *TP53* gene, which is the most common gene to be mutated in GBM, is not mutated in classical GBM tumours. In response to aggressive treatment regimens, patients with classical GBM tumours survived the longest when compared to the other GBM subtypes (115).

The neural GBM subtype has many of the same gene mutations as the other subgroups, with no particular mutation being shown as having a higher or lower frequency than the other groups. Neural GBM tumours are therefore characterised by the expression of standard genes of normal, non-cancerous

brain neurons and nerve cells. Patients with this type of GBM are normally older and do not respond as positively to aggressive treatment compared to the classical and mesenchymal subtypes (115).

## 1.8 Project rationale

GBM is the most common and most aggressive type of primary brain tumour. It is associated with very poor prognosis and a high mortality rate. The invasive phenotype of this cancer contributes to the low therapeutic response rate of patients and highlights the need for novel compounds that can target migration and invasion of these tumours. The work contained within this thesis aims to identify new targets of migration and develop novel approaches in which to stop invasion in GBM.

### 1.8.1 Aims and objectives

1. **Characterise the migrational properties of established glioma cell lines and assess the effect of known actin polymerisation and RhoA signalling pathway inhibitors on these cell lines**

Glioma cell lines U87 and U251 will be tested to evaluate their migratory properties *in vitro* using a range of 2D and 3D assays. A panel of actin polymerisation and migration inhibitors will be used to assess their effect on the candidate cell lines. This will lead to novel findings on characterisation of migratory abilities among glioma cell lines and on the activity inhibitors on glioma cell migration.

2. **Select candidate inhibitor from the panel and determine mechanisms of inhibition in the actin polymerisation pathway**

The study will focus on the activity of an inhibitor selected from the initial panel to assess for effect on cell migration in terms of motility and morphology in detail. This will uncover new mechanisms and pathways that promote GBM cell

migration and to focus on for the development of novel strategies to improve GBM survival rates.

3. **Establish advanced 3D technologies for the assessment of drug activity for improved accuracy of *in vitro* drug development**

There is a need for more representative *in vitro* assays and data analysis for anti-migratory drug development as most drugs taken forward to clinical trials fail in this field of brain tumour research. By developing a new technique that mimics the physiological environment within the brain, candidate drugs are selected more efficiently for application in preclinical trials.

# Chapter 2: Inhibitors of the actin polymerisation pathway and their effects on glioma cell migration

## 2.1 Introduction

Actin polymerisation is a key process in cell migration. As previously mentioned, it drives rearrangements of the actin cytoskeleton allowing cells to rapidly change their morphology to respond to external cues for efficient migration. Inhibition of G-actin monomer polymerisation into an actin filament prevents actin rearrangements resulting in loss of cell migration (116).

### 2.1.1 Inhibitors of the actin polymerisation pathway

Pharmacological inhibitors that interfere with actin polymerisation, depolymerisation and actin cytoskeletal rearrangements are commonly used to investigate the role of actin dynamics in a number of different cellular processes. These inhibitors can be grouped into several different classes (117). The most prominent class of inhibitors includes those targeting actin polymerisation. Examples of drugs in this class include latrunculin, which directly sequesters the free G-actin monomers preventing their polymerisation onto the filament chain, and cytochalasin, which binds with high affinity to the barbed end of the actin filament stopping the addition of G-actin (118,119). Another class of actin inhibitors comprises compounds that prevent the disassembly of actin filaments. An example of this class is the drug jasplakinolide, which is commonly used as a stabilising drug for actin filament polymerisation (120). However, at high concentrations, it can interfere with depolymerisation by joining the majority of free G-actin monomers to the filament and lowering the dissociation rate (121). A further class of actin inhibitors includes drugs that have an effect on actin

rearrangement. Myosin II is a motor protein involved in the reorganisation of the actin network causing cells to shift from generating protrusions to contraction (122). Blebbistatin is a small molecule inhibitor that blocks myosin in an actin-detached state preventing acto-myosin crosslinking (123). Other drugs in this class inhibit myosin II activators such as the ROCK inhibitor Y-27632 (124).

Actin inhibitor studies have not only allowed the identification of actin cytoskeletal-dependent cellular processes but have also become a useful tool in investigations in clinical studies (Table 2). There have been a number of successful clinical trials with actin inhibitors. In the field of optometry, such studies include latrunculin B and cytochalasin B. In a phase I clinical trial using latrunculin B it was observed that the inhibitor reduced intraocular pressure in glaucoma patients through its inhibition of ROCK, which induces muscle relaxation (125). Cytochalasin B was used in a phase I clinical trial to investigate its effect in patients after a coronary angioplasty. This study showed that delivering cytochalasin B directly to the arterial walls decreases restenosis (an abnormal recurrence of narrowing of the artery or valve wall after corrective surgery) by preventing the depolymerisation in vascular smooth muscle cells that occurs as a result of balloon angioplasty trauma (118). Another successful actin inhibitor clinical trial includes the drug HA-1077 (fasudil), another ROCK inhibitor and vasodilator (126). It was found that fasudil significantly reduces cerebral vasospasm and cerebral infarction occurrence in patients with subarachnoid haemorrhage, improving the clinical prognosis of these patients. The initial study based on a small sample size produced promising results, with further validation envisaged in a larger clinical trial (127).

In GBM research, a drug repurposing study identified fluvoxamine, a clinically used anti-depressant, to be a potent inhibitor of the actin polymerisation pathway, with the capability to block GBM cell invasion through the inhibition of FAK and Akt. It was shown that fluvoxamine did not produce a direct effect on actin or Arp2/3 (a protein complex involved in the regulation of the actin cytoskeleton) as it did not inhibit Arp2/3-dependent actin polymerisation. This shows that actin polymerisation inhibition by fluvoxamine is induced via the inhibition of actin polymerisation-related proteins in the brain cytosol and not by the direct inhibition of Arp2/3 or actin itself (128).

| Actin Polymerisation Inhibitor | Chemical Formula | Target | Clinical Trials | Applicability |
|---|---|---|---|---|
| Latrunculin A | $C_{22}H_{31}NO_5S$ | Globular actin | N/A | N/A |
| Latrunculin B | $C_{20}H_{29}NO_5S$ | Globular actin | Glaucoma | Decreased intraocular pressure which leads to glaucoma (10) |
| CCG-1423 | $C_{18}H_{13}ClF_6N_2O_3$ | MKL1 | N/A | N/A |
| Y-27632 | $C_{14}H_{21}N_3O.2HCl$ | ROCK1/2 | N/A | N/A |
| Cytochalasin B | $C_{29}H_{37}NO_5$ | Filamentous actin | Coronary angioplasty and restenosis | Can be safely administered, further study needed for efficacy in reducing restenosis (14) |
| Cytochalasin D | $C_{30}H_{37}NO_6$ | Filamentous actin | N/A | N/A |
| CK666 | $C_{18}H_{17}FN_2O$ | Arp2/3 complex | N/A | N/A |
| Wiskostatin | $C_{17}H_{18}Br_2N_2O$ | N-WASP | N/A | N/A |
| HA-1077 (Fasudil) | $C_{14}H_{17}N_3O_2S.HCl$ | ROCK | Cerebral vasospasm | Current treatment for the disease (11) |
| NSC23766 | $C_{24}H_{38}Cl_3N_7$ | Rac1 | N/A | N/A |

Table 2. Examples of inhibitors targeting different effectors of the actin polymerisation pathway, their application in clinical trials and applicability in practice.

### 2.1.2 Selection of candidate inhibitors of the actin polymerisation pathway

For initial assessment of compound activity on actin polymerisation, a panel of commercially available inhibitors was chosen that target different steps in the pathway (Figure 5). The panel included 5 inhibitors of the actin polymerisation pathway and the Rho signalling pathway. The chosen inhibitors included 6-bromoindirubin-oxime (BIO) and lithium chloride (LiCl), which both target GSK-3, Y-27632, which targets ROCK, latrunculin A which targets G-actin and CCG-1423, which targets MKL1.

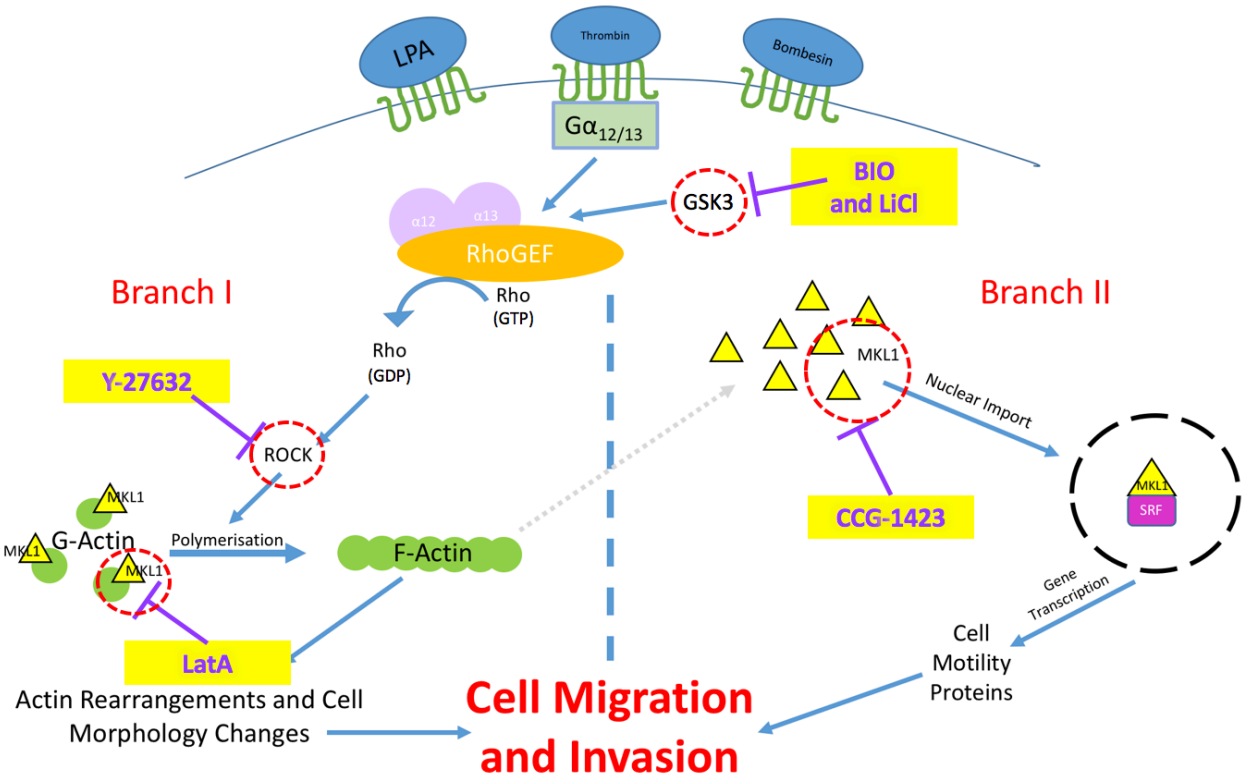


Figure 5. A simplified schematic diagram of the actin polymerisation pathway and the RhoA signalling pathway. Inhibitor targets are shown circled in red. BIO and LiCl target GSK3, Y-27632 targets ROCK, LatA targets actin monomers and CCG-1423 targets MKL1.

The first candidate drug in the panel of inhibitors, BIO, is part of the indirubin family; a family of bis-indole isomers, isolated from various natural sources

including varieties of marine mollusc, recombinant bacteria and mammalian urine (130). They are the active ingredient of Danggui Longhui Wan, a traditional Chinese medicine that has been successfully used for treatment of chronic myelocytic leukaemia (131). The cell permeable compound indirubin-3'-monoxine possesses anti-mitotic properties, pushing cells into endoreplication and cell death (132). Indirubins have been shown to be potent inhibitors of glycogen synthase kinase-3 (GSK-3), a serine/threonine kinase which targets actin cytoskeletal dynamics through its regulation of RhoGAPs and actin polymerisation (133). The indirubins have been of great interest for the development of pharmacological interventions in a number of neurological diseases. In both sporadic and familial types of Alzheimer's disease, over-activity of GSK-3 has been implied in hyper-phosphorylation of tau, increased β-amyloid production, memory impairment and microglial-mediated inflammatory response to local plaques, all hallmarks of Alzheimer's disease (134). By utilising the indirubins' potential to inhibit GSK-3, the development of pharmacological interventions for diseases such as Alzheimer's can be investigated. Common to members of the indirubin family is a naturally occurring product, 6-bromoindirubin, whose synthetic derivative is BIO. This cell-permeable indirubin has been shown to be an inhibitor of GSK-3 both *in vitro* and *in vivo* (135). Studies using BIO demonstrated reduced glioma cell invasion (*in vitro* and *in vivo*) and improved the survival of mice in intracranial xenograft models. In both intracranial and orthotopic xenograft models, it was also shown to reduce angiogenesis by blocking the migration of blood vessel endothelial cells (136). A study into colorectal cancer showed that BIO upregulated stemness, adhesion and chemoresistance. It was also shown that it is a non-specific inhibitor with targets

including JAK1, TYK2, GSK3α and, of course, GSK3. The molecular mechanisms causing increases in stemness, adhesion and chemoresistance in colorectal cancer cells after treatment with BIO still need to be further investigated (137).

The second drug candidate in the inhibitor panel was LiCl, which also targets GSK-3. LiCl was one of the first GSK-3 inhibitors to be described and inhibits cell migration both directly and indirectly by increasing the inhibitory phosphorylation of GSK-3 (138). Its other targets include inositol monophophatase (IMPase), phosphomonoesterases and phosphoglucomutase, which are structurally similar to GSK-3, as well as the arrestin-2/Akt complex (139). Although there is a broad range of targets, Patel et al. showed that LiCl effectively inhibits GSK-3 as it activates glycogen synthase, increases intracellular β-catenin levels and reduces the phosphorylation of tau in neurons (140). LiCl has been used for the treatment of bipolar disorder as a mood stabiliser and, like BIO, has been evaluated for its use in neurodegenerative diseases such as motor neuron disease and Alzheimer's disease (141–143). In glioma, LiCl was found to be a potent inhibitor of cell migration in spheroid, wound-healing and brain slice assays. Its effect was found to be specifically targeting cell migration, as it did not affect cell viability at predetermined concentrations used for cell migration studies. LiCl induced morphological changes, with cells becoming more rounded and concomitant loss of cell protrusions. Although LiCl has many targets, there is evidence that LiCl targets GSK-3 in glioma cell migration. Examination of LiCl different known targets, including inositol monophophatase (IMPase) and the large family of related phosphomonoesterases, showed that there was no effect on migration

upon the inhibition of IMPase whereas there was with inhibition of GSK-3 (144,145).

The third inhibitor in the panel was Y-27632; a selective ROCK inhibitor. Its inhibitory effect showed a 100x greater selectivity for ROCK over other kinases including protein kinase C, cAMP-dependent kinase and myosin light chain kinase (146). Y-27632 activity has been shown to reduce platelet shape change and activation (147,148), relax aortic smooth muscle contractions (149) and reduce hypertrophy of cardiomyocytes (150), amongst other effects. In cancer studies using rat MM1 hepatoma cells, Y-27632 has proven to be a promising tool in the pharmacological manipulation of the Rho pathway to control tumour invasion. *In vitro* and *in vivo* studies have shown that Y-27632 does not inhibit tumour growth, however, in an *in vivo* study for multiple myeloma involving an 11-day treatment regimen in rats it considerably reduced tumour cell dissemination with no apparent adverse side effects, suggesting chemotherapeutic potential for preventing invasion and metastasis (151). Y-27632 has also been shown to decrease breast cancer cell invasion *in vitro* and metastasis *in vivo* in a human breast to bone cancer metastasis model in mice (152). Other cancer types targeted by Y-27632 activity include ovarian, colon and hepatocellular carcinomas (153–155). In glioma *in vitro* research studies, Y-27632 profoundly inhibited glioma cell migration as determined in transwell and brain slice assays (156). Y-27632 is not completely ROCK-specific or isoform-specific and, at similar concentrations, it can block a wide range of kinases, which has been shown to result in a number of undesired side effects including hypotension and reduction in resting cerebral blood flow, which can lead to brain

hypo-perfusion. This has also been previously observed in mice treated with Y-27632 during stroke (157).

The inhibitor panel also included a naturally occurring macrolide, isolated from the Red Sea sponge *Negombata magnifica,* latrunculin A (LatA) (158). It was first identified as an inhibitor of actin polymerisation by its effects on cell morphology and actin filament distribution in non-smooth muscle cells (159). An *in vitro* study on the effects of LatA on the steady state of F-actin showed that its effects are consistent with direct sequestering of G-actin monomers (119). Its binding site was established based on an investigation into the effects of LatA on yeast actin mutations, which revealed that the binding site of LatA is on/near the actin nucleotide binding cleft (160,161). Currently, a clinical trial is under way to explore the ability of LatA to aid oocyte vitrification in humans and preserve fertility capabilities (162). Previous *in vitro* studies indicated that LatA activity induced stabilisation of the oocyte actin cytoskeleton promoting oocyte robustness prior to cryopreservation and increasing the survival rates of oocytes after thawing (163). LatA has also been found to aid normal chromosomal segregation by improving accurate F-actin formation in cloned mice embryos. As abnormal chromosome segregation is a major cause of developmental failure in cloned embryos, treatment with LatA improved the formation of F-actin and increased the birth rate of the cloned embryos (164). A further study revealed the potential of LatA for further investigation and application in cancer research by reducing peritoneal dissemination of gastric cancer. *In vitro,* LatA-induced a loss of the cell adhesion complex in the gastric cancer cell lines MKN45 and NUGC-4, leading to cell rounding. After a 72-hour treatment, cells treated with LatA lost focal

contact with concomitant shrinkage or bursting resulting in a LatA-induced morphological change. *In vivo,* mice inoculated with MKN45 and NUGC-4 tumours exhibited a significant increase in survival when treated with LatA via intraperitoneal injection (165). *In vitro* glioma cell migration studies showed that LatA significantly reduces the movement and velocity of glioma cells and causes alterations in cell morphology, resulting in cell rounding and thinning of cell protrusions (166).

The final drug in the inhibitor panel was a small molecule inhibitor called CCG-1423, which elicits its effects downstream of both RhoA and actin polymerisation by blocking the nuclear import of MKL1 and preventing the activation of MKL1/SRF-dependent transcription (167). In doing so, CCG-1423 inhibits the production of CCN1 (also known as Cysteine-rich angiogenic inducer 61 or CYR61); a multifunctional matricellular protein involved in cell adhesion and mesenchymal cell migration (168). *In vivo* studies using CCG-1423 recognised its anti-fibrotic potential in skin, lung and vascular fibrosis mouse models. In all three cases, CCG-1423 was shown to reduce fibrosis in blood vessels, skin and lungs when injected intraperitoneally (169–171). A proof of concept study was carried out as a follow up to the initial studies which revealed that local delivery of CCG-1423 decreases scar tissue formation in a preclinical model of fibrosis (172). In cancer studies, CCG-1423 was found to significantly affect the Rho transcription signalling pathway in the aggressive human prostate cancer cell line PC-3, resulting in the inhibition of PC-3 invasion and the disruption of a number of biological processes including cell cycle, DNA repair and replication, apoptosis, G1/S checkpoints and endoplasmic reticulum stress. In addition, targets of the

E2F family (Rho targeted transcription factors) and genes related to melanoma progression and metastasis were strongly repressed by CCG-1423 (173). In glioma-associated studies on Wnt5a-induced GBM invasion CCG-1423 treatment reduced Wnt5a-induced stress fibre formation and decreased GBM cell invasion in the U251 and T98MG GBM cell lines, assessed by the Boyden chamber assay with a pore size of 0.8μm, confirming the involvement of Wnt5a in promoting GBM invasion via the RhoA signalling pathway (174).

### 2.1.3 Two-D vs 3D migration

In their natural physiological environment, migratory cells connect with each other by cell-cell interactions, as well as with the ECM for mechanical support enabling the cells to move efficiently in all three dimensions. The traditional 2D *in vitro* environment - cell monolayers attaching to a plastic support - is not a true representation of such biological microenvironments; they do not reflect cellular processes occurring *in vivo*. These processes include gene expression, apoptosis and drug uptake and delivery, as well as cell migration (175). Using a 3D model *in vitro* system provides a more accurate representation of the *in vivo* environment and represents the intermediate step between 2D and *in vivo* modelling. One fundamental difference between 2D and 3D *in vitro* systems is the absence of steric hindrance in 2D migration. Only frictional (drag) forces from the 2D surface and surrounding liquid need to be overcome in 2D migration resulting in a higher migration speed. In addition to the frictional forces, 3D migrating cells need to overcome the forces associated with the steric hindrance of the matrix network. Under these conditions cells are presented with two options, to distort themselves enough to fit through the pores or to

distort/manipulate the matrix to ensure that the size of the pore is large enough to pass through. The first option is now known as path-finding migration, whereas the second option as path-laying, which involves matrix degradation (176).

A 2D tissue culture environment exerts a significantly different effect on cell morphology than a 3D culture. For example, breast cancer cell line BT474 (ER/PR-positive, HER2-positive) grown in a 2D culture forms patches on a flat solid support. When grown in suspension culture conditions, cells from the same cell line grow as spheroids with a seemingly smooth surface. In contrast, HCC1954 cells (a ER/PR-negative, HER2-positive breast cancer cell line) do not grow in clusters but prefer to grow more spread out and independently when grown in 2D culture. In 3D, these cells form very tight spheroids with a rougher surface than BT474 (177,178). The differences between 2D and 3D culturing techniques present a problem when trying to determine drug efficacy. Drug development and lead selection is firstly based on 2D *in vitro* drug screens to identify candidate drugs from a large panel for further testing. However, comparisons of 2D and 3D *in vitro* methods using, for example, the anti-cancer drugs neratinib and docetaxel showed that cells grown in 3D cultures displayed greater drug resistance compared to the same cells grown in 2D. In addition to this, levels of specific proteins involved in cell survival and growth also targets of the drugs were all increased in cells grown in 3D. The increase in protein expression levels likely contributed to the observed drug resistance as overexpression of these proteins had previously been linked to the facilitation of acquired drug resistance (177).

Historically, 2D methods of cell culture and analysis have been favoured due to their feasibility, ease and as the gold standard of tissue culturing. However, 3D technologies and cultivation including the use of bioreactors and hydrogels, are now becoming more popular as they offer a more physiologically applicable environment in which to investigate the behaviours of cells and tissues. The increasingly expanding field of 3D cell culturing is continuously evolving to address the current challenges in research, particularly around drug development. Currently, it is still necessary to employ 2D screening methods because of associated cost implications and ease of performance, however, 3D studies do yield more accurate and reproducible results in terms of observed cellular processes and interactions *in vivo* and can be carried out in combination with 2D testing (179).

## 2.2 Materials and methods

### 2.2.1 Cell lines and media

The adult glioma cell lines U87 (Grade IV, GBM) and U251 (Grade IV, GBM) were used in this study, originally established by Pontén and colleagues (180). These cells have been comprehensively characterised in terms of genomic alterations and gene expression patterns. Cells were grown in Dulbecco's Modified Eagles medium (DMEM) (Sigma) with 10% heat-inactivated foetal calf serum (HI-FCS) (Labtech) and 0.5% penicillin-streptomycin (Sigma) (complete medium). They were free of mycoplasma contamination as confirmed by Sarah Perry (In house testing at LICAP) and had been genotypically profiled by University of Leeds in-house services (Claire Taylor).

### 2.2.2 Cell culture

Cells were cultured in a Sanyo $CO_2$ incubator at 37°C in a humidified atmosphere of 5% $CO_2$ (in air). Cells were maintained in plastic tissue culture flasks (Corning) and harvested at or near confluence by washing with PBS and adding trypsin (10x solution, diluted 1:10 in Hanks Balanced Salt Solution, (Sigma)). Cells were viewed/imaged with a Nikon eclipse TS100 microscope and counted using an improved Neubauer haemocytometer (Weber Scientific).

### 2.2.3 Chemicals

Chemicals/inhibitors used were LiCl (Sigma), BIO (Calbiochem), ROCK Inhibitor Y-27632 (Abcam), RhoA Inhibitor CCG-1423 (Tocris) and Latrunculin A (Sigma Aldrich), all reconstituted as stock solutions in lab grade DMSO (Sigma).

### 2.2.4 Live cell imaging

U251 and U87 cells were adjusted to a density of $1.5x10^3$/ml in complete medium. 100μl of U251 or U87 cell suspension was pipetted into each well of a flat bottomed 96 well plate (half a plate per cell line) and incubated for 24 hours at 37°C. Following incubation, 100μl of complete medium (control) or known inhibitor (20mM LiCl, 5μM BIO, 10μM ROCK inhibitor, 500nM CCG-1423, 10μM LatA) was added. The plate was imaged using the IncuCyte Zoom System for 72 hours at 37°C. Movies were generated using the IncuCyte Zoom System software and analysed in ImageJ.

### 2.2.5 Two-D transwell migration assay

The underside of 24 well, 8μm pore Transwell Inserts (Greiner Bio-one) were pre-coated with 5μg/ml of fibronectin (Sigma) in PBS for one hour at 37°C. Cell lines were pre-treated with either 20mM LiCl, 5μM BIO, 10μM ROCK inhibitor, 500nM CCG-1423, 10μM LatA (all pre-determined anti-migratory concentrations) or control medium for one hour before 50μl $5x10^4$ cells were placed into the transwell insert for each condition in triplicate and allowed to migrate for four hours. Migrated cells were fixed with 1% glutaraldehyde (Sigma) in PBS for 10 minutes and, after several washes with PBS followed by $H_2O$, visualised by staining with 0.1μg/ml 4',6-diamidino-2-phenylindole (DAPI) (Biotium).

### 2.2.6 Three-D spheroid invasion assay in collagen

Spheroids were formed by placing $5x10^3$ cells/ml in an ultra-low attachment round bottom 96-well plate (Costar, Corning Lifesciences) and then incubated for 72 hours at 37°C (93). The media was removed and 100μl of neutralised (1M NaOH,

supplemented with 5xDMEM) rat tail collagen 1 (BD Biosciences) was added to each well and allowed to polymerise at 37°C for 15 minutes to entrap the spheroid. For evaluation of the effects of inhibitors on migration, the collagen was then overlaid with 100µl of complete medium (control) or individual inhibitor in complete medium (2X 20mM LiCl, 5µM BIO, 10 µM Y27632, 500nM CCG-1423). Each condition was repeated in multiple repeats but at least in triplicate for each plate. Each experiment was repeated three times. Spheroid expansion and invasion into the collagen matrix was monitored for 72 hours using the EVOS cell imaging system (Advanced Microscopy Group, Life technologies) at x4 magnification.

### 2.2.7 Migration on nanofiber plates

$2x10^4$/ml cells of GFP labelled U251 (obtained from Dr Nora Suas) were suspended in 20µl drops from the lids of petri dishes for 72 hours to allow the formation of cell spheroids. Cell spheroids were manually transferred into wells of aligned poly-ε-caprolactone nanofiber coated culture plates (Nanofiber solutions), which promotes cell migration on a 3D scaffold stimulated by topographic cues. The spheroids were then incubated at 37°C in either 20mM LiCl, 5µM BIO, 10µM ROCK inhibitor, 500nM CCG-1423, 10µM LatA or complete medium (control) in triplicate and migration was monitored for 72 hours using the EVOS cell imaging system at x4 magnification.

### 2.2.8 Data analysis

Three-D spheroid invasion and nanofiber plate assays were analysed by creating a migration index using Volocity 3D Image Analysis software according to Cockle

et al, 2015 (181). ImageJ (http://rsbweb.nih.gov/ij) and Excel (Microsoft, USA). Live cell imaging distance and direction were analysed using the MTrackJ tool in ImageJ (http://rsbweb.nih.gov/ij). Transwell assays were analysed by quantifying the area covered by migrating cells using Velocity 3D Image Analysis software (Perkin-Elmer inc). Data was examined for normality using an online Shapiro-Wilk test (http://sdittami.altervista.org/shapirotest/ShapiroTest.html). Differences between control cells and treated cells were compared using a two-tailed T-test (Excel). P-values $\leq 0.05$ were considered statistically significant.

## 2.3 Results

### 2.3.1 Adult glioma cell lines display different migration patterns

The cell lines used in this study were the established adult glioma cell lines U251 and U87. The U251 cell line was derived from a malignant astrocytoma from a male patient and was established in the 1960s by the Wallenbery Lab in Uppsala, Sweden (182). This cell line is characterised by glial markers presenting as GFAP positive and β3-tubulin negative. In contrast, U87 presents as GFAP negative and β3-tubulin positive, thus representing a more neuronal phenotype. The U87 cell line was also established in the Wallenbery Lab in the 1960s from a 44-year-old female patient (183). Although these cell lines appear morphologically different, previous studies have shown that both migrate in a mesenchymal pattern, a key characteristic of invading GBM cells (184). U251 cells display this phenotype more distinctly, with pronounced lamellipodia at the leading edge, whereas U87 cells present with longer singular protrusions (Figure 6).

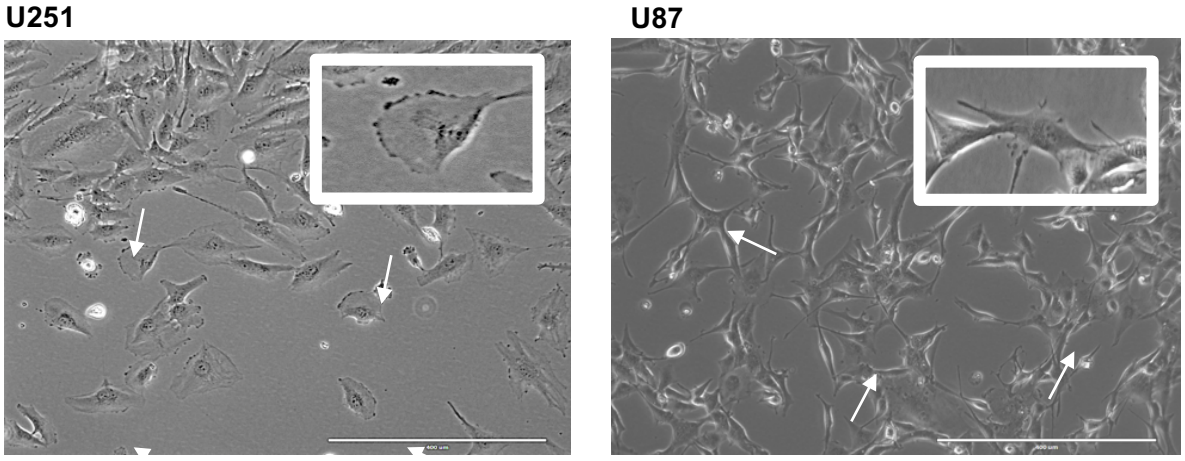


Figure 6. U251 and U87 display different patterns of migration. The cell lines were grown in complete DMEM medium and pictured at x10 magnification. Arrows indicate differences in the leading edges of U251 and U87, which are highlighted in the boxed images. Pronounced lamellipodia are a characteristic in U251 cells whereas single elongated protrusions are observed in U87. Scale bar = 400μm.

Cell morphologies changed in a 3D setting in collagen. Migrating cells in close proximity to the original spheroid core assumed a rounded morphology, which changed to an elongated morphology as the cells migrated away from the original core. U251 cells appeared to migrate in chains and prefer cellular contact with each other as they moved away from the original core with the cell furthest away in the chain seemingly detaching once a certain distance from the original spheroid was reached. U87 cells appeared to preferentially migrate as single cells (Figure 7).

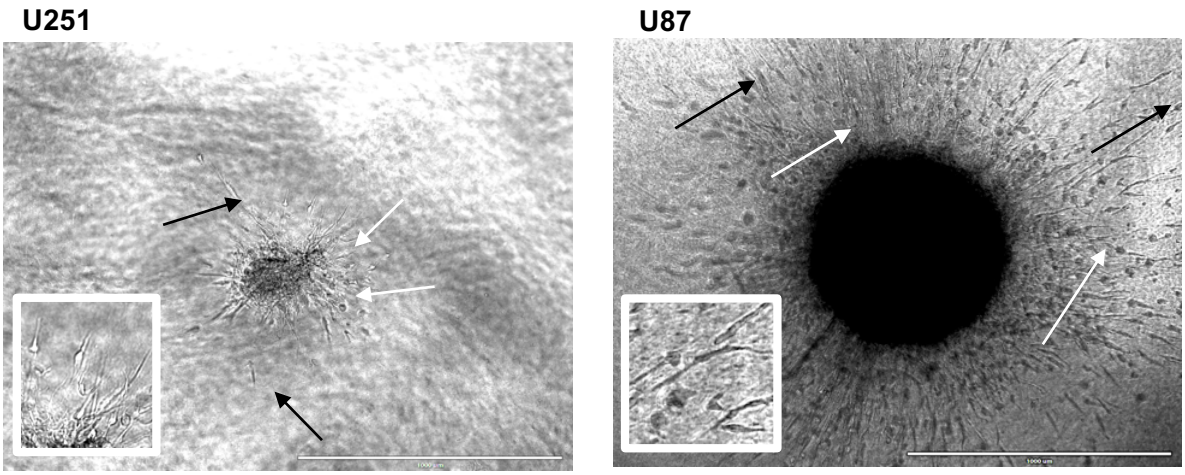


Figure 7. U251 and U87 spheroids in collagen were incubated in complete DMEM medium and imaged at x4 magnification at 72 hours. White arrows indicate rounded cells near the core and black arrows indicate elongated cells at the migration edge. Examples of the migratory phenotypes are highlighted in the boxes U251 cells migrated in interconnected strings with the cell furthest away from the original core detaching into the surrounding matrix, whereas U87 appeared to migrate as single cells. Scale bar = 1000μm.

### 2.3.2 Inhibitors targeting different steps in the actin polymerisation pathway exert distinct effects on cell morphology and migration

Live cell imaging of the two cell lines revealed distinct differences in cell morphology (Figure 8) and cell migration as measured by distance travelled and direction (Figure 9) after treatment with the different inhibitors. Directional

migration as measured by cell displacement is promoted by the creation of a leading edge through intracellular signalling of Rho GTPases (185).

After treatment with BIO, migration (both in terms of distance and displacement) was significantly reduced in both cell lines in comparison to the control. The effects of BIO were observed almost immediately, within minutes of treatment, in both cell lines and were maintained throughout the 72 hours of imaging. There was a notable change in morphology in U251 cells, with a shift to a more elongated morphology whereas U87 cells were characterised by mixture of both elongated and rounded cells. U251 treated with BIO travelled an average distance of 809.7μm +/- 40.2μm, which was significantly different to the control (3864.1μm +/- 162.5μm) ($P=2.87x10^{-16}$). The displacement of U251 treated with BIO was 100.5μm +/- 12.5μm, which was significantly different to the control (451.9μm +/- 26.1μm) ($P=4.30x10^{-11}$). U87 treated with BIO travelled an average distance of 513.2μm +/- 21.5μm, which was significantly different to the control (3061.6μm +/- 258.7μm) ($P=7.96x10^{-9}$). The displacement of U87 treated with BIO was 77.4μm +/- 6.6μm, which was significantly different to the control (335.6μm +/- 6.4μm) ($P=1.62x10^{-22}$).

LiCl also had a significant inhibitory effect on glioma invasion. Cell rounding was observed in both cell lines, indicating an anti-migratory activity of LiCl. The effect of the inhibitor on cell morphology was firstly noted after 12 hours, post drug addition, for both cell lines but appeared more pronounced in U87 cells compared to U251 cells, with the majority of the cells seemingly retracting their protrusions and exhibiting a rounded morphology. The effect of LiCl on U87 appeared to

wane around the 48-hour mark, with the cells starting to recover and adopting their normal cell morphology. In comparison, U251 cells did not recover and remained rounded for the duration of the imaging. U251 treated with LiCl travelled an average distance of 934.8μm +/- 33.4μm, which was significantly different to the control (3864.1μm +/- 162.5μm) ($P=8.09x10^{-16}$). The displacement of U251 treated with LiCl was 87.4μm +/- 6.0μm, which was significantly different to the control (451.9μm +/- 26.1μm) ($P=1.94x10^{-12}$). U87 treated with LiCl travelled an average distance of 551.1μm +/- 50.1μm, which was significantly different to the control (3061.6μm +/- 258.7μm) ($P=1.56x10^{-8}$). The displacement of U87 treated with LiCl was 84.9μm +/- 8.6μm, which was significantly different to the control (335.6μm +/- 6.4μm) ($P=8.48x10^{-20}$).

A marked change in morphology was also observed in both cell lines when treated with Y-27632. The observed change was the most striking compared to the phenotypes seen after addition of the other inhibitors in the panel. The cells became extremely elongated taking on a very neuronal-like morphology, with the inability to retract the trailing tail when attempting to migrate. Y-27632 induced the observed changes after addition of drug within 24 hours and maintained its effect beyond the 72-hour imaging period for both U251 and U87, before the cells recovered. U251 treated with Y-27632 travelled an average distance of 717.9μm +/- 22.0μm, which was significantly different to the control (3864.1μm +/- 162.5μm) ($P=5.75x10^{-17}$). The displacement of U251 treated with Y-27632 was 91.1μm +/- 3.7μm, which was significantly different to the control (451.9μm +/- 26.1μm) ($P=1.66x10^{-12}$). U87 treated with Y-27632 travelled an average distance

of 644.5μm +/- 11.5μm, which was significantly different to the control (3061.6μm +/- 258.7μm) ($P=2.45x10^{-8}$). The displacement of U87 treated with Y-27632 was 78.2μm +/- 0.8μm, which was significantly different to the control (335.6μm +/- 6.4μm) ($P=4.69x10^{-28}$).

Treatment with CCG-1423 produced a mixed population of cells with a rounded and elongated morphology, which was observed in both cell lines after 12 hours and persisted for 72 hours, after which the cells recovered. Unlike the other inhibitors, the effect of the drug on distance travelled only just reached statistical significance for both U251 and U87. Significance was not reached in either cell line for displacement. U251 treated with CCG-1423 travelled an average distance of 3320.0μm +/- 78.1μm, which just reached significance in comparison to the control (3864.1μm +/- 162.5μm) (P=0.03). The displacement of U251 treated with CCG-1423 was 526.8μm +/- 29.6μm, which was not significantly different to the control (451.9μm +/- 26.1μm) (P=0.16). U87 treated with CCG-1423 travelled an average distance of 2030.8μm +/- 132.0μm, which reached significance in comparison to the control (3061.6μm +/- 258.7μm) (P= 0.013). The displacement of U87 treated with CCG-1423 was 427.4μm +/- 36.2μm, which was not significantly different to the control (335.6μm +/- 6.4μm) (P=0.07).

LatA exerted an immediate anti-migratory effect in the two cell lines, leading to cell rounding instantaneously after drug addition, which was maintained for 72 hours. However, observation beyond the 72-hour mark showed that the cells recovered as they returned to an elongated, migratory morphology. U251 treated

with LatA travelled an average distance of 595.6μm +/- 36.7μm, which was significantly different to the control (3864.1μm +/- 162.5μm) ($P=2.79x10^{-17}$). The displacement of U251 treated with LatA was 73.4μm +/- 6.4μm, which was significantly different to the control (451.9μm +/- 26.1μm) ($P=7.37x10^{-13}$). U87 treated with LatA travelled an average distance of 270.6μm +/- 12.8μm, which was significantly different to the control (3061.6μm +/- 258.7μm) ($P=8.88x10^{-10}$). The displacement of U87 treated with LatA was 57.5μm +/- 1.3μm, which was significantly different to the control (335.6μm +/- 6.4μm) ($P=4.26x10^{-29}$).

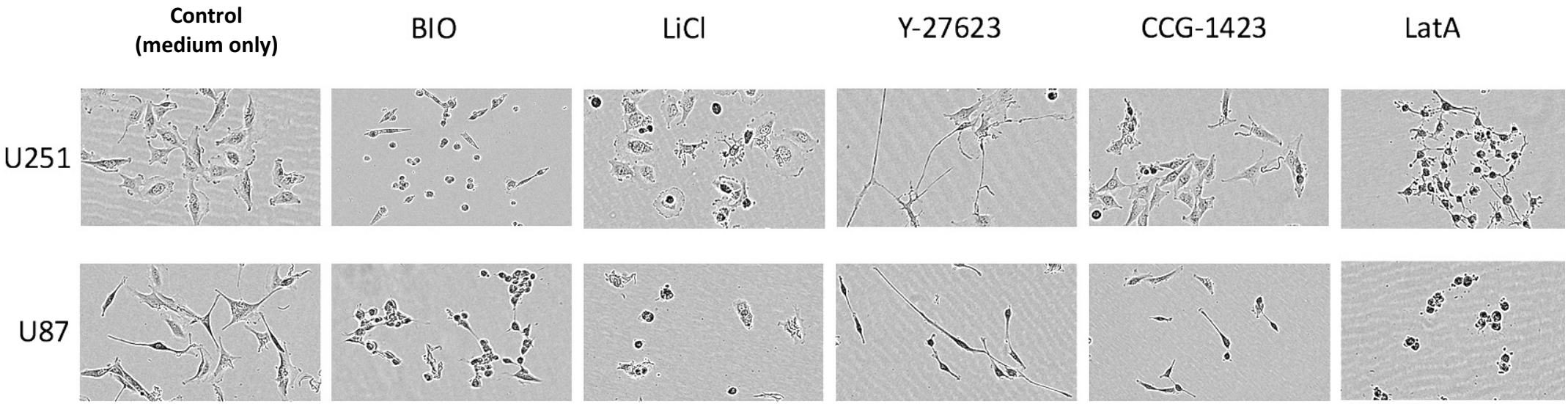


Figure 8. U251 and U87 cell lines display morphological changes in response to treatment with the same inhibitors. Cell lines were grown in a 96 well plate in complete DMEM medium in the presence of the inhibitors. They were imaged with the Incucyte Imaging system for 72 hours at x10 magnification. Drugs were added at time point 0-hours. Movie stills were generated from exported movies. Specific morphological changes induced by addition of the various drugs were observed for both cell lines.

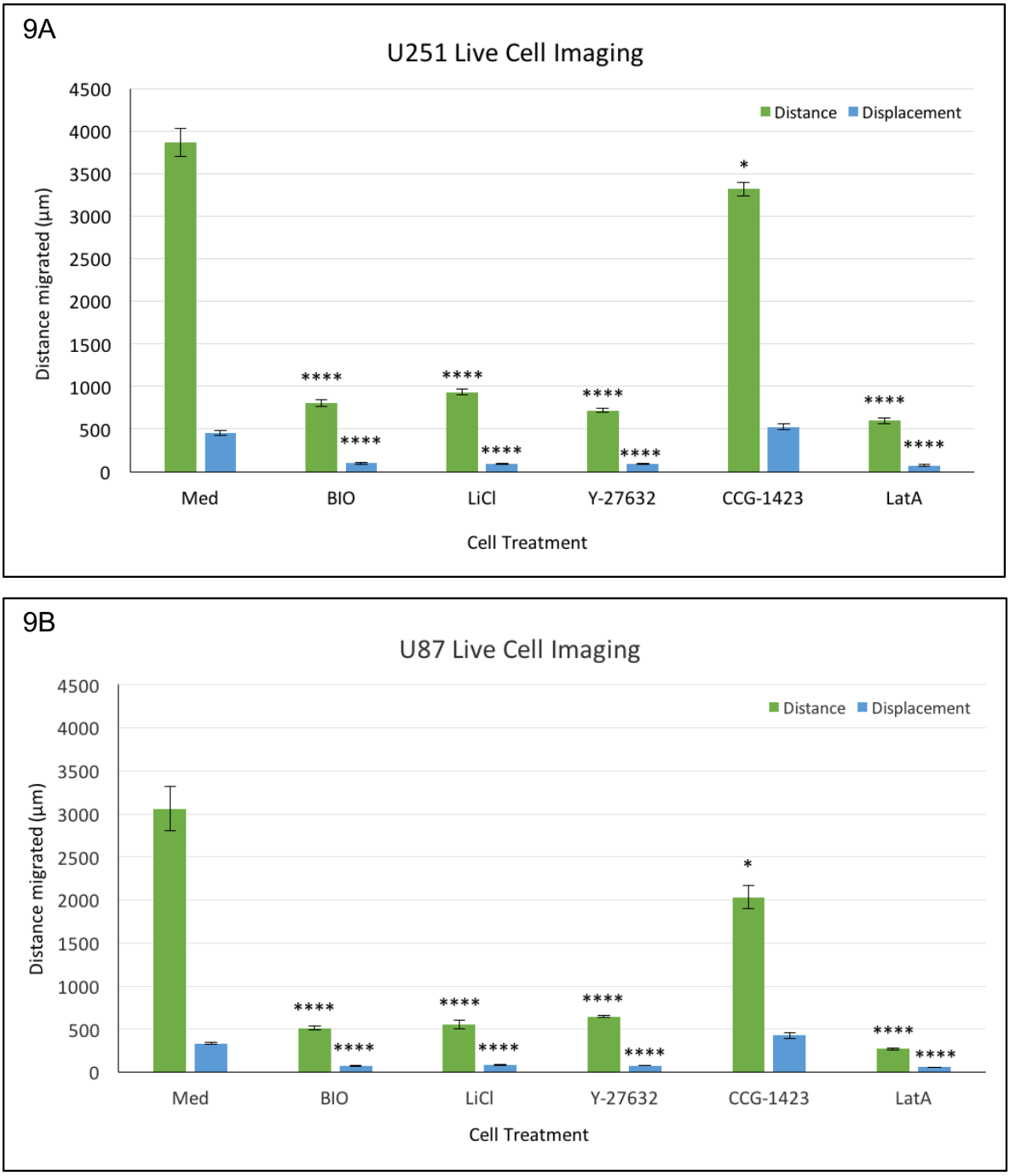


Figure 9. Cell migration is inhibited by a panel of inhibitors acting on different stages of the actin polymerisation pathway. Graphs show the effects of the inhibitors on cell migration as measured by distance travelled and cell displacement. 9A shows the effects of the inhibitors in U251 cells. 9B shows the effects of the inhibitors in U87 cells. Experiments were repeated in triplicate Asterisks indicate statistically significant results compared to the control (Med). *P≤ 0.05, ****P≤ 0.0001.

### 2.3.3 Inhibitors targeting the actin polymerisation pathway exert anti-migratory effects in a 3D migration assay

Tumour spheroids were generated using a 96-well round bottom low adherence plate. Both U251 and U87 readily formed spheroids within 72 hours with U87 forming bigger spheroids due to a higher proliferation rate compared to U251 (186). These spheroids are a more representative model of 3D tumours since they possess a 3D multicellular and morphological structure as reported for gliomas (187). Once embedded in collagen, cells migrated away from the original spheroid core into the surrounding collagen. The migration front and the migration edge were both measured and expressed as a migration index (MI) to analyse the ability of the cells to migrate under different treatment conditions. The migration front refers to 75% of the total migrated area of the cells. The migration edge refers to the outer most area where the furthest cells have migrated to. As results may be skewed as a result of individual cells migrating more efficiently compared to the majority, the MIs were determined for both the migration edge and front. Differences in the migratory performance of individual cells may also be important in terms of drug development targeting cell subpopulations with seemingly different migratory abilities. Therefore, both the migration front and the migration edge were measured. A migration index (MI) was then calculated by dividing the area of the tumour spheroid core by the area of the migration front or the migration edge. Treatment with the various inhibitors revealed that the ROCK inhibitor Y-27632 had the most pronounced anti-migratory effect on U87 spheroids with almost no migration being observed away from the core (Figure 10). The most effective inhibitor for U251 spheroid invasion appeared to be LiCl (Figure 10) as it led to the greatest reduction in migration.

U251 cells treated with LiCl had an average MI for the migration front, at 24-hours, of 0.21 +/- 0.05 which was statistically significant compared to the control (0.51 +/- 0.03) (P=0.014). The MI for the migration edge of U251 cells treated with LiCl at 72 hours was 0.69 +/- 0.06 which was also significantly different compared to the control at 72 hours (0.83 +/- 0.02) (P=0.017). Significance was not reached for the 48-hour time point for the migration front. For the migration edge at the 24-hour time point, U251 cells treated with LiCl had an MI of 0.34 +/- 0.08 which was statistically significant compared to the control (0.72 +/- 0.02) (P=0.004). At 48 hours, U251 cells treated with LiCl had an MI of 0.67 +/- 0.05 which is significantly different to the control (0.72 +/- 0.02) (P=0.021). There was also statistical significance at the 72-hour time point with the average MI being 0.81 +/- 0.01 compared to the control (0.72 +/- 0.02) (P=0.0002). U87 cells treated with LiCl had an average MI for the migration front, at 24-hours, of 0.54 +/- 0.06 which reached statistical significance compared to the control (0.72 +/- 0.04) (P=0.02). The MI for the migration edge of U87 cells treated with LiCl at 72 hours was 0.70 +/- 0.05 which was also significantly different compared to the control at 72 hours (0.82 +/- 0.005) (P=0.002). Significance was not reached for the MI at the 48-hour time point for the migration front. For the migration edge at the 24-hour time point, U87 cells treated with LiCl had an MI of 0.71 +/- 0.07 which was statistically significant compared to the control (0.87 +/- 0.004) (P=0.01). This was the only time point to reach statistical significance for the migration edge in U87 cells treated with LiCl.

Statistical significance was not reached for any of the time points for the MI of the migration front in U251 cells treated with BIO. For the MI of the migration edge, there was significant difference in all the time points (24 hours = 0.48 +/- 0.05, 48 hours = 0.71 +/- 0.02, 72 hours = 0.83 +/- 0.01) compared to the control (24 hours = 0.72 +/- 0.02, 48 hours = 0.87 +/- 0.01, 72 hours = 0.93 +/- 0.01) (P=0.01, P=0.05, P=0.03). The MI of U87 cells treated with BIO reached statistical significance for the 72-hour time point only for the migration front (0.61 +/- 0.05) when compared to the control (0.82 +/- 0.005) (P=0.014). There was significant difference in all the time points for the migration edge (24 hours = 0.56 +/- 0.10, 48 hours = 0.67 +/- 0.07, 72 hours = 0.73 +/- 0.03) compared to the control (24 hours = 0.87 +/- 0.004, 48 hours = 0.87 +/- 0.004, 72 hours = 0.87 +/- 0.004) (P=0.01, P=0.05, P=0.03).

The MI results for U251 cells treated with Y-27632 did not reach statistical significance for the migration front or the migration edge. The MI results for U87 cells treated with Y-27632 reached high statistical significance for all time points of the migration front (24 hours = 0.06 +/- 0.04, 48 hours = 0.13 +/- 0.07, 72 hours = 0.11 +/- 0.06) compared to the control (24 hours = 0.72 +/- 0.01, 48 hours = 0.76 +/- 0.006, 72 hours = 0.82 +/- 0.005) ($P=2.03\times10^{-10}$, $P=5.5\times10^{-7}$, $P=9.9\times10^{-9}$). The MI of U87 cells treated with Y-27632 reached high statistical significance for all time points of the migration edge (24 hours = 0.09 +/- 0.06, 48 hours = 0.15 +/- 0.08, 72 hours = 0.13 +/- 0.07) compared to the control (24 hours = 0.87 +/- 0.004, 48 hours = 0.87 +/- 0.004, 72 hours = 0.87 +/- 0.004) ($P=6.84\times10^{-12}$, $P=2.6\times10^{-8}$, $P=9.3\times10^{-9}$).

The MI of U251 cells treated with CCG-1423 did not reach statistical significance for the migration front or the migration edge when compared to the control. The MI of U87 cells treated with CCG-1423 also did not reach statistical significance at the 24-hour time point for the migration front when compared to the control. At the 48-hour time point for the migration front in U87 cells treated with CCG-1423, the MI was 0.47 +/- 0.08 which was significantly different compared to the control (0.76 +/- 0.006) (P=0.04). At the 72-hour time point for the migration front in U87 cells treated with CCG-1423, the MI was 0.45 +/- 0.01 which was also significantly different compared to the control (0.82 +/- 0.005) (P=0.015). For the migration edge, the MI of U87 cells treated with CCG-1423 was 0.40 +/- 0.1 at the 24-hour time point which was significantly different to the control (0.87 +/- 0.004) (P=0.003). At the 48-hour time point, the MI was 0.55 +/- 0.09 for the migration edge, which was also significantly different to the control (0.87 +/- 0.02) (P=0.001). The MI at the 72-hour time point of the migration edge was 0.50 +/- 0.10, which, again, was significantly different to the control (0.87 +/- 0.02) (P=0.01).

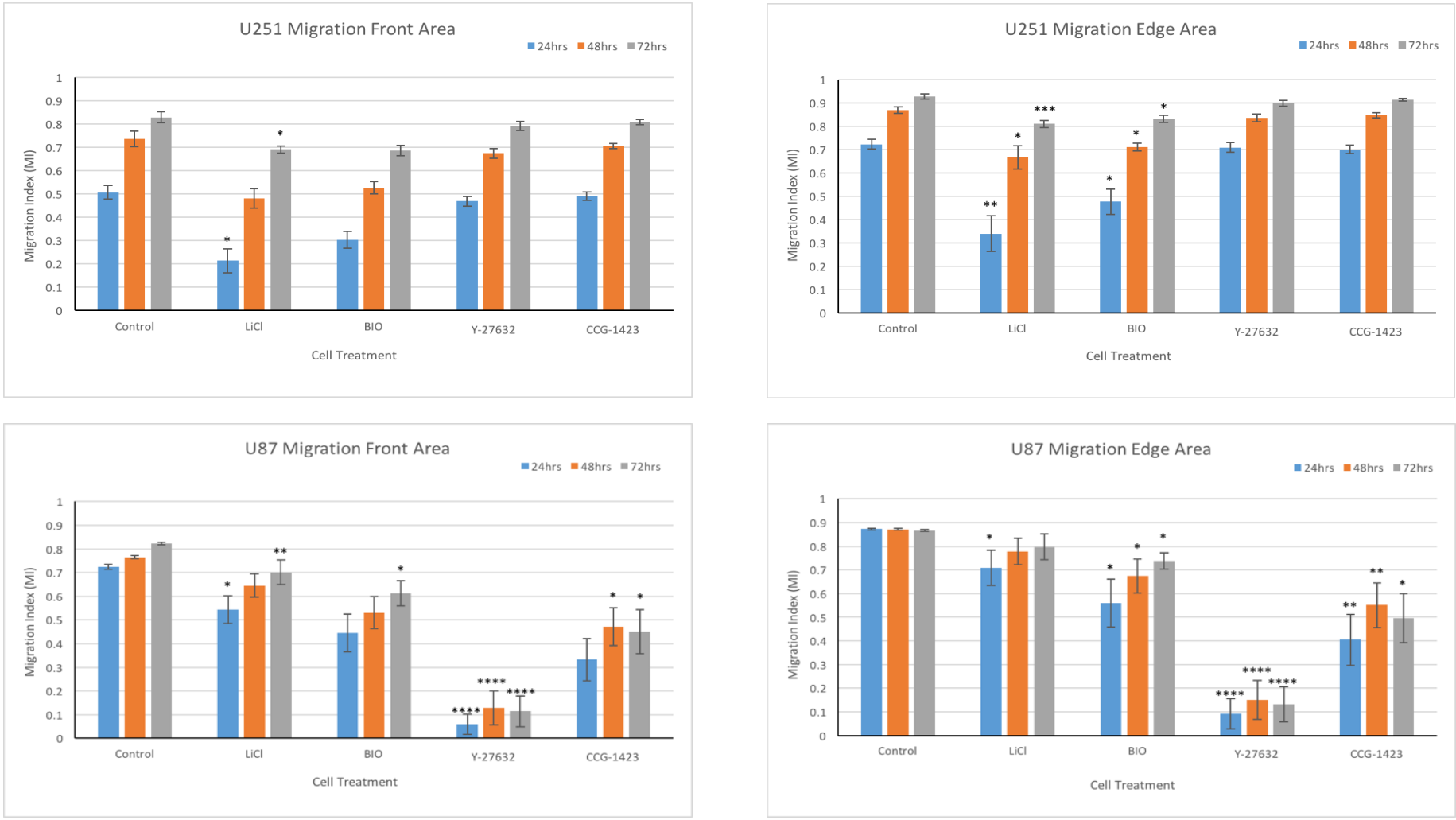


Figure 10. The anti-migratory effect of various inhibitors on cell migration in a 3D invasion assay. Graphical illustration of the effects of inhibitors in a 3D collagen invasion assay for cell lines U251 and U87. Spheroids were embedded in collagen with or without inhibitor and allowed to migrate over 72 hours. At 24 hour intervals images of the individual spheroids and migratory cells were taken. The migration front indicates the distance travelled by 75% of the migrating cell population. The migration edge indicates the furthest point of migration. Results were obtained from at least three individual repeats. Differences in anti-migratory activity of the individual drugs were observed in both cell lines. Asterisks indicate statistically significant results. *P≤ 0.05, **P≤ 0.01, ***P≤ 0.001 ****P≤ 0.0001.

### 2.3.4 Inhibitors targeting the actin polymerisation pathway display reduced anti-migratory activity on cells in a 2D transwell and nanofiber migration assay in comparison to random cell migration and 3D invasion assays

Inhibition of cell migration was observed in the 2D transwell assay in the presence of all the chosen inhibitors in both cell lines (Figure 11). For treatment of U251 cells with BIO, the average number of cells to migrate through the transwell insert was 49 +/- 9, which was significantly different to the control (162 +/- 33) (P=0.03). The average number of U251 cells to migrate through the insert when treated with LiCl was 43 +/- 7, which was, again, significantly different to the control (162 +/- 33) (P=0.02). For treatment with Y-27632, the number of cells to migrate through the insert was 43 +/- 8, which was significantly different to the control (162 +/- 33) (P=0.02). Treatment using CCG-1423 was also significantly different with the number of cells migrating through the insert being 51 +/- 12 compared to the control (162 +/- 33) (P=0.03). LatA treatment was the most effective inhibitor of migration in U251 through the transwell insert. The number of cells that migrated through the insert with LatA treatment was 25 +/- 4 which was significantly different to the control (162 +/- 33) (P=0.01).

For treatment of U87 cells with BIO, the average number of cells to migrate through the transwell insert was 33 +/- 4, which was significantly different to the control (213 +/- 17) (P=0.0005). The average number of U87 cells to migrate through the insert when treated with LiCl was 34 +/- 3, which was, again, significantly different to the control (213 +/- 17) (P=0.0005). Y-27632 treatment was the most effective inhibitor against the migration of U87 through the transwell insert. The number of cells that migrated through the insert with Y-27632

treatment was 19 +/- 3, which was significantly different to the control (213 +/- 17) (P=0.0003). Treatment using CCG-1423 was also significantly different with the number of cells migrating through the insert being 36 +/- 7 compared to the control (213 +/- 17) (P=0.0007). The number of cells that migrated through the insert with LatA treatment was 20 +/- 3 which was significantly different to the control (213 +/- 17) (P=0.0004).

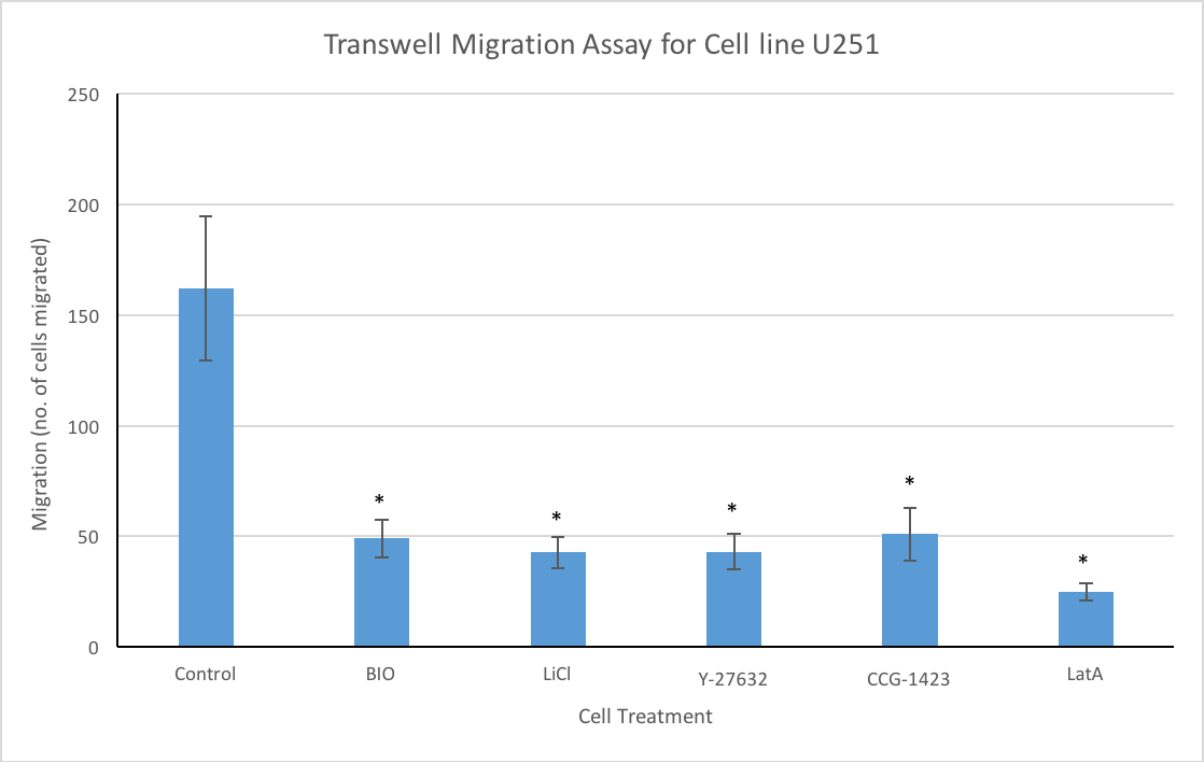


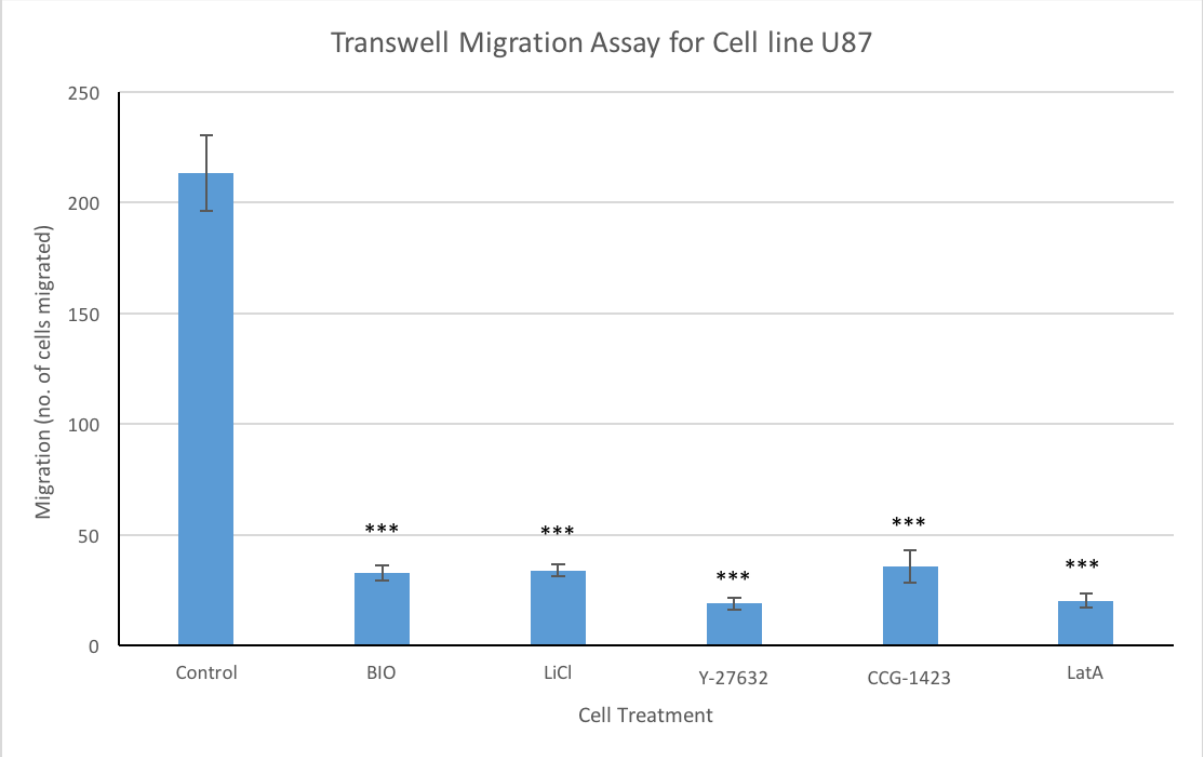


Figure 11. Effect of various inhibitors on migration through a transwell. Graphs showing the results for the 2D transwell migration assay for U251 and U87 cell lines treated with the chosen inhibitors. All inhibitors had an anti-migratory effect on U87 and U251 cell migration. The results were obtained from at least three repeat experiments. Asterisks indicate statistically significant results. *P≤ 0.05, ***P≤ 0.001.

GFP-labelled U251 cells were used to generate tumour spheroids according to the hanging drop cell culture protocol and placed onto aligned nanofiber plates. They were allowed to attach to the nanofibers and then treated with the inhibitors at the predetermined concentrations. Images were taken at 24 hour intervals for 72 hours. U251 cells displayed migratory activity away from the original spheroid along the nanofiber tracks for all treatments (Figure 12). BIO and LiCl treated cells displayed the least migration after 72 hours compared to the control and CCG-1423 treated cells showed the greatest migratory activity, even greater than the control (Figure 13).

The MI for U251 cells treated with BIO after 24 hours was 0.39 +/- 0.05 which was significantly different to the control (2.32 +/- 0.34) ($P=6.53x10^{-6}$). After 48 hours of BIO treated, the MI of U251 cells was 0.80 +/- 0.07 which was also significantly different to the control (4.8 +/- 0.46) ($P=4.7x10^{-6}$). At the 72-hour time point the MI was 1.28 +/- 0.09 which was, again, significantly different to the control (6.33 +/- 0.51) ($P=1.65x10^{-5}$). The MI for U251 cells treated with LiCl after 24 hours was 1.18 +/- 0.08 which was significantly different to the control (2.32 +/- 0.34) (P=0.002). After 48 hours of LiCl treated, the MI of U251 cells was 2.06 +/- 0.13 which was also significantly different to the control (4.8 +/- 0.46) (P=0.0003). At the 72-hour time point the MI was 2.66 +/- 0.1 which was, again, significantly different to the control (6.33 +/- 0.51) (P=0.0002). Statistical significance was not reached for any of the time points for U251 cells treated with Y-27632 or CCG-1423. For treatment with LatA, statistical significance was reached for the 24-hour time point. The MI was 1.24 +/- 0.08, which was significantly different to the control (2.32 +/- 0.34) (P=0.05).

Changes in the spheroid core size over the 72-hour treatment period were observed. Interestingly, the control spheroids seemingly disintegrated structurally over time with all cells being lost from the original core and migrating away. When treated with inhibitors the cells maintained the original rounded spheroid core structure which appeared to increase in size over time. After 24 hours, change in U251 spheroid core size treated with BIO did not reach statistical significance compared to the control. At the 48-hour time point, the average size of the cores treated with BIO was 19561$\mu m^3$ +/- 1283$\mu m^3$ which was significantly different to the control (9339$\mu m^3$ +/- 3537$\mu m^3$) (P=0.02). At the 72-hour time point, the average size of the cores treated with BIO was 21827$\mu m^3$ +/- 1700$\mu m^3$ which was significantly different to the control (4918$\mu m^3$ +/- 4180$\mu m^3$) (P=0.001).

After 24 hours, U251 spheroid cores treated with LiCl did not reach statistical significance compared to the control. At the 48-hour time point, the average size of the cores treated with LiCl was 20167$\mu m^3$ +/- 1264$\mu m^3$ which was significantly different to the control (9339$\mu m^3$ +/- 3537$\mu m^3$) (P=0.003). At the 72-hour time point, the average size of the cores treated with LiCl was 23366$\mu m^3$ +/- 2009$\mu m^3$ which was significantly different to the control (4918$\mu m^3$ +/- 4180$\mu m^3$) (P=0.0005).

After 24 hours of treatment with Y-27632, U251 spheroids had an average core size of 49289$\mu m^3$ +/- 7419$\mu m^3$ which was significantly different to the control (19271$\mu m^3$ +/- 2848$\mu m^3$) (P=4.23x$10^{-5}$). At the 48-hour time point, the average size of the cores treated with Y-27632 was 33938$\mu m^3$ +/- 6056$\mu m^3$ which was

significantly different to the control (9339$\mu m^3$ +/- 3537$\mu m^3$) (P=2.72x$10^{-5}$). At the 72-hour time point, the average size of the cores treated with Y-27632 was 49260$\mu m^3$ +/- 10265$\mu m^3$ which was significantly different to the control (4918$\mu m^3$ +/- 4180$\mu m^3$) (P=7.18x$10^{-6}$).

After 24 hours of treatment with CCG-1423, U251 spheroids had an average core size of 28632$\mu m^3$ +/- 2053$\mu m^3$ which was significantly different to the control (19271$\mu m^3$ +/- 2848$\mu m^3$) (P=4.23x$10^{-5}$). At the 48-hour time point, the average size of the cores treated with CCG-1423 was 24473$\mu m^3$ +/- 2367$\mu m^3$ which was significantly different to the control (9339$\mu m^3$ +/- 3537$\mu m^3$) (P=0.0009). At the 72-hour time point, the average size of the cores treated with CCG-1423 was 29964$\mu m^3$ +/- 3737$\mu m^3$ which was significantly different to the control (4918$\mu m^3$ +/- 4180$\mu m^3$) (P=0.0001).

After 24 hours of treatment with LatA, U251 spheroids had an average core size of 40305$\mu m^3$ +/- 3071$\mu m^3$ which was significantly different to the control (19271$\mu m^3$ +/- 2848$\mu m^3$) (P=0.0003). At the 48-hour time point, the average size of the cores treated with LatA was 38846$\mu m^3$ +/- 5031$\mu m^3$ which was significantly different to the control (9339$\mu m^3$ +/- 3537$\mu m^3$) (P=0.001). At the 72-hour time point, the average size of the cores treated with LatA was 35310$\mu m^3$ +/- 7132$\mu m^3$ which was significantly different to the control (4918$\mu m^3$ +/- 4180$\mu m^3$) (P=0.001).

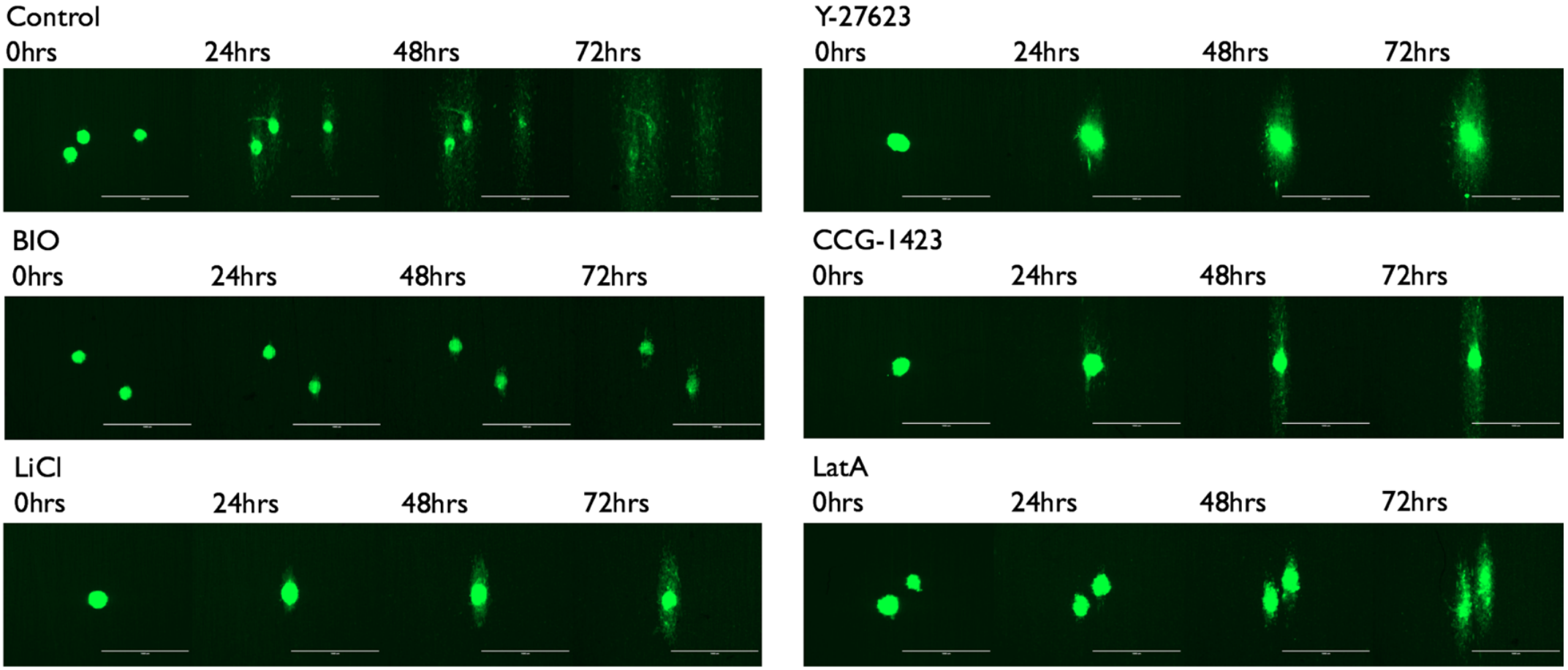


Figure 12. Effect of various inhibitors on cell migration along nanofiber tracks. GFP labelled U251 tumour spheroid cell migration on nanofiber plates imaged at 24 hour intervals over a 72-hour period with different inhibitor treatments. Representative examples for each treatment are shown. Imaged on the EVOS cell imaging system at x4 magnification. Scale bar = 1000μm.

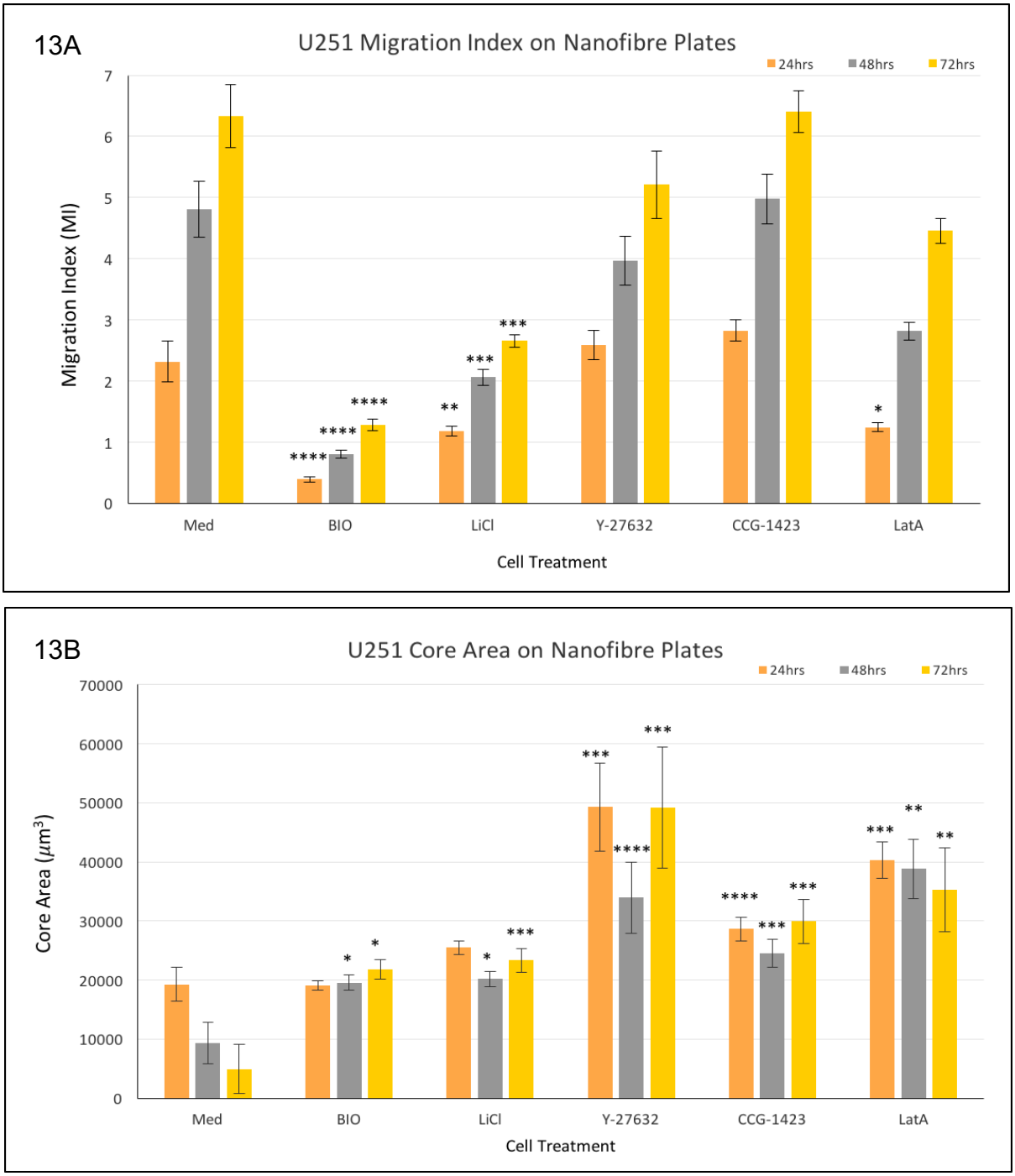


Figure 13. Effect of various inhibitors on cell migration along nanofiber tracks and spheroid core size. U251 tumour spheroid cell migration on nanofiber plates over 72 hours with inhibitor treatments. 13A. Migration away from the core as presented by the MI and the changes over 72 hours with different inhibitor treatments. 13B. The core size area measured in $\mu m^3$ and the changes over 72 hours with different inhibitor treatments. Different effects on cell migration in both cell lines by the inhibitors were observed. At least three repeats of the experiment were carried out. Asterisks indicate statistically significant results. *P≤ 0.05, **P≤ 0.01, ***P≤ 0.001 ****P≤ 0.0001.

## 2.4 Discussion

Cell migration is an integral feature of tumour dissemination and metastasis in cancer. The glioma cell lines U87 and U251 were demonstrated to be highly migratory as established by 2D random migration and 3D invasion assays. Although both cell lines were originally isolated from high grade gliomas they intriguingly differed in the way they migrated in 2D and 3D. Whereas U87 adopted a spindle-like morphology with pronounced single protrusions in 2D and preferred to migrate as single cells in a 3D environment, U251 was characterised by the formation of elaborate lamellipodia and the presence of a pronounced tail region in 2D and chain-like migration with eventual cell budding in 3D; these observations highlight the heterogeneity found within high grade gliomas (186). Both cell lines displayed a mesenchymal migratory phenotype as observed by live cell imaging, however, U87 adopted a more neuronal cell-like morphology when compared to the U251 cell line. The range of assays used here were chosen to reproduce biological processes or represent components of the brain environment. Live cell imaging of random cell migration provided insight into the inert migratory ability of glioma cells without external cues and a first assessment of morphological changes that can be induced with different anti-migratory inhibitors. By using a 3D invasion assay, the brain environment can be replicated more accurately as the cells have to actively migrate through a matrix (i.e. collagen in the assay), which is not achieved when growing cells on monolayers in culture. Utilisation of a model more representative of the brain environment will result in more biologically relevant results supporting the advancement in our understanding of cell migration in brain tumour research (93). The transwell assay captures the ability of cells to migrate towards a chemoattractant. It is

believed that glioma cells follow action potentials generated by axons acting as a signal or chemoattractant to migrate towards (188), which is mimicked in the transwell assay and highlights the capacity of cells to migrate towards signals in their external environment. The nanofiber assay replicates the migration method of glioma cells following blood vessels or white matter tracts in the brain, using them as a guide to migrate along (189). The nanofiber plates consist of synthetic aligned fibres that run vertically in the wells, providing tracks for cells to follow, thus replicating blood vessel and white matter tract structure.

### 2.4.1 Inhibiting glioma cell migration in 2D and 3D assays

Live cell imaging of random cell migration suggested morphological changes over 72-hours as well as the effect on the rate of migration in response to inhibitors, which was drastically reduced with treatment of all the inhibitors except for CCG-1423, where the rate of migration was only slightly reduced (U251 = 3320.0μm +/- 78.1μm, U87 = 2030.8μm +/- 132.0μm) compared to the control (U251 = 3864.1μm +/- 162.5μm P=0.03, U87 = 3061.6μm +/- 258.7μm P= 0.013). In terms of drug development, this gives a first insight into the mechanisms that could be manipulated in order to stop glioma cell migration.

It is now well established that cells grown utilising a 3D *in vitro* cultivation technique form structures that more closely resemble tissues than those grown in 2D. In 2D cells are maintained on a flat plastic surface leading to unnatural cell attachments to a synthetic surface (190). In tissues and organs, cell-cell attachments and attachments to the ECM allow important biological instructions to be communicated between the cells. This enables effective cell processes

such as proliferation and motility. In addition, drug activity on and penetrance of 3D structures is a more representative approach for the selection and testing of candidate drugs before they are considered for *in vivo* testing. Growing cells into a 3D structure creates a more natural environment and produces advantages over 2D generated monolayers. Cells in monolayers in a 2D environment are directly affected by a drug upon exposure unlike cells maintained within a 3D structure, which are more resistant due to their multicellular structure (179). Again, this provides a closer imitation to *in vivo* (191). The observations made from the MIs of the 3D collagen invasion assay and the distance travelled (μm) in the live cell imaging corresponded with this as the inhibitors had a much more pronounced effect on both U251 and U87 cells in the 2D live cell imaging than on the tumour spheroids in the 3D invasion assay in terms of cell motility. This may be due to the easy uptake of inhibitors by cells attached to a matrix in a monolayer than cells that are connected and integrated in a dense structure such as a spheroid. Studies using HepG2 liver cancer cells showed a greater cell viability and a reduced sensitivity to cytotoxic compounds when grown in 3D cultures compared to 2D monolayers (192). Biological barriers *in vivo* are not sufficiently imitated in 2D monolayers nor is the diffusion distance for drugs into a monolayer of cells which is reasonably short when compared to *in vivo* tissue environments (193). Studies into a 3D culture system that mimics the histology of GBM, demonstrated a reproducibility of the clinical results of 3 molecular targeted therapies, showing a vast improvement and reliability over 2D methods that have failed to predict drug efficacy (194).

It has been reported that glioma cells prefer to migrate along white matter tracts in the brain as well as blood vessels (189). When following anatomical structures that resemble fibres, glioma cells migrate much further as they have a topographic cue (195). Nanofiber plates mimic this providing tracks for cells to follow, allowing a more accurate representation of the brain environment (43). In the nanofiber experiments migration was observed with all the inhibitors after treatment of the spheroids, although the greatest reduction was observed after treatment with LiCl or BIO in comparison to the control. The cells readily attached to the fibre tracts and migrated away from the core, in a directed manner, along the vertical axes of the plate. The cells became elongated as they migrated along the tracks responding to the specific pattern of the topographic cue. The observed continued migration, despite inhibitor treatment, may be explained by the ability of the cells to compensate the effects of the inhibitor due to the external cues presented in this assay. Cells can be prompted to migrate not only through chemotaxis, but also by haptotaxis (along a gradient of chemoattractants or adhesion sites), durotaxis (in response to rigidity gradients), mechanotaxis (in response to mechanical cues such as fluidic shear stress) and galvanotaxis (migration towards or away from electrical currents) (196–200). In the other migration assays, the cells had no directional cues, thus the drugs had fewer cellular processes to overcome and therefore their effects were more apparent. This demonstrates how drug efficacy can be overestimated in 2D assays and a reason for failure of drug development at the clinical trial stage.

The GSK3 inhibitors BIO and LiCl have been used in many glioma invasion studies. LiCl is known to be a potent and reversible inhibitor and was discovered

by Nowicki *et al* to cause a near complete block of cell invasion *in vitro* using the 3D collagen invasion assay. To confirm these findings a wound healing assay was used, which supported the anti-migratory drug activity of LiCl at 20mM, the same working concentration used here (144). BIO, along with LiCl, was shown to increase the activity of β-catenin transcriptional co-activation. Among other cellular functions, β-catenin is known for its role in the Wnt signalling cascade; it is an important effector responsible for stimulating transcription of Wnt-specific genes involved in numerous cellular processes including cell fate, polarity and migration (201,202). A study by Williams *et al* using the glioma cell lines U251, U87 and GBM9, showed that by knocking down β-catenin, glioma cell migration increases. This suggested that the activation of GSK3 increases cell migration through the phosphorylation and downregulation of β-catenin. Therefore inhibiting GSK3 with BIO or LiCl will increase levels of β-catenin and reduce glioma cell migration (136). In the data presented here, U251 and U87 reacted differently to BIO and LiCl treatments. In the 3D invasion assay, BIO inhibited U87 cell migration more effectively than U251 and LiCl inhibited U251 cell migration more effectively than U87. This suggests that although these inhibitors share the same target, the cell lines respond to drug activity in different ways and can overcome inhibition through different cellular mechanisms. When comparing protein expression levels in U251 and U87, it has been shown that U251 has lower protein expression levels in 263 different proteins when compared to U87 (203). This demonstrates that, although both glioma cell lines, there are significant differences between the two cell lines, which could lead to differences in cell signalling pathways such as efflux pathways and drug metabolism.

In gliomas, the ROCK inhibitor Y-27632 has been used to study the expansion of glioblastoma stem cells (GSCs) *in vitro*. Because ROCK inhibitors suppress apoptosis, they have been used to increase stem cell numbers for cloning efficiencies (204). Y-27632 is a myosin-II-based contractility inhibitor (117). This means that the traction forces exerted by myosin II at the retracting ends of migrating cells are blocked, and the cells can no longer migrate (205). These effects of Y-27632 were evident in the studies undertaken here, as a lack of migrating cells was observed coinciding with an increase of the original tumour core when analysing the nanofiber images. The MI of U251 cells treated with Y-27632 failed to reach statistical significance, when compared to the control, for all times points (24 hours P=0.62, 48 hours P=0.40, 72 hours P=0.94), however, the size of the area of the core reached extreme significance when compared to the control for all time points in the nanofiber assay (24 hours $P=4.23x10^{-5}$, 48 hours $P=2.72x10^{-5}$, 72 hours $P=7.18x10^{-6}$). Y-27632 has been previously shown to stimulate proliferation of bovine corneal endothelial cells and prevent apoptosis. When used on spheroids, it decreased cell death inside the spheroid core and promoted proliferation of the cells on the edge of the spheroid (206,207). This corresponds with the above results. By reducing cell death and migration and enhancing proliferation, Y-27632 stimulates an increase in spheroid size. Different results were also observed in the 3D invasion assay between the two glioma cell lines as U87 migration was significantly affected by treatment with Y-27632. This suggests that U87 migration in 3D is regulated by cell signalling pathways different to those employed by U251; potentially based on their phenotypic background and the differences in protein expression between U251 and U87 as previously stated (203).

LatA disrupts actin filament organisation by sequestering G-actin in a 1:1 complex, preventing the formation of F-actin (208). LatA has been used in a number of studies to inhibit actin polymerisation. It was found to inhibit asymmetric segregation of Neuroglia antigen 2 (NG2) cells (209). NG2 is a rat integral membrane proteoglycan commonly found in GBM tumours. GBM NG2+ cells are associated with aggressive tumorigenicity by the overexpression of proteins involved in mitosis and cell cycling (210). LatA has also been shown to effectively inhibit transwell migration in the C6 glioma cell line, which correlates with our own studies using this type of migration assay (156).

CCG-1423 has been shown to reduce the expression of CCN1, thus inhibiting cell migration and proliferation (211). CCG-1423 is also a potent inhibitor of EMT, which is closely associated with cancer progression (212). This inhibition is caused by the blockage of MKL1, which is a key element in EMT, however, the inhibitory effect of CCG-1423 in this respect is restricted to conditions in which the G-actin pool is depleted (213). Cell migration is stimulated by many different factors, including proteins such as CCN1. It is secreted by cells and regulates cell migration as well as proliferation, angiogenesis and cell survival. CCN1 expression is stimulated by G-protein coupled receptor (GPCR) agonists leading to activation of RhoA; a key driver of actin polymerisation (214). It is able to interact with the cell it is secreted from as well as surrounding cells through autocrine-paracrine signalling. It applies its mechanism through its interaction with 5 integrins, $\alpha_v\beta_3$, $\alpha_v\beta_5$, $\alpha_6\beta_1$, $\alpha_{IIb}\beta_3$, $\alpha_M\beta_2$, and heparan sulphate proteoglycans (215). In GBM cells, CCN1 is frequently overexpressed and rapidly secreted,

which may contribute to the invasive nature of the disease (216). CCG-1423 exerted a different effect on each cell line in the 3D invasion assay. It appeared to have no anti-migratory activity in U251 cells but a significant effect on U87 cells, suggesting that different or compensating signalling pathways are activated by U251 resulting in continued migration. Different responses to drugs between these two cell lines have been previously reported. Studies on glioma cell proliferation and migration showed that drugs that target purine metabolism have a higher toxicity to U251 cells than U87 cells. It was these studies that showed the 263 proteins that are expressed lower in U251 are involved in drug resistance to platinum based drugs (203). In addition, U251 and U87 possess different genetic mutations in p53, p21, CDKN2A and PTEN, which also affect the anti-cancer properties in drugs containing platinum (217). This highlights the importance of personalised treatments for patients with brain tumours as cell heterogeneity can cause chemoresistance and different cellular reactions to drugs.

### 2.4.2 The effect of CCG-1423 activity on glioma cell migration

Considering the overall anti-migratory effect of all inhibitors on cell migration, CCG-1423 stands out as being the least effective at preventing cell migration. This is surprising given that it has been reported to be a potent inhibitor of cell migration in other cancer types including prostate cancer and melanoma (167). CCG-1423 displayed a varied ability to inhibit migration depending on the assay used. In the 3D spheroid migration assay, CCG-1423 had no anti-migratory effect on U251 cells but did exert some reduction in migration in U87. CCG-1423 showed little or no inhibitory effect in the live cell imaging random migration and

nanofiber assays, however, it efficiently inhibited migration in the transwell assay. An explanation for these results could be that CCG-1423 is driving MAT in the cells. As previously stated CCG-1423 inhibits the production of CCN1, which promotes mesenchymal migration. As the cells continue to migrate after treatment in most assays, they could be doing so by a switch to an amoeboid migration phenotype. This type of migration is characterised by a more rounded cell morphology and may be adopted by cancer cells when faced with adverse external cues such as inhibitors targeting mesenchymal migration (218). The same cell shape may be preventing the cells from being able to physically pass through a transwell insert of this size, thus presenting the drug as a potent inhibitor in the transwell insert assay. In a previous study, CCG-1423 was shown to inhibit migration in U251 cells, however, the assay used for assessing invasion was the Boyden chamber assay that also used pores with a 0.8μm diameter (212). This could be due to drug-induced changes in lamin-A, a nucleoskeletal protein filament that is responsible for the stabilisation and stiffening of the nucleus through the assembly of juxtaposed networks within nuclei. This has been shown to contribute to cell survival in such migration assays that involve constrictive microspores. High levels of lamin-A promote nucleus stiffness and suppress nuclear distortion, therefore preventing cells from being physically able to squeeze through pores (219).

This work reports, for the first time, the migratory behaviour of glioma cell lines in different environments, the effect of anti-migratory inhibitors targeting the actin polymerisation pathway on cell migration and the potential ability of glioma cells to change from one migratory behaviour to another in response to external cues

such as treatment with inhibitors (Table 3). MAT is an important consideration for the development of novel anti-migratory drugs. Anti-migratory combination treatments to prevent tumour cells migrating to healthy parts of the brain will have to be developed to circumvent a potential migratory switch from one phenotype to another.

| | Live Cell Imaging | 3D Invasion Assay | Transwell Assay | Nanofiber Assay |
|---|---|---|---|---|
| **BIO** | U251/U87 =<br>↓ Migration<br>Rounded Morphology | U251 =<br>Migration slightly ↓<br>U87 =<br>↓ Migration | U251/U87 =<br>↓ Migration | U251 =<br>↓ Migration |
| **LiCl** | U251/U87 =<br>↓ Migration<br>Rounded Morphology | U251 =<br>Migration slightly ↓<br>U87 =<br>↓ Migration | U251/U87 =<br>↓ Migration | U251 =<br>↓ Migration |
| **Y-27632** | U251/U87 =<br>↓ Migration<br>Elongated Morphology | U251 =<br>Migration unaffected<br>U87 =<br>↓ Migration | U251/U87 =<br>↓ Migration | U251 =<br>Migration slightly ↓ |
| **CCG-1423** | U251/U87 =<br>Migration unaffected<br>Rounded Morphology | U251 =<br>Migration unaffected<br>U87 =<br>↓ Migration | U251/U87 =<br>↓ Migration | U251 =<br>Migration unaffected |
| **LatA** | U251/U87 =<br>↓ Migration<br>Rounded Morphology | N/A | U251/U87 =<br>↓ Migration | U251 =<br>Migration slightly ↓ |

Table 3. A table summarising the panel of inhibitor effects on U251 and U87 cells in different migration assays.

# Chapter 3: The small molecule inhibitor CCG-1423 and its effects on glioma cell migration

## 3.1 Introduction

The intriguing results gained with CCG-1423 led us to focus on this inhibitor to look more closely at its mechanism. Potentially, CCG-1423 could be utilised as a tool to induce MAT allowing for the identification of key molecules involved in this process and therefore potential targets for inhibitor development. There are very few pharmacological compounds that specifically target the Rho signalling pathways in cancer treatment. A lot of work has focussed on the inhibition of COOH-terminal isoprenylation of Rho GTPases, which is a necessary modification made to lipids in order to allow localisation of activated Rho proteins to the cell membrane resulting in cell proliferation, migration, adhesion and invasion. Common inhibitors that prevent this lipid modification include statin drugs, geranylgeranyltransferase and farnesyltransferase, however, these drugs are non-specific and therefore their effects cannot be accurately analysed as Rho GTPase inhibitors (220). Studies have also been conducted to inhibit ROCK, a Rho effector kinase molecule, which is involved in regulating cell shape and movement. Inhibitors of this molecule, such as Y-27632, have shown favourable anti-metastatic effects, however, there are some contrasting studies that have stated Y-27632 has a pro-invasive effect in some cancer cell types in 3D invasion assays (2, 3). One inhibitor has been identified as being specific to Rho GTPases. NSC23766 is a specific inhibitor of Rac1, but with only low potency, which poses a problem for cancer treatment (79).

With a clear need for specific inhibitors of the Rho signalling pathway, the small molecule inhibitor CCG-1423 was identified at the University of Michigan through a transcription based high-throughput serum response element-luciferase screening assay. A selective probe of RhoA-induced gene transcription in the form of a modified SRE luciferase reporter that lacked the ternary complex factor binding sites was utilised. The Rho signalling pathway was then stimulated at different steps to determine the site of CCG-1423 action (223). This process identified CCG-1423 as a specific inhibitor that elicits its effects downstream of RhoA and actin polymerisation, targeting MKL1 and importation into the nucleus to form the MKL/SRF complex (167).

### 3.1.1 The mechanism of CCG-1423

MKL1 is a protein that shuttles between the cytoplasm and nucleus in cells. In the nucleus, it acts as a transcriptional co-activator with SRF, where they form a complex that activates the transcription of SRF-dependent genes (224). In the cytoplasm, MKL1 is bound to G-actin via its N-terminal basic (NB) domain between the RPEL motifs 2 and 3. When actin polymerisation is activated via the Rho signalling pathway, MKL1 disassociates with G-actin to allow for the formation of actin filaments, leaving MKL1 unbound in the cytoplasm. Once unbound, MKL1 can be imported into the nucleus by the transporter protein complex importin $\alpha/\beta$, which binds to the NB domain of MKL1. Once in the nucleus, it then forms the transcription complex with SRF (6, 7).

CCG-1423 acts upon the free cytoplasmic MKL1, where it binds to the NB domain, preventing the binding of importin $\alpha/\beta$ and, consequently, the nuclear

import of MKL1 (Figure 14). This action causes a build-up of MKL1 in the cell cytoplasm and inhibits the transcription of SRF-dependent genes (225). This site of action was determined by activating the Rho signalling pathway at multiple different points in the prostate cancer cell line PC-3. Through control experiments to assess the effect of CCG-1423 on membrane activator proteins, it was shown that the compound shows non-specific binding between the membrane-associated heterotrimeric G proteins, $G\alpha_{12}$ and $G\alpha_{13}$. Other up-stream steps were also eliminated as being the target of CCG-1423 through the use of RhoA and RhoC G14V mutants (167). The activation of these proteins does not depend on upstream activators of the Rho signalling pathway. CCG-1423 inhibited RhoA-G14V and RhoC-G14V activity, suggesting its action lies downstream (226). It was also shown that ROCK was not the target of this inhibitor as its activity was unaffected *in vitro.* Further investigations were focused on the effectiveness of CCG-1423 downstream targeting of the transcriptional processes. The effects of transcription induced by numerous different transcription factors and co-activators determined that CCG-1423 inhibited transcription induced by MKL1 co-activation with SRF (167).

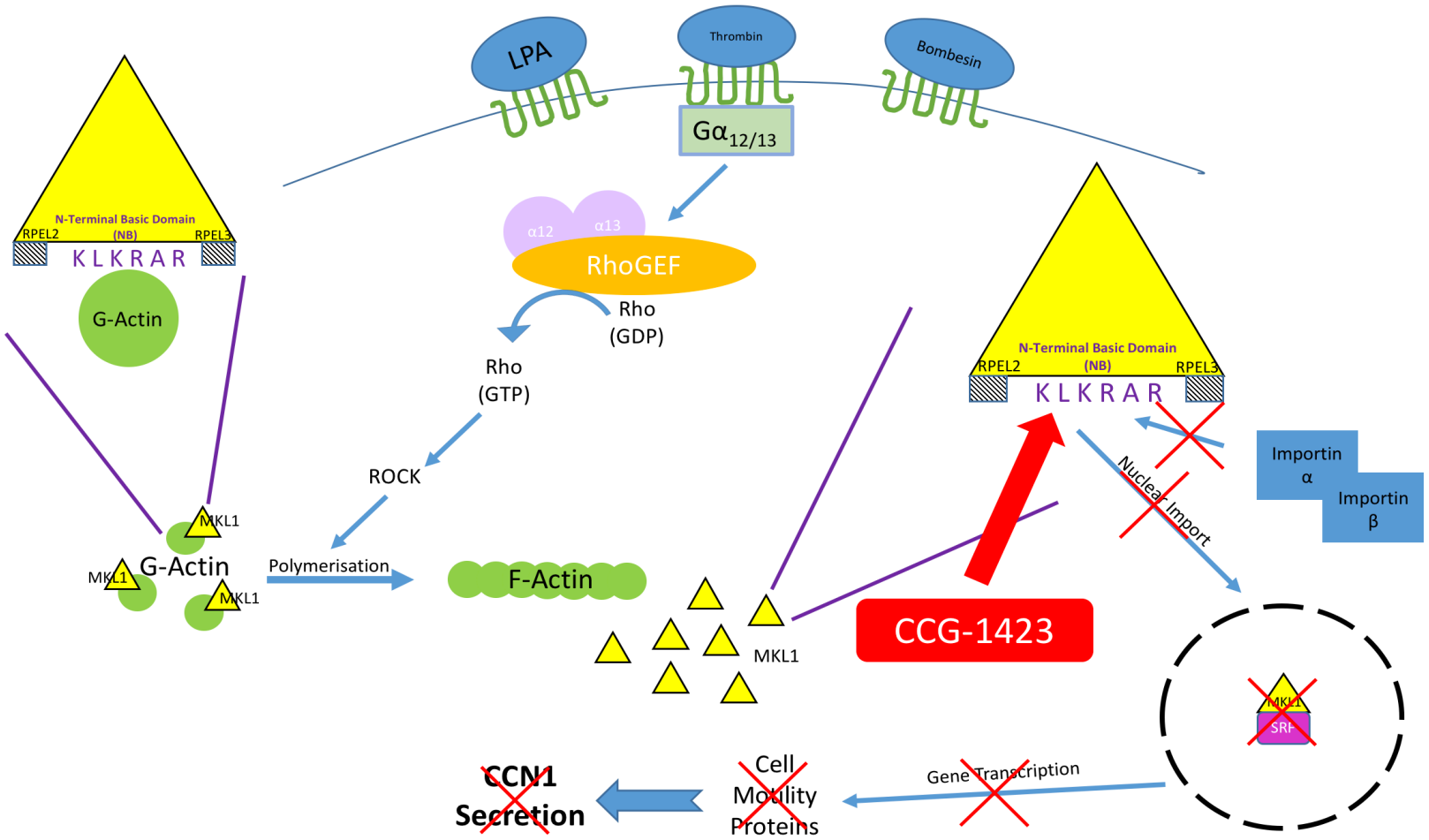


Figure 14. A schematic diagram showing the Rho signalling pathway and the mechanism of the small molecule inhibitor CCG-1423. In the cytoplasm, MKL1 is bound to G-actin via its N-terminal basic (NB) domain between the RPEL motifs 2 and 3. When actin polymerisation is activated via the Rho signalling pathway, MKL1 disassociates with G-actin to allow for the formation of actin filaments, leaving MKL1 free in the cytoplasm. Once free, MKL1 can be imported into the nucleus by the transporter protein complex importin α/β, which binds to the NB domain of MKL1. Once in the nucleus, it then forms the transcription complex with SRF and activates the transcription of SRF-dependent genes. The actions of CCG-1423 target the free cytoplasmic MKL1, where it binds to the NB domain, preventing the binding of importin α/β and, consequently, the nuclear import of MKL1. This action causes a build-up of MKL1 in the cell cytoplasm and inhibits the transcription of SRF-dependent genes, including CCN1.

### 3.1.2 The cell adhesion protein CCN1

CCG-1423 selectively elicits its effects on transcription stimulated by the Rho signalling pathway. One such transcription product affected by this is the multifunctional matricellular protein called CCN1 (also known as cysteine-rich 61 [CYR61]). This protein has an essential role in a number of different biological processes including embryogenesis, wound healing, fibrogenesis and inflammation (168). CCN1 is a member of the CCN protein family, which contains 6 members in mammals. The name CCN is derived from the first 3 members of the family **C**YR61, **C**TGF (connective tissue growth factor) and **N**OV (nephroblastoma overexpressed). The 6 members of the CCN family have been renamed in order of their discovery CCN1-6 (227). The function of CCNs was originally thought to be regulating cell proliferation having been identified through their stimulation by oncogenes, mitogenic growth factors and transformation. It is now known that they closely associate with the ECM upon secretion and directly bind to integrin receptors aiding cell adhesion (228). Although CCN1 does not solely promote cell proliferation, it does enhance the DNA synthesis that is stimulated by other mitogens (229).

The tight association of CCN1, the ECM and the surface of cells supports cell adhesion and stimulates adhesive signalling. From these interactions, focal adhesions form and activation of focal adhesion kinase (FAK), paxillin and Rac is induced leading to reorganisation of the actin cytoskeleton and lamellipodia and filopodia formation (14, 15). CCN1 stimulates the migration of fibroblasts, endothelial cells, smooth muscle cells and some types of cancer cells (232). It can also promote proliferation induced by growth factors in PC-3 prostate cancer

cells and ovarian cancer cells through its synergy with other mitogenic growth factors, resulting in an increase of growth-factor induced DNA synthesis (233).

Rac1 is a member of the GTPase family and promotes invasion and metastasis (234). The activities of Rac1 are moderated by CCN1 in a number of different cancers including pancreatic, lymphoma and prostate (233). It has been shown that Rac1 is an important downstream effector of integrins, and that its activation is considerably augmented when CCN1 expression is enhanced (235). The elongated movement of mesenchymal migration is driven by Rac1 activation, which promotes WASP-family verprolin-homologous protein 2 (WAVE2)-mediated actin polymerisation (236). This signalling pathway also suppresses rounded movement in cells by reducing the contractibility of actomyosin (237).

### 3.1.3 CCN1 in cancer

Dysregulated CCN1 expression has been identified in a number of different diseases including cancer. In tumour progression, CCN1 has been shown to promote invasion, angiogenesis, cell proliferation, cell survival and metastasis (168). Silencing CCN1 expression in HeLa cells *in vitro*, for example, leads to loss of invasion supporting an important role for CCN1 in cancer metastasis and invasion (231). In addition, in immunodeficient mice implanted with human gastric adenocarcinoma cells, overexpression of CCN1 effectively induces angiogenesis, which increases tumour vascularisation and promotes tumour growth (238). Consequently, further studies based on CCN1 overexpression have shown increases in tumour growth in xenografts of prostate (233), ovarian (239), breast (240) and squamous carcinoma cells (241). Consistent with these

findings, a decrease in tumour growth was demonstrated in xenografts of prostate (233) and pancreatic cancer cells when CCN1 expression was silenced (242). These findings have been supported by clinical observations correlating CCN1 expression with tumour, size, stage, lymph node positivity and poor prognosis in cancers including glioma (243), prostate (244) and breast (240,245). A particularly striking example of the effects of CCN1 in cancer includes the breast cancer cell line MCF7, which is dependent on oestrogen for growth. When CCN1 is overexpressed in these cells, they become oestrogen-independent and extremely resistant to apoptosis, partly due to the upregulation of XIAP; an anti-apoptotic protein (246–248). This anti-apoptotic role of CCN1 is facilitated through the integrin receptor $\alpha_v\beta_3$. The expression of this integrin receptor is also stimulated by CCN1 (249).

Interestingly, CCN1 also has the ability to induce cell senescence and apoptosis, two key processes of tumour suppression. CCN1 activity may regulate proliferation of damaged cells, thereby preventing tumorigenesis (250,251). For example, as previously mentioned, CCN1 can stimulate the proliferation of prostate cancer cells and therefore tumour growth, however, it can also induce apoptosis when in the presence of TRAIL; an immune surveillance cytokine involved in inducing apoptosis (233,252). In addition to this, CCN1 expression is high in prostate cancer cells that possess mutant or null *p53* and low in cells that express wild-type *p53*, which suggests that together, CCN1 and p53 can promote apoptosis in tumour cells and that high CCN1 levels can, in fact, be tolerated in cells that possess mutant *p53* (253).

### 3.1.4 CCN1 in gliomas

CCN1 has been found to be highly expressed in primary gliomas, as well as in high-grade glioma cell lines (243). It has been shown to be highly expressed in the astrocytoma cell lines U87, U373 and T98G and only weakly expressed in the less invasive U343 cell line. In a study by Xie *et al*, expression of CCN1 was quantified using real-time PCR for 98 primary brain cancer samples and four normal brain tissues. The results revealed overexpression of CCN1 in 68% of the GBM samples, 22% in the astrocytomas and 14% in the less invasive oligodendrogliomas suggesting that CCN1 plays a role in tumour progression in GBM (254). Mirroring the observations in the previously mentioned study with the breast cancer cell line MCF7 (246), forced expression of CCN1 in U343 cells increased proliferation, angiogenesis and tumorigenicity *in vivo*. Cells overexpressing CCN1 migrated more readily and produced larger, more vascularised tumours in nude mice (254).

CCN1 induces its effects through its involvement in a number of different pathways. It has been shown that CCN1 induces tumorigenesis in gliomas through its activation of the Akt pathway and by stabilising β-catenin and its nuclear import. This results in the activation of the β-catenin-TCF/Lef signalling pathway, a key pathway in cell proliferation (254,255). In addition, CCN1-expressing glioma cells activate the PI3K pathway through integrin-linked kinase (ILK) and also inhibit GSK3 in U343 cells through its phosphorylation, as well as promote the nuclear translocation of β-catenin. These effects are most likely produced through the activation of ILK, which has been previously shown, in breast epithelial cells, to inhibit GSK3 by its direct phosphorylation, causing the

nuclear translocation of β-catenin (256). β-catenin is an important regulator of the Wnt signalling pathway. It acts as a co-activator to form a key complex with TCF/Lef transcription factors to induce transcription of a number of different target genes that are involved in cell proliferation (257). These genes include those that code for cyclin D1, E-Cadherin, c-Jun and c-Myc (258–260).

Abnormal expression of receptor tyrosine kinases (RTK) is involved in a number of different mechanisms that stimulates malignant processes. The RTK known as c-Met, along with its ligand hepatocyte growth factor (HGF), are overexpressed in a number of different tumour types, correlating with poor prognosis (261,262). Activation of the c-Met/HGF pathway results in numerous biological processes including proliferation, angiogenesis and migration/invasion (263–265). Studies into this pathway found that CCN1 is, in part, responsible for the activation and mediation of the c-Met/HGF pathway and that intra-tumour levels of CCN1 directly correlate with c-Met levels. Furthermore, inhibiting the *CCN1* gene overrides Akt-dependent cell signalling as well as the biological processes that respond to c-Met/HGF activation. More specifically, CCN1 siRNAs were shown to inhibit HGF-dependent cell migration and growth in the glioma cell lines U87, U373 and SNB-19, both *in vitro* and *in vivo* using nude mice. These findings show that the activation of CCN1 prolongs HGF-stimulated Akt-dependent signalling and the downstream effects. In addition, CCN1 protein levels in gliomas could be used as a biological marker of c-Met/HGF inhibition in tumours that are dependent on HGF (243).

The Cancer Genome Atlas (TCGA) includes a dataset of primary brain tumour samples from approximately 400 GBM patients (266). TCGA generated a Kaplan-Meier plot to determine association of *CCN1* expression and survival of GBM patients. The dataset revealed a statistically significant lower survival rate ($P=3.84x10^{-4}$) in GBM patients with high expression of *CCN1* compared to those with low expression (Figure 15). Another online dataset, the Repository for Molecular Brain Neoplasia Data (REMBRANDT), is a joint project of the National Cancer Institute and the National Institute of Neurological Disorders and Stroke consisting of clinically annotated data created through the Glioma Molecular Diagnostic Initiative. It consists of 874 glioma samples containing 566 gene expression arrays, 834 copy number arrays and 13,472 clinical phenotype data points (267). The REMBRANDT data for *CCN1* gene expression reveals elevated levels in GBM samples compared to lower grade gliomas and normal brain tissue (Figure 16). This suggests that *CCN1* expression plays an important role in glioma biology with clinical relevance and applicability as proposed by this research.

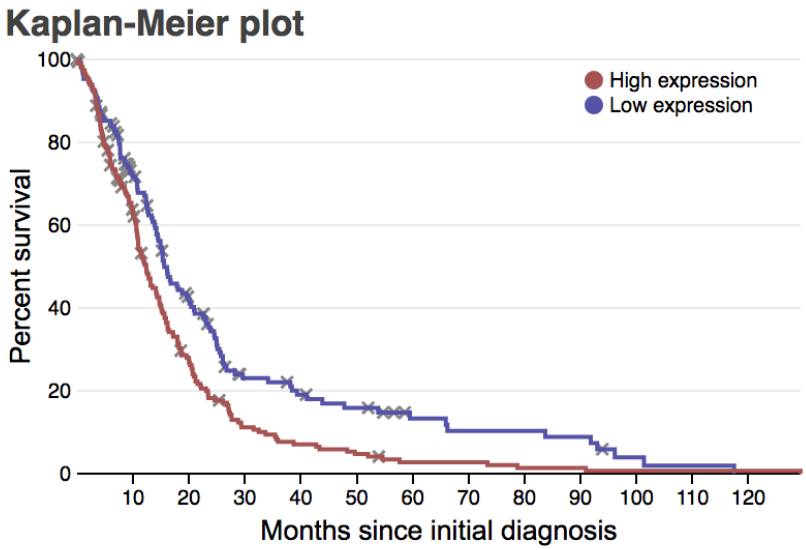


Figure 15. A Kaplan-Meier plot graph taken from TCGA showing percentage patient survival in GBM patients with high expression of *CCN1* and low expression of *CCN1* over months following their initial diagnosis. This data was taken from approximately 400 GBM patients and revealed a statistically significant lower survival rate ($P=3.84x10^{-4}$) in GBM patients with high expression of CCN1 compared to those with low expression (50).

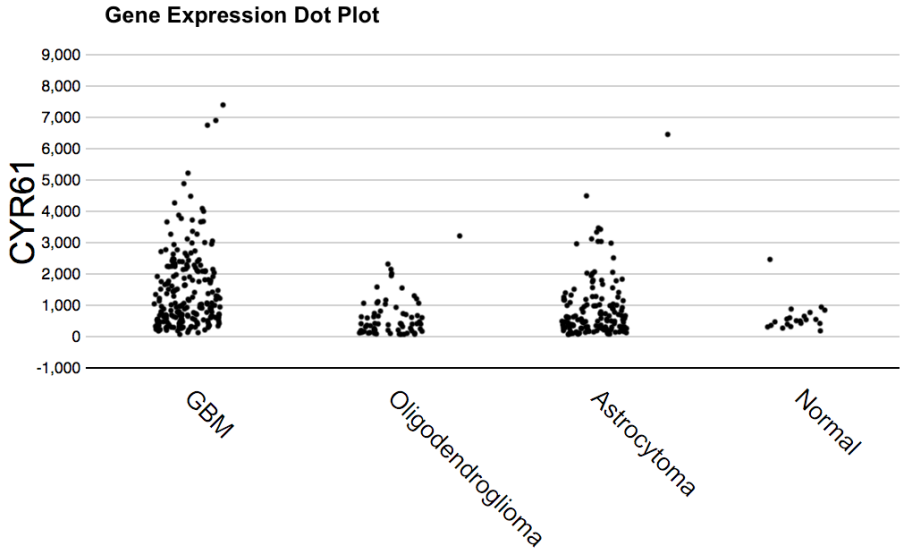


Figure 16. A gene expression plot taken from REMBRANDT showing CCN1 (CYR61) expression in glioma subtypes; GBM, oligodendroglioma, astrocytoma and normal brain tissue. REMBRANDT consists of 874 glioma samples containing 566 gene expression arrays, 834 copy number arrays and 13,472 clinical phenotype data points (51). The data for CCN1 gene expression shows elevated levels in GBM samples compared to lower grade gliomas and normal brain tissue, suggesting that CCN1 expression plays an important role in glioma biology with clinical relevance and applicability as proposed by this research.

### 3.1.5 CCG-1423 and MAT

CCG-1423 appears to promote distinct cellular responses in highly migratory glioma cells. This small molecule inhibitor targets the RhoA transcription signalling pathway (167) and seemingly induces MAT in treated cells. Mesenchymal and amoeboid modes of migration are interchangeable as switching between the two can be induced in cancer cells in response to changes in the extracellular environment including external pressures such as drug selection (85). This cellular switch may potentially allow the identification of pathways involved in this mechanism and enhance drug development. This is extremely important as a combination approach targeting both migration modes may be favoured to fully stop migratory activity in cancer cells. A high-resolution method of imaging and analysis is needed in order to observe and assess the characteristics of a phenotypic switch that occurs in MAT in cells treated with CCG-1423, especially in a 3D environment, as well as to confirm the previous results of this thesis. The limitations of 2D analysis in 3D cellular imaging impair the accuracy of research findings in biological studies. An approach of 3D analysis for advanced data acquisition and interpretation is needed to improve the accuracy and reliability of results gained for drug development.

### 3.1.6 Three-D analysis of 2D images

Traditionally cancer drug screens rely on the assessment of drug activity on 2D cell monolayers recording cytotoxic effects. The advantages of this approach are clear and include high throughput screening, determination of direct effects on cell viability and advancing our understanding of cancer biology (268). However, the disappointing hit rate of drug discovery when translated into clinical trials has

highlighted the importance to target cancer cells in a setting more appropriate for recapitulating the 3D structure of an original tumour (269). In addition, there has been a steady increase in the development of anti-migratory drugs as adjuvant treatment to target the dissemination of highly invasive cancers such as gliomas. Screening of cells migrating in a 3D environment aids a more representative assessment of drug activity than within a 2D environment (270). Initial assessment of MAT so far has relied on the interpretation of 2D images created by light microscopy from, for example, 3D spheroid invasion assays. However, interpretation of such images has to be treated with caution as there are limitations to assessing images with a 3D background captured on 2D images. Images generated by 2D image capture suggest that drugs have distinctive effects on migratory cells, but, so far, a more accurate high resolution analysis of 3D generated imagery is in its infancy. As such, standard microscopy may miss important details of drug activity because of imaging, for example, one focal plane at a given time. This can lead to imprecise data interpretation such as overestimation of drug efficacy.

### 3.1.7 Instant structured illumination microscopy (iSIM)

Structured illumination microscopy (SIM) has an improved resolution of twofold over that of widefield microscopy. It also provides a much faster acquisition rate and computationally discards out of focus light that emerges from anywhere but the focal plane. These advantageous properties allow for optically-sectioned super-resolution imaging from hundreds of 3D time-points (271). SIM uses a moderately low number of widefield images in order to capture the information needed to increase resolution, as well as causing less irradiation to the samples

compared to other such techniques, thus deeming it more useful for imaging live samples (272). It is also compatible with all the fluorophores commonly used with confocal and widefield microscopy and can be used to produce depth-sectioning with an excitation pattern structured in three dimensions (273). To extract high spatial frequency information using SIM, multiple images of the sample must be obtained using a number of different orientations, which then need to be processed to acquire the final image (274).

The speed of image acquisition using SIM was improved upon by multifocal SIM (MSIM) to several frames per second by the use of a digital mirror device which generates numerous excitation foci scanned across the sample. The generated foci are then ordered into a pattern. Every time this pattern is translated by the digital mirror device, a fluorescence image is produced. This image is then processed in a software that pinholes the fluorescence from each excitation spot. This is achieved by setting the pinhole to 0, past a certain radius, in order to reject light outside the focal plane. This is repeated until the entire field of view has been scanned. All the images are then scaled by a factor of 0.5 and summed to produce one frame (275).

This was then developed further into iSIM. iSIM uses optical hardware which performs automatic summing of all images resulting in an ‘instant’ visualisation of a high-resolution image (271). A lenslet array generates a set of beamlets that are focussed onto the sample. This causes a fluorescence image to be generated which is then passed through a set of pinholes in order to reject light outside the focal plane. The image is then passed through a second lenslet array which

causes the beamlets to focus, resulting in each image from each excitation spot to be scaled by a factor of 0.5. These resulting images are then scanned by a mirror, which also scans the excitation across the sample to provide a single image comprised of all the fluorescence images that are generated. The resulting, instantly presented single image has an increased resolution to previous imaging techniques and an extremely rapid image attainment of more than 100 frames per second (274). A z-stack can be generated, with an interval of 10ms between slices, using iSIM whereby the optimum start and end points can be chosen manually. The start point is then set to 0, the end point to the value of the final desired frame. Each image is then automatically captured and saved as a 16-bit TIFF single file containing the multiple slices of the z-stack (274).

The advanced technology of iSIM was chosen to capture MAT in glioma cells treated with CCG-1423. The super-resolution of iSIM and extremely fast image acquisition was deemed capable of visualising the change from elongated morphology to rounded morphology in CCG-1423 treated U251 cells migrating away from the core of tumour spheroids set in a collagen bed. With a twofold improvement on widefield microscopy for 3D resolution, this method could provide more accurate and reliable results for drug efficacy studies. By pairing this technology with other experimental assays, the mechanisms of CCG-1423 on glioma cells can be more accurately explored, allowing for a more detailed understanding of the abilities of these invasive cells.

## 3.2 Materials and methods

### 3.2.1 Cell lines and culture medium

The adult glioma cell lines U87 (Grade IV, GBM) and U251 (Grade IV, GBM) were used in this study, originally established by Pontén and colleagues (180). These cells have been comprehensively characterised in terms of genomic alterations and gene expression patterns. Cells were grown in Dulbecco's Modified Eagles medium (DMEM) (Sigma) with 10% heat-inactivated foetal calf serum (HI-FCS) (Labtech) and 0.5% penicillin-streptomycin (Sigma) (complete medium). They were free of mycoplasma contamination as confirmed by Sarah Perry (In house testing at LICAP) and had been genotypically profiled by University of Leeds in-house services (Claire Taylor).

### 3.2.2 Cell culture

Cells were cultured in a Sanyo $CO_2$ incubator at 37°C in a humidified atmosphere of 5% $CO_2$ (in air). Cells were maintained in plastic tissue culture flasks (Corning) and harvested at or near confluence by washing with PBS and then adding trypsin (10x solution, diluted 1:10 in Hanks Balanced Salt Solution, (Sigma)). Cells were viewed/imaged with a Nikon eclipse TS100 microscope and counted using an improved Neubauer haemocytometer (Weber Scientific).

### 3.2.3 MTT assay

U251 and U87 cells were seeded at a density of $2.5x10^3$ per well in a 96 well plate (Corning) and incubated overnight at 37°C. One row was kept clear of cells as a background control. The supernatant of the cells was then removed and replaced with either 100μl of fresh medium or 100μl of medium containing CCG-

1423 (Tocris) in serial dilutions of 50μM, 5μM, 0.5μM, 0.05μM, 0.005μM or 0.0005μM. A control of 0.5% DMSO (Sigma) was also used as well as the empty wells just containing medium. The plate was then incubated for 72 hours at 37°C. The supernatants were removed and replaced with 100μl of medium with 10μl of MTT reagent (Sigma) and incubated at 37°C for 3 hours. All media was removed and replaced with 100μl of lab grade DMSO (Sigma) and read on a colorimetric plate reader (Thermo Fisher) at 540nm.

### 3.2.4 Enzyme-linked immunosorbent assay (ELISA)

U251 and U87 cells were cultured at a density of $2x10^3$ in 6 well plates (Costar, Corning Lifesciences, USA) and incubated for 24 hours at 37°C. Following incubation, the media was removed and replaced with 2ml of complete medium (control) or medium with 500nM of CCG-1423 (Tocris). The cell supernatants were collected at 24, 48 and 72-hour time points. A commercially available Human CYR61/CCN1 Quantikine ELISA kit (R&D Systems) was used for the solid phase sandwich ELISA for CCN1. Forty-eight microplate well strips were removed from the plate frame (3 wells per time point per cell line and 8 for the standard curve) and 100μl of assay diluent was added to each well, followed by 50μl of cell supernatant, control or standard. The wells were covered with a plate sealer and incubated on a plate shaker at room temperature for 2 hours. The wells were aspirated and washed 3 times with wash buffer. 200μl of human CCN1 conjugate was added to each well and incubated for 2 hours on a plate shaker. The wells were washed 3 times with wash buffer before adding 200μl of substrate buffer to each well. The wells were incubated for 30 minutes at room temperature

covered with foil. 50µl of stop solution was added to each well and the plate was immediately read on a plate reader at 540nm (Thermo Fisher).

### 3.2.5 Immunofluorescence staining

U251 cells were cultured at a density of $2x10^3$ on sterile 25x25 coverslips in 6 well plates (Costar, Corning Lifesciences, USA) and incubated for 24 hours at 37°C. Following incubation, the media was removed and replaced with 2ml of complete medium (control) or medium with 500nM of CCG-1423 (Tocris). The plates were incubated for a further 48 hours at 37°C. The cells were fixed using 4% PFA (Thermo Scientific) and blocked for 1 hour using 5% normal goat serum (Abcam). The cells were stained by immunofluorescence for MKL1 (anti-MKL1 Rb, Abcam) at 1:100 and incubated for 24 hours at 4°C. The cells were washed 3 times with PBS and incubated for an hour at room temperature with the secondary antibody anti-rabbit Alexa fluor 488 (Abcam) at 1/500. The cells were washed 3 times in PBS and mounted on glass slides using Mowiol with Hoechst (Sigma). The slides were imaged on a Bioimaging Zeiss LSM880 Inverted Confocal microscope (Zeiss).

### 3.2.6 Western blotting

Cell lysates were obtained from cells grown in 25 $cm^2$ plastic tissue culture flasks (Corning) treated with 500nM of CCG-1423 (Tocris) for 24, 48 and 72 hours. Cells were placed on ice and washed twice with ice cold PBS. The cells were collected and centrifuged at 400g for 5 minutes. The PBS was removed and the pellet was resuspended in 0.5ml of Tris-HCl lysis buffer 25 µl/ml protease inhibitor (Sigma-Aldrich) for 5 minutes. The cells were centrifuged at 400g for 10 minutes.

Supernatants containing the cytoplasmic extract were collected and transferred into clean tubes.

Protein concentration of each cell lysate was determined by Bradford protein assay (Bio-Rad), whereby 2µl of protein sample was added to 700µl of Bradford protein assay solution in a cuvette (Sigma). Included in this was a 'blank' consisting of 2µl of Tris-HCl buffer in 700µl Bradford protein assay solution. The samples were measured at 595nm on a spectrophotometer and normalised to the lowest concentrated lysate using Tris-HCl buffer.

10µl of Laemmli buffer (Bio-Rad) was added to the cell lysates, which were boiled for 5 minutes at 95°C in a dry bath. Fifty microlitres of cell lysate was loaded into wells in a 4-20% TGX stain-free precast gel (Bio-Rad) with a pre-stained protein ladder (Bio-Rad) to estimate protein size. Proteins were separated by sodium dodecyl sulphate polyacrylamide gel electrophoresis (SDS-PAGE) at 120V for approximately 90 minutes in a tank filled with running buffer (Bio-Rad). They were transferred to PVDF membranes at 250mAmp over 90 minutes in a tank filled with transfer buffer (Bio-Rad). Once unpacked, the PVDF was washed in Tris-Buffered Saline and Tween®20 (TBST) and blocked in 5% milk in TBST for 45 minutes. The PVDF was probed with an antibody against MKL1 (1:300, Abcam) in 5% milk in TBST overnight. PVDF was washed 3 times in TBST and exposed for 90 minutes to the secondary antibody HRP-conjugated donkey anti-rabbit IgG antibody (1:1000, GE Healthcare). Following a further 3 washes with TBST, proteins were detected by SuperSignal West Femto maximum sensitivity substrate (Thermo Fisher), according to the provided protocol and visualised

using a ChemiDoc MP imaging system (Bio Rad) and Image Lab software (BioRad). Protein band intensity was analysed using Image J software. The intensity of each band was normalised to the corresponding β-actin control.

### 3.2.7 Three-D spheroid generation and invasion assay

For inhibitor studies, U251 cells were seeded at $1x10^3$/well in low adherence 96 well plates (Nunc, UK) as previously described (Cheng et al., 2015). Three days after seeding, spheroids contained within the wells were embedded in rat tail collagen V (Corning Life Science, US), polymerisation was achieved with 1M NaOH. The inhibitor CCG-1423 (Tocris Bioscience, US) was resuspended in DMSO and was added at a predetermined anti-migratory concentration at 2X (500nM). Some spheroids were mock-treated with DMSO-supplemented medium only. Invasion into collagen was observed over 72 hours at 24-hour interval and images captured with the EVOS Cell Imaging System (Advanced Microscopy Group) at 4x magnification.

### 3.2.8 Preparation of spheroids and migratory cells for iSIM imaging

We have previously reported the staining of collagen embedded spheroids and associated migratory cells with fluorescent dyes such as phalloidin and DAPI (Cheng et al., 2015). Here, this technique was improved and amended to allow antibody labelling. The whole procedure was adapted so that it can be carried out in the original low adherence 96-well plate (Nunc, US). After completion of the invasion assay, the wells were carefully washed with PBS three times; this was achieved using 200µl pipette tips and pastettes to add and remove fresh PBS. The collagen plugs were fixed using 4% PFA for 40 minutes. For permealisation,

0.5% Triton-X100 was added for 30 minutes; three washes of PBS were followed by blocking with 0.01% Marvel skimmed milk powder in PBS for five minutes. The collagen plugs were incubated with Alexa Fluor 488 phalloidin at 1/500 (Molecular probes, Invitrogen US) and anti-acetylated tubulin antibody (1/500) (Abcam, UK), which had been prepared in the blocking solution (0.01% Marvel skimmed milk powder) and spun down for 5 minutes at 13,000 rpm. After a two-hour incubation, the collagen plugs were washed three times with PBS for five minutes each; the secondary antibody, Alexa Fluor 488 (conjugated to Alexa Fluor 488 phalloidin) (1/500; Molecular probes, Invitrogen US), was added at a 1/500 concentration along with DAPI (1/500, according to manufacturer instructions), prepared as for the primary antibody solution. Incubation was for 1 hour after which the collagen plugs were washed three times with PBS. The collagen plugs were carefully lifted out of the wells and transferred onto glass slides. Fluoromount G (Thermo Fisher Scientific, UK) was added to the plugs and coverslips were gently lowered onto the collagen plugs.

### 3.2.9 iSIM imaging

The iSIM used for this study was built and housed at the University of Leeds (Dr Alistair Curd). The objective lens used was a x60 NA 1.2 objective (Olympus). This iSIM has a frame rate of 100 frames per second (fps) with lateral sampling at 56nm per pixel. Deconvolution was performed on all final images using the Image plugin DeconvolutionLab (Biomedical Imaging Group, EPFL, Switzerland).

### 3.2.10 Data analysis

MTT and ELISA assays were analysed using a plate reader and ascent computer software (Thermo Fisher). For the ELISA, the optical density of each sample was read at 540nm. The standard curve was generated in Excel and used to calculate the concentration of each sample in pg/ml. Immunofluorescence for MKL1 was analysed using particle analyser in the ImageJ software (http://rsbweb.nih.gov/ij). The data generated using ImageJ was collected by generating an outline of a single cell (minus the nucleus) and an outline of the nucleus using the DAPI image. These were then used to measure the mean gray value of the fluorescent MKL1 in the cytoplasm and the nucleus. This method ensured that there was no overlap of particles in either measurement, creating accurate results. For all experiments, differences between control cells and treated cells were compared using a two-tailed T-test (Excel). P-values $\leq 0.05$ were considered statistically significant.

### 3.2.11 ImageJ plugin for data analysis

A novel ImageJ plugin was developed together with Dr Arndt Rohwedder to specifically measure the number of filopodia and major protrusions, of treated and untreated U251 cells, from the images captured with iSIM. The plugin takes the current image/image stack and generates an internal copy for the analysis. In the case of an image stack, each slice is evaluated individually. Firstly, a black and white image is generated using auto-threshold. To remove small single pixel (‘noise’), a rank filter is applied to the image using median and bright outliers filters. The function ParticleAnalyser is then used for isolating the cells/cell cluster. This is achieved with the options EXCLUDE_EDGE_PARTICLES,

requiring objects not touching the frame, INCLUDE_HOLES, resulting in the detection of the outer objects border only and CENTER_OF_MASS for analysing of lateral shifts. Size limits are calculated in percentage from the minimum coverage value from the menu and a reduced width and height value for maximum. The particle analyser will try to find an object based on those values first. When it fails, it starts reducing the minimum size value until an object is identified. When an object is found, the resulting ROI is stored for analysis as a linear array.

## 3.3 Results

### 3.3.1 MTT assay for assessing cell viability following CCG-1423 treatment

The effect of CCG-1423 on cell viability was confirmed by using an MTT assay (Figure 17). Viable cells with metabolic activity convert MTT into a purple formazan product. This reduction reaction reflects the amount of living cells in the well (276). By using this technique on cells that have been treated with CCG-1423, we can assess at which concentration the drug is killing the cells rather than exerted its anti-migratory effects. In previous studies, CCG-1423 had been used at 500nM. Concentrations were therefore chosen above and below 500nM. The concentrations were 50μM, 5μM, 0.5μM (500nM), 0.05μM, 0.005μM and 0.0005μM. The results of the MTT assay were expressed as a percentage of the control.

CCG-1423 did not significantly affect cell viability of U251 cells at 0.0005μM (98.2% +/- 3.9%) (P=0.37), 0.005μM (96.8% +/- 3.3%) (P=0.07) or 0.5μM (95.9% +/- 6.2%) (P=0.38), when compared to the control. At a concentration of 0.05μM, CCG-1423 did not affect cell viability of U251 cells (96.5% +/- 1.8%), however, slight statistical significance was reached when compared to the control (P=0.02). CCG-1423 at a concentration of 5μM, significantly affected cell viability of U251 cells (13.4% +/- 1.2%) when compared to the control ($P=2.06x10^{-7}$). CCG-1423 also significantly affected U251 cell viability at a concentration of 50μM (6.1% +/- 1.0%) when compared to the control ($P=1.84x10^{-8}$) (Figure 17A).

CCG-1423 did not significantly affect cell viability of U87 cells at 0.0005μM (99.2% +/- 5.5%) (P=0.11), 0.005μM (99.2% +/- 7.4%) (P=0.13), 0.05μM (99.1%

+/- 7.8%) (P=0.21) or 0.5μM (97.3% +/- 7.0%) (P=0.46), when compared to the control. CCG-1423 at a concentration of 5μM, significantly affected cell viability of U87 cells (6.3% +/- 0.3%) when compared to the control ($P=5.8x10^{-10}$). CCG-1423 also significantly affected U87 cell viability at a concentration of 50μM (6.1% +/- 0.23%) when compared to the control ($P=1.81x10^{-11}$) (Figure 17B).

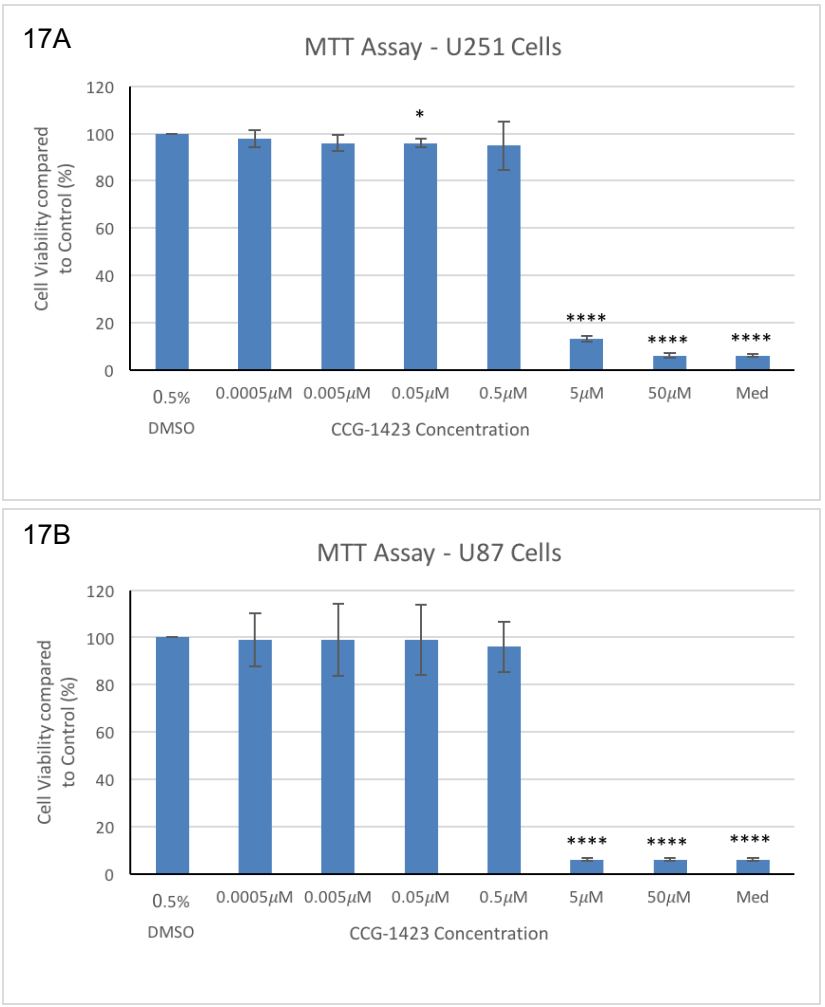


Figure 17. Cell viability of U251 and U87 monolayers treated with CCG-1423. Serial dilutions of CCG-1423 were added to U251 cells (17A) and U87 cells (17B). Cell viability was confirmed by a MTT assay and was expressed as a percentage of the control. This was carried out before continuing further CCG-1423 studies to confirm that the recommended inhibition concentration was correct and that observed rounding effects of CCG-1423 on glioma cell lines was not due to cell death. Experiments were repeated in triplicate. Asterisks indicate statistical significance where **** = p≤0.0001.

### 3.3.2 ELISA for the detection of CCN1 secretion

To investigate the effects of CCG-1423 on CCN1 secretion in the cell lines, a sandwich ELISA was used to detect the presence of secreted CCN1 in the supernatants of U251 and U87 cell cultures over 72 hours. The cells were seeded at a density of $2x10^3$ in 6 well plates and incubated for 24 hours at 37°C. The medium was then replaced with fresh medium (control) or medium containing 500nM of CCG-1423. The supernatants were then removed at time points of 24, 48 and 72 hours and tested by ELISA. The optical density was obtained from running the plate on a colorimetric plate reader at 540nm. The concentration of CCN1 in the medium did not increase in the treated cells, whereas there was a detectable increase in CCN1 levels in the supernatants from untreated cells over time (Figure 18). At the 24-hour time point, the supernatant of U251 cells treated with CCG-1423 had a CCN1 concentration of 0.47pg/ml +/- 0.51pg/ml, which was not significantly different to the control (2.19pg/ml +/- 0.17pg/ml). At the 48-hour time point, the concentration of CCN1 in the supernatant of U251 cells treated with CCG-1423 was 1.33pg/ml +/- 0.87pg/ml, which was significantly different to the control (16.88pg/ml +/- 0.86pg/ml) (P=0.04). At the 72-hour time point, the concentration of CCN1 in the supernatant of U251 cells treated with CCG-1423 was 4.79pg/ml +/- 1.2pg/ml, which was significantly different to the control (50.15pg/ml +/- 3.08pg/ml) (P=0.03).

At the 24-hour time point, the supernatant of U87 cells treated with CCG-1423 had a CCN1 concentration of 4.0pg/ml +/- 0.17pg/ml, which was not significantly different to the control (4.38pg/ml +/- 0.32pg/ml). At the 48-hour time point, the concentration of CCN1 in the supernatant of U87 cells treated with CCG-1423

was 4.38pg/ml +/- 0.69pg/ml, which was significantly different to the control (17.79pg/ml +/- 0.51pg/ml) (P=0.02). At the 72-hour time point, the concentration of CCN1 in the supernatant of U87 cells treated with CCG-1423 was 2.47pg/ml +/- 85pg/ml, which was significantly different to the control (29.29pg/ml +/- 1.2pg/ml) (P=0.015).

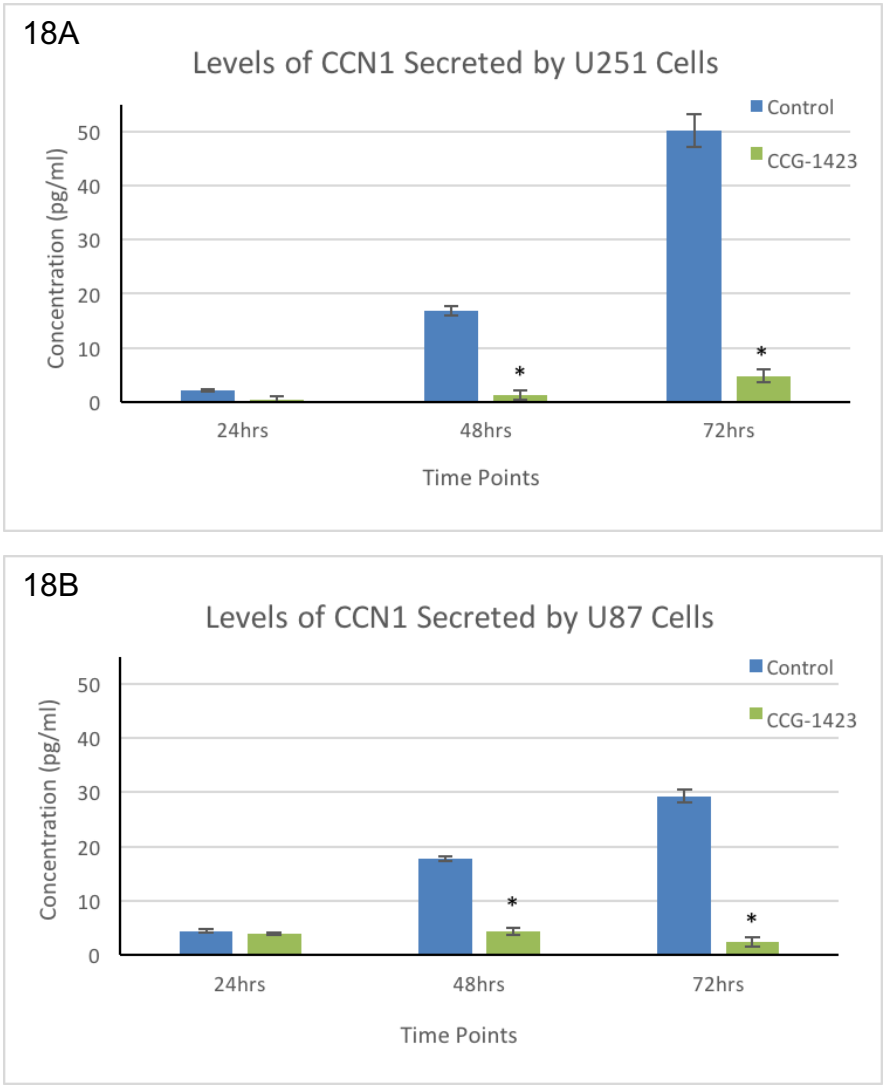


Figure 18. An ELISA was carried out to determine CCN1 levels in the supernatants of U251 and U87 cell lines over a 72-hour period. Cells were incubated for 24, 48 and 72 hours +/- CCG-1423. The supernatants were collected for each time point and tested for CCN1 by ELISA. CCN1 concentration levels were reduced in the supernatants of treated U251 (18A) and U87 cells (18B), at the 48 and 72-hour time points, when compared to the untreated controls as indicated by decreased concentration. Experiments were repeated in triplicate. Asterisks indicate statistical significance where * = p≤0.05.

### 3.3.3 The effects of CCG-1423 on MKL1 nuclear import

The reduction in CCN1 secretion by cells treated with CCG-1423 is thought to be a result of the inhibition of MKL1 nuclear import, based on published data (225). Immunofluorescence was used to visualise a potential build-up of MKL1 in the cytoplasm of cells treated with CCG-1423 in comparison to untreated control cells. From observation of the confocal images, there appeared to be a marked increase in cytoplasmic MKL1 in cells treated with CCG-1423 with a concomitant loss of nuclear MKL1 (Figure 19). To quantify these observed results, the mean gray value of 30 imaged cells per repeat was calculated for cytoplasmic staining and nuclear staining of MKL1 using ImageJ (Figure 20). The mean gray value for nuclear staining of MKL1 in U251 cells treated with CCG-1423 was 54.54 +/- 1.75, which was significantly different to the control (99.35 +/- 4.33) ($P=4.65x10^{-19}$). For cytoplasmic staining of MKL1, the mean gray value for treated U251 cells was 62.11 +/- 2.08, which was also extremely significant compared to the control (36.24 +/- 1.66) ($P=1.25x10^{-16}$).

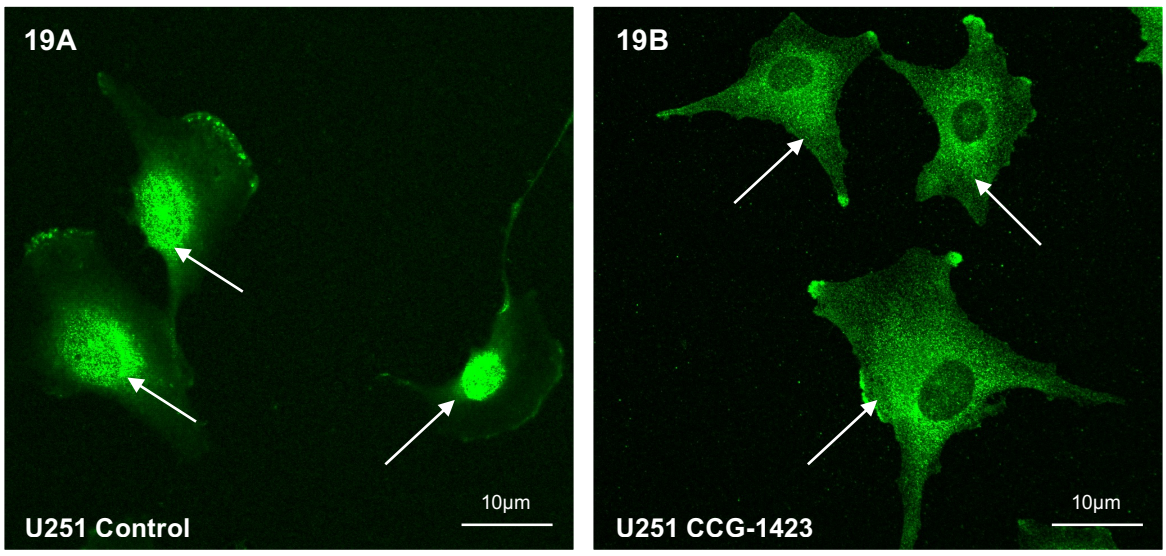


Figure 19. Immunofluorescence staining of MKL1 in untreated U251 cells (19A) and U251 cells that have been treated with CCG-1423 (19B) for 48 hours. Arrows show a build-up of MKL1 in the cytoplasm of treated cells compared to the control cells which show pronounced nuclear staining. Imaged on a confocal microscope at a magnification of x60. Green fluorescent stain = MKL1; Scale bar = 10µm.

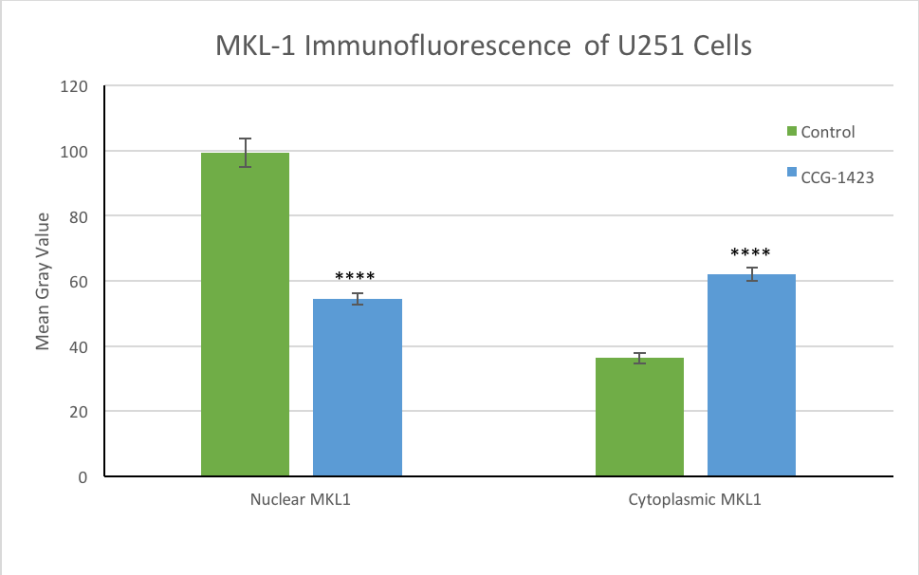


Figure 20. Quantification of immunofluorescence staining of MKL1 to determine differences in nuclear and cytoplasmic MKL1 localisation in untreated (control) U251 cells and U251 cells treated with CCG-1423. The images were analysed using ImageJ where a mean gray value was calculated for the nucleus and the cytoplasm of each cell. A total of 90 cells were analysed over 3 repeat experiments. Asterisks indicate statistical significance where **** = p≤0.0001.

To confirm the results from the immunofluorescence imaging of MKL1, western blots were carried out to determine cytoplasmic protein levels of MKL1 in untreated (control) and CCG-1423 treated U251 cells over a 72-hour period. During sample preparations of cell lysates, nuclear-associated components were discarded, therefore the results from the western blot are representative cytoplasmic MKL1. The U251 cell line showed an increase in MKL1 build-up in the cytoplasm when treated with CCG-1423 (Figure 21). The intensity of the MKL1 band at the 24-hour time point was 1.44 +/- 0.39, which was significantly different to the control (0.46 +/- 0.04) (P=0.04). At the 48-hour time point, the intensity of the CCG-1423 treated MKL1 band was 1.81 +/- 0.39, which was significantly different to the control (1.22 +/- 0.07) (P=0.05). At the 72-hour time point, the intensity of the CCG-1423 treated MKL1 band was 0.54 +/- 0.11, which was not significantly different to the control (0.48 +/- 0.08).

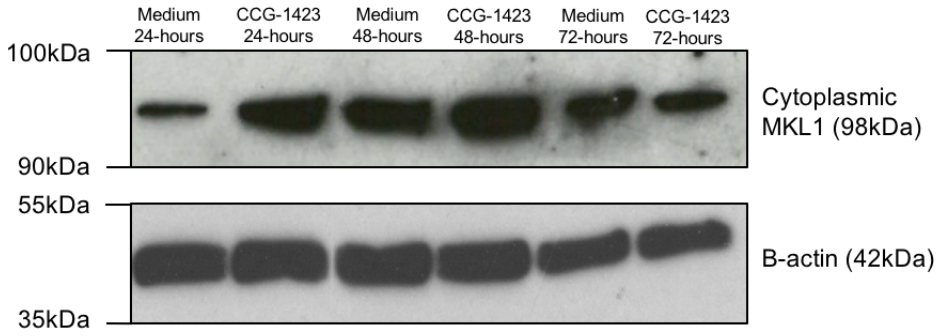


Figure 21A. The U251 cell line was treated with 500nM of CCG-1423 and incubated for 24, 48 and 72 hours before cell lysates were obtained. Protein levels of MKL1 were then determined by western blot. A beta-actin control was included as a protein loading and transfer control.

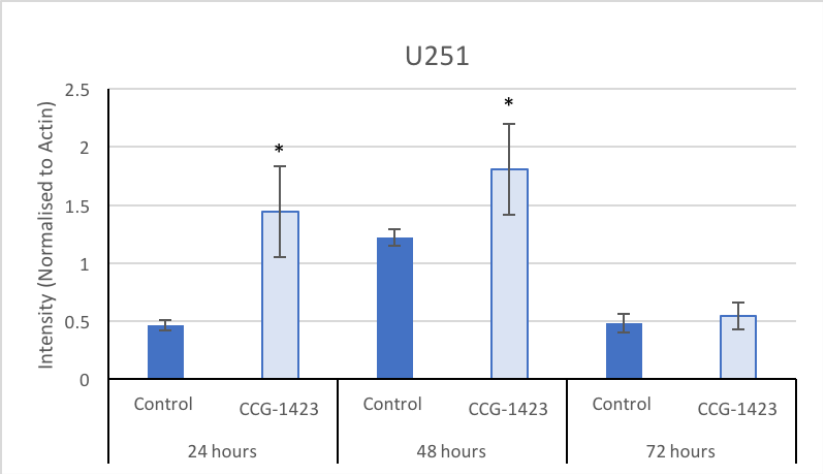


Figure 21B. Western blot analysis of the effects of CCG-1423 on glioma cell lines. Glioma cell line U251 was treated ± 500nM CCG-1423. Following 24, 48 and 72-hour incubations, cell lysates were obtained. Expression of cytoplasmic MKL1 was determined by western blotting including a β-actin control to evaluate protein loading and transfer. MKL1 band intensity was quantified and normalised to the β-actin control using Image J software. Graphs show mean ± SEM of 3 individual experiments. Asterisks show statistical significance where * = p≤0.05.

### 3.3.4 iSIM technology generates high-resolution 3D single cell images

Previous results suggest the induction of MAT in glioma cells by treatment with CCG-1423. To visualise this transition, iSIM was used to capture morphological changes from elongated (mesenchymal) to rounded (amoeboid); a notable sign of MAT. Following the newly established and optimised staining technique, the fixed and fluorescently labelled tumour spheroids and single migratory cells embedded in collagen were successfully imaged using iSIM (Figure 22). High-resolution images were created allowing the detailed visualisation of cell morphology and actin cytoskeletal changes. Z-stacks generated from the iSIM data, with applied colour depth, provides the means to accurately analyse effects of anti-migratory inhibitors on glioma cells in a 3D setting.

22A

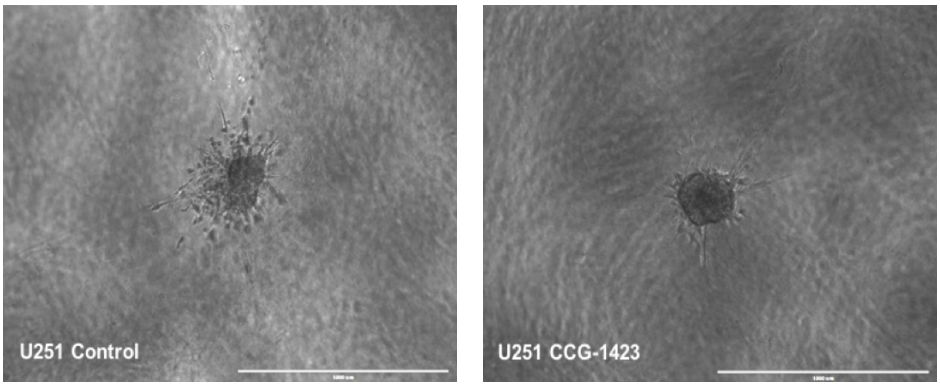


22B

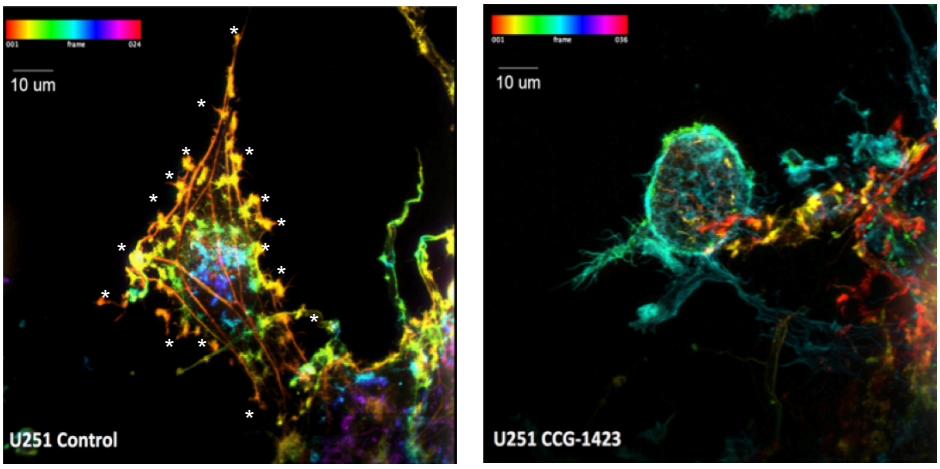


Figure 22. A. Brightfield images of U251 glioma cells after 72h incubation, embedded in collagen, in 96-well low adherent plates. Untreated spheroid and spheroid treated with CCG-1423. In the untreated spheroids elongated cells are visible migrating into the collagen, whereas in the treated spheroids the morphology has seemingly changed to a more rounded phenotype. Scale bar = 1000µm.
B. High resolution 3D iSIM imaging of fixed spheroids and migrating cells within collagen plugs. Left image: a single cell in untreated spheroids emanating from the original spheroid core. Asterisks show filopodia. Right image: the elongated shape disappears after treatment with inhibitor and is replaced by a rounded phenotype. Fluorescent label = Alexa Fluor 488 phalloidin. Scale bar = 10µm. Colour bar: sample depth.

### 3.3.5 CCG-1423 reduces the formation of major protrusions and increases filopodia formation in treated U251 cells

The images obtained by iSIM were imported into ImageJ and analysed using the novel, newly developed ImageJ plugin to calculate the number of major protrusions and filopodia (Figure 23). The frequency of these cellular extensions differs in mesenchymal and amoeboid migratory cells and as such may be used as an indicator of MAT. The average number of filopodia in U251 cells treated with CCG-1423 was 27.14 +/- 3.60 which was significantly different to the control (21.41 +/- 2.21) ($P= 1.40x10^{-15}$). The average number of major protrusions in U251 cells treated with CCG-1423 was 0.55 +/- 0.25 which was also significantly different to the control (1.48 +/- 0.67) ($P=7.14x10^{-15}$). This data was generated from 90 cells per treatment type, over 3 repeats.

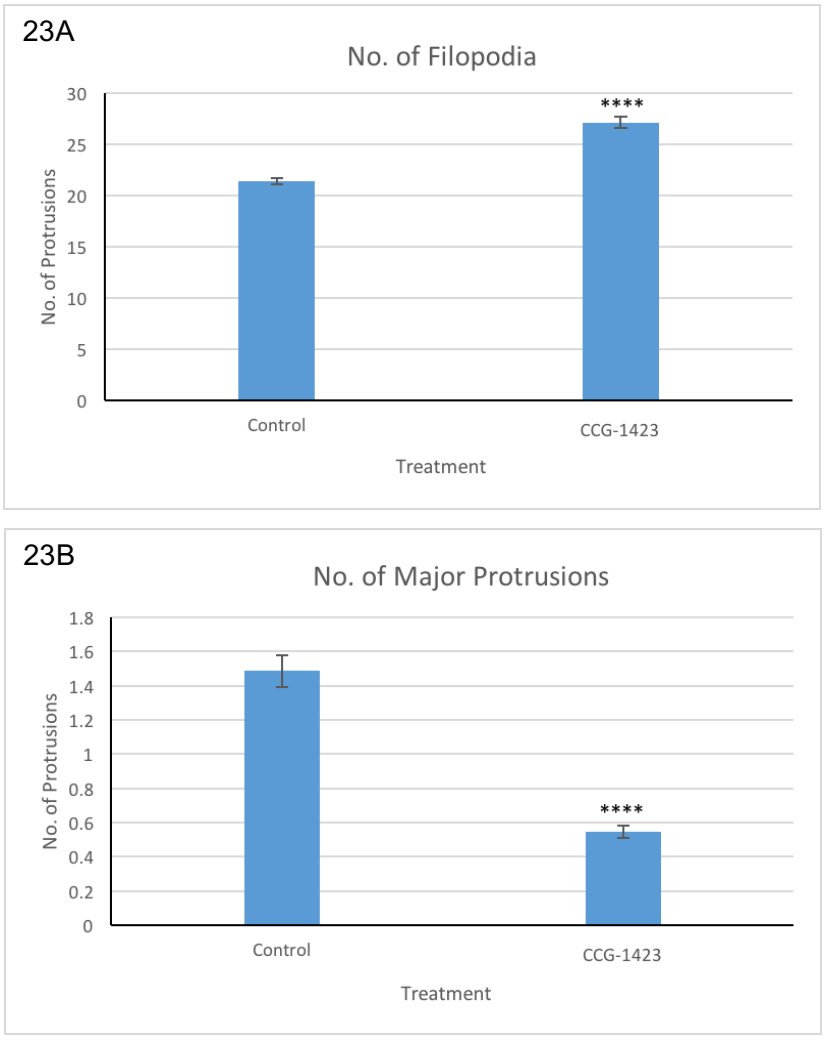


Figure 23. A graph showing the difference in the number of filopodia (23A) and major protrusions (23B) in untreated U251 cells compared to cells treated with CCG-1423. A total of 90 cells per treatment were analysed using a novel ImageJ plugin from the Z-stack images captured by iSIM. The plugin calculates the number of filopodia and major protrusions of each image in the Z-stack and generates an overall number. Asterisks indicate statistical significance where **** = p≤0.0001.

## 3.4 Discussion

### 3.4.1 CCG-1423 inhibits the nuclear import of MKL1

CCG-1423 was investigated for its role in migration in gliomas and as a potential inducer of MAT. It is evident that CCG-1423 has a marked effect on glioma cell lines. Immunofluorescence staining of MKL1 revealed a striking relocalisation of this co-transcriptional activator from nuclear to cytoplasmic when U251 cells were treated with CCG-1423. Quantification of the images confirmed these observations with high statistical significance being reached for both nuclear ($P=4.65x10^{-19}$) and cytoplasmic ($P=1.25x10^{-16}$) MKL1 in treated cells, when compared to the control. The clear build-up of MKL1 in the cytoplasm of cells treated with CCG-1423 is consistent with previous inhibitor studies using NIH3T3 cells. These studies showed that the action of CCG-1423 was promoted by its binding to MKL1 and the inhibition of MKL1 and importin $\alpha/\beta$ interactions and not MKL1 and G-actin interactions, resulting in the prevention of MKL1 nuclear import (167,213). The immunofluorescence results presented here were confirmed by western blot using U251 cells. Like the immunofluorescence results, a build-up of MKL1 in the cytoplasm of cells treated with CCG-1423 at 24 and 48-hour time points was determined. It appeared that the cells recovered after 72 hours as the control and treated bands were not significantly different in their intensity at the 72-hour time point. This is consistent with the live cell imaging results in which cells treated with CCG-1423 started to recover at the 72-hour time point and is also consistent with the original CCG-1423 studies conducted by Evelyn et al. using PC-3 cells, whereby the cells recovered following withdrawal of CCG-1423 (167).

### 3.4.2 CCG-1423 affects CCN1 secretion and migration in glioma cells

The results from the ELISA assays showed a significant decrease in CCN1 secretion in cells treated with CCG-1423. In both U251 and U87, the reduction in CCN1 concentration in cell culture supernatants at the 48 and 72-hour time points were statistically significant (U251 48-hour [P=0.03], 72-hour [P=0.03], U87 48-hour [P=0.02], 72-hour [P=0.01]) compared to the control. Potentially, the reduced levels of CCN1 secretion are a consequence of the inhibition of MKL1 nuclear import by CCG-1423 activity as evidenced by the western blot and immunofluorescence results and as *CCN1* gene transcription is a product of the MKL1/SRF complex. By inhibiting CCN1 secretion, Rac1 activation is inhibited resulting in reduced mesenchymal migration and loss of focal adhesions with a concomitant increase in rounded cell movement (235). The extensions of the plasma membrane in lamellipodia of cells is primarily driven by Rac-activated actin polymerisation. *In vivo*, protruding lamellipodia are extended at one part of the plasma membrane of a single migrating cell and at the front of the leading cells during collective migration, which allows the cells to ‘crawl’ along a migratory surface (277). For example, lamellipodia in dendritic cells are used to crawl towards lymph nodes along lymphatic endothelial vessels (278). An essential part of migration involving lamellipodia is integrin-mediated adhesion, as this maintains activated Rac in a positive feedback loop whereby integrins at the leading edge of a cell stimulate Rac activation (279). Rac recruits activated integrins to the leading edge to promote cell migration (280). Among these is the integrin αvβ3, whose expression is stimulated by CCN1 (249). By inhibiting CCN1, integrin αvβ3 will not be activated and therefore, will not be recruited by Rac to stimulate the positive feedback loop and promote elongated cell migration.

Because of this reduced Rac activation, rounded motility of cells will be elevated via a bleb-driven cell migration, such as, amoeboid migration. This motility type correlates with a high level of active RhoA/ROCK signalling and is driven by cortical actomyosin contractility (281). This migratory activity is often seen *in vivo* and in low-adhesion *in vitro* systems. Cells have the ability to readily transition between bleb-based migration (amoeboid) and lamellipodia-based migration (mesenchymal) *in vivo* in order to adapt to their surroundings as they migrate (282).

CCG-1423 activity targets events downstream of the RhoA signalling pathway but upstream of CCN1 production and therefore Rac activation. Not only does this explain the reduction in CCN1 cell secretion but also the changes in phenotype from elongated to rounded described in the previous chapter. This correlates with the concept that CCG-1423 is inducing MAT in these cells *in vitro,* allowing them to continue to migrate after treatment with CCG-1423 by amoeboid migration. To investigate this transition and the associated changes of cell morphology in more detail, it was necessary to develop an integrated workflow of specimen preparation, high-resolution imaging and data processing for quantification.

### 3.4.3 iSIM advances accurate and reliable MAT analysis in single migrating glioma cells at subcellular level

The advanced technology of iSIM allows high resolution imaging and captures z-stacks with an interval of 10ms between slices (274). iSIM technology was investigated for applicability to image CCG-1423 treated glioma cells seemingly

adopting a more rounded (amoeboid) morphology in stark contrast to their normal elongated (mesenchymal) migratory morphology. As there was no existing protocol for the preparation of migratory cells encased in collagen for use with the iSIM technology, a staining methodology was developed, which allowed the labelling of the original spheroid and migratory cells trapped in the surrounding collagen whilst still maintained within the original 96 well low adherence plate. All washing steps and antibody incubations were carried out in the plate without loss of, or damage to the specimen.

iSIM was used to generate Z-stacks of single migratory cells moving away from the original spheroid core to allow detailed characterisation of changes in migratory phenotypes. Single migratory cells were detected at high resolution with this technology, as well as morphological features, such as, for example, single actin fibres (Figure 22A and B). iSIM associated features allowed us to improve our understanding of the mechanisms of CCG-1423 drug activity on cell migration and confirmed the previous results and hypothesis that the inhibitor is causing the cells to adopt a rounded phenotype. A novel ImageJ plugin was developed to quantify these observations. The plugin was used to calculate the number of major protrusions, such as lamellipodia, and filopodia in the cells under treated versus untreated conditions. Lamellipodia and filopodia formation is regulated by the activity of small RhoGTPases, Rac1 and Cdc42, orchestrators of MAT (85). There was a distinct loss of major protrusions/lamellipodia in treated cells compared to the control cells, which was concurrent with an increase in the number of filopodia in treated cells compared to control cells, a striking feature of MAT (Figure 23). These results support a direct effect on actin dynamics and cell

morphology indicative of MAT when cells are treated with CCG-1423. Liu et al. investigated how adhesion and confinement affect MAT in a number of different cancer cells including HeLa cells (human cervix cancer cells), MDA-MB231 cells (human breast adenocarcinoma), HT29 cells (human colon adenocarcinoma), A375P and A375M2 cells (human melanoma) and HT1080 cells (human fibrosarcoma). They found that under confinement conditions and in the absence of focal adhesions, mesenchymal cells can spontaneously transition to an amoeboid phenotype. They also identified two distinct types of amoeboid migration or 'fast-migration', namely A1 and A2, A2 being the faster of the two. It was discovered that transformed cells were more disposed to adopting the A2 migration mode. However, it was also shown that the various modes of amoeboid migration can be observed in a single cell line by slight changes in the levels of confinement and adhesion. This is a significant observation, which suggests that physical properties of the tumour environment, for example, the confining space around the tumour caused by surrounding tissue, could induce MAT resulting in a faster mode of cell migration and an invasive cancer (25). This could also explain why studies into the inhibition of MMPs fail, due to an increase in tumour confinement resulting in the promotion of MAT (283). If cells can spontaneously undergo MAT to escape a primary tumour in response to the physical environment around them with no pharmacological intervention or genetic alteration, it is more than likely that these strategies can also be adopted by the cells in response to drug treatment, such as CCG-1423.

The use of iSIM has allowed visualisation of the phenotypic changes that occur in MAT. The combined workflow of sample preparation, image acquisition with

this advanced technology and application of a novel ImageJ analysis plugin has confirmed the previous findings of this thesis and supports the proposed phenotype switch in migrating glioma cells after treatment with the inhibitor CCG-1423 in 3D environments. The combined iSIM and plugin technologies may be applicable to other investigations of detailed protein localisation, phenotypic changes and protein co-localisation in a 3D setting; in cancer research, it will advance pharmacological intervention by producing more accurate predictions of drug efficacy.

In the context of this research, confirmatory and additional information has been generated to support the theory of MAT in glioma cells induced by CCG-1423 and has highlighted the need for combination treatments to target both mesenchymal and amoeboid cell migration to fully prevent glioma cell migration and invasion.

# Chapter 4: Clinical relevance of CCG-1423

## 4.1 Introduction

The results presented in the previous chapters support CCG-1423 as a MAT inducer in glioma cell lines and suggest a potential switch between the two migratory modes through the inhibition of CCN1 secretion. The pro-migratory effects of this drug via the RhoA signalling pathway could provide an explanation as to why anti-migratory drugs have a high failure rate when taken to clinical trial. Drug activity of other inhibitors may potentially be exerting similar effects and instead of targeting migration, they are promoting cell migration via induction of different cellular pathways. This highlights the importance and necessity of adopting combination treatments for cancer patients. In addition, new and advancing technologies provide a platform on which to gain a more accurate insight into the effects that drugs will have when moving forward towards clinical trial, including novel 3D technologies for drug investigation and screening, as well as advances in mass spectrometry for accurate detection of drug localisation and diffusion in tissue samples.

### 4.1.1 CCN1 and its role in cancer

CCG-1423 inhibits the Rac signalling pathway through the inhibition of CCN1. Previous studies have shown CCN1 to be associated with cancer progression and invasion. Holloway *et al* (2005) investigated ECM proteins associated with tumour cell metastasis and described CCN1 expression in peritoneal metastases of pancreatic tumours. Analysis of gene expression profiles from a high-density microarray in metastases compared to the primary tumour, showed that there was a greater than two-fold increase in CCN1 expression in the metastases. At

the protein level, immunohistochemistry studies with pancreatic adenocarcinoma cells also showed an increase in CCN1 protein and a persistent expression of the integrin αvβ3 in the peritoneal metastases, suggesting that the interaction between CCN1 and αvβ3 promotes metastasis in pancreatic cancer (284).

In ovarian cancer, CCN1 expression has been found to be abnormally expressed in a large number of ovarian tumours as well as in normal ovarian tissue. In normal ovaries, it was shown that CCN1 plays a role in the formation and regression of the corpus luteum which involves vascular network changes. This process is extremely similar to angiogenesis, which was observed in ovarian tumour formation and is associated with high levels of CCN1. This suggests that CCN1 is a key regulator of biological processes in both normal and cancerous ovaries. Furthermore, CCN1 has been linked to chemoresistance in ovarian cancer. High levels of CCN1 protein was found in cisplatin-resistant ovarian cancer cells when compared to cells that had been sampled before the patient received cisplatin chemotherapy (239). In addition to ovarian cancer, CCN1 has been associated with chemoresistance in MCF-7 breast cancer cells. As CCN1 activates the CCN1 integrin αvβ3, it has been suggested that the observed upregulation of CCN1 in breast cancer may induce the metastatic phenotype by autocrine signalling whereby proliferation is activated by the ERK/MAPK pathway and apoptosis is inhibited by the AKT pathway, therefore influencing breast tumour cells to develop chemoresistance (248).

In gliomas, CCN1 has similar role to breast cancers promoting proliferation and inhibiting apoptosis. In agreement with other cancer types, it is also more highly

expressed in the more invasive tumour types, again, suggesting that CCN1 is involved in tumour progression and metastasis. In other studies, CCN1 was found to be highly expressed in the invasive glioma cell lines U87, T98G and U373 and with low expression in the less invasive U343 cell line. When forced expression was induced in U343 cells, a marked increase in their proliferation and vascularisation was observed. When used in *in vivo* studies, these cells produced much larger and highly vascularised tumours in nude mice, which more readily migrated as assessed by immunohistochemistry (254).

### 4.1.2 CCG-203971

Following the identification of CCG-1423 by Evelyn et al., it was shown that although it was a significantly potent inhibitor, it was also highly cytotoxic (167). This led to several molecular modifications of the lead compound CCG-1423 in order to reduce cytotoxicity and improve its potency and selectivity. One molecular modification, CCG-203971 (Figure 24), was successful in reducing cytotoxicity and improving potency in the PC-3 cell line and the melanoma cell lines A275M2 and SK-Mel-147 when assessed for cell migration inhibition by a scratch wound assay. Studies into the mechanisms of CCG-203971 indicated that it too prevents the nuclear localisation of MKL1. This analog of CCG-1423 was taken forward to an *in vivo* tolerability study in normal mice, which showed that CCG-203971 was well-tolerated in doses up to 100mg/kg/day injected intraperitoneally for 5 days (225).

**24A – CCG-1423**

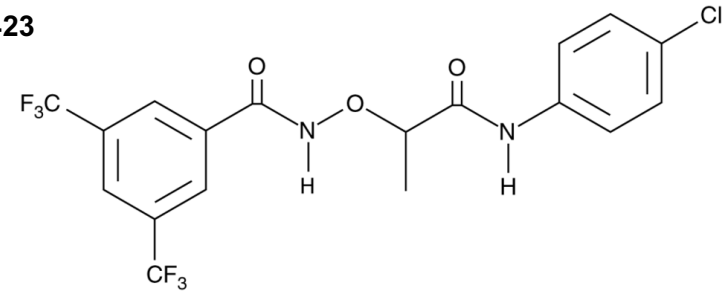


**24B – CCG-203971**

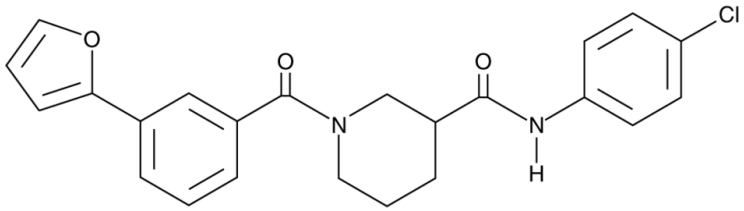


Figure 24. The chemical structures of CCG-1423 (24A) and its analog CCG-203971 (24B). The structural changes occurred as a result of a series of modifications to the aromatic rings and purification by acidic Amberlyst-15 resin.

### 4.1.3 Mass spectrometry imaging

Mass spectrometry imaging (MSI) is a technique that allows for unlabelled analyses of the spatial distribution of a variety of molecules in different samples, including lipids, peptides, metabolites and proteins. Characterisation of biological samples can be chemically analysed through the combination of the vast information produced by mass spectrometry and the actual visualisation of molecular distribution in thin sections of samples (285). Sample preparation is a crucial step in MSI and must be done carefully and accurately to obtain informative results. Consequently, a grid is defined over the sample surface for the mass spectrometer to follow. The mass spectrometer then ionises molecules on the sample surface and for each pixel, collects a mass spectrum. The resultant spatial resolution is dependent on the size of each pixel. The specialised computer software of the mass spectrometer is then used to select the mass-to-

charge (*m/z*) value of interest and extract the intensity of that *m/z* at each pixel. All the *m/z* intensities are collected together to form a heat map image showing the distribution of the *m/z* on the sample (285,286). Figure 25 shows a typical MSI workflow.

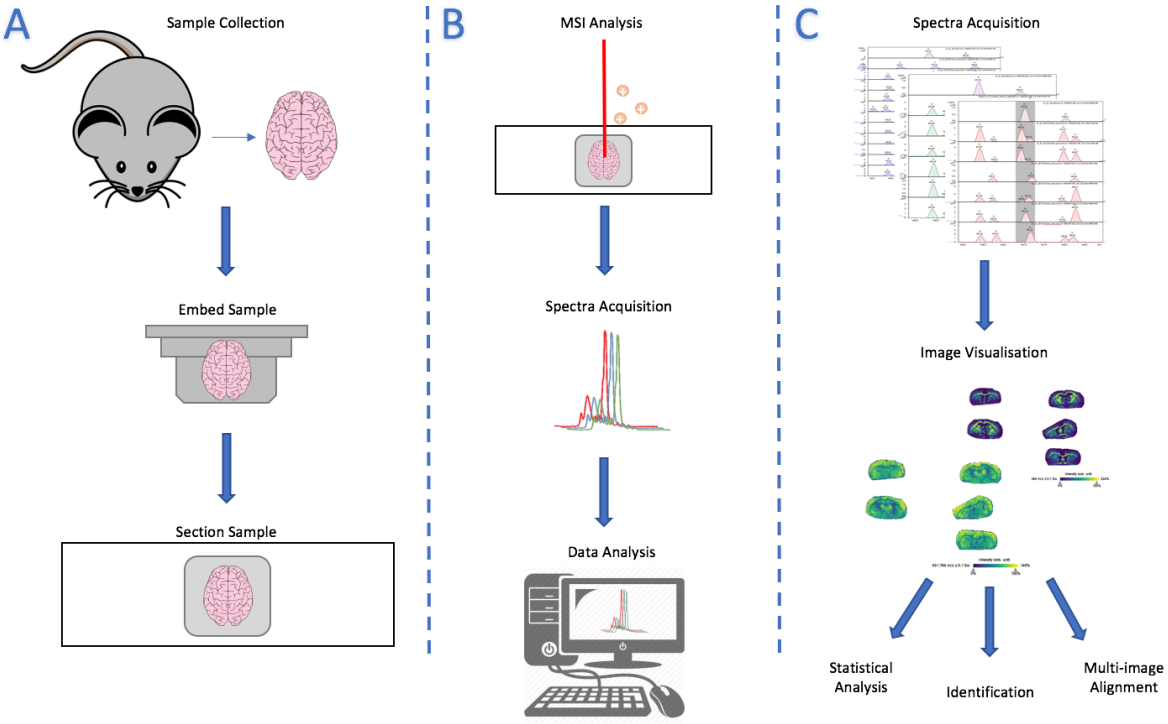


Figure 25. MSI workflow. Following sample collection from the animal, the sample is embedded in optimal cutting temperate (OCT) compound for sectioning onto slides (A). The slides are placed into the mass spectrometer for spectra acquisition whereby a grid is positioned on the sample and a spectrum is extracted at each pixel on the sample surface by a laser which ionises the molecules (B). After spectra acquisition, the distribution of selected molecules can be visualised. From there, identification of the m/z values and statistical analysis between different images can occur (C).

There are several different techniques for ionisation with MSI, each involving a different sample preparation process. One of the more prevalent techniques is matrix-assisted laser desorption/ionisation (MALDI) due to its widespread capabilities in molecular species and weights (287). However, in order to create proper ionisation of samples, it requires a matrix, which has led to the

development of unique matrixes and laserspray ionisation to ensure different molecules can be detected. As different molecules require different methods for successful results, the optimisation process for MALDI is extremely important, with most of the focus being on the matrix application process (288). When using MALDI for molecule ionisation, a matrix is required to allow for accurate ionisation of the desired molecule. Once applied, the matrix crystallises causing analytes to be extracted from the sample and co-crystallise with it. With MALDI, it is unlikely that analytes will be ionised if they are not within this crystal structure that is created by the matrix. For the best MALDI results, the matrix should produce a small crystal size, homogeneous application and appropriate analyte extraction (289). Examples of popular matrixes include 2,5-dihydroxybenzoic acid (DHB), α-cyano-4-hydroxycinnamic acid (CHCA) and 2,4,6-trihydroxyacetophenone monohydrate (THAP). Researchers used to spray the matrixes by hand using airbrush sprayers, however, based on inter-personal and institutional inconsistencies, automated sprayers were developed, which improved reproducibility of results, showing the importance of sample preparation when using this MSI technique (290).

Another MSI technique, called liquid extraction surface analysis (LESA), allows for the detection of analytes directly from the sample surface by the formation of a liquid microjunction from a solvent droplet placed directly on the tissue. The analytes in the tissue are dissolved into the solvent droplet, which is then suctioned up and sprayed directly into the mass spectrometer for spectra acquisition. The area of detection can be manually chosen through computer software, whether this be specific dots in precise regions of the sample or a grid

over the whole sample. LESA does not require a matrix as the solvent is dropped directly onto the tissue surface (291).

## 4.2 Materials and methods

Several experiments included in this chapter were undertaken during a 3-month secondment at Harvard Medical School (HMS). These experiments include western blots for cell lines G9, G44, GL261, CNS1 and U251, the aortic ring assay, MALDI and LESA experiments and the animal studies.

### 4.2.1 Cell lines and media

The primary human glioma cell lines G9 and G44, the murine glioma cell line GL261 and the rat glioma cell line CNS1 were all obtained and grown in the Neurosurgery department at HMS, Brigham and Women's Hospital. G9 and G44 were grown as neurospheres suspended in neurobasal medium (Gibco) containing B27 supplement, 0.5% penicillin-streptomycin (Gibco), glutamine (Gibco), EGF and FGF (Gibco). GL161 and CNS1 were grown in Dulbecco's Modified Eagles medium (DMEM) (Sigma) with 10% heat-inactivated foetal calf serum (HI-FCS) (Labtech) and 0.5% penicillin-streptomycin (Sigma) (complete medium). They were free of mycoplasma contamination as confirmed by in house testing at HMS.

### 4.2.2 Western blots

Cell lysates were obtained from cells grown in 25 $cm^2$ plastic tissue culture flasks (Corning) treated with 500nM of CCG-1423 (Tocris) for 24, 48 and 72 hours. Cells were placed on ice and washed twice with ice cold PBS. The cells were collected and centrifuged at 400g for 5 minutes. The PBS was removed and the pellet was resuspended in 0.5ml of Tris-HCl lysis buffer 25 µl/ml protease inhibitor (Sigma-Aldrich) for 5 minutes. The cells were centrifuged at 400g for 10 minutes.

Supernatants containing the cytoplasmic extract were collected and transferred into clean tubes.

Protein concentration of each cell lysate was determined by Bradford protein assay (Bio-Rad), whereby 2µl of protein sample was added to 700µl of Bradford protein assay solution in a cuvette (Sigma). Included in this was a 'blank' consisting of 2µl of Tris-HCl buffer in 700µl Bradford protein assay solution. The samples were measured at 595nm on a spectrophotometer and normalised to the lowest concentrated lysate using Tris-HCl buffer.

10µl of Laemmli buffer (Bio-Rad) was added to the cell lysates, which were boiled for 5 minutes at 95°C in a dry bath. Fifty microlitres of cell lysate was loaded into wells in a 4-20% TGX stain-free precast gel (Bio-Rad) with a pre-stained protein ladder (Bio-Rad) to estimate protein size. Proteins were separated by sodium dodecyl sulphate polyacrylamide gel electrophoresis (SDS-PAGE) at 120V for approximately 90 minutes in a tank filled with running buffer (Bio-Rad). They were transferred to PVDF membranes at 250mAmp over 90 minutes in a tank filled with transfer buffer (Bio-Rad). Once unpacked, the PVDF was washed in Tris-Buffered Saline and Tween®20 (TBST) and blocked in 5% milk in TBST for 45 minutes. The PVDF was probed with an antibody against MKL1 (1:300, Abcam) in 5% milk in TBST overnight. PVDF was washed 3 times in TBST and exposed for 90 minutes to the secondary antibody HRP-conjugated donkey anti-rabbit IgG antibody (1:1000, GE Healthcare). Following a further 3 washes with TBST, proteins were detected by SuperSignal West Femto maximum sensitivity substrate (Thermo Fisher), according to the provided protocol and visualised

using a ChemiDoc MP imaging system (Bio Rad) and Image Lab software (BioRad). Protein band intensity was analysed using Image J software. The intensity of each band was normalised to the corresponding β-actin control.

### 4.2.4 Immunohistochemistry (IHC) of patient samples

Patient GBM samples were collected, processed and stored by the Leeds Multidisciplinary Routine Tissue Banking (RTB) service from GBM patients undergoing surgery at the Leeds General Infirmary (ethical approval no. RTB 15/YH/0080). Tumour tissues were embedded in paraffin wax, sectioned on a microtome (Leica) at 8μm and placed on glass slides to dry for 24 hours. The slides were dewaxed by 2x 1-minute washes in xylene (Sigma), followed by 2x 1-minute washes in ethanol (Sigma) and 3x 1-minute washes in water. Antigen retrieval was completed using Tris EDTA pH9 (Abcam) in a pressure cooker for 2 minutes. The slides were incubated for 1 hour with the primary antibody anti-CYR61/CCN1 rabbit polyclonal at a concentration of 1:250 (Abcam). The slides were washed 3x 1 minute in PBS and incubated for 30 minutes with the secondary antibody anti-rabbit IgG HRP polymer (ready to use) (Vector). After secondary incubation, the slides were washed 3x 1-minute in PBS and stained using the chromogen DAB (Abcam) for 10 minutes. The slides were washed again 3x 1-minute in PBS and a glass coverslip applied. The slides were analysed by calculating and combining two scores for the CCN1 staining; as above, staining intensity and percentage covered. Strength of staining was scored from 0-3 with 0 being no staining and 3 being strong staining. Percentage of staining was scored out from 0-4 with 0 being 0% covered, 1 being 1-25% covered, 2

being 26-50% covered, 3 being 51-75% covered and 4 being 75%+ covered. The final score is out of 7. The samples were randomised to avoid biased scoring.

### 4.2.5 Patient blood sample ELISA

Matched GBM patient blood samples were collected, processed and stored by the Leeds Multidisciplinary Routine Tissue Banking (RTB) service from GBM patients undergoing surgery at the Leeds General Infirmary (ethical approval no. RTB 15/YH/0080). A commercially available Human CYR61/CCN1 Quantikine ELISA kit (R&D Systems) was used for the solid phase sandwich ELISA for CCN1. 100μl of assay diluent was added to each well of the microplate, followed by 50μl of patient blood serum, control blood serum or standard. The wells were covered with a plate sealer and incubated on a plate shaker at room temperature for 2 hours. The wells were aspirated and washed 3 times with wash buffer. 200μl of human CCN1 conjugate was added to each well and incubated for 2 hours on a plate shaker. The wells were washed 3 times with wash buffer before adding 200μl of substrate buffer to each well. The wells were incubated for 30 minutes at room temperature covered with foil. 50μl of stop solution was added to each well and the plate was immediately read on a plate reader at 540nm (Thermo Fisher).

### 4.2.6 Aortic ring assay

An aorta was isolated from a C57BL/6 mouse and transferred into a petri dish containing PBS. Under a dissection microscope (Nikon SMZ1000), all the extraneous fat, tissue and branching vessels were removed with forceps and a scalpel. The aorta was then cut into approximate 0.5mm rings and set aside.

Matrigel (Corning) was thawed on ice. Once thawed, 50μl of Matrigel was added per well to 21 wells of a flat bottomed 96 well culture plate (Greiner Bio-One) and incubated at 37°C for 15 minutes to allow polymerisation of the Matrigel. One aortic ring per well was placed on top of the Matrigel followed by another 50μl of Matrigel on top. The plate was then incubated at 37°C for 15 minutes to allow polymerisation of the second Matrigel layer. Once set, 100μl of endothelial cell medium (ScienCell) with human VEGF (Abcam) was then added to each well and the plate was incubated at 37°C overnight. Concentrations of 0.1μM, 1μM and 10μM of CCG-1423 and CCG-203971 (Tocris) were prepared in endothelial cell medium. The medium in the wells was then replaced with 100μl of drug or with fresh endothelial cell medium. Each concentration and control were carried out in triplicate. The plate was then imaged after 1 week using a confocal microscope (Nikon Eclipse Ti) to assess the effect of CCG-1423 and CCG-203971 on blood vessel formation.

### 4.2.7 Preparation, optimisation and detection using MALDI

CCG-1423 and CCG-203971 (Tocris) was reconstituted in DMSO (Sigma) to a stock concentration of 10mM. Concentrations of 1mM, 100μM, 10μM, 5μM, 1μM and 100nM of CCG-1423 and CCG-203971 were then made up for detection with MALDI (Bruker Rapiflex). 0.3μl of each drug concentration was spotted onto an Indium-Tin-Oxide (ITO) coated slide (Sigma) directly onto the glass and directly on to mouse brain homogenate (for optimisation of MALDI settings) sectioned at 8μm. This was repeated 3 times on half a slide for optimisation of 3 different MALDI matrices. The slides were then dried in a slide desiccator for 1.5 hours. The 3 different matrices were made up in 70% methanol with 0.1% trifluoroacetic

acid (TFA) and 1% DMSO (Sigma). 2, 5-Dihydroxybenzoic acid (DHB) (Sigma) was made up to 160mg/ml, α-cyano-4-hydroxycinnamic acid (CHCA) (Sigma) was made up to 5mg/ml and 2, 4, 6- trihydroxyacetophenone monohydrate (THAP) (Sigma) was made up to 40mg/ml. These were then sonicated and sprayed onto half a slide each using a TM sprayer (HTX Imaging). The DHB slide then underwent recrystallization by heating in a lab oven (HeraTherm, Thermo Fisher) for 2 minutes at 85°C followed by a further 6 minutes of heating at 85°C in a glass chamber with an acetic acid-soaked paper towel. The slides were then dried and ready for detection by MALDI.

### 4.3.8 Preparation, optimisation and detection using LESA

CCG-1423 and CCG-203971 (Tocris) was reconstituted in DMSO (Sigma) to a stock concentration of 10mM. Concentrations of 1mM, 100μM, 10μM, 5μM, 1μM and 100nM of CCG-1423 and CCG-203971 were then made up to be tested for detection with LESA (Bruker Rapiflex). 0.3μl of each drug concentration was spotted onto a glass slide (Thermo Fisher) directly onto the glass and directly on to mouse brain homogenate sectioned at 8μm. The slides were then dried in a slide desiccator for 1.5 hours and ready for detection by LESA.

### 4.2.9 Animal studies

All animal experiments were performed in 6-8-week-old female immunodeficient athymic mice (FoxN1 nu/nu, n=6, Envigo, South Easton, MA), in compliance with all relevant ethical regulations applied to the use of small rodents and with approval by the Institutional Animal Care and Use Committees (IACUC) at the Brigham and Women's Hospital and Harvard Medical School. For intracranial

tumour implantation, a stereotactic frame was used to insert 50,000 G9 cells (re-suspended in 2µl PBS) in each animal's right striatum (2mm right lateral and 0.5mm frontal to the bregma at 3.5mm depth). CCG-203971 (Tocris) reconstituted in a 1:4 1-methyl-2-pyrrolidinone (MPRL) (Sigma), Kollisolve PEG E 300 (Sigma) mix was administered *in vivo* by intraperitoneal injection at a concentration of 100mg/kg for 5 consecutive days starting from the 7th day after intracranial tumour implantation. The control mice were intraperitoneally injected with the control vehicle (MPRL/Kollisolve) for 5 consecutive days starting on the $7^{th}$ day after intracranial tumour implantation. Mice were euthanized 2 hours after the final CCG-203971 injection on day 5 by carbon dioxide overdose followed by tissue dissection to isolate the brain and liver, which were frozen immediately in liquid nitrogen. The brains and livers were embedded in optimal cutting temperate (OCT) compound (Leica) and sectioned at 8µM on a cryostat (Leica) and placed onto glass slides (Thermo Fisher) for LESA and on ITO coated slides (Sigma) for MALDI.

### 4.2.10 Data analysis

Western blot protein band intensities were analysed using ImageJ software. The intensity of each band was normalised to the corresponding β-actin control. For the ELISA, the optical density of each sample was read at 540nm. The standard curve was generated in Excel and used to calculate the concentration of each sample in pg/ml. The aortic ring assays were analysed by creating a migration index using Velocity 3D Image Analysis software according to Cockle et al, 2015 (doi: 10.1038/bjc.2015.16), ImageJ (http://rsbweb.nih.gov/ij) and Excel (Microsoft, USA). For all experiments, differences between control cells and

treated cells were compared using a two-tailed T-test (Excel). P-values $\leq 0.05$ were considered statistically significant. For MALDI and LESA, data was analysed using the Bruker Rapiflex software system.

## 4.3 Results

### 4.3.1 CCG-1423 and CCG-203971 activity on a panel of glioma cell lines

To confirm the effects of CCG-1423 on patient-derived glioma cell lines as well as on murine and rat glioma cell lines for *in vivo* studies, western blots were carried out on the patient derived cell lines G9 and G44, the murine glioma cell line GL261 and the rat glioma cell line CNS1 (Figures 26-27). G9 is of the mesenchymal GBM subtype, which is associated with poor prognosis and high invasiveness (115). G44 is of the proneural GBM subtype and is associated with better prognosis (114). GL261 is an orthotopic model for murine glioma. Although invasive, this cell line is not known to metastasise and is considered a lot less invasive than other GBM cell lines (292). CNS1 is a highly invasive rat glioma cell line that very closely simulates the growth patterns of human gliomas (293).

During sample preparations of cell lysates, nuclear-associated components were discarded, therefore the results from the western blots are representative cytoplasmic MKL1. All data obtained from the western blot experiments were normalised to β-actin. The G9 cell line showed an increase in MKL1 build-up in the cytoplasm when treated with CCG-1423. The intensity of the MKL1 band at the 24-hour time point was 1.04 +/- 0.16, which was significantly different to the control (0.48 +/- 0.08) (P=0.008). At the 48-hour time point, the intensity of the CCG-1423 treated MKL1 band was 1.24 +/- 0.12, which was significantly different to the control (0.58 +/- 0.03) (P=0.004). At the 72-hour time point, the intensity of the CCG-1423 treated MKL1 band for G9 cells was 1.70 +/- 0.18, which was significantly different to the control (0.82 +/- 0.15) (P=0.003) (Figure 27A).

The G44 cell line showed an increase in MKL1 build-up in the cytoplasm when treated with CCG-1423. The intensity of the MKL1 band at the 24-hour time point was 1.43 +/- 0.08, which was significantly different to the control (0.78 +/- 0.06) (P=0.002). At the 48-hour time point, the intensity of the CCG-1423 treated MKL1 band was 1.31 +/- 0.15, which was significantly different to the control (0.80 +/- 0.03) (P=0.009). At the 72-hour time point, the intensity of the CCG-1423 treated MKL1 band for G44 cells was 1.13 +/- 0.07, which was significantly different to the control (0.61 +/- 0.08) (P=0.008) (Figure 27B).

The GL261 cell line showed an increase in MKL1 build-up in the cytoplasm when treated with CCG-1423. The intensity of the MKL1 band at the 24-hour time point was 1.02 +/- 0.10, which was significantly different to the control (0.70 +/- 0.04) (P=0.02). At the 48-hour time point, the intensity of the CCG-1423 treated MKL1 band was 1.03 +/- 0.12, which was significantly different to the control (0.88 +/- 0.07) (P=0.04). At the 72-hour time point, the intensity of the CCG-1423 treated MKL1 band for GL261 cells was 1.12 +/- 0.05, which was significantly different to the control (0.82 +/- 0.02) (P=0.004) (Figure 27C).

The CNS1 cell line showed an increase in MKL1 build-up in the cytoplasm when treated with CCG-1423. The intensity of the MKL1 band at the 24-hour time point was 1.42 +/- 0.08, which was significantly different to the control (0.98 +/- 0.07) (P=0.01). At the 48-hour time point, the intensity of the CCG-1423 treated MKL1 band was 1.21 +/- 0.08, which was significantly different to the control (0.75 +/- 0.05) (P=0.003). At the 72-hour time point, the intensity of the CCG-1423 treated

MKL1 band for CNS1 cells was 0.94 +/- 0.04, which was significantly different to the control (0.70 +/- 0.06) (P=0.02) (Figure 27D).

Western blots were also carried out on U251 and G9 cell lysates that had been treated with CCG-203971 in order to confirm inhibitor activity in comparison to CCG-1423 for *in vivo* experiments. The western blots showed that CCG-203971 led to results comparable to CCG-1423 and was consequently taken forward for *in vivo* work (Figures 28-29).

The U251 cell line showed an increase in MKL1 build-up in the cytoplasm when treated with CCG-203971. The intensity of the MKL1 band at the 24-hour time point was 1.45 +/- 0.04, which was significantly different to the control (0.73 +/- 0.02) (P=0.0002). At the 48-hour time point, the intensity of the CCG-203971 treated MKL1 band was 1.21 +/- 0.08, which was significantly different to the control (0.75 +/- 0.02) (P=0.002). At the 72-hour time point, the intensity of the CCG-203971 treated MKL1 band for U251 cells was 0.94 +/- 0.09, which was not significantly different to the control (0.93 +/- 0.04) (P=0.34) (Figure 29A).

The G9 cell line showed an increase in MKL1 build-up in the cytoplasm when treated with CCG-203971. The intensity of the MKL1 band at the 24-hour time point was 1.44 +/- 0.13, which was significantly different to the control (0.87 +/- 0.04) (P=0.001). At the 48-hour time point, the intensity of the CCG-203971 treated MKL1 band was 1.42 +/- 0.07, which was significantly different to the control (0.73 +/- 0.08) (P=0.004). At the 72-hour time point, the intensity of the

CCG-203971 treated MKL1 band for G9 cells was 0.96 +/- 0.05, which was significantly different to the control (0.77 +/- 0.03) (P=0.007) (Figure 29B).

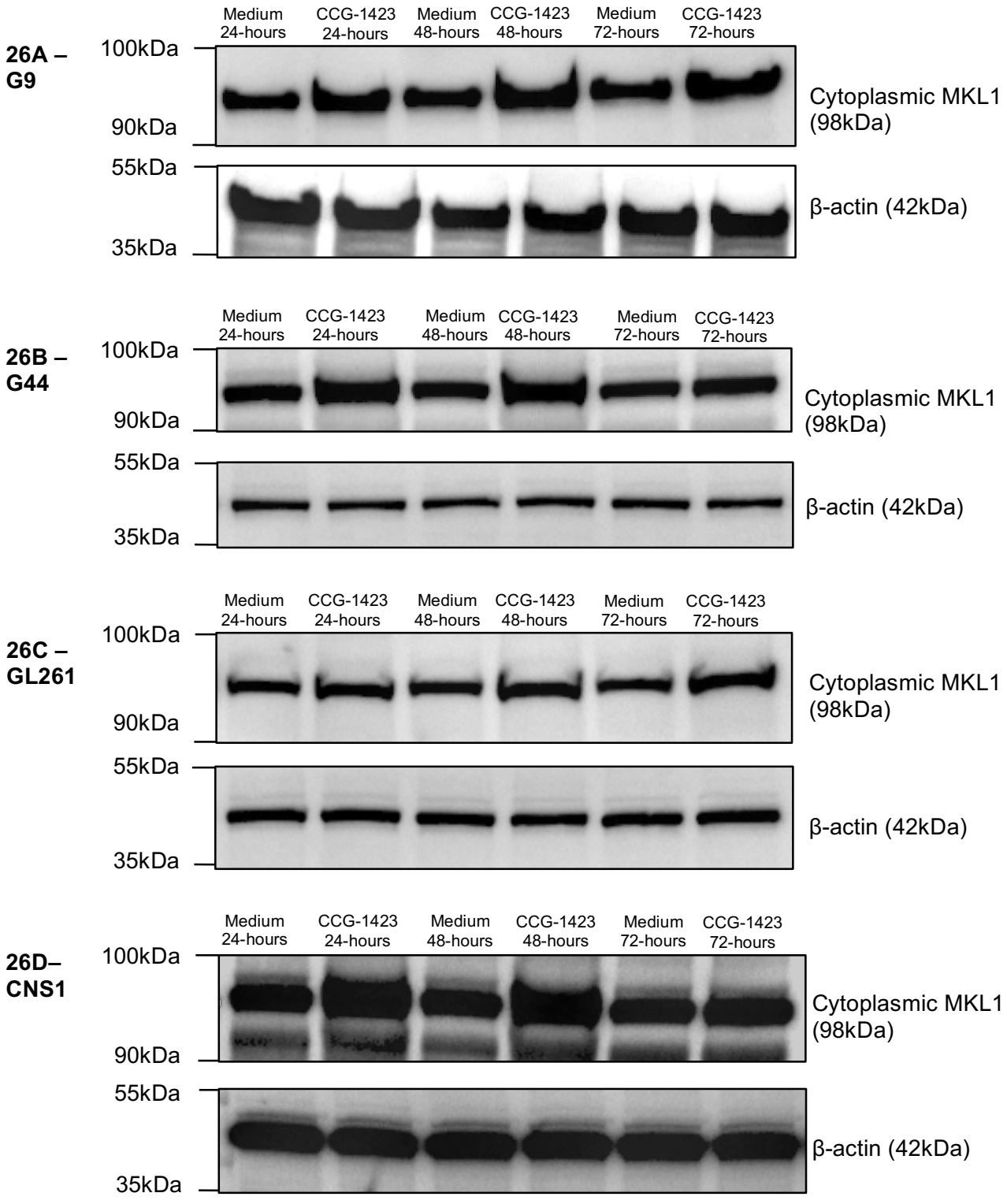


Figure 26. Western blot analysis of the effects of CCG-1423 on glioma cell lines. Patient derived cell lines G9 (26A) and G44 (26B), murine glioma cell line GL261 (26C) and rat glioma cell line CNS1 (26D) were treated ± 500nM CCG-1423. Following 24, 48 and 72-hour incubations, cell lysates were obtained. Expression of cytoplasmic MKL1 was determined by western blotting including a β-actin control to evaluate protein loading and transfer.

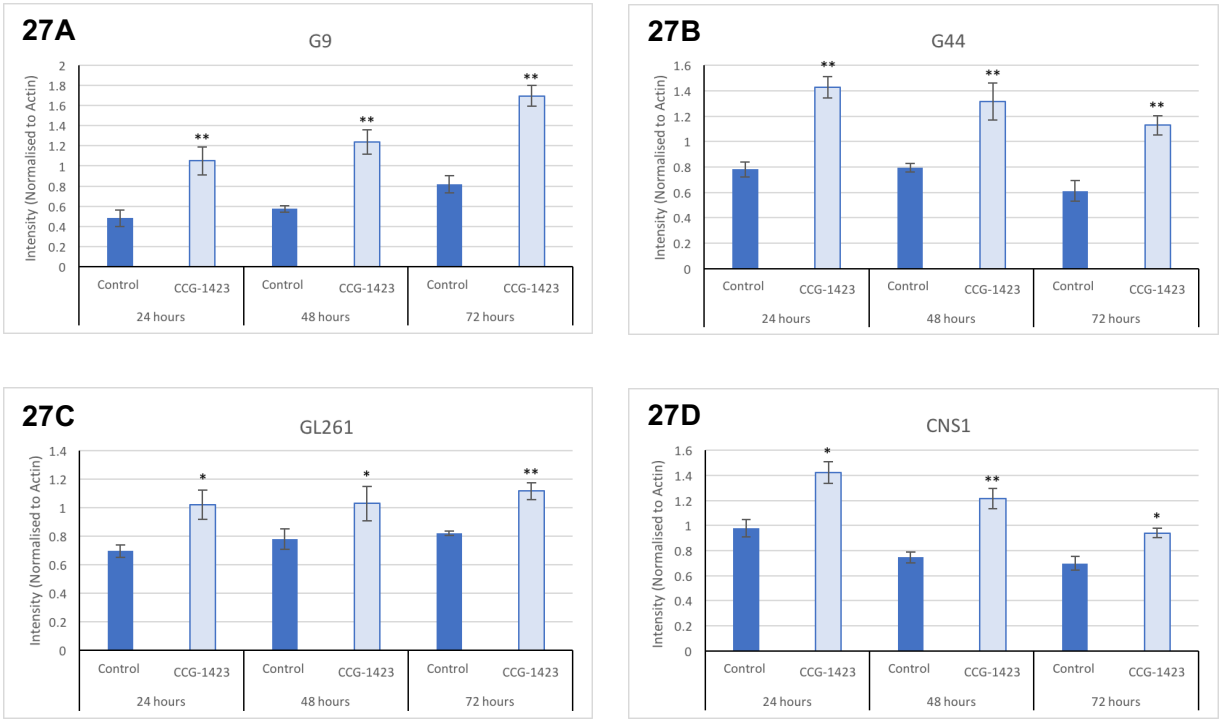


Figure 27. Western blot analysis of the effects of CCG-1423 on glioma cell lines. Patient derived cell lines G9 (27A) and G44 (27B), murine glioma cell line GL261 (27C) and rat glioma cell line CNS1 (27D) were treated ± 500nM CCG-1423. Following 24, 48 and 72-hour incubations, cell lysates were obtained. Expression of cytoplasmic MKL1 was determined by western blotting including a β-actin control to evaluate protein loading and transfer. MKL1 band intensity was quantified and normalised to the β-actin control using Image J software. Graphs show mean ± SEM of 3 individual experiments. Asterisks show statistical significance where * = p≤0.05, ** = p≤0.01, *** = p≤0.001.

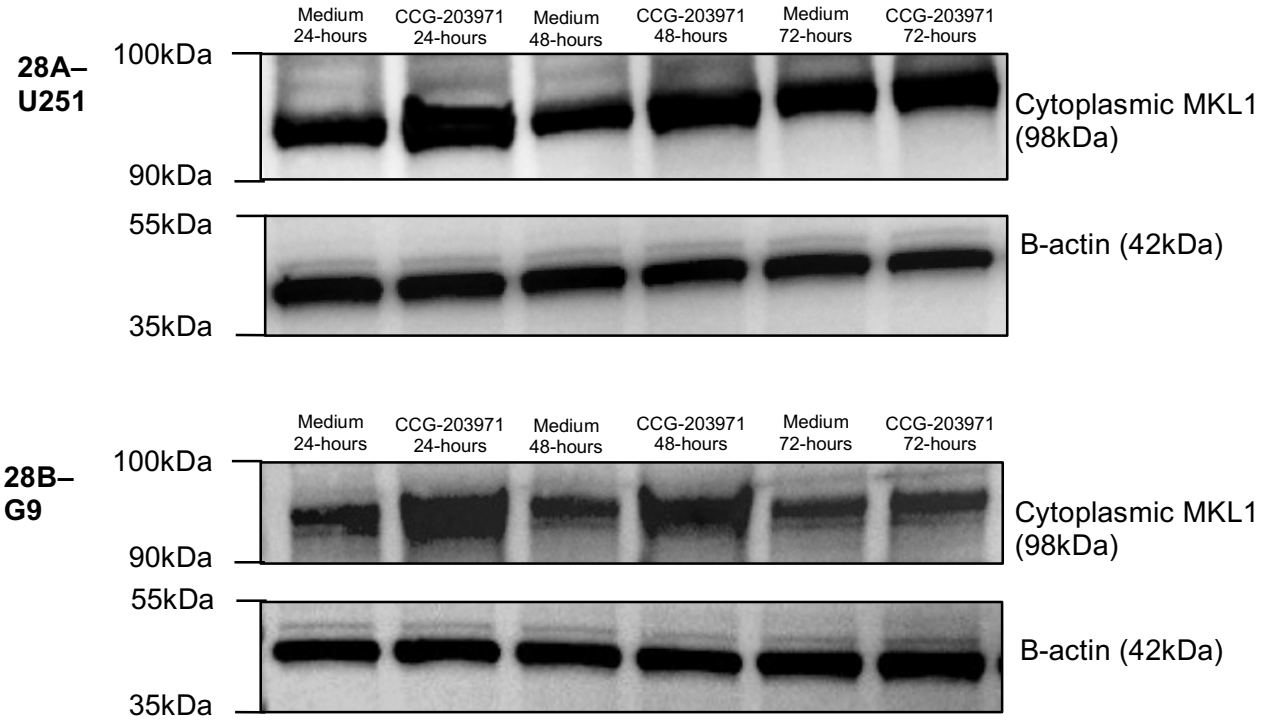


Figure 28. Western blot analysis of the effects of CCG-203971 on glioma cell lines. Glioma cell line U251 (28A) and patient derived cell line G9 (28B) were treated ± 500nM CCG-203971. Following 24, 48 and 72-hour incubations, cell lysates were obtained. Expression of cytoplasmic MKL1 was determined by western blotting including a β-actin control to evaluate protein loading and transfer.

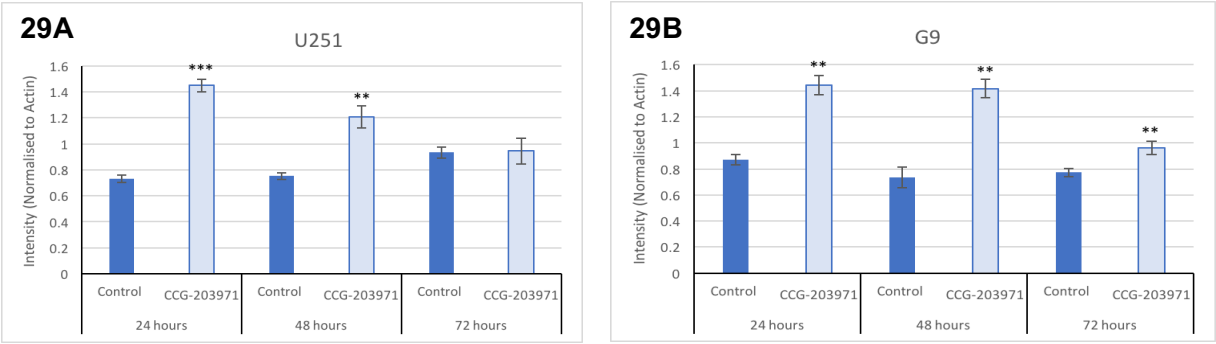


Figure 29. Western blot analysis of the effects of CCG-1423 on glioma cell lines. Glioma cell line U251 (29A) and patient derived cell line G9 (29B) were treated ± 500nM CCG-203971. Following 24, 48 and 72-hour incubations, cell lysates were obtained. Expression of cytoplasmic MKL1 was determined by western blotting including a β-actin control to evaluate protein loading and transfer. MKL1 band intensity was quantified and normalised to the β-actin control using Image J software. Graphs show mean ± SEM of 3 individual experiments. Asterisks show statistical significance where ** = p≤0.01, *** = p≤0.001.

### 4.3.2 CCN1 expression in patient tissues (TMA)

A commercially available brain cancer TMA including 63 cases/cores and 1 control core was stained for CCN1. Of the 63 cases, there were 31 astrocytomas grade 1 and 2, 7 astrocytomas grade 3, 14 GBMs, 6 oligodendrogliomas, 1 ependymoma, 1 medulloblastoma, 3 cancer adjacent brain tissue cores and 1 adrenal core as the control. Because of the small sample size of the ependymoma and medulloblastoma, these were not included in the data analysis (Figure 30). Cytoplasmic and membranous CCN1 staining was observed in the tumour cells with strong staining patterns observed in elongated cells and in cells in close proximity to blood vessels. Figure 31 shows examples of strong and weak CCN1 staining in astrocytoma cores as well as a positive control (pheochromocytoma) and cancer adjacent brain tissue. The clinical characteristics associated with the samples, including age, sex, and tumour grade are shown in Table 4. The samples were dichotomised into low and high CCN1 expression with low scoring samples having a score of 3 or less and high scoring samples having a score of 4 or more.

The average score for the astrocytoma grade 1-2 cores was 2 +/- 0.30, which was not significantly different to the control (0.67 +/- 0.67). Astrocytoma grade 3 cores had an average score of 3.43 +/- 0.72, which was significantly different to the control (0.67 +/- 0.67) (P=0.05). GBM cores had an average score of 4.93 +/- 0.40, which was significantly different to the control (0.67 +/- 0.67) (P=0.0003). The average score for oligodendroglioma cores was 3 +/- 0.45, which was also significantly different to the control (0.67 +/- 0.67) (P=0.02).

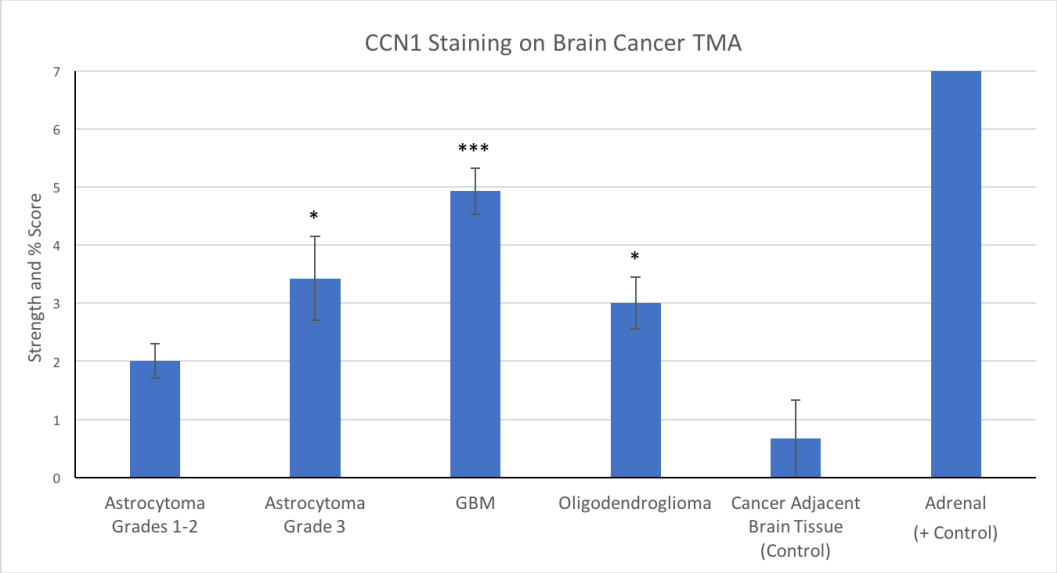


Figure 30. A graph showing a combined score of CCN1 staining strength and percentage of the core covered on a TMA containing astrocytomas grade 1-2, GBM, oligodendroglioma, cancer adjacent brain tissue as a control and an adrenal core as a positive control. Asterisks indicate statistical significance.

| Clinical Characteristics | Low CCN1 Expression (score ≤3, n=28) | High CCN1 Expression (score ≥4, n=24) | P Value |
|---|---|---|---|
| **AGE** | | | |
| Under 25 | 1 (3%) | 3 (13%) | |
| 26-60 | 26 (94%) | 17 (70%) | p=0.28 |
| Over 60 | 1 (3%) | 4 (17%) | |
| **SEX** | | | |
| Male | 15 (54%) | 13 (54%) | p=0.97 |
| Female | 13 (46%) | 11 (46%) | |
| **TUMOUR GRADE** | | | |
| 1 | 1 (3%) | 0 (0%) | |
| 2 | 24 (86%) | 8 (33%) | $p=4.79x10^{-7}$ |
| 3 | 3 (11%) | 4 (17%) | **** |
| 4 | 0 (0%) | 12 (50%) | |

Table 4. The clinical characteristics of the TMA astrocytoma samples. The results reveal associations of CCN1 expression levels with tumour grade**.** Eighty-six percent of the samples with low CCN1 expression are grade 2 astrocytomas, whilst 50% of the samples with high CCN1 expression are grade 4 astrocytomas (GBM). There were no associations of CCN1 levels with age or sex.

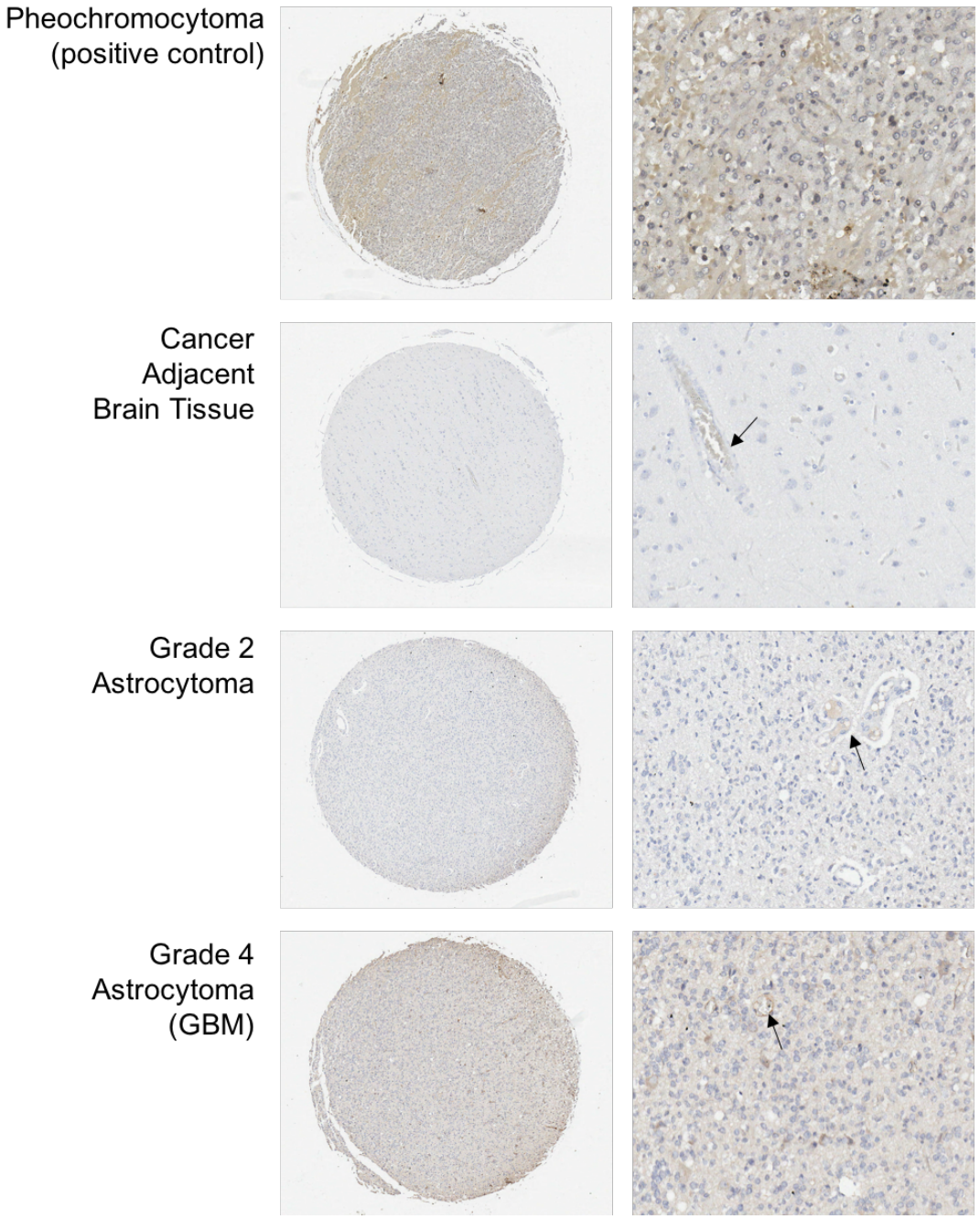


Figure 31. CCN1 levels vary in tumour tissue samples from patients as determined by IHC. Examples of strong and weak staining in TMA cores at low and high magnification. Membranous and cytoplasmic labelling was observed. Top core shows a representative sample for positive stain (pheochromocytoma); the second core represents a sample from cancer adjacent brain tissue; the third core represents a sample from a grade 2 astrocytoma and the bottom core is an example of a grade 4 astrocytoma (GBM) (Individual cores x10 magnification; magnified examples × 20). Arrows indicate CCN1 staining around vessels.

### 4.3.3 CCN1 expression in a cohort of GBM patients including recurrent tumours

Sixteen GBM samples collected from 9 patients (Table 5) undergoing surgery were stained for CCN1 by immunohistochemistry. Scores for CCN1 staining were obtained as described for the TMA (Figure 32). Two of the patients had surgery for recurrent tumours, of which samples were also collected (Figure 33). Tumour edge samples, defined as 200μm from the tumour boundary, and tumour core samples, defined as the tumour region outside the edge margins (294), were collected from 4 of the 9 patients (Figure 34), 1 of which also had a sample of cancer adjacent tissue collected.

| | Clinical Characteristics | | | |
|---|---|---|---|---|
| **Patient no.** | **Age** | **Sex** | **Treatment** | **Survival** |
| 30<br>30R | 50<br>52 | Female | Surgery<br>Radiotherapy post recurrent surgery<br>Chemotherapy post recurrent surgery | Death 24 months post first operation |
| 40 | 66 | Male | Surgery<br>Radiotherapy post-surgery | Death 18 months post first operation |
| 48 | 69 | Male | Surgery<br>Radiotherapy post-surgery<br>Chemotherapy post recurrent surgery | Death 12 months post first operation |
| 49 | 56 | Male | Surgery<br>Chemotherapy post-surgery | Death 10 months post first operation |
| 52 | 56 | Male | Surgery<br>Radiotherapy post-surgery<br>Chemotherapy post-surgery | Death 9 months post first operation |
| 58 | 66 | Female | Surgery<br>Radiotherapy post-surgery | Death 12 months post first operation |
| 63<br>63R | 57<br>57 | Male | Surgery<br>Radiotherapy post primary surgery<br>Chemotherapy post primary and recurrent surgery | Death 18 months post first operation |
| 74 | 55 | Female | Surgery<br>Radiotherapy post-surgery<br>Chemotherapy post-surgery | Death 12 months post first operation |
| 75 | Unknown | Male | Surgery<br>Radiotherapy post-surgery<br>Chemotherapy post-surgery | Death 30 months post first operation |

Table 5. Clinical variables recorded for GBM patient samples. Details of the 9 GBM patients including age (primary and recurrent, where applicable), sex, treatment and survival.

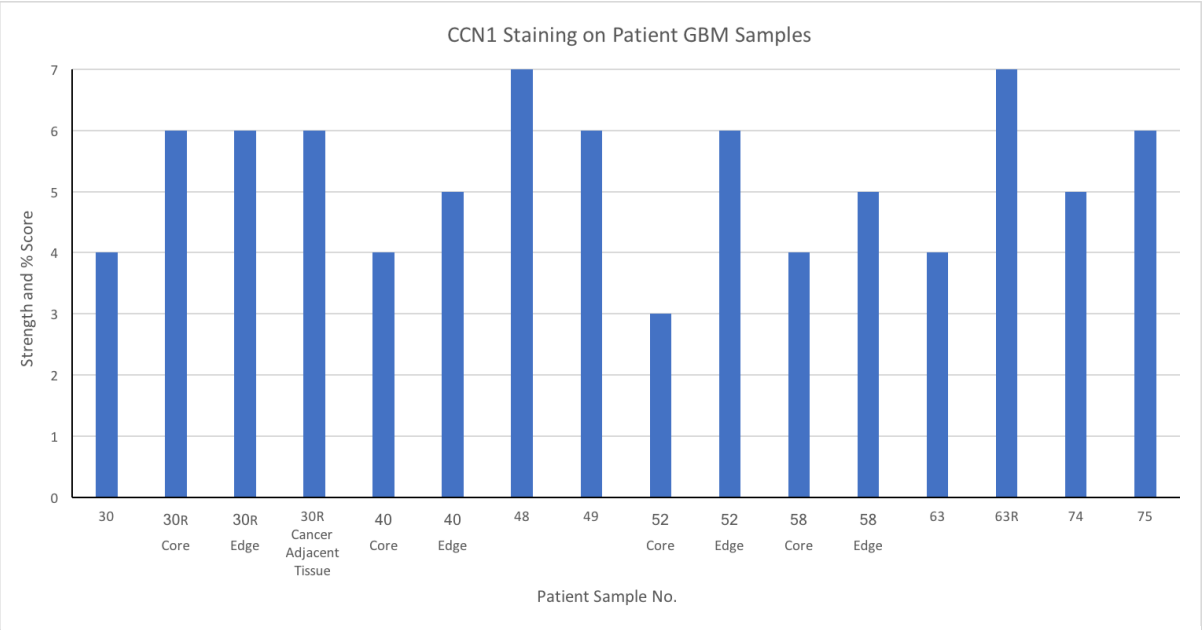


Figure 32. A graph showing the combined scores of CCN1 staining intensity and percentage of staining covering the sample collected from 9 GBM patients during surgery. Recurrent tumour samples were also collected for patients 30 and 63 (30R and 63R). Samples of the core and edge of the tumour were collected for patients 30, 40, 52 and 58. Patient 30 also had a sample of cancer adjacent tissue collected.

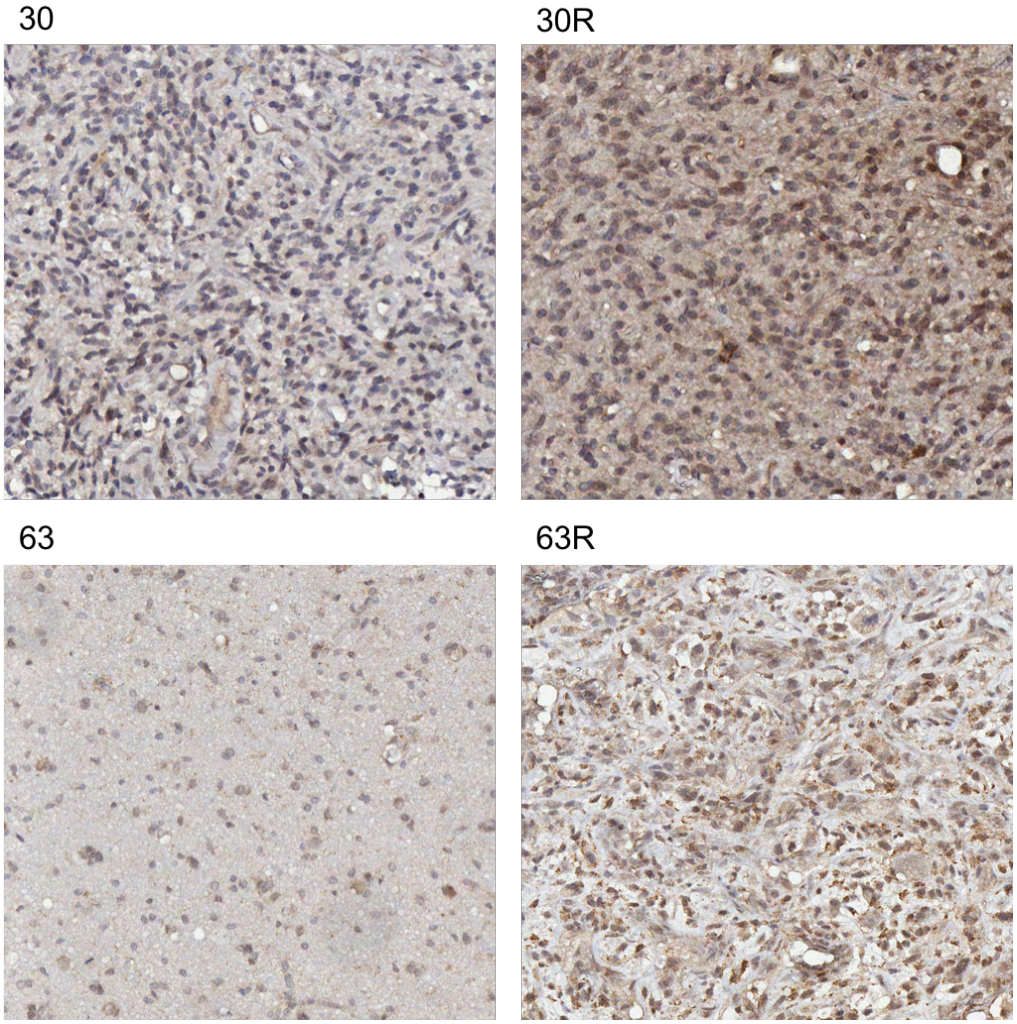


Figure 33. CCN1 levels vary between patient GBM primary and recurrent tumour samples as determined by IHC. Different intensities of CCN1 antibody labelling were observed between the primary and recurrent tumours of patients 30 and 63 (recurrent tumours = 30R and 63R) as indicated by brown staining. Magnification x20.

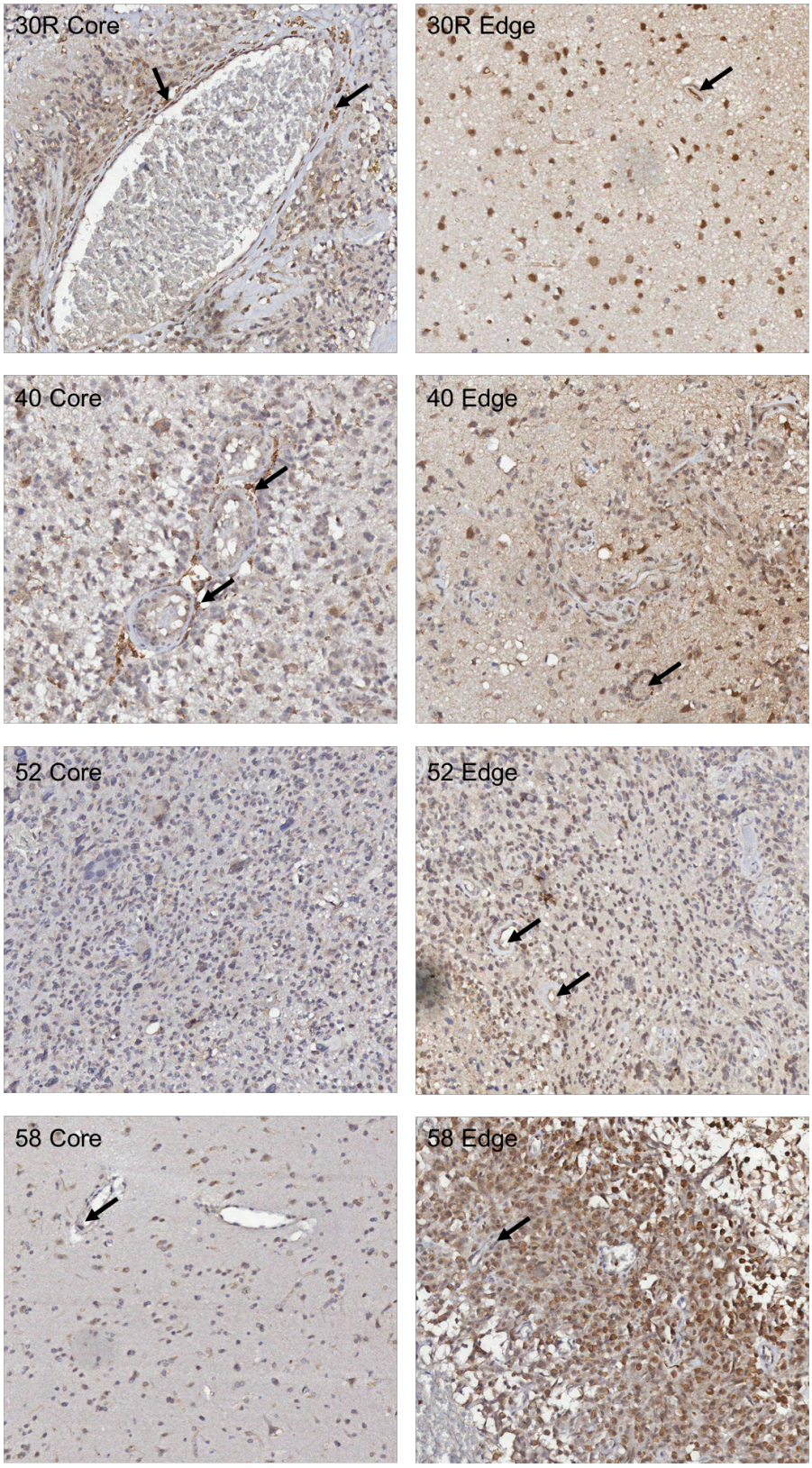


Figure 34. CCN1 levels vary between patient GBM core and edge tumour samples as determined by IHC. Different intensities of CCN1 antibody labelling were observed between the core and edge tumour samples of patients 30R, 40, 52 and 58 as indicated by brown staining. Arrows indicate CCN1 staining around vessels. Magnification x20.

### 4.3.4 CCN1 levels in matched blood samples from GBM patients

The serum from the matched patients blood samples was separated and collected for determination of CCN1 concentration by ELISA. The concentration of CCN1 was calculated from the absorbance values using the standard curve as well as the percentage increase as before (Figure 35).

The average concentration of CCN1 in the serum of the primary tumour of patient no. 30 was 60.43pg/ml +/- 1.55pg/ml, which was significantly different to the control (45.26pg/ml +/- 2.15pg/ml) (P=0.0049). The recurrent tumour blood sample for patient no. 30 (30R) had an average CCN1 concentration of 825.32pg/ml +/- 2.36pg/ml, which was very significantly different to the control (45.26pg/ml +/- 2.15pg/ml) ($P=1.68x10^{-9}$) as well as the primary tumour blood sample for patient no. 30 ($P=1.12x10^{-9}$). Patient no. 40 had an average CCN1 concentration of 134.51pg/ml +/- 15.48pg/ml, which was significantly different to the control (45.26pg/ml +/- 2.15pg/ml) (P=0.0047). Patient no. 48 had an average CCN1 concentration of 2588.041pg/ml +/- 466.45pg/ml, which was significantly different to the control (45.26pg/ml +/- 2.15pg/ml) (P=0.0055). The average CCN1 concentration of patient no. 49 was 119.34pg/ml +/- 21.66pg/ml, which was also significantly different to the control (45.26pg/ml +/- 2.15pg/ml) (P=0.028). Patient no. 52 had a CCN1 concentration of 51.51pg/ml +/- 2.44pg/ml, which was not significantly different to the control (45.26pg/ml +/- 2.15pg/ml). The average concentration for patient no. 58 was 122.02pg/ml +/- 15.84pg/ml, which was significantly different to the control (45.26pg/ml +/- 2.15pg/ml) (P=0.0089). The primary tumour for patient no. 63 had a CCN1 concentration of 54.19pg/ml +/- 1.19pg/ml, which was significantly different to the control (45.26pg/ml +/-

2.15pg/ml) (P=0.027). The recurrent tumour blood sample for patient no. 63 (63R) had a CCN1 concentration of 933.32pg/ml +/- 73.82pg/ml, which was significantly different to the control (45.26pg/ml +/- 2.15pg/ml) (P=0.0003) as well as the primary tumour blood sample for patient no. 63 (P=0.0002). The CCN1 concentration for patient no. 74 was 92.57pg/ml +/- 2.84pg/ml, which was significantly different to the control (45.26pg/ml +/- 2.15pg/ml) (P=0.0002). Finally, patient no. 75 had a CCN1 concentration of 1010.96pg/ml +/- 106.57pg/ml, which was also significantly different to the control (45.26pg/ml +/- 2.15pg/ml) (P=0.0008).

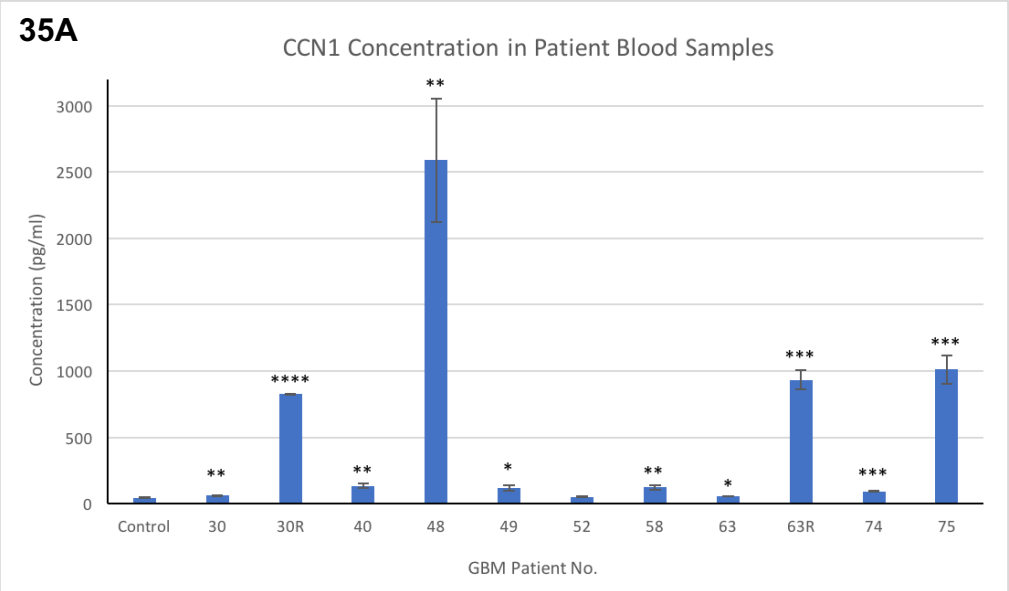


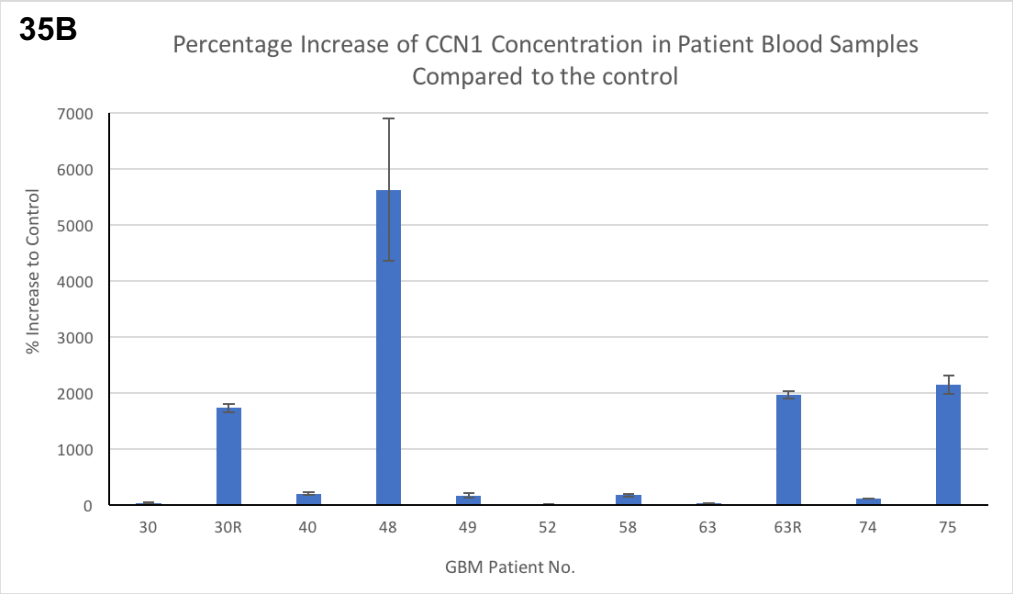


Figure 35. A graph to show CCN1 concentration in 9 patient blood serum samples (35A). Blood samples from patient no. 30 and 63 were also collected at their recurrent GBM tumour surgery (30R and 63R). The percentage increase of each patient compared to the control was also calculated (35B). Asterisks show statistical significance. *P≤ 0.05, **P≤ 0.01, ***P≤ 0.001 ****P≤ 0.0001.

### 4.3.5 The effects of CCG-1423 and CCG-203971 on angiogenesis in the aortic ring assay

The aortic ring assay is a tool used to assess angiogenic or anti-angiogenic effects of inhibitors. Vessels grow away from the aortic ring allowing anti-angiogenic effects to be evaluated by the number of vessels that grow in comparison to an untreated control (Figure 37). Both CCG-1423 and CCG-203971 were used for this experiment in comparison at concentrations of 10μM, 1μM and 0.1μM to confirm that they were having similar effects on angiogenesis (Figure 36). The average MI for the aortic rings treated with 10μM of CCG-1423 was 3.00 +/- 0.06, which was significantly different to the control (9.72 +/- 0.75) (P=0.0009). For the rings treated with 1μM of CCG-1423, the average MI was 3.58 +/- 0.32, which was significantly different to the control (9.72 +/- 0.75) (P=0.002). The average MI for rings treated with 0.1μM of CCG-1423 was 4.24 +/- 0.42, which was also significantly different to the control (9.72 +/- 0.75) (P=0.003). For rings treated with 10μM of CCG-203971, the average MI was 2.53 +/- 0.05, which was significantly different to the control (9.72 +/- 0.75) (P=0.0007). The average MI for rings treated with 1μM of CCG-203971 was 3.36 +/- 0.17, which was significantly different to the control. Finally, the average MI for rings treated with 0.1μM of CCG-203971 was 4.01 +/- 0.12, which was also significantly different to the control (9.72 +/- 0.75) (P=0.002).

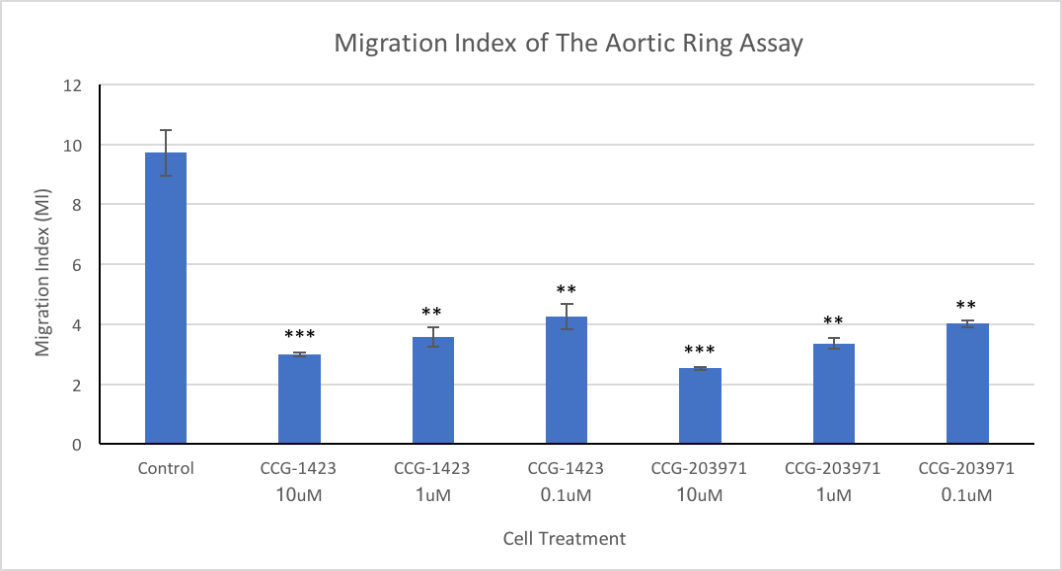


Figure 36. A graph showing the MI of endothelial cells in the aortic ring assay. Aortic rings embedded in Matrigel were treated with 10μM, 1μM or 0.1μM of CCG-1423, CCG-203971 or untreated and incubated for 7 days. The rings were imaged using a confocal microscope (Nikon Eclipse Ti) and the area of migration was measured using ImageJ and the MI calculated. Asterisks show statistical significance. **P≤ 0.01, ***P≤ 0.001. n=3.

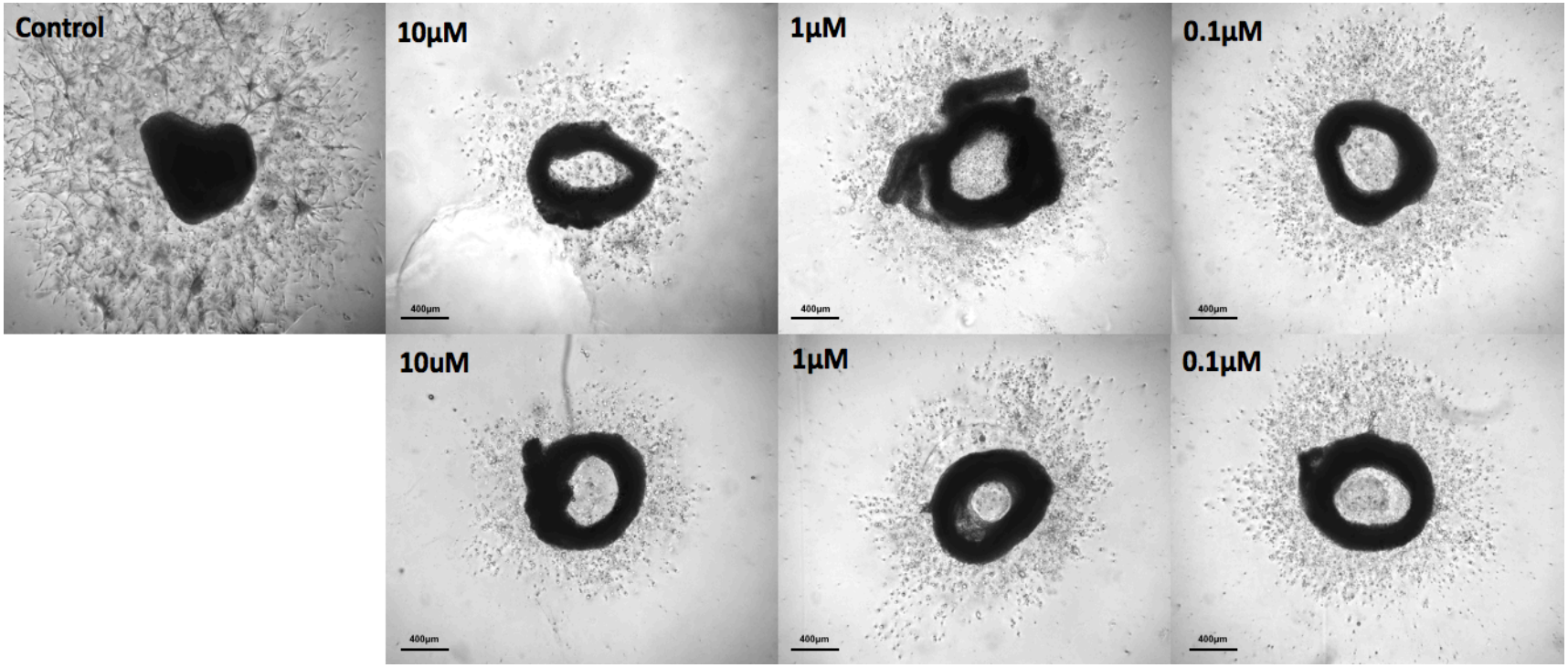


Figure 37. Images of mouse aortas treated with 10µM, 1µM or 0.1µM of CCG-1423 or CCG-203971 or untreated (control). Once treated, rings were incubated for 7 days to allow vessel formation away from the ring. The rings were imaged using a confocal microscope (Nikon Eclipse Ti). The area of vessel formation was measured using ImageJ and the MI was calculated. Note the highest reduction in vessel formation at 10µM for both inhibitors. Scale bar = 400µm.

### 4.3.6 CCG-1423 and CCG-203971 detection and optimisation with MALDI and LESA

The optimisation phase of MALDI using CCG-1423, determined that the preferred matrix to use for drug detection was DHB (160mg/ml) with recrystallization and the preferred isotopic pattern to detect was the sodium adduct $[M+Na]^+$. The concentration of drug detected by MSI differs by a factor of 10.931 on glass versus on a tissue section. This value is calculated by using the following equation to first calculate the volume (V) of the tissue in µl.

$V = \pi \times r^2 \times h$, where r = radius of droplet and h = thickness of tissue section.

The volume of the tissue is then used to calculate the concentration of the solution on tissue using the calculation:

$$\text{Concentration of tissue} = \frac{\text{Concentration of solution spiked} \times \text{Volume spiked}}{\text{Volume of the tissue}}$$

Detection of CCG-1423 by MALDI when spotted directly onto the glass slide was limited to a cut-off concentration of 55µM. The lowest concentration detected on tissue was 1.09mM. In order to improve the detection levels on tissue, modifications to the DHB matrix preparation was completed. The three modifications in attempt to improve detectability were DHB 40mg/ml in 90:10 ACN:0.1% TFA and 1% DMSO, DHB 40mg/ml in 70:30 ACN:0.1% TFA and 1% DMSO and DHB 40mg/ml in 90:10 methanol:0.1% TFA and 1% DMSO. Unfortunately, these modifications were unsuccessful and the lowest

concentration detectable on tissue by MALDI was 1.09mM, which is considered a high concentration for MALDI detection as the detectable range for MALDI is sub-μM (295). LESA was then used in attempt to improve the detectability of CCG-1423 at a lower concentration. The detectability was improved with LESA providing a detection limit of 10.93μM on tissue (Table 6, Figure 38). Although a vast improvement, the optimum detection on tissue homogenate is 1μM and therefore it was unlikely CCG-1423 would be detected in the mouse brain sections.

| CCG-1423 Concentration on glass slide (μM) | CCG-1423 Concentration in Tissue (μM) | Ion Intensity |
|---|---|---|
| 1000 | 10930 | 372887968 |
| 100 | 1093 | 59215388 |
| 10 | 109.3 | 7936420 |
| 5 | 54.65 | 3515311 |
| 1 | 10.93 | 1793659 |
| 0.1 | 1.093 | 527391 |
| 0 | 0 | 573856 |

Table 6. The different concentrations of CCG-1423 on glass and in tissue. The concentration of drug detected by MSI differs by a factor of 10.931 on glass versus on a tissue section calculated by using the volume of tissue, volume of the drug and concentration of the drug. The ion intensity for each concentration of CCG-1423 is shown. The lower limit of quantification using LESA is the concentration of CCG-1423 where the ion intensity is 5x the blank. For CCG-1423 the lowest limit of detection is 10.93μM.

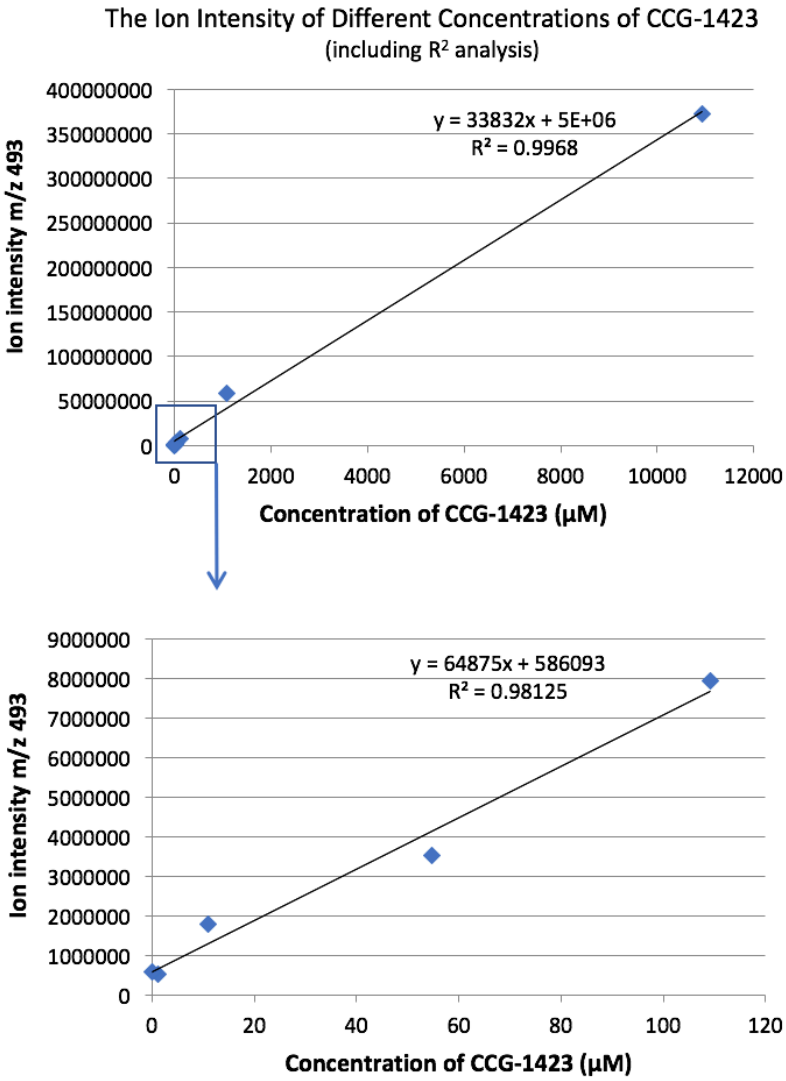


Figure 38. Graphs showing the ion intensity of different concentrations of CCG-1423 detected by LESA mass spectrometry. The graphs include the equation of a straight line and linear regression analysis ($R^2$) to assess the relationship between the variables. As $R^2$ is close to 1, ion intensity and CCG-1423 concentration are strongly related.

During the optimisation phase of MALDI using CCG-203971, again, the best matrix to use for detection of the drug was DHB (160mg/ml) with recrystallization, however, the best isotopic pattern to detect this time was the potassium adduct $[M+K]^+$. Detection of CCG-203971 by MALDI when spotted directly onto the glass slide was possible with a cut-off concentration of 1.09μM. The lowest concentration detected on tissue was 10.93μM, which is a vast improvement on CCG-1423 but still not as low as is required for MALDI detection. LESA was then used in attempt to improve the detectability of CCG-203971 at a lower concentration. Detectability was improved with LESA providing a detection limit of 1.09μM on tissue, which is the required drug concentration to reach at the optimisation phase using tissue homogenate (Table 7, Figure 39). CCG-203971 was then taken forward to *in vivo* experiments for brain tissue collection and detection by LESA and MALDI.

| Solution Concentration (μM) | Concentration in Tissue (μM) | Ion Intensity |
|---|---|---|
| 1000 | 10930 | 676181376 |
| 100 | 1093 | 190719952 |
| 10 | 109.3 | 20417112 |
| 5 | 54.65 | 9598493 |
| 1 | 10.93 | 4303222 |
| 0.1 | 1.093 | 2388824 |
| 0 | 0 | 671175 |

Table 7. The different concentrations of CCG-203971 on glass and in tissue. The concentration of drug detected by MSI differs by a factor of 10.931 on glass versus on a tissue section calculated by using the volume of tissue, volume of the drug and concentration of the drug. The ion intensity for each concentration of CCG-203971 is shown. The lower limit of quantification using LESA is the concentration of CCG-203971 where the ion intensity is 5x the blank. For CCG-203971 the lowest limit of detection is 1.09μM.

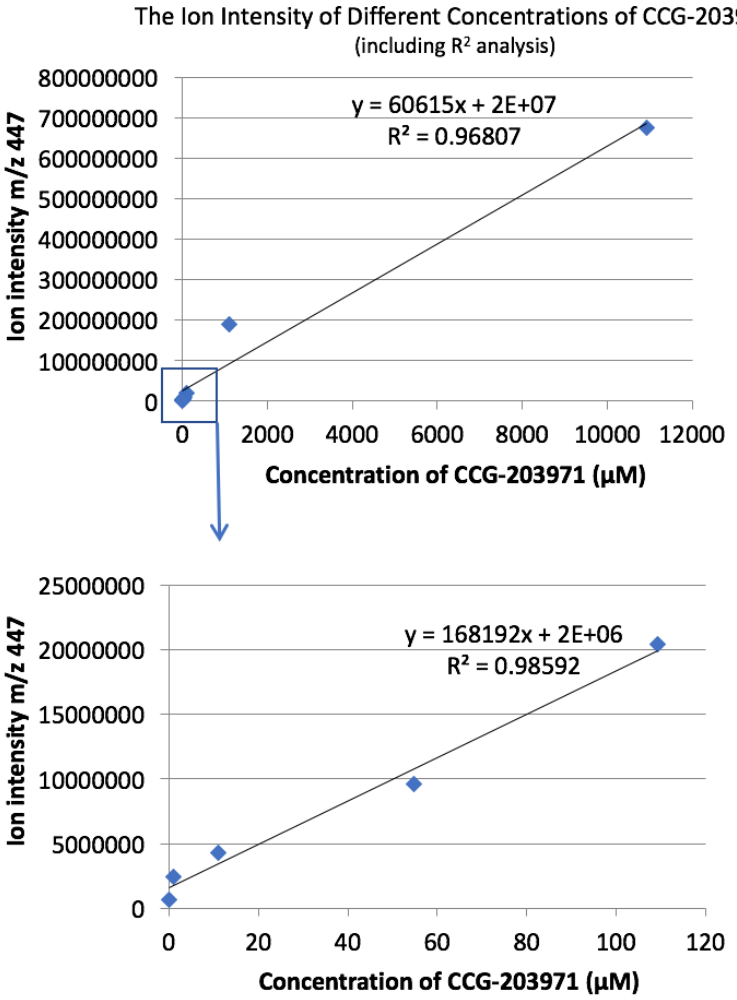


Figure 39. Graphs showing the ion intensity of different concentrations of CCG-203971 detected by LESA mass spectrometry. The graphs include the equation of a straight line and linear regression analysis ($R^2$) to assess the relationship between the variables. As $R^2$ is close to 1, ion intensity and CCG-203971 concentration are strongly related.

### 4.3.7 CCG-203971 drug detection in mouse brains and livers with MALDI

Although the concentration of CCG-203971 was high for MALDI detection on the tissue homogenate sections, attempts were still made to use this method of detection for the brain samples. As predicted, the brain samples were all below the detection threshold of CCG-203971 using MALDI. The tumours were identified on the acquired MALDI images by using the long-chain fatty acid palmitoylcarnitine, a known tumour marker, and an unnamed tumour marker (*m/z* 744.724). Previous work has shown that palmitoylcarnitine is upregulated in tumours, hence it can be accurately detected (296) (Figure 40).

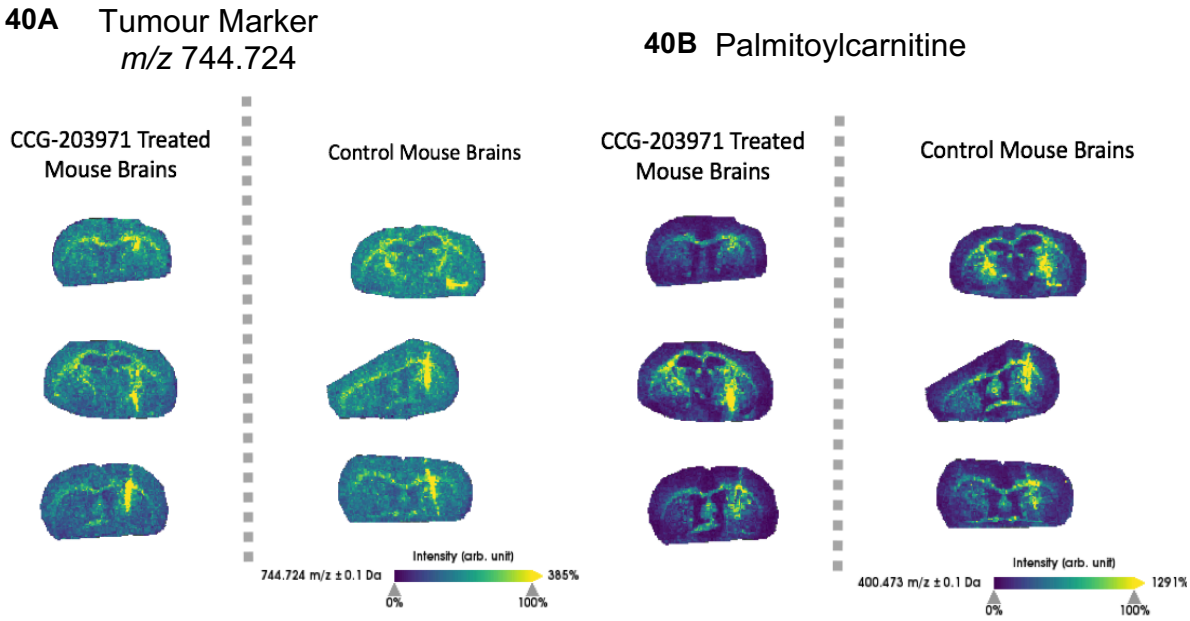


Figure 40. Two tumour markers applied to the MALDI images of CCG-203971 treated mouse brains and untreated control mouse brains. Figure 40A is an unnamed tumour marker with a *m/z* of 744.724. Figure 40B shows the long-chain fatty acid palmitoylcarnitine which is involved in the metabolism of fatty acids and is upregulated in tumours. The colour spectrum shows the intensity of the tumour markers within the brain tissue samples.

CCG-203971 was also not detected in the matched liver samples, however, metabolic changes between the treated and control mouse livers were picked up showing that the drug was metabolised (Figure 41-42). Although the molecules cannot be identified, the image analysis and receiver operating characteristic (ROC) curves (from the Human Metabolome Database) show significant changes in chemical composition between the CCG-203971 treated mouse livers and the control mouse livers. These different chemical compositions were investigated in order to gain more information on whether the drug was present and having an effect despite being unable to detect CCG-203971 itself.

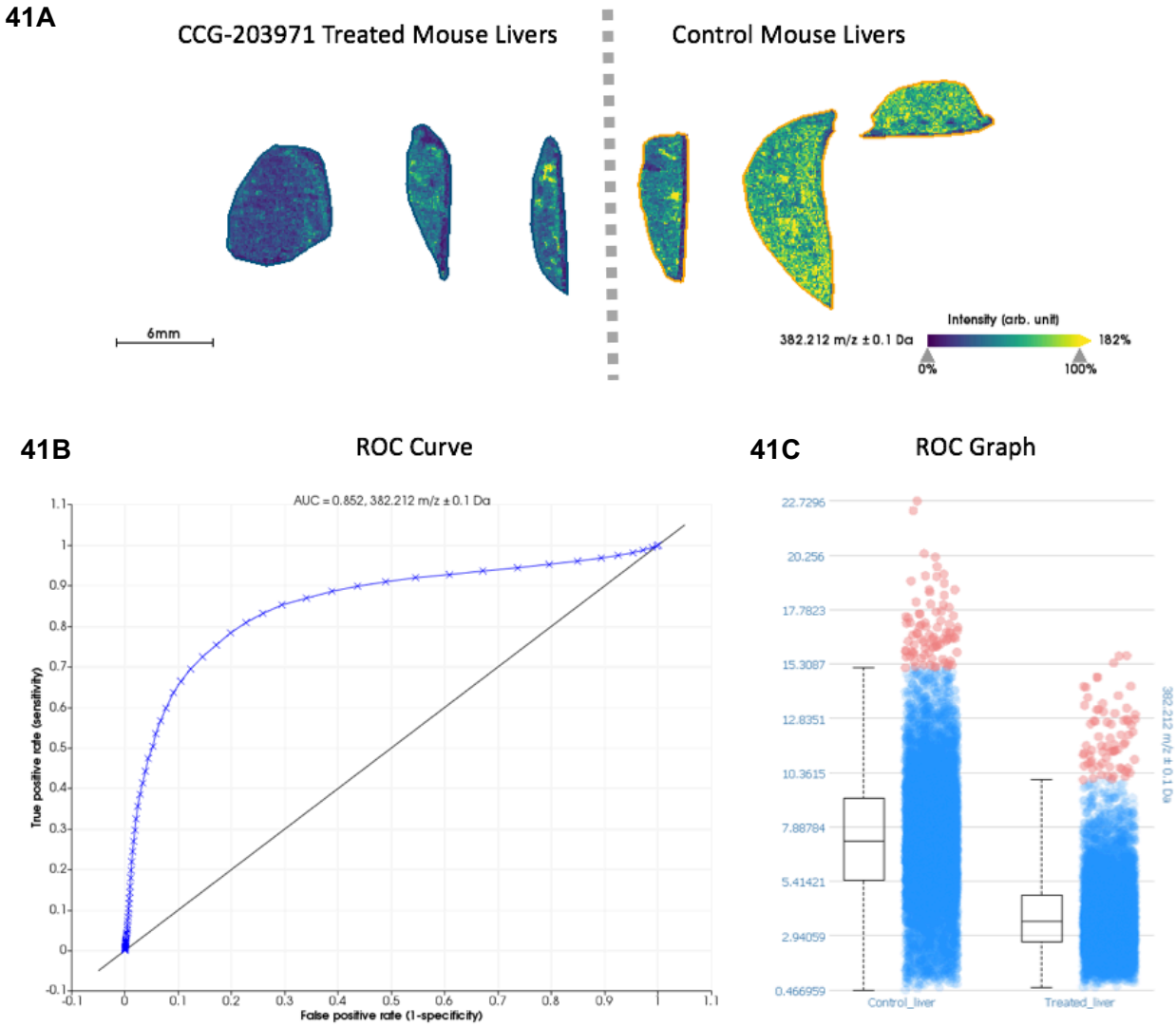


Figure 41. Differences in the chemical composition of mouse livers treated with CCG-203971 and untreated control livers with detected compound *m/z* 382.212. The colour spectrum shows the intensity of compound *m/z* 382.212 within the liver tissue samples (41A). This compound appears to be significantly downregulated in treated livers as shown in the ROC graph (41C). The area under the ROC curve (AUC) value is 0.852 (close to 1) meaning the differences in compound *m/z* 382.212 are very distinguishable between treated and untreated liver samples (41B). This method of analysis allows for less false positive results and the accurate identification of distinct changes between treated and untreated samples.

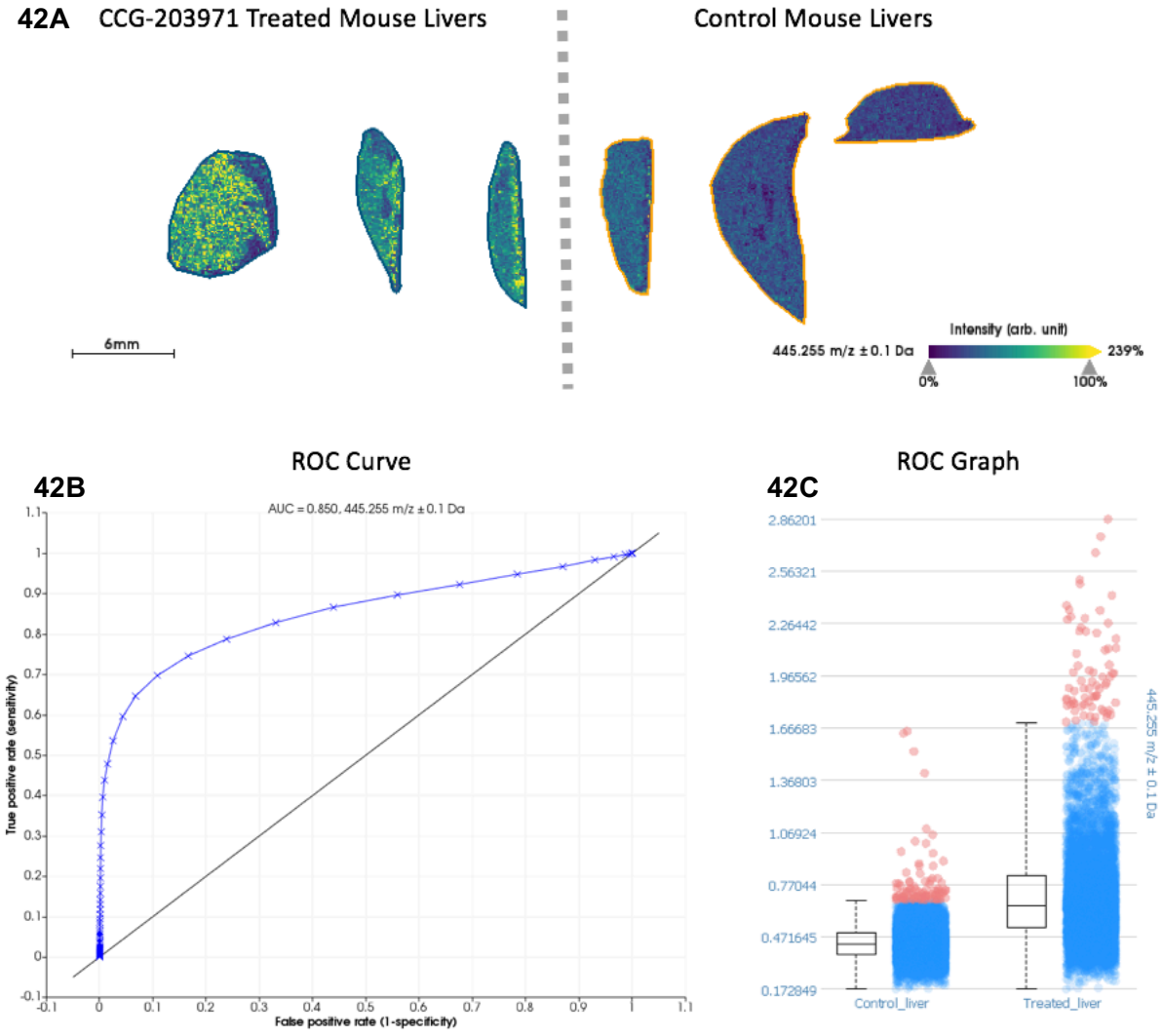


Figure 42. Differences in the chemical composition of mouse livers treated with CCG-203971 and untreated control livers with detected compound *m/z* 445.255. The colour spectrum shows the intensity of compound *m/z* 445.255 within the liver tissue samples (42A). This compound appears to be significantly upregulated in treated livers as shown in the ROC graph (42C). The area under the ROC curve (AUC) value is 0.850 (close to 1) meaning the differences in compound *m/z* 445.255 are very distinguishable between treated and untreated liver samples (42B). This method of analysis allows for less false positive results and the accurate identification of distinct changes between treated and untreated samples.

### 4.3.8 CCG-203971 detection in mouse brains and livers with LESA

LESA mass spectrometry was also unable to detect CCG-203971 in the brain or livers of treated mice. The detected target mass of CCG-203971 was the potassium adduct ($[M+K]^+$) at m/z 447.02. However, the mass spectra of the CCG-203971 calibration samples detected on glass slides did not match the spectra of the CCG-203971 treated brain or liver samples (Figure 43) meaning it was not possible to detect the drug in the brain or liver samples. As the mass spectrum peaks of the brain and liver samples were close to the calibration peaks, fragmentation (MS/MS) was performed in another attempt to detect CCG-203971 but this was also unsuccessful. Figure 44 shows the spectra of all brain samples and Figure 45 for all liver samples.

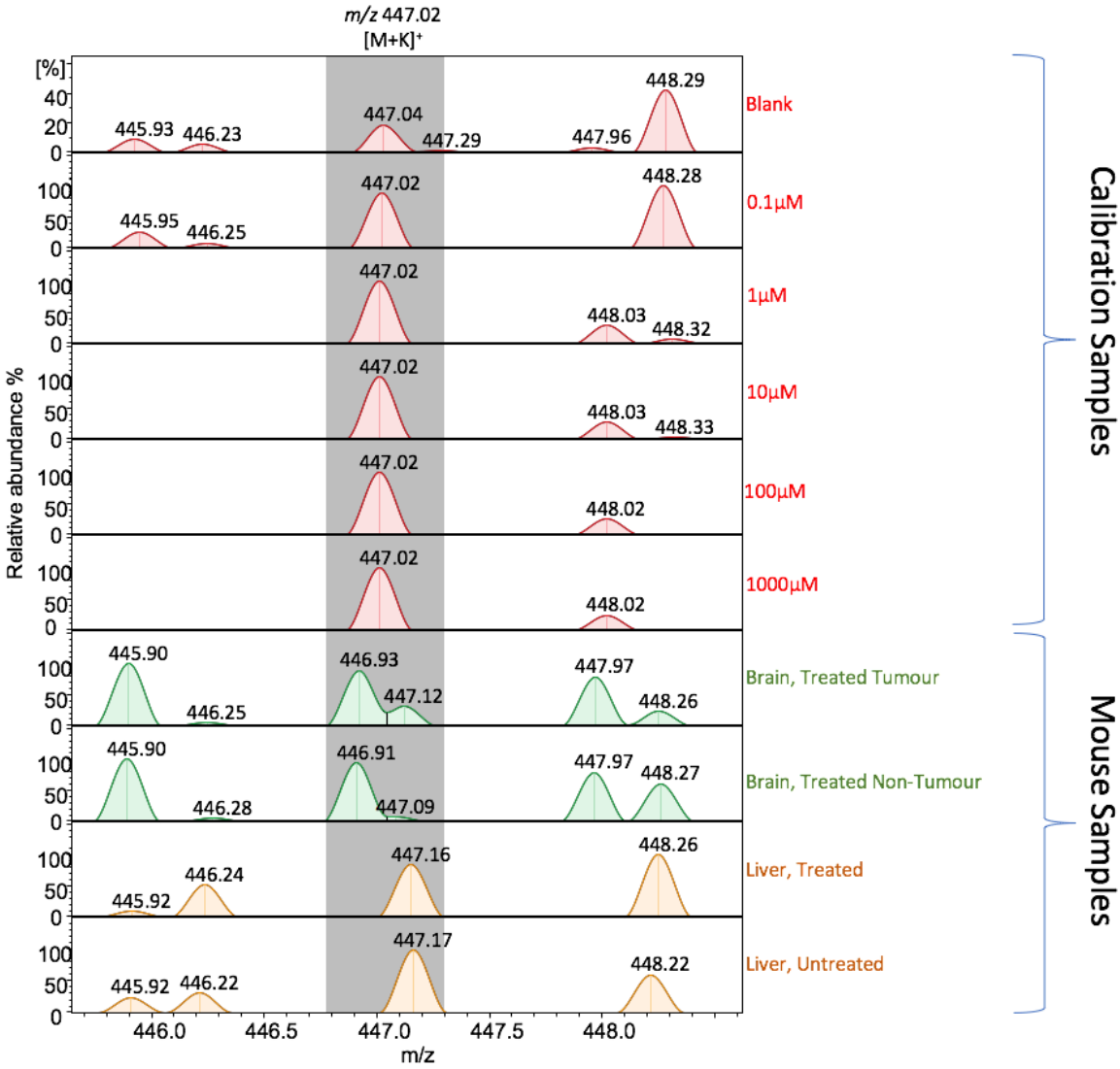


Figure 43. Calibration mass spectra of CCG-203971 (m/z 447.02 $[M+K]^+$) as a percentage of relative abundance. Mass spectra shown include the CCG-203971 calibration samples spotted onto glass slides at concentrations of 0.1µM, 1µM, 10µM, 100µM, 1000µM (red spectra) showing the m/z 447.02 of the drug. The green spectra show examples of the CCG-203971 treated mouse brain samples (including a tumour and non-tumour sample) that do not show the correct m/z of 447.02, meaning the drug has not been detected. The yellow spectra show examples of the CCG-203971 treated and untreated mouse liver samples that again do not show the correct m/z of 447.02, meaning the drug has not been detected.

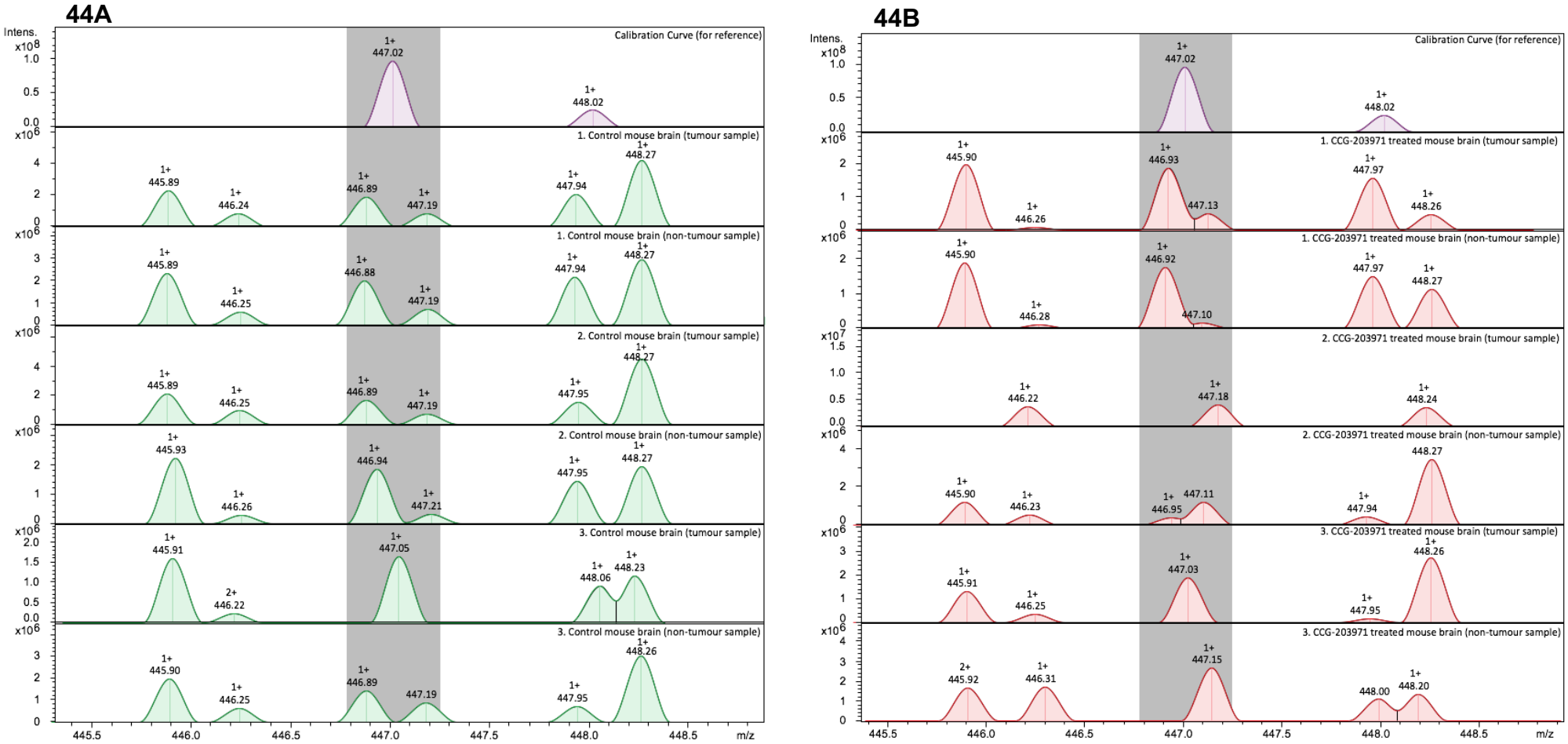


Figure 44. CCG-203971 treated and untreated brain sample mass spectra (m/z 447.02 $[M+K]^+$) measured as ion intensity. Mass spectra shown include a calibration sample for reference (purple spectra) showing the target m/z of CCG-203971 at 447.02. The green spectra show the untreated mouse brain samples (in the tumour and outside of the tumour) (44A). The red spectra show examples of the CCG-203971 treated mouse brain samples (in the tumour and outside of the tumour) that again do not show the correct m/z of 447.02, meaning the drug has not been detected (44B).

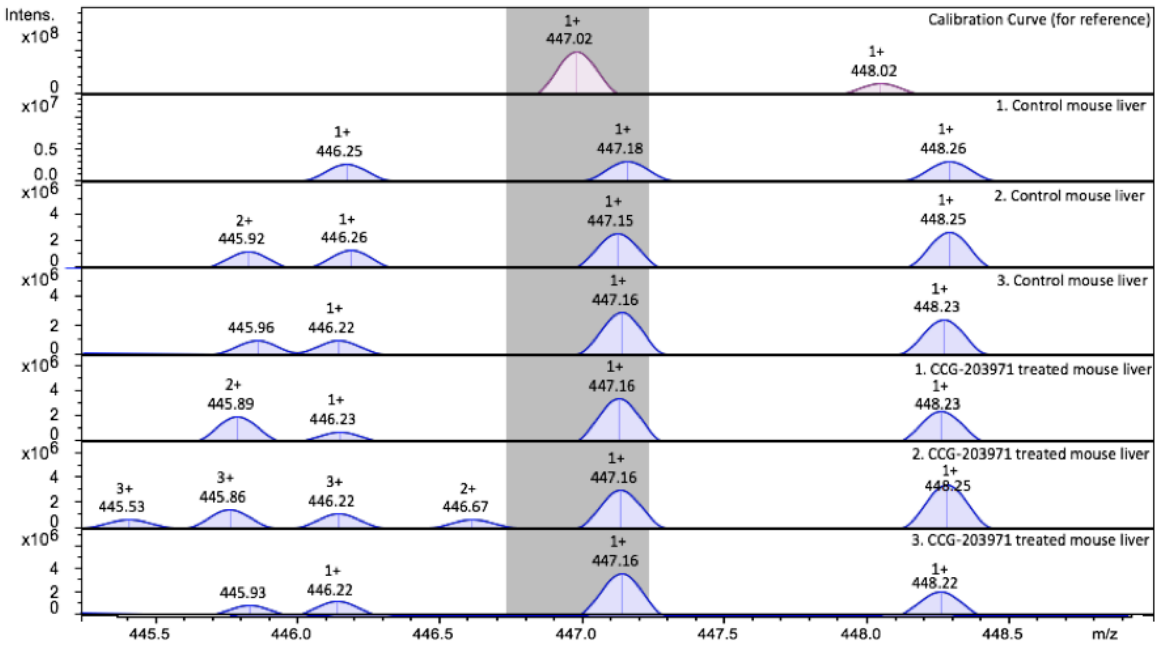


Figure 45. CCG-203971 treated and untreated liver sample mass spectra (m/z 447.02 $[M+K]^+$) measured as ion intensity. Mass spectra shown include a calibration sample for reference (purple spectra) showing the target m/z of CCG-203971 at 447.02. The blue spectra show the CCG-203971 treated and untreated mouse liver samples that do not show the correct m/z of 447.02, meaning the drug has not been detected.

## 4.4 Discussion

### 4.4.1 Cytoplasmic MKL1 is increased in a panel of glioma cell lines when treated with CCG-1423 and CCG-203971

To determine clinical relevance of CCN1 the effects of CCG-1423 were firstly tested in a panel of glioma cell lines at Harvard Medical School, Brigham and Women's Hospital, including patient derived cell lines G9 and G44, murine glioma cell line GL261 and the rat glioma cell line CNS1. All cell lines showed an increase in cytoplasmic MKL1 when treated with CCG-1423 and analysed by western blotting, confirming similar results using the cell line U251 carried out at the University of Leeds. Interestingly, GL261 produced the least build-up of cytoplasmic MKL1, which corresponds with this particular cell line being the least invasive out of all the tested cell lines. This observation may also be linked to MKL1 as a driver of gene transcription of *CCN1* (226), which in turn has been shown to be associated with tumour aggressiveness and invasiveness (239,242,284). From *in vivo* experiments with CCG-1423, it was realised that this inhibitor is highly cytotoxic and compound modifications have been attempted in order to reduce the cytotoxic effect for drug tolerability studies in xenograft models. Through a survey involving aromatic substitutions to CCG-1423, one analogue, CCG-203971, was identified having reduced cytotoxicity and improved potency to the inhibition of PC-3 cell migration. Therefore, CCG-203971 was taken forward in tolerability studies in normal mice using doses up to 100mg/kg/day over 5 days injected intraperitoneally (225). Based on the published data on CCG-203971, western blots were carried out on U251 and G9 cells treated with 500nM of CCG-203971 to firstly reproduce results obtained with CCG-1423. Similar effects on cytoplasmic MKL1 build up were observed for

CCG-203971 and this inhibitor was taken forward to *in vivo* models. This drug has not yet been reported in *in vivo* studies to investigate effects on the brain, therefore this experiment was one of the first using CCG-203971 in glioma research.

### 4.4.2 CCN1 expression is increased in GBM patient samples

CCN1 levels were elevated both in its secreted form and in tumour tissues from glioma patients. In the tissue, CCN1 was expressed in the cytoplasm of tumour cells, with highly stained cells appearing to be associated with blood vessels. Analysis of the TMA generated data revealed an association of CCN1 expression levels with high grade tumours in comparison to lower grade gliomas and cancer tissue adjacent to normal brain tissue. This data suggests that CCN1 expression is correlated with tumour invasiveness and aggressiveness, which confirms previous studies that performed a semi-quantitative IHC analysis of 100 gliomas and 12 normal brain samples correlating CCN1 with tumour grade. The IHC staining showed that in 88% of the WHO grade IV samples, CCN1 was overexpressed and that expression was positively correlated with the expression of c-Met, a receptor tyrosine kinase involved in proliferation, migration and invasion. When investigated *in vivo* using a U87 xenograft in mouse models, CCN1 siRNAs significantly inhibited proliferation by 57% compared to the control (243).

Interestingly, levels of secreted CCN1 in the GBM tissue samples were mirrored in the matched patient blood in comparison to normal bloods. Figure 46 shows CCN1 staining of the patient GBM tissue samples with the lowest and highest

levels of CCN1 found in the matched blood samples. Patient no. 52 (core) presented with the lowest concentration of CCN1 in the matched blood sample (51.51pg/ml), whilst patient no. 48 presented with the highest concentration of CCN1 in the matched blood sample (2588.041pg/ml), which is apparent in the IHC staining of the GBM tissue samples.

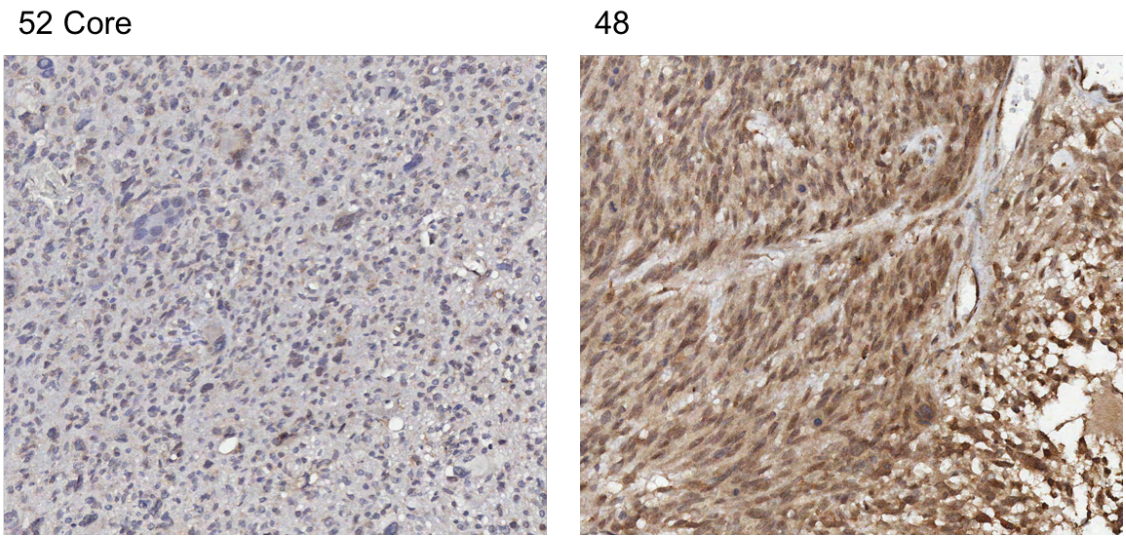


Figure 46. CCN1 IHC staining correlates with the CCN1 concentration determined for the matched blood samples. The GBM tissue sample from patient no. 52 (core) presented with the lowest concentration of CCN1 in the blood (51.51pg/ml) which correlates with the low intensity CCN1 staining in the tissue sample. The GBM tissue sample from patient no. 48 presented with the highest concentration of CCN1 in the blood (2588.041pg/ml), which correlates with the high intensity CCN1 staining in the tissue sample. Magnification x20.

From the results of the IHC, it is evident that the edge samples contain a higher concentration of CCN1 when compared to the core samples of the same patient, which correlates with tumour edge cells being more invasive than tumour core cells. This observation complements studies that have shown tumour-associated macrophages to have a key role at the tumour edge where they enable invasive cell phenotypes and drive tumour cell invasion via a paracrine signalling loop. The recruitment of these cells to the tumour edge has been shown to be activated

by CCN1 in both breast cancer and glioma (297). Furthermore, a study into oncolytic virus therapy in GBM showed that activation of CCN1 inhibited the efficacy of the oncolytic virus through this recruitment of tumour-associated macrophages. Following antibody neutralisation of CCN1, the response to the oncolytic virus therapy improved in glioma, most considerably in GBMs that possessed a high macrophage count (298).

In addition, the samples from the patients with the recurrent tumours, including blood samples, showed a significant increase in CCN1 levels both in the tumour tissues and in the blood sample in comparison to the primary tumour and blood sample. Compared to the control, the recurrent tumour sample for, for example, patient 30 (30R) achieved a percentage increase of 1723.5% compared to the control and a percentage increase of 1265.7% compared to the primary tumour blood sample. For patient 63, the percentage increase of the recurrent tumour (63R) compared to the control was 1962% and compared to the primary tumour blood sample, it was 1622.4%. The observed increases in CCN1 levels between primary and secondary tumour blood samples are considerable; therefore, after validation of the preliminary data using larger sample size and further experiments, CCN1 could potentially be an extremely useful blood biomarker for the monitoring of brain tumour patients following initial primary tumour surgery to predict disease recurrence. This means that a simple blood test for the monitoring of secreted CCN1 may be developed for the early detection of recurrent tumours leading to advanced treatment options and improved survival rates in GBM patients. There were also significant differences in CCN1 concentrations between the control and primary tumour blood samples. Improved sensitivity to enhance

the detection levels of an ELISA based screening system may lead to the development of a cost-effective and non-invasive diagnostic tool for advanced early detection of brain tumours considering that early diagnosis of brain tumours is still limited. The molecular subtyping of brain tumours themselves has advanced diagnosis and treatment options; however, a conclusive diagnosis is still largely based on the interpretation of the histopathology of tumour samples, which may be open to human error and bias. The growing identification and use of biomarkers and genomics will enhance brain tumour diagnosis by providing more detailed information when paired with the traditional histopathology method (299).

### 4.4.3 CCG-1423 and CCG-203971 prevent blood vessel formation (angiogenesis) in the aortic ring assay

Both inhibitors exerted the same effect in the aortic ring assay, leading to a significant reduction in vessel formation. As part of the data analysis for this type of assay, the number of vessels that have formed in the control and in the treated are counted (300). Intriguingly, both drugs fully suppressed vessel formation, as the aortic endothelial cells appeared to round up and migrate away from the aorta. For this reason, the area of migration was measured by calculating a MI rather than the number of vessels. With increased concentration of CCG-1423 or CCG-203971 a lower MI was observed. This may be indicative of the critical role that CCN1 plays in angiogenesis and may also address its association with tumour invasiveness, however further investigation would be needed to confirm this. Previous studies have also concluded that CCG-1423 possesses an anti-angiogenic effect by also producing a near complete inhibition of vessel formation

in the aortic ring assay as well as in *in vivo* angiogenesis experiments using zebrafish embryos (301). Angiogenesis is an essential process in tumour growth. With an enhanced vascular network, tumours can be supplied with oxygen and nutrients and dispose of their metabolic waste, all of which support tumour invasion and metastasis (302). Furthermore, during the development of the heart, endothelial cells differentiate into mesenchymal cells through endothelial-mesenchymal transition in the endocardial cushion, a critical step in the formation of cardiac valves. This has also been implemented in the development of a number of cardiac diseases including myocardial infarction, atherosclerosis and cardiac fibrosis (303,304). Based on the findings from the previous chapter on MAT it is conceivable that as the aortic endothelial cells are undergoing endothelial-mesenchymal transition, CCG-1423 and CCG-203971 activity forces the transitioned endothelial cells to round up but allows them to continue to migrate, mirroring the effect observed in glioma cells. Further experiments are needed to investigate this theory. Live cell imaging of the aortic rings over 3 days would allow for visualisation of the MAT process and continued migration of the cells. In addition to this, repeating the 3D spheroid invasion assay with endothelial cells could be advantageous in observing the migratory switch as for the tumour cells. This paired with the iSIM microscopy would provide a detailed look at the effect of CCG-1423 and CCG-203971 on endothelial cells and angiogenesis. Previous studies have been successful in using spheroid assays for angiogenesis investigations, highlighting the assay's high sensitivity and endothelial cell compatibility. The assay was successfully used for the identification of pro and anti-angiogenic drugs (305).

### 4.4.4 Mass spectrometry imaging of CCG-203971 in mouse brains

Both the MALDI and LESA experiments performed to investigate localisation and effect of CCG-203971 on the brain tissue and the tumours *in vivo* were unsuccessful. Preliminary results indicate that the drug was present in the circulation of the treated animals but was unable to cross the blood brain barrier (BBB). Although it was also undetected in the liver samples, metabolic changes were observed in the livers. The inability to detect CCG-203971 in the liver may be due to the fact that animal sacrifice was performed too late after the final dose was given (2 hours) due to the fact that metabolic changes were identified between treated and untreated liver samples but not the drug itself. This time frame was, however, in keeping with the tolerability study from Bell et al. who reported plasma levels of the drug to exceed the previous PC-3 cell migration $IC_{50}$ of 4.2μM for up to 3 hours after a single dose *in vivo* (225). Figure 47 shows the calibration peak with a *m/z* of 447.02 and a CCG-203971 treated tumour sample with a *m/z* of 447.03, suggesting the drug has been detected in 1 of the treated brain tumour samples. Upon inspection of the treated brain tumour sample slide and the droplet placement using LESA, the drug was detected in a ventricle of a treated brain sample suggesting that the drug was present in the cerebral spinal fluid (CSF) within the ventricle. Drug presence in the CSF within the brain compartments cannot be taken as an indicator of transport across the BBB. The choroid plexus, which is the regulator of drug transfer from the blood to the CSF, is made up of different epithelial/endothelial barriers to the brain capillary endothelium that comprises the BBB (306). As it was not detected within the brain tissue, this suggests that CCG-203971 cannot cross the BBB, however,

despite unsuccessful detection in the liver samples, this provides more evidence to the chemical composition differences that the drug was circulating in the animal's systems.

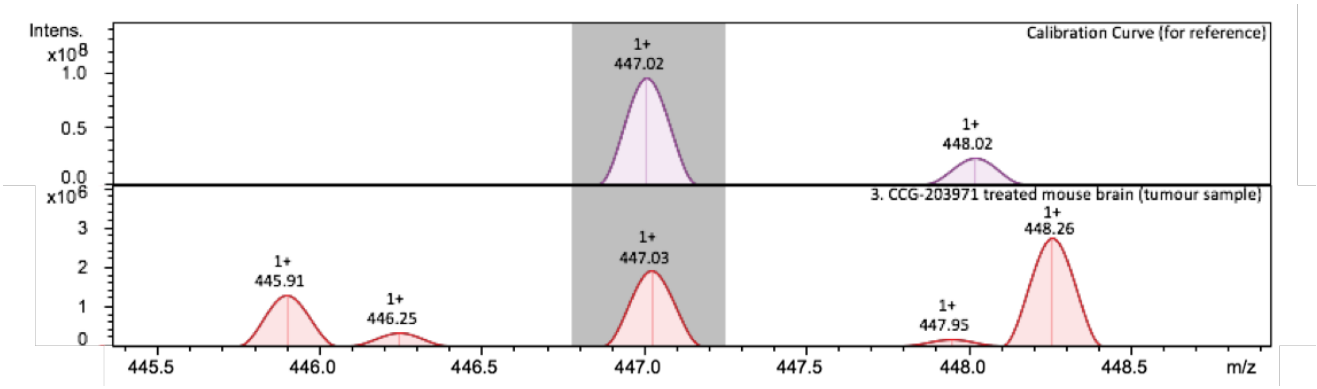


Figure 47. Calibration mass spectrum (m/z 447.02 $[M+K]^+$) and CCG-203971 treated brain sample mass spectra (m/z 447.03 $[M+K]^+$) measured as ion intensity. The purple spectrum shows the calibration curve with a m/z of 447.02, meaning the drug has been detected. The red spectrum shows a CCG-203971 treated mouse brain tumour sample with a m/z of 447.03, also suggesting the drug has been detected in this sample.

Further experiments should include growing bigger tumours for easier tumour identification and better representation of brain tumour side effects such as a leaky BBB. Increasing the CCG-203971 dosage would also be advantageous to the study in order to increase the possibility of drug detection, as the animals responded extremely well at 100mg/kg/day with no abnormal side effects compared to the control animals. Based on the striking phenotypes observed in the aortic ring assay and the predominant localisation of CCN1 with blood vessels in brain tumours it would also be interesting to look into monitoring angiogenesis using MALDI. Haem can be used as a marker to visualise the lumen of blood vessels in the brain. By utilising this and pairing it with protein imaging for CCN1, again using MALDI, a better representation of the relationship between CCN1, tumour invasiveness and angiogenesis may be obtained. Furthermore, the

continued development of CCG-1423 and its analogues could prove more successful in *in vivo* studies for brain tumour research.

## Chapter 5: Conclusion

Gliomas are highly aggressive tumours that possess diffuse and invasive behaviours. The infiltrative nature of these cancers contributes towards poor patient prognosis and highlights the need for clinical intervention to target the mechanisms that control cell migration and invasion. Understanding the relevant biology offers a unique opportunity to improve treatment of the most invasive and highly migratory tumours, such as GBM, and to enhance our understanding of tumour cell migration and invasion.

Current treatment of GBM comprises surgical resection of the tumour followed by radiotherapy and adjuvant chemotherapy; most commonly with temozolomide (307). Further treatment may include immunotherapy, angiogenesis inhibitors in combination with chemotherapy and gene/antibody therapy. In spite of these treatment options, success in curing GBM has not ensued due to its invasiveness and cell migrating abilities (308). With recurrence being reported 2-3cm from the original tumour site, in more than 90% of patients with glioma, there is a strong need for the development of successful anti-migratory drugs (309).

There has been a number of potential anti-migratory drug candidates reported through drug-repurposing. One such study, uncovered the therapeutic potential of anti-psychotic drugs as effective agents in glioma management. One of the drugs tested was a second-generation anti-psychotic drug called olanzapine which was shown to suppress cell migration in the glioma cell line A172 as well as enhance temozolomide activity when used in conjunction. However, contradicting studies found that olanzapine upregulated the protein expression of

the neurotrophin growth factor, brain-derived neurotrophic factor (BDNF) by 22% and seemingly induced tumour-promoting effects (310). These opposing results highlight the importance of gaining a more in depth understanding of the mechanisms involved in glioma cell migration. By delving deeper into the molecular biology of these cancers, research can focus on targeting multiple processes within tumour cells in order to completely arrest glioma cell motility and invasion, resulting in more successful treatments.

Another study looked into the anti-cancer potential of the anti-hyperglycaemic agent, metformin in the treatment of GBM. This drug is used in the treatment of type 2 diabetes and was investigated for its effects on the serine/threonine-specific protein kinase Akt (protein kinase B) in the PI3K pathway; a key process involved in cell migration (311). Not only was metformin shown to decrease SF268 and U87 cell motility in 2D wound healing assays by 80% but it presented with a potential role in the inhibition of the PI3K pathway by inactivating Akt. This demonstrates the possible use of metformin as an anti-invasive and anti-migratory agent in GBM management (312). Although successful in 2D *in vitro* assays, as previously stated within this thesis, this can lead to overestimation of drug efficacy and produce inaccurate data, ultimately causing failure when taken forward into *in vivo* models. Screening drugs on migrating cells in a 3D environment aids a more representative assessment of the activity of anti-migratory drug candidates and could produce successful *in vivo studies* that can then be taken forward to clinical trial.

There have also been investigations into effects of anti-epidermal growth factor receptor (EGFR) and anti-vascular endothelial growth factor receptors (VEGFR) agents on cell migration in glioma. Lapatinib is a drug currently used in the treatment of HER2-positive breast cancer. It is an ATP-competitive tyrosine kinase inhibitor for both EGFR and HER2/neu. EGFR is overexpressed in 50% of GBM patients and has a considerable role in the oncogenic activity of GBM. The anti-VEGFR agent investigated, called Sunitinib, is used in the treatment of renal carcinoma and refractory gastrointestinal stromal tumours. This tyrosine kinase inhibitor targets VEGFR and platelet-derived growth factor receptors. As cell migration is driven by the association of integrins with growth factors, this study by Dimitropoulos *et al* focussed on the formation of complex integrin β1/EGFR and complex integrin β3/VEGFR. It was shown that lapatinib inhibited complex integrin β1/EGFR formation within 30 minutes of application in GBM cell lines U87 and M059K, inhibiting cell migration. Sunitinib also inhibited cell migration through its disruption of complex integrin β3/VEGFR formation, within 2 hours of drug application (313). These drugs have been used in small phase I/II clinical trials, however, used alone they did not show promising anti-cancer activity in recurrent GBM patients (313, 314). As GBMs implement many pathways in progression and invasion, using these drugs in combination may prove to be more effective. This will enable multiple pathways to be inhibited at one time, thus increasing the efficacy of anti-migratory treatments.

The investigations within this thesis demonstrate a need to focus research on anti-migratory agents for GBM. In particular, the use of 3D assays in drug screening for a more accurate representation of tumour environment and drug

efficacy, and combination treatments for multiple pathway targeting to stop cell migration, reduce tumour recurrence and increase treatment successes. The first aim of these studies was met by exploring the migratory characteristics of different glioma cell lines as well as their response to different drug treatments. Distinct differences in cell response to treatment in terms of phenotype, migration mode and invasiveness were observed and analysed. A wide range of migration assays and a panel of chemical inhibitors to target the actin polymerisation pathway were utilised to investigate cellular responses to drug treatment in U87 and U251 glioma cells. The second aim of these studies was met by identifying one compound, CCG-1423, from the inhibitor screen that uniquely failed to halt glioma cell migration and invasion in 3D invasion assays in spite of predicted anti-migratory activity. It was hypothesised that MAT was induced by CCG-1423 activity driving the switch from one migratory modality to another. By using iSIM, and a novel ImageJ plugin, the third aim of these studies was met by developing this unique workflow and analysis technique to investigate MAT in glioma cells treated with CCG-1423, confirming a distinct switch in cell phenotype in treated cells compared to control cells. This switch has so far not been characterised in great detail in GBM biology and targeting cellular components driving MAT in GBM may be explored to completely inhibit cell migration.

Results from MKL1 immunofluorescence and western blotting profiles confirmed the action of CCG-1423 blocking MKL1 nuclear import, and subsequently, CCN1 transcription, with significantly increased levels of MKL1 in the cytoplasm in treated cells compared to untreated cells. ELISA assays also confirmed CCG-1423 activity with reduced secreted CCN1 levels following treatment. IHC was

used to confirm CCN1 expression in patient samples, an association with high grade tumours and as such clinical relevance. The results from this screen revealed a correlation between tumour grade and CCN1 expression, suggesting CCN1 has a key role in GBM progression and invasion. In addition to this, 9 in-house patient samples were also stained for CCN1 including 2 patients with primary and secondary tumour samples and 4 patients with tumour edge and core samples. There was a significant increase in CCN1 expression between the primary and the secondary samples as well as between the edge and core samples. This also suggests that CCN1 is involved in GBM progression and invasion due to the fact that tumour edge cells are known to be invading cells that eventually reseed a tumour. Importantly, CCN1 was detected in the matched patient blood samples. Although all blood samples showed an increase in CCN1 concentration in comparison to bloods from healthy donors, the matched secondary blood samples after recurrence showed a significant increase in CCN1 levels, correlating with the CCN1 expression in the associated tissue samples. CCN1 has therefore presented itself as a potential biomarker for monitoring GBM progression and possibly, with increased sensitivity, a diagnostic marker. This could lead to earlier diagnosis and increased survival rates for GBM patients.

CCG-1423, and its less toxic analogue CCG-203971, were used in western blot experiments of patient derived cell lines G9 and G44, murine glioma cell line GL261 and rat glioma cell line CNS1 to assess the similarity in effect of both drugs in order to take CCG-203971 forward into *in vivo* studies for MSI. CCG-203971 showed inhibitor activity similar to those observed with CCG-1423 and therefore was used in *in vivo* studies due to its reduced toxicity and enhanced *in*

*vivo* tolerability. Following successful *in vivo* experiments with patient derived G9 cells, MSI experiments were undertaken using MALDI and LESA. Although unsuccessful in locating CCG-203971 in the brain samples, the preliminary results will guide future *in vivo* work with this drug.

The main novel findings presented here are becoming increasingly relevant in GBM research. Recently, it has been shown that microRNA, miR-634 sensitises glioma cells to temozolomide treatment via CCN1. miR-634 expression was significantly decreased in glioma tissue compared to normal tissue and was associated with tumour grade with miR-634 expression being higher in grades I and II compared to III and IV. In addition, patients with lower miR-634 expression had lower survival rates compared to those with higher expression. Furthermore, it was found that downregulation of miR-634 was involved in drug resistance in glioma cells. As it is known that CCN1 is a target of miR-634, this study investigated and showed that miR-634 can sensitise temozolomide resistant glioma cells by targeting CCN1 (316). As we have shown, not only does CCN1 have a key role in glioma invasion but also in other aspects of glioma progression including drug-resistance.

In addition, CCN1 affects the efficacy of oncolytic virus therapy. Activation of CCN1 elicits a number of anti-viral responses in this topical treatment option for GBM patients including macrophage recruitment and the induction of interferon-α secretion leading to reduced efficacy of oncolytic virus therapy (213,295). As CCN1 can be detected in patient blood, it could be used as a predictor of patient response in oncolytic virus therapy. Patient blood test results with high

concentrations of CCN1 could identify low responses to oncolytic virus therapy due to the associated anti-viral responses induced by CCN1. Consequently, this could lead to the development of combination treatments involving CCN1 inhibition as well as oncolytic virus therapy, thus enhancing a patient's positive response to the treatment. By delving deeper into the role of CCN1, in all aspects of GBM biology, a greater understanding can be gained in its mechanism and how to target this protein for improved patient outcome. All in all, CCN1 can be utilised to measure patient progress, patient response to treatment and potentially as a diagnostic marker.

In conclusion, the studies contained within this thesis present the importance of moving cell migration research into a 3D setting in order to gain more accurate drug efficacy results in an environment that replicates that of a tumour. Furthermore, it provides interesting and compelling evidence that glioma cells can undergo MAT in response to pharmacological intervention intended to prevent migration, resulting in continued migration and invasion, highlighting the need for more specific anti-migratory combination treatments. In addition, these studies have uncovered an important role for CCN1 in disease progression supporting CCN1 as potential biomarker for GBM, which could improve survival rates of this devastating disease.

## References


1. Stratton MR, Campbell PJ, Futreal PA. The cancer genome. Nature. 2009 Apr 9;458(7239):719–24.

2. Hanahan D, Weinberg RA. The Hallmarks of Cancer. Cell. 2000 Jan 7;100(1):57–70.

3. Guan X. Cancer metastases: challenges and opportunities. Acta Pharm Sin B. 2015 Sep;5(5):402–18.

4. Jiang WG, Sanders AJ, Katoh M, Ungefroren H, Gieseler F, Prince M, et al. Tissue invasion and metastasis: Molecular, biological and clinical perspectives. Semin Cancer Biol. 2015 Dec 1;35:S244–75.

5. Martin TA, Ye L, Sanders AJ, Lane J, Jiang WG. Cancer Invasion and Metastasis: Molecular and Cellular Perspective [Internet]. Landes Bioscience; 2013 [cited 2018 May 22]. Available from: https://www.ncbi.nlm.nih.gov/books/NBK164700/

6. Mahmoud O, Tunceroglu A, Chokshi R, Benevenia J, Beebe K, Patterson F, et al. Overall survival advantage of chemotherapy and radiotherapy in the perioperative management of large extremity and trunk soft tissue sarcoma; a large database analysis. Radiother Oncol. 2017 Aug 1;124(2):277–84.

7. Haeger A, Wolf K, Zegers MM, Friedl P. Collective cell migration: guidance principles and hierarchies. Trends Cell Biol. 2015 Sep 1;25(9):556–66.

8. Yamaguchi H, Condeelis J. Regulation of the actin cytoskeleton in cancer cell migration and invasion. Biochim Biophys Acta BBA - Mol Cell Res. 2007 May;1773(5):642–52.

9. Huttenlocher A, Horwitz AR. Integrins in Cell Migration. Cold Spring Harb Perspect Biol. 2011 Jan 9;3(9):a005074.

10. Lee JM. The Actin Cytoskeleton and the Regulation of Cell Migration. San Rafael, Calif. (1537 Fourth Street, San Rafael, CA 94901 USA): Morgan & Claypool Life Sciences; 2013. 78 p.

11. Hall A. Rho family GTPases. Biochem Soc Trans. 2012 Dec 1;40(6):1378–82.

12. Kraynov VS, Chamberlain C, Bokoch GM, Schwartz MA, Slabaugh S, Hahn KM. Localized Rac Activation Dynamics Visualized in Living Cells. Science. 2000 Oct 13;290(5490):333–7.

13. Parri M, Chiarugi P. Rac and Rho GTPases in cancer cell motility control. Cell Commun Signal CCS. 2010 Sep 7;8:23.

14. Vial E, Sahai E, Marshall CJ. ERK-MAPK signaling coordinately regulates activity of Rac1 and RhoA for tumor cell motility. Cancer Cell. 2003 Jul;4(1):67–79.

15. Frantz C, Stewart KM, Weaver VM. The extracellular matrix at a glance. J Cell Sci. 2010 Dec 15;123(24):4195–200.

16. Huang J-Y, Cheng Y-J, Lin Y-P, Lin H-C, Su C-C, Juliano R, et al. Extracellular Matrix of Glioblastoma Inhibits Polarization and Transmigration of T Cells: The Role of Tenascin-C in Immune Suppression. J Immunol. 2010 Jan 8;185(3):1450–9.

17. Lu P, Takai K, Weaver VM, Werb Z. Extracellular Matrix Degradation and Remodeling in Development and Disease. Cold Spring Harb Perspect Biol [Internet]. 2011 Dec [cited 2016 May 2];3(12). Available from: http://www.ncbi.nlm.nih.gov/pmc/articles/PMC3225943/

18. Bonnans C, Chou J, Werb Z. Remodelling the extracellular matrix in development and disease. Nat Rev Mol Cell Biol. 2014 Dec;15(12):786–801.

19. Andrew N, Insall RH. Chemotaxis in shallow gradients is mediated independently of PtdIns 3-kinase by biased choices between random protrusions. Nat Cell Biol. 2007 Feb;9(2):193–200.

20. Sahai E, Marshall CJ. Differing modes of tumour cell invasion have distinct requirements for Rho/ROCK signalling and extracellular proteolysis. Nat Cell Biol. 2003 Aug;5(8):711–9.

21. Matsuoka T, Yashiro M. Rho/ROCK signaling in motility and metastasis of gastric cancer. World J Gastroenterol WJG. 2014 Oct 14;20(38):13756–66.

22. Mayor R, Etienne-Manneville S. The front and rear of collective cell migration. Nat Rev Mol Cell Biol [Internet]. 2016 Jan 4 [cited 2016 Jan 6];advance online publication. Available from: http://www.nature.com/nrm/journal/vaop/ncurrent/full/nrm.2015.14.html

23. Affolter M, Weijer CJ. Signaling to Cytoskeletal Dynamics during Chemotaxis. Dev Cell. 2005 Jul;9(1):19–34.

24. Kramer N, Walzl A, Unger C, Rosner M, Krupitza G, Hengstschläger M, et al. In vitro cell migration and invasion assays. Mutat Res Mutat Res. 2013 Jan 1;752(1):10–24.

25. Liu Y-J, Le Berre M, Lautenschlaeger F, Maiuri P, Callan-Jones A, Heuzé M, et al. Confinement and Low Adhesion Induce Fast Amoeboid Migration of Slow Mesenchymal Cells. Cell. 2015 Feb 12;160(4):659–72.

26. Trzpis M, McLaughlin PMJ, de Leij LMFH, Harmsen MC. Epithelial Cell Adhesion Molecule. Am J Pathol. 2007 Aug;171(2):386–95.

27. Halbleib JM, Nelson WJ. Cadherins in development: cell adhesion, sorting, and tissue morphogenesis. Genes Dev. 2006 Jan 12;20(23):3199–214.

28. Maître J-L, Heisenberg C-P. Three Functions of Cadherins in Cell Adhesion. Curr Biol. 2013 Jul 22;23(14):R626–33.

29. Gumbiner BM. Regulation of cadherin-mediated adhesion in morphogenesis. Nat Rev Mol Cell Biol. 2005 Aug;6(8):622–34.

30. Pećina-Šlaus N. Tumor suppressor gene E-cadherin and its role in normal and malignant cells. Cancer Cell Int. 2003 Oct 14;3:17.

31. Noh M-G, Oh S-J, Ahn E-J, Kim Y-J, Jung T-Y, Jung S, et al. Prognostic significance of E-cadherin and N-cadherin expression in Gliomas. BMC Cancer [Internet]. 2017 Aug 29;17. Available from: https://www.ncbi.nlm.nih.gov/pmc/articles/PMC5575836/

32. Miyasaka M. Selectins (CD62-E/L/P). In: Delves PJ, editor. Encyclopedia of Immunology (Second Edition) [Internet]. Oxford: Elsevier; 1998. p. 2158–61. Available from: http://www.sciencedirect.com/science/article/pii/B0122267656005600

33. Natoni A, Macauley MS, O'Dwyer ME. Targeting Selectins and Their Ligands in Cancer. Front Oncol [Internet]. 2016 Apr 18;6. Available from: https://www.ncbi.nlm.nih.gov/pmc/articles/PMC4834419/

34. Danen EHJ. Integrins: An Overview of Structural and Functional Aspects [Internet]. Landes Bioscience; 2013 [cited 2018 Sep 17]. Available from: https://www.ncbi.nlm.nih.gov/books/NBK6259/

35. Trimboli AJ, Fukino K, Bruin A de, Wei G, Shen L, Tanner SM, et al. Direct Evidence for Epithelial-Mesenchymal Transitions in Breast Cancer. Cancer Res. 2008 Feb 1;68(3):937–45.

36. Cavallaro U, Christofori G. Cell adhesion and signalling by cadherins and Ig-CAMs in cancer. Nat Rev Cancer. 2004 Feb;4(2):118–32.

37. Di Cera E. Serine Proteases. IUBMB Life. 2009 May;61(5):510–5.

38. Rakash S, a, Rana F, Rafiq S, Masood A, Amin S. Role of proteases in cancer: A review. Biotechnol Mol Biol Rev. 2012 Oct 31;7(4):90–101.

39. Mohanam S, Gladson CL, Rao CN, Rao JS. Biological significance of the expression of urokinase-type plasminogen activator receptors (uPARs) in brain tumors. Front Biosci J Virtual Libr. 1999 Feb 15;4:D178-187.

40. Levičar N, Strojnik T, Kos J, Dewey RA, Pilkington GJ, Lah TT. Lysosomal Enzymes, Cathepsins in Brain Tumour Invasion. J Neurooncol. 2002 May 1;58(1):21–32.

41. Chen D, Frezza M, Schmitt S, Kanwar J, Dou QP. Bortezomib as the First Proteasome Inhibitor Anticancer Drug: Current Status and Future Perspectives. Curr Cancer Drug Targets. 2011 Mar;11(3):239–53.

42. Rao JS. Molecular mechanisms of glioma invasiveness: the role of proteases. Nat Rev Cancer. 2003 Jul;3(7):489–501.

43. Alberts B, Johnson A, Lewis J, Raff M, Roberts K, Walter P. Molecular Biology of the Cell. 4 edition. Boca Raton, FL: Garland Science; 2002. 1616 p.

44. Dominguez R, Holmes KC. Actin Structure and Function. Annu Rev Biophys. 2011 Jun 9;40:169–86.

45. Blanchoin L, Boujemaa-Paterski R, Sykes C, Plastino J. Actin Dynamics, Architecture, and Mechanics in Cell Motility. Physiol Rev. 2014 Jan 1;94(1):235–63.

46. Sept D, McCammon JA. Thermodynamics and kinetics of actin filament nucleation. Biophys J. 2001 Aug;81(2):667–74.

47. Pollard TD, Cooper JA. Actin, a Central Player in Cell Shape and Movement. Science. 2009 Nov 27;326(5957):1208–12.

48. Pollard TD, Borisy GG. Cellular Motility Driven by Assembly and Disassembly of Actin Filaments. Cell. 2003 Feb 21;112(4):453–65.

49. Kirschner MW. Implications of treadmilling for the stability and polarity of actin and tubulin polymers in vivo. J Cell Biol. 1980 Jul 1;86(1):330–4.

50. Plopper G. Principles of Cell Biology. Jones & Bartlett Publishers; 2012. 530 p.

51. Lu Q, Longo FM, Zhou H, Massa SM, Chen Y-H. Signaling Through Rho GTPase Pathway as Viable Drug Target. Curr Med Chem. 2009;16(11):1355–65.

52. Tcherkezian J, Lamarche-Vane N. Current knowledge of the large RhoGAP family of proteins. Biol Cell. 2007 Feb 1;99(2):67–86.

53. Rho GTPase-dependent transformation by G protein-coupled receptors. Publ Online 30 March 2001 Doi101038sjonc1204188 [Internet]. 2001 Mar 30 [cited 2017 Sep 13];20(13). Available from: http://www.nature.com/onc/journal/v20/n13/full/1204188a.html

54. Bridges TM, Lindsley CW. G-protein-coupled receptors: from classical modes of modulation to allosteric mechanisms. ACS Chem Biol. 2008 Sep 19;3(9):530–41.

55. Dovas A, Couchman JR. RhoGDI: multiple functions in the regulation of Rho family GTPase activities. Biochem J. 2005 Aug 15;390(Pt 1):1–9.

56. Siehler S. Regulation of RhoGEF proteins by G12/13-coupled receptors. Br J Pharmacol. 2009 Sep;158(1):41–9.

57. Miano JM, Long X, Fujiwara K. Serum response factor: master regulator of the actin cytoskeleton and contractile apparatus. Am J Physiol - Cell Physiol. 2007 Jan 1;292(1):C70–81.

58. Muehlich S, Wang R, Lee S-M, Lewis TC, Dai C, Prywes R. Serum-Induced Phosphorylation of the Serum Response Factor Coactivator MKL1 by the Extracellular Signal-Regulated Kinase 1/2 Pathway Inhibits Its Nuclear Localization. Mol Cell Biol. 2008 Oct 15;28(20):6302–13.

59. Sun Y, Boyd K, Xu W, Ma J, Jackson CW, Fu A, et al. Acute Myeloid Leukemia-Associated Mkl1 (Mrtf-a) Is a Key Regulator of Mammary Gland Function. Mol Cell Biol. 2006 Aug;26(15):5809–26.

60. Vartiainen MK, Guettler S, Larijani B, Treisman R. Nuclear Actin Regulates Dynamic Subcellular Localization and Activity of the SRF Cofactor MAL. Science. 2007 Jun 22;316(5832):1749–52.

61. Alan JK, Lundquist EA. Mutationally activated Rho GTPases in cancer. Small GTPases. 2013 Jul 1;4(3):159–63.

62. Wu D, Asiedu M, Wei Q. MyoGEF regulates the invasion activity of MDA-MB-231 breast cancer cells through activation of RhoA and RhoC. Oncogene. 2009 Jun 4;28(22):2219–30.

63. Adams HC, Chen R, Liu Z, Whitehead IP. Regulation of breast cancer cell motility by T-cell lymphoma invasion and metastasis-inducing protein. Breast Cancer Res BCR. 2010;12(5):R69.

64. Wolf RM, Draghi N, Liang X, Dai C, Uhrbom L, Eklöf C, et al. p190RhoGAP can act to inhibit PDGF-induced gliomas in mice: a putative tumor suppressor encoded on human Chromosome 19q13.3. Genes Dev. 2003 Feb 15;17(4):476–87.

65. Jiang WG, Watkins G, Lane J, Cunnick GH, Douglas-Jones A, Mokbel K, et al. Prognostic Value of Rho GTPases and Rho Guanine Nucleotide Dissociation Inhibitors in Human Breast Cancers. Clin Cancer Res. 2003 Dec 15;9(17):6432–40.

66. Tapper J, Kettunen E, El-Rifai W, Seppälä M, Andersson LC, Knuutila S. Changes in gene expression during progression of ovarian carcinoma. Cancer Genet Cytogenet. 2001 Jul 1;128(1):1–6.

67. Sahai E, Marshall CJ. ROCK and Dia have opposing effects on adherens junctions downstream of Rho. Nat Cell Biol. 2002 Jun;4(6):408–15.

68. Zhou J, Zhao L-Q, Xiong M-M, Wang X-Q, Yang G-R, Qiu Z-L, et al. Gene expression profiles at different stages of human esophageal squamous cell carcinoma. World J Gastroenterol. 2003 Jan 15;9(1):9–15.

69. Chin VT, Conway J, Nagrial A, Chantrill LA, Chou A, Steinmann A, et al. Targeting the Rho-ROCK pathway to treat pancreatic cancer: The use of unique preclinical models to ascertain the effects on cancer growth and metastasis. J Clin Oncol. 2015 Jan 20;33(3_suppl):312–312.

70. Wong CC-L, Wong C-M, Tung EK-K, Man K, Ng IO-L. Rho-kinase 2 is frequently overexpressed in hepatocellular carcinoma and involved in tumor invasion. Hepatology. 2009 May 1;49(5):1583–94.

71. Nakajima M, Hayashi K, Egi Y, Katayama K, Amano Y, Uehata M, et al. Effect of Wf-536, a novel ROCK inhibitor, against metastasis of B16 melanoma. Cancer Chemother Pharmacol. 2003 Oct 1;52(4):319–24.

72. Ying H, Biroc SL, Li W, Alicke B, Xuan J-A, Pagila R, et al. The Rho kinase inhibitor fasudil inhibits tumor progression in human and rat tumor models. Mol Cancer Ther. 2006 Sep 1;5(9):2158–64.

73. Torka R, Thuma F, Herzog V, Kirfel G. ROCK signaling mediates the adoption of different modes of migration and invasion in human mammary epithelial tumor cells. Exp Cell Res. 2006 Nov 15;312(19):3857–71.

74. Vishnubhotla R, Sun S, Huq J, Bulic M, Ramesh A, Guzman G, et al. ROCK-II mediates colon cancer invasion via regulation of MMP-2 and MMP-13 at the site of invadopodia as revealed by multiphoton imaging. Lab Invest. 2007 Nov;87(11):1149–58.

75. Kinsella BT, Erdman RA, Maltese WA. Carboxyl-terminal isoprenylation of ras-related GTP-binding proteins encoded by rac1, rac2, and ralA. J Biol Chem. 1991 May 25;266(15):9786–94.

76. Golen KL van, Bao L, DiVito MM, Wu Z, Prendergast GC, Merajver SD. Reversion of RhoC GTPase-induced Inflammatory Breast Cancer Phenotype by Treatment with a Farnesyl Transferase Inhibitor 1 Supported by National Cancer Institute Grant R01 CA 77612 (to S. D. M.); Grant DAMD 17-00-1-0345, from The Department of Defense, United States Army Breast Cancer Program (to S. D. M.); and Grant 5T32 CA 09537 (to S. D. M.) and a postdoctoral fellowship (to K. L. v. G.) from the Susan G. Komen Breast Cancer Foundation.1. Mol Cancer Ther. 2002 Jun 1;1(8):575–83.

77. Bustelo XR. A transcriptional cross-talk between RhoA and c-Myc inhibits the RhoA/Rock-dependent cytoskeleton. Small GTPases. 2010;1(1):69–74.

78. Shutes A, Onesto C, Picard V, Leblond B, Schweighoffer F, Der CJ. Specificity and Mechanism of Action of EHT 1864, a Novel Small Molecule Inhibitor of Rac Family Small GTPases. J Biol Chem. 2007 Jul 12;282(49):35666–78.

79. Gao Y, Dickerson JB, Guo F, Zheng J, Zheng Y. Rational design and characterization of a Rac GTPase-specific small molecule inhibitor. Proc Natl Acad Sci U S A. 2004 May 18;101(20):7618–23.

80. Seyfried TN, Huysentruyt LC. On the Origin of Cancer Metastasis. Crit Rev Oncog. 2013;18(1–2):43–73.

81. Gandalovičová A, Rosel D, Fernandes M, Veselý P, Heneberg P, Čermák V, et al. Migrastatics—Anti-metastatic and Anti-invasion Drugs: Promises and Challenges. Trends Cancer. 2017 Jun;3(6):391–406.

82. Housman G, Byler S, Heerboth S, Lapinska K, Longacre M, Snyder N, et al. Drug Resistance in Cancer: An Overview. Cancers. 2014 Sep 5;6(3):1769–92.

83. Price A, Shi Q, Morris D, Wilcox ME, Brasher PMA, Rewcastle NB, et al. Marked Inhibition of Tumor Growth in a Malignant Glioma Tumor Model by a Novel Synthetic Matrix MetalloproteinaseInhibitor AG3340. Clin Cancer Res. 1999 Apr 1;5(4):845–54.

84. Coussens LM, Fingleton B, Matrisian LM. Matrix metalloproteinase inhibitors and cancer: trials and tribulations. Science. 2002 Mar 29;295(5564):2387–92.

85. Paňková K, Rösel D, Novotný M, Brábek J. The molecular mechanisms of transition between mesenchymal and amoeboid invasiveness in tumor cells. Cell Mol Life Sci. 2010 Jan;67(1):63–71.

86. Giannoni E, Taddei ML, Parri M, Bianchini F, Santosuosso M, Grifantini R, et al. EphA2-mediated mesenchymal–amoeboid transition induced by endothelial progenitor cells enhances metastatic spread due to cancer-associated fibroblasts - Springer [Internet]. 2012 [cited 2016 Jan 6]. Available from: http://link.springer.com/article/10.1007/s00109-012-0941-9/fulltext.html

87. Taddei ML, Giannoni E, Comito G, Chiarugi P. Microenvironment and tumor cell plasticity: An easy way out. Cancer Lett. 2013 Nov 28;341(1):80–96.

88. Jacquemet G, Baghirov H, Georgiadou M, Sihto H, Peuhu E, Cettour-Janet P, et al. L-type calcium channels regulate filopodia stability and cancer cell invasion downstream of integrin signalling. Nat Commun. 2016 Dec 2;7:13297.

89. Smith B, Land H. Anti-cancer activity of the cholesterol exporter ABCA1 gene. Cell Rep. 2012 Sep 27;2(3):580–90.

90. Zhao W, Prijic S, Urban BC, Tisza MJ, Zuo Y, Li L, et al. Candidate anti-metastasis drugs suppress the metastatic capacity of breast cancer cells by reducing membrane fluidity. Cancer Res. 2016 Jan 29;canres.1970.2015.

91. Evensen NA, Li J, Yang J, Yu X, Sampson NS, Zucker S, et al. Development of a High-Throughput Three-Dimensional Invasion Assay for Anti-Cancer Drug Discovery. PLOS ONE. 2013 Dec 11;8(12):e82811.

92. Harrison RK. Phase II and phase III failures: 2013–2015. Nat Rev Drug Discov. 2016 Nov 4;15:817.

93. Cheng V, Esteves F, Chakrabarty A, Cockle J, Short S, Brüning-Richardson A. High-content analysis of tumour cell invasion in three-dimensional spheroid assays. Oncoscience. 2015 Jun 14;2(6):596–606.

94. Gladson CL, Prayson RA, Liu W (Michael). The Pathobiology of Glioma Tumors. Annu Rev Pathol. 2010;5:33–50.

95. Louis DN, Perry A, Reifenberger G, von Deimling A, Figarella-Branger D, Cavenee WK, et al. The 2016 World Health Organization Classification of Tumors of the Central Nervous System: a summary. Acta Neuropathol (Berl). 2016 Jun 1;131(6):803–20.

96. KOMORI T. The 2016 WHO Classification of Tumours of the Central Nervous System: The Major Points of Revision. Neurol Med Chir (Tokyo). 2017 Jul;57(7):301–11.

97. Goodenberger ML, Jenkins RB. Genetics of adult glioma. Cancer Genet. 2012 Dec;205(12):613–21.

98. Brain, other CNS and intracranial tumours statistics [Internet]. Cancer Research UK. 2015 [cited 2016 Aug 8]. Available from: http://www.cancerresearchuk.org/health-professional/cancer-statistics/statistics-by-cancer-type/brain-other-cns-and-intracranial-tumours

99. Worldwide data | World Cancer Research Fund International [Internet]. [cited 2016 Aug 8]. Available from: http://www.wcrf.org/int/cancer-facts-figures/worldwide-data

100. Gliomas | Johns Hopkins Medicine Health Library [Internet]. [cited 2016 Aug 8]. Available from: http://www.hopkinsmedicine.org/healthlibrary/conditions/nervous_system_disorders/gliomas_134,22/

101. Holland EC. Glioblastoma multiforme: The terminator. Proc Natl Acad Sci U S A. 2000 Jun 6;97(12):6242–4.

102. Soeda A, Hara A, Kunisada T, Yoshimura S, Iwama T, Park DM. The Evidence of Glioblastoma Heterogeneity. Sci Rep. 2015 Jan 27;5:7979.

103. Sottoriva A, Spiteri I, Piccirillo SGM, Touloumis A, Collins VP, Marioni JC, et al. Intratumor heterogeneity in human glioblastoma reflects cancer evolutionary dynamics. Proc Natl Acad Sci. 2013 May 3;110(10):4009–14.

104. Sampetrean O, Saya H. Characteristics of glioma stem cells. Brain Tumor Pathol. 2013 Apr 13;30(4):209–14.

105. Alves TR, Lima FRS, Kahn SA, Lobo D, Dubois LGF, Soletti R, et al. Glioblastoma cells: A heterogeneous and fatal tumor interacting with the parenchyma. Life Sci. 2011 Oct 10;89(15–16):532–9.

106. Goffart N, Kroonen J, Rogister B. Glioblastoma-Initiating Cells: Relationship with Neural Stem Cells and the Micro-Environment. Cancers. 2013 Aug 14;5(3):1049–71.

107. Saio. Tumor-associated macrophage/microglia infiltration in human gliomas is correlated with MCP-3, but not MCP-1. Int J Oncol [Internet]. 2009 May 7 [cited 2016 Feb 24];34(6). Available from: http://www.spandidos-publications.com/ijo/34/6/1621

108. Nishida N, Yano H, Nishida T, Kamura T, Kojiro M. Angiogenesis in Cancer. Vasc Health Risk Manag. 2006 Sep;2(3):213–9.

109. Calabrese C, Poppleton H, Kocak M, Hogg TL, Fuller C, Hamner B, et al. A Perivascular Niche for Brain Tumor Stem Cells. Cancer Cell. 2007 Jan;11(1):69–82.

110. Brooks MD, Sengupta R, Snyder SC, Rubin JB. Hitting Them Where They Live: Targeting the Glioblastoma Perivascular Stem Cell Niche. Curr Pathobiol Rep. 2013 Jun 1;1(2):101–10.

111. Glioblastoma Multiforme Treatment & Management: Medical Care, Surgical Care, Consultations. 2016 Jun 1 [cited 2016 Jul 6]; Available from: http://emedicine.medscape.com/article/283252-treatment

112. Preusser M, de Ribaupierre S, Wöhrer A, Erridge SC, Hegi M, Weller M, et al. Current concepts and management of glioblastoma. Ann Neurol. 2011 Jul 1;70(1):9–21.

113. Verhaak RGW, Hoadley KA, Purdom E, Wang V, Qi Y, Wilkerson MD, et al. An integrated genomic analysis identifies clinically relevant subtypes of glioblastoma characterized by abnormalities in PDGFRA, IDH1, EGFR and NF1. Cancer Cell. 2010 Jan 19;17(1):98.

114. Olar A, Aldape KD. Using the Molecular Classification of Glioblastoma to Inform Personalized Treatment. J Pathol. 2014 Jan;232(2):165–77.

115. Four Subtypes of Glioblastoma Discovered [Internet]. The Cancer Genome Atlas - National Cancer Institute. [cited 2016 Aug 31]. Available from: http://cancergenome.nih.gov/researchhighlights/researchbriefs/foursubtypes

116. Ridley AJ, Schwartz MA, Burridge K, Firtel RA, Ginsberg MH, Borisy G, et al. Cell Migration: Integrating Signals from Front to Back. Science. 2003 Dec 5;302(5651):1704–9.

117. Peng GE, Wilson SR, Weiner OD. A pharmacological cocktail for arresting actin dynamics in living cells. Mol Biol Cell. 2011 Nov 1;22(21):3986–94.

118. Casella JF, Flanagan MD, Lin S. Cytochalasin D inhibits actin polymerization and induces depolymerization of actin filaments formed during platelet shape change. Nature. 1981 Sep 24;293:302.

119. Coué M, Brenner SL, Spector I, Korn ED. Inhibition of actin polymerization by latrunculin A. FEBS Lett. 1987 Mar 23;213(2):316–8.

120. Holzinger A. Jasplakinolide: An Actin-Specific Reagent that Promotes Actin Polymerization. In: Gavin RH, editor. Cytoskeleton Methods and Protocols [Internet]. Totowa, NJ: Humana Press; 2010 [cited 2018 Oct 11]. p. 71–87. (Methods in Molecular Biology). Available from: https://doi.org/10.1007/978-1-60761-376-3_4

121. Bubb MR, Spector I, Beyer BB, Fosen KM. Effects of Jasplakinolide on the Kinetics of Actin Polymerization AN EXPLANATION FOR CERTAIN IN VIVO OBSERVATIONS. J Biol Chem. 2000 Feb 18;275(7):5163–70.

122. Lodish H, Berk A, Zipursky SL, Matsudaira P, Baltimore D, Darnell J. Myosin: The Actin Motor Protein. Mol Cell Biol 4th Ed [Internet]. 2000 [cited 2018 Oct 11]; Available from: https://www.ncbi.nlm.nih.gov/books/NBK21724/

123. Kovács M, Tóth J, Hetényi C, Málnási-Csizmadia A, Sellers JR. Mechanism of Blebbistatin Inhibition of Myosin II. J Biol Chem. 2004 Aug 20;279(34):35557–63.

124. Svoboda KKH, Moessner P, Field T, Acevedo J. ROCK Inhibitor (Y27632) Increases Apoptosis and Disrupts the Actin Cortical Mat in Embryonic Avian Corneal Epithelium. Dev Dyn Off Publ Am Assoc Anat. 2004 Mar;229(3):579–90.

125. Rasmussen CA, Kaufman PL, Ritch R, Haque R, Brazzell RK, Vittitow JL. Latrunculin B Reduces Intraocular Pressure in Human Ocular Hypertension and Primary Open-Angle Glaucoma. Transl Vis Sci Technol [Internet]. 2014 Sep 3 [cited 2016 Aug 17];3(5). Available from: http://www.ncbi.nlm.nih.gov/pmc/articles/PMC4164113/

126. Tanaka K, Minami H, Kota M, Kuwamura K, Kohmura E. Treatment of cerebral vasospasm with intra-arterial fasudil hydrochloride. Neurosurgery. 2005 Feb;56(2):214–23; discussion 214-223.

127. Liu GJ, Wang ZJ, Wang YF, Xu LL, Wang XL, Liu Y, et al. Systematic assessment and meta-analysis of the efficacy and safety of fasudil in the treatment of cerebral vasospasm in patients with subarachnoid hemorrhage. Eur J Clin Pharmacol. 2012 Feb;68(2):131–9.

128. Hayashi K, Michiue H, Yamada H, Takata K, Nakayama H, Wei F-Y, et al. Fluvoxamine, an anti-depressant, inhibits human glioblastoma invasion by disrupting actin polymerization. Sci Rep. 2016 Mar 18;6:23372.

129. Lehmann KG, Popma JJ, Werner JA, Lansky AJ, Wilensky RL. Vascular remodeling and the local delivery of cytochalasin B after coronary angioplasty in humans. J Am Coll Cardiol. 2000 Mar 1;35(3):583–91.

130. Polychronopoulos P, Magiatis P, Skaltsounis A-L, Myrianthopoulos V, Mikros E, Tarricone A, et al. Structural Basis for the Synthesis of Indirubins as Potent and Selective Inhibitors of Glycogen Synthase Kinase-3 and Cyclin-Dependent Kinases. J Med Chem. 2004 Feb 1;47(4):935–46.

131. Meijer L, Shearer J, Bettayeb K, Ferandin Y. Diversity of the intracellular mechanisms underlying the anti-tumor properties of indirubins. Int Congr Ser. 2007;Complete(1304):60–74.

132. Damiens E, Baratte B, Marie D, Eisenbrand G, Meijer L. Anti-mitotic properties of indirubin-3′-monoxime, a CDK/GSK-3 inhibitor: induction of endoreplication following prophase arrest. Oncogene. 2001 Jun;20(29):3786.

133. Sun T, Rodriguez M, Kim L. Glycogen synthase kinase 3 in the world of cell migration. Dev Growth Differ. 2009 Dec 1;51(9):735–42.

134. Hooper C, Killick R, Lovestone S. The GSK3 hypothesis of Alzheimer's disease. J Neurochem. 2008 Mar;104(6):1433–9.

135. Meijer L, Skaltsounis A-L, Magiatis P, Polychronopoulos P, Knockaert M, Leost M, et al. GSK-3-Selective Inhibitors Derived from Tyrian Purple Indirubins. Chem Biol. 2003 Dec 1;10(12):1255–66.

136. Williams SP, Nowicki MO, Liu F, Press R, Godlewski J, Abdel-Rasoul M, et al. Indirubins Decrease Glioma Invasion by Blocking Migratory Phenotypes in Both the Tumor and Stromal Endothelial Cell Compartments. Cancer Res. 2011 Aug 15;71(16):5374–80.

137. Liu K, Liu K, Li J, Li J, Wu X, Wu X, et al. GSK-3β inhibitor 6-bromo-indirubin-3'-oxime promotes both adhesive activity and drug resistance in colorectal cancer cells. Int J Oncol. 2017 Dec 1;51(6):1821–30.

138. Jope RS. Lithium and GSK-3: one inhibitor, two inhibitory actions, multiple outcomes. Trends Pharmacol Sci. 2003 Sep 1;24(9):441–3.

139. O'Brien WT, Klein PS. Validating GSK3 as an in vivo target of lithium action. Biochem Soc Trans. 2009 Oct;37(Pt 5):1133–8.

140. Patel S, Doble BW, MacAulay K, Sinclair EM, Drucker DJ, Woodgett JR. Tissue-Specific Role of Glycogen Synthase Kinase 3β in Glucose Homeostasis and Insulin Action. Mol Cell Biol. 2008 Oct;28(20):6314–28.

141. Eldar-Finkelman H, Martinez A. GSK-3 Inhibitors: Preclinical and Clinical Focus on CNS. Front Mol Neurosci [Internet]. 2011 Oct 31 [cited 2018 Oct 17];4. Available from: https://www.ncbi.nlm.nih.gov/pmc/articles/PMC3204427/

142. Nunes MA, Viel TA, Buck HS. Microdose lithium treatment stabilized cognitive impairment in patients with Alzheimer's disease. Curr Alzheimer Res. 2013 Jan;10(1):104–7.

143. Forlenza OV, Diniz BS, Radanovic M, Santos FS, Talib LL, Gattaz WF. Disease-modifying properties of long-term lithium treatment for amnestic mild cognitive impairment: randomised controlled trial. Br J Psychiatry J Ment Sci. 2011 May;198(5):351–6.

144. Nowicki MO, Dmitrieva N, Stein AM, Cutter JL, Godlewski J, Saeki Y, et al. Lithium inhibits invasion of glioma cells; possible involvement of glycogen synthase kinase-3. Neuro-Oncol. 2008 Jan 10;10(5):690–9.

145. Phiel CJ, Klein PS. Molecular Targets of Lithium Action. Annu Rev Pharmacol Toxicol. 2001;41(1):789–813.

146. Ishizaki T, Uehata M, Tamechika I, Keel J, Nonomura K, Maekawa M, et al. Pharmacological properties of Y-27632, a specific inhibitor of rho-associated kinases. Mol Pharmacol. 2000 May;57(5):976–83.

147. Paul BZS, Daniel JL, Kunapuli SP. Platelet Shape Change Is Mediated by both Calcium-dependent and -independent Signaling Pathways ROLE OF p160 Rho-ASSOCIATED COILED-COIL-CONTAINING PROTEIN KINASE IN PLATELET SHAPE CHANGE. J Biol Chem. 1999 Jan 10;274(40):28293–300.

148. Klages B, Brandt U, Simon MI, Schultz G, Offermanns S. Activation of G12/G13 results in shape change and Rho/Rho-kinase-mediated myosin light chain phosphorylation in mouse platelets. J Cell Biol. 1999 Feb 22;144(4):745–54.

149. Fu X, Gong MC, Jia T, Somlyo AV, Somlyo AP. The effects of the Rho-kinase inhibitor Y-27632 on arachidonic acid-, GTPγS-, and phorbol ester-induced Ca2+-sensitization of smooth muscle. FEBS Lett. 1998 Nov 27;440(1–2):183–7.

150. Kuwahara K, Saito Y, Nakagawa O, Kishimoto I, Harada M, Ogawa E, et al. The effects of the selective ROCK inhibitor, Y27632, on ET-1-induced hypertrophic response in neonatal rat cardiac myocytes – possible involvement of Rho/ROCK pathway in cardiac muscle cell hypertrophy. FEBS Lett. 1999 Jun 11;452(3):314–8.

151. Itoh K, Yoshioka K, Akedo H, Uehata M, Ishizaki T, Narumiya S. An essential part for Rho–associated kinase in the transcellular invasion of tumor cells. Nat Med. 1999 Feb;5(2):221–5.

152. Liu S, Goldstein RH, Scepansky EM, Rosenblatt M. Inhibition of Rho-Associated Kinase Signaling Prevents Breast Cancer Metastasis to Human Bone. Cancer Res. 2009 Nov 15;69(22):8742–51.

153. Jeong KJ, Park SY, Cho KH, Sohn JS, Lee J, Kim YK, et al. The Rho/ROCK pathway for lysophosphatidic acid-induced proteolytic enzyme

expression and ovarian cancer cell invasion. Oncogene. 2012 Sep;31(39):4279–89.

154. de Toledo M, Anguille C, Roger L, Roux P, Gadea G. Cooperative Anti-Invasive Effect of Cdc42/Rac1 Activation and ROCK Inhibition in SW620 Colorectal Cancer Cells with Elevated Blebbing Activity. PLoS ONE [Internet]. 2012 Nov 7 [cited 2018 Oct 17];7(11). Available from: https://www.ncbi.nlm.nih.gov/pmc/articles/PMC3492328/

155. Mikuriya Y, Tashiro H, Kuroda S, Nambu J, Kobayashi T, Amano H, et al. Fatty liver creates a pro-metastatic microenvironment for hepatocellular carcinoma through activation of hepatic stellate cells. Int J Cancer. 2015 Feb 15;136(4):E3–13.

156. Ivkovic S, Beadle C, Noticewala S, Massey SC, Swanson KR, Toro LN, et al. Direct inhibition of myosin II effectively blocks glioma invasion in the presence of multiple motogens. Mol Biol Cell. 2012 Feb 15;23(4):533–42.

157. Niego B, Lee N, Larsson P, De Silva TM, Au AE-L, McCutcheon F, et al. Selective inhibition of brain endothelial Rho-kinase-2 provides optimal protection of an in vitro blood-brain barrier from tissue-type plasminogen activator and plasmin. PLoS ONE [Internet]. 2017 May 16 [cited 2018 Nov 6];12(5). Available from: https://www.ncbi.nlm.nih.gov/pmc/articles/PMC5433693/

158. Hong J. Natural product diversity and its role in chemical biology and drug discovery. Curr Opin Chem Biol. 2011 Jun;15(3):350.

159. Spector I, Shochet N, Kashman Y, Groweiss A. Latrunculins: novel marine toxins that disrupt microfilament organization in cultured cells. Science. 1983 Feb 4;219(4584):493.

160. Ayscough KR, Stryker J, Pokala N, Sanders M, Crews P, Drubin DG. High Rates of Actin Filament Turnover in Budding Yeast and Roles for Actin in Establishment and Maintenance of Cell Polarity Revealed Using the Actin Inhibitor Latrunculin-A. J Cell Biol. 1997 Apr 21;137(2):399–416.

161. Belmont LD, Patterson GM, Drubin DG. New actin mutants allow further characterization of the nucleotide binding cleft and drug binding sites. J Cell Sci. 1999 May 1;112(9):1325.

162. Oocyte Vitrification Aided With Latrunculin A - Full Text View - ClinicalTrials.gov [Internet]. [cited 2018 Oct 18]. Available from: https://clinicaltrials.gov/ct2/show/NCT03678571

163. Bogliolo L, Murrone O, Piccinini M, Ariu F, Ledda S, Tilocca S, et al. Evaluation of the impact of vitrification on the actin cytoskeleton of in vitro matured ovine oocytes by means of Raman microspectroscopy. J Assist Reprod Genet. 2015 Feb;32(2):185–93.

164. Terashita Y, Yamagata K, Tokoro M, Itoi F, Wakayama S, Li C, et al. Latrunculin A Treatment Prevents Abnormal Chromosome Segregation

for Successful Development of Cloned Embryos. PLOS ONE. 2013 Oct 24;8(10):e78380.

165. Konishi H, Kikuchi S, Ochiai T, Ikoma H, Kubota T, Ichikawa D, et al. Latrunculin A Has a Strong Anticancer Effect in a Peritoneal Dissemination Model of Human Gastric Cancer in Mice. Anticancer Res. 2009 Jan 6;29(6):2091–7.

166. Monzo P, Chong YK, Guetta-Terrier C, Krishnasamy A, Sathe SR, Yim EKF, et al. Mechanical confinement triggers glioma linear migration dependent on formin FHOD3. Mol Biol Cell. 2016 Feb 24;27(8):1246–61.

167. Evelyn CR, Wade SM, Wang Q, Wu M, Iñiguez-Lluhí JA, Merajver SD, et al. CCG-1423: a small-molecule inhibitor of RhoA transcriptional signaling. Mol Cancer Ther. 2007 Aug;6(8):2249–60.

168. Lau LF. CCN1/CYR61: The Very Model of a Modern Matricellular Protein. Cell Mol Life Sci CMLS. 2011 Oct;68(19):3149–63.

169. Minami T, Kuwahara K, Nakagawa Y, Takaoka M, Kinoshita H, Nakao K, et al. Reciprocal expression of MRTF-A and myocardin is crucial for pathological vascular remodelling in mice. EMBO J. 2012 Nov 28;31(23):4428–40.

170. Haak AJ, Tsou P-S, Amin MA, Ruth JH, Campbell P, Fox DA, et al. Targeting the Myofibroblast Genetic Switch: Inhibitors of Myocardin-Related Transcription Factor/Serum Response Factor–Regulated Gene Transcription Prevent Fibrosis in a Murine Model of Skin Injury. J Pharmacol Exp Ther. 2014 Jun;349(3):480–6.

171. Sisson TH, Ajayi IO, Subbotina N, Dodi AE, Rodansky ES, Chibucos LN, et al. Inhibition of Myocardin-Related Transcription Factor/Serum Response Factor Signaling Decreases Lung Fibrosis and Promotes Mesenchymal Cell Apoptosis. Am J Pathol. 2015 Apr;185(4):969–86.

172. Yu-Wai-Man C, Spencer-Dene B, Lee RMH, Hutchings K, Lisabeth EM, Treisman R, et al. Local delivery of novel MRTF/SRF inhibitors prevents scar tissue formation in a preclinical model of fibrosis. Sci Rep [Internet]. 2017 Mar 31 [cited 2018 Oct 18];7. Available from: https://www.ncbi.nlm.nih.gov/pmc/articles/PMC5428058/

173. Evelyn C, Lisabeth E, Wade S, Haak A, Johnson C, Lawlor E, et al. Small-Molecule Inhibition of Rho/MKL/SRF Transcription in Prostate Cancer Cells: Modulation of Cell Cycle, ER Stress, and Metastasis Gene Networks. Microarrays. 2016 May 28;5(2):13.

174. Liu G, Yan T, Li X, Sun J, Zhang B, Wang H, et al. Daam1 activates RhoA to regulate Wnt5a-induced glioblastoma cell invasion. Oncol Rep. 2018 Feb;39(2):465–72.

175. Baker BM, Chen CS. Deconstructing the third dimension – how 3D culture microenvironments alter cellular cues. J Cell Sci. 2012 Jul 1;125(13):3015–24.

176. Bradbury P, Fabry B, O'Neill GM. Occupy tissue. Cell Adhes Migr. 2012 Sep 20;6(5):424–520.

177. Breslin S, O'Driscoll L. The relevance of using 3D cell cultures, in addition to 2D monolayer cultures, when evaluating breast cancer drug sensitivity and resistance. Oncotarget. 2016 Jun 10;7(29):45745–56.

178. Dai X, Cheng H, Bai Z, Li J. Breast Cancer Cell Line Classification and Its Relevance with Breast Tumor Subtyping. J Cancer. 2017 Sep 12;8(16):3131–41.

179. Duval K, Grover H, Han L-H, Mou Y, Pegoraro AF, Fredberg J, et al. Modeling Physiological Events in 2D vs. 3D Cell Culture. Physiology. 2017 Jul;32(4):266–77.

180. Pontén J. Neoplastic Human Glia Cells in Culture. In: Fogh J, editor. Human Tumor Cells in Vitro [Internet]. Boston, MA: Springer US; 1975. p. 175–206. Available from: http://dx.doi.org/10.1007/978-1-4757-1647-4_7

181. Cockle JV, Picton S, Levesley J, Ilett E, Carcaboso AM, Short S, et al. Cell migration in paediatric glioma; characterisation and potential therapeutic targeting. Br J Cancer. 2015 Feb 17;112(4):693–703.

182. Torsvik A, Stieber D, Enger PØ, Golebiewska A, Molven A, Svendsen A, et al. U-251 revisited: genetic drift and phenotypic consequences of long-term cultures of glioblastoma cells. Cancer Med. 2014 Aug;3(4):812–24.

183. Allen M, Bjerke M, Edlund H, Nelander S, Westermark B. Origin of the U87MG glioma cell line: Good news and bad news. Sci Transl Med. 2016 Aug 31;8(354):354re3-354re3.

184. Zhong J, Paul A, Kellie SJ, O'Neill GM, Zhong J, Paul A, et al. Mesenchymal Migration as a Therapeutic Target in Glioblastoma, Mesenchymal Migration as a Therapeutic Target in Glioblastoma. J Oncol J Oncol. 2010 Jun 21;2010, 2010:e430142.

185. Petrie RJ, Doyle AD, Yamada KM. Random versus directionally persistent cell migration. Nat Rev Mol Cell Biol. 2009 Aug;10(8):538–49.

186. Motaln H, Koren A, Gruden K, Ramšak Ž, Schichor C, Lah TT. Heterogeneous glioblastoma cell cross-talk promotes phenotype alterations and enhanced drug resistance. Oncotarget. 2015 Oct 20;6(38):40998–1017.

187. Zanoni M, Piccinini F, Arienti C, Zamagni A, Santi S, Polico R, et al. 3D tumor spheroid models for *in vitro* therapeutic screening: a systematic approach to enhance the biological relevance of data obtained. Sci Rep. 2016 Jan 11;6:19103.

188. Soroceanu L, Manning TJ, Sontheimer H. Modulation of Glioma Cell Migration and Invasion Using Cl− and K+ Ion Channel Blockers. J Neurosci. 1999 Jul 15;19(14):5942–54.

189. Cuddapah VA, Robel S, Watkins S, Sontheimer H. A neurocentric perspective on glioma invasion. Nat Rev Neurosci. 2014 Jun 20;15(7):455–65.

190. Three Dimensional (3D) Cell Culture Versus Two Dimensional (2D) Cell Culture [Internet]. [cited 2016 Aug 9]. Available from: http://www.microtissues.com/three_dimensional_3d_cell_culture_versus_two_dimensional_2d_cell_culture.htm

191. Edmondson R, Broglie JJ, Adcock AF, Yang L. Three-Dimensional Cell Culture Systems and Their Applications in Drug Discovery and Cell-Based Biosensors. Assay Drug Dev Technol. 2014 May 1;12(4):207–18.

192. Bokhari M, Carnachan RJ, Cameron NR, Przyborski SA. Culture of HepG2 liver cells on three dimensional polystyrene scaffolds enhances cell structure and function during toxicological challenge. J Anat. 2007;211(4):567–76.

193. Achilli T-M, McCalla S, Meyer J, Tripathi A, Morgan JR. Multilayer Spheroids To Quantify Drug Uptake and Diffusion in 3D. Mol Pharm. 2014 Jul 7;11(7):2071–81.

194. Gomez-Roman N, Stevenson K, Gilmour L, Hamilton G, Chalmers AJ. A novel 3D human glioblastoma cell culture system for modeling drug and radiation responses. Neuro-Oncol. 2017 Feb;19(2):229–41.

195. Nelson MT, Short A, Cole SL, Gross AC, Winter J, Eubank TD, et al. Preferential, enhanced breast cancer cell migration on biomimetic electrospun nanofiber ‘cell highways’. BMC Cancer. 2014;14:825.

196. Devreotes P, Horwitz AR. Signaling Networks that Regulate Cell Migration. Cold Spring Harb Perspect Biol. 2015 Jan 8;7(8):a005959.

197. Rikitake Y, Takai Y. Chapter three - Directional Cell Migration: Regulation by Small G Proteins, Nectin-like Molecule-5, and Afadin. In: Jeon KW, editor. International Review of Cell and Molecular Biology [Internet]. Academic Press; 2011 [cited 2019 Mar 21]. p. 97–143. Available from: http://www.sciencedirect.com/science/article/pii/B9780123860439000037

198. DuChez BJ, Doyle AD, Dimitriadis EK, Yamada KM. Durotaxis by Human Cancer Cells. Biophys J. 2019 Feb 19;116(4):670–83.

199. Li S, Butler P, Wang Y, Hu Y, Han DC, Usami S, et al. The role of the dynamics of focal adhesion kinase in the mechanotaxis of endothelial cells. Proc Natl Acad Sci. 2002 Mar 19;99(6):3546–51.

200. Mycielska ME, Djamgoz MBA. Cellular mechanisms of direct-current electric field effects: galvanotaxis and metastatic disease. J Cell Sci. 2004 Apr 1;117(9):1631–9.

201. Valenta T, Hausmann G, Basler K. The many faces and functions of β-catenin. EMBO J. 2012 Jun 13;31(12):2714–36.

202. Komiya Y, Habas R. Wnt signal transduction pathways. Organogenesis. 2008;4(2):68–75.

203. Qi S, Liu Y. Differences in protein expression between the u251 and u87 cell lines. Turk Neurosurg [Internet]. 2016 [cited 2019 Jun 5]; Available from: http://www.turkishneurosurgery.org.tr/summary_en_doi.php3?doi=10.5137/1019-5149.JTN.17746-16.1

204. Tilson SG, Haley EM, Triantafillu UL, Dozier DA, Langford CP, Gillespie GY, et al. ROCK Inhibition Facilitates In Vitro Expansion of Glioblastoma Stem-Like Cells. PLoS ONE [Internet]. 2015 Jul 13 [cited 2016 Aug 10];10(7). Available from: http://www.ncbi.nlm.nih.gov/pmc/articles/PMC4500389/

205. Iwadate Y, Yumura S. Actin-based propulsive forces and myosin-II-based contractile forces in migrating Dictyostelium cells. J Cell Sci. 2008 Apr 15;121(Pt 8):1314–24.

206. Li S, Wang C, Dai Y, Yang Y, Pan H, Zhong J, et al. The stimulatory effect of ROCK inhibitor on bovine corneal endothelial cells. Tissue Cell. 2013 Dec;45(6):387–96.

207. Guo Y, Liu Q, Yang Y, Guo X, Lian R, Li S, et al. The Effects of ROCK Inhibitor Y-27632 on Injectable Spheroids of Bovine Corneal Endothelial Cells. Cell Reprogramming. 2015 Feb 1;17(1):77–87.

208. Latrunculin A (CAS 76343-93-6) [Internet]. [cited 2016 Aug 11]. Available from: https://www.caymanchem.com/product/10010630

209. Sugiarto S, Persson AI, Munoz EG, Waldhuber M, Lamagna C, Andor N, et al. Asymmetry-defective oligodendrocyte progenitors are glioma precursors. Cancer Cell. 2011 Sep 13;20(3):328–40.

210. Al-Mayhani MTF, Grenfell R, Narita M, Piccirillo S, Kenney-Herbert E, Fawcett JW, et al. NG2 expression in glioblastoma identifies an actively proliferating population with an aggressive molecular signature. Neuro-Oncol. 2011 Aug;13(8):830–45.

211. Young N, Van Brocklyn JR. Roles of Sphingosine-1-Phosphate (S1P) Receptors in Malignant Behavior of Glioma Cells. Differential Effects of S1P2 on Cell Migration and Invasiveness. Exp Cell Res. 2007 May 1;313(8):1615–27.

212. Watanabe B, Minami S, Ishida H, Yoshioka R, Nakagawa Y, Morita T, et al. Stereospecific Inhibitory Effects of CCG-1423 on the Cellular Events Mediated by Myocardin-Related Transcription Factor A. PLOS ONE. 2015 Aug 21;10(8):e0136242.

213. Hayashi K, Watanabe B, Nakagawa Y, Minami S, Morita T. RPEL Proteins Are the Molecular Targets for CCG-1423, an Inhibitor of Rho Signaling. PLOS ONE. 2014 Feb 18;9(2):e89016.

214. Zhao X, Ding EY, Yu O, Xiang SY, Tan-Sah VP, Yung BS, et al. Induction of the matricellular protein CCN1 through RhoA and MRTF-A contributes to ischemic cardioprotection. J Mol Cell Cardiol. 2014 Oct;75:152–61.

215. Chen Y, Du X-Y. Functional properties and intracellular signaling of CCN1/Cyr61. J Cell Biochem. 2007;100(6):1337–45.

216. Haseley A, Boone S, Wojton J, Yu L, Yoo JY, Yu J, et al. Extracellular matrix protein CCN1 limits oncolytic efficacy in glioma. Cancer Res. 2012 Mar 15;72(6):1353–62.

217. Kutwin M, Sawosz E, Jaworski S, Wierzbicki M, Strojny B, Grodzik M, et al. Assessment of the proliferation status of glioblastoma cell and tumour tissue after nanoplatinum treatment. PLOS ONE. 2017 May 31;12(5):e0178277.

218. Taddei ML, Giannoni E, Morandi A, Ippolito L, Ramazzotti M, Callari M, et al. Mesenchymal to amoeboid transition is associated with stem-like features of melanoma cells. Cell Commun Signal CCS. 2014 Apr 1;12:24.

219. Harada T, Swift J, Irianto J, Shin J-W, Spinler KR, Athirasala A, et al. Nuclear lamin stiffness is a barrier to 3D migration, but softness can limit survival. J Cell Biol. 2014 Mar 3;204(5):669–82.

220. Aznar S, Fernández-Valerón P, Espina C, Lacal JC. Rho GTPases: potential candidates for anticancer therapy. Cancer Lett. 2004 Apr 8;206(2):181–91.

221. Jiang L, Wen J, Luo W. Rho‐associated kinase inhibitor, Y‐27632, inhibits the invasion and proliferation of T24 and 5367 bladder cancer cells. Mol Med Rep. 2015 Nov 1;12(5):7526–30.

222. Vishnubhotla R, Bharadwaj S, Sun S, Metlushko V, Glover SC. Treatment with Y-27632, a ROCK Inhibitor, Increases the Proinvasive Nature of SW620 Cells on 3D Collagen Type 1 Matrix [Internet]. International Journal of Cell Biology. 2012 [cited 2019 Jan 7]. Available from: https://www.hindawi.com/journals/ijcb/2012/259142/

223. Suzuki N, Nakamura S, Mano H, Kozasa T. Gα12 activates Rho GTPase through tyrosine-phosphorylated leukemia-associated RhoGEF. Proc Natl Acad Sci U S A. 2003 Jan 21;100(2):733–8.

224. An J, Nagaishi T, Watabe T, Naruse TK, Watanabe M, Kimura A. MKL1 expressed in macrophages contributes to the development of murine colitis. Sci Rep. 2017 Oct 20;7(1):13650.

225. Bell JL, Haak AJ, Wade SM, Kirchhoff PD, Neubig RR, Larsen SD. Optimization of novel nipecotic bis(amide) inhibitors of the Rho/MKL1/SRF transcriptional pathway as potential anti-metastasis agents. Bioorg Med Chem Lett. 2013 Jul 1;23(13):3826–32.

226. Duggirala A, Kimura TE, Sala-Newby GB, Johnson JL, Wu Y-J, Newby AC, et al. cAMP-induced actin cytoskeleton remodelling inhibits MKL1-dependent expression of the chemotactic and pro-proliferative factor, CCN1. J Mol Cell Cardiol. 2015 Feb 1;79:157–68.

227. Brigstock DR, Goldschmeding R, Katsube K, Lam SC-T, Lau LF, Lyons K, et al. Proposal for a unified CCN nomenclature. Mol Pathol. 2003 Apr;56(2):127–8.

228. Yang GP, Lau LF. Cyr61, product of a growth factor-inducible immediate early gene, is associated with the extracellular matrix and the cell surface. Cell Growth Differ Mol Biol J Am Assoc Cancer Res. 1991 Jul;2(7):351–7.

229. Kireeva ML, MO FE, Yang GP, Lau LF. Cyr61, a product of a growth factor-inducible immediate-early gene, promotes cell proliferation, migration, and adhesion. Mol Cell Biol. 1996 Apr;16(4):1326–34.

230. Chen C-C, Chen N, Lau LF. The Angiogenic Factors Cyr61 and Connective Tissue Growth Factor Induce Adhesive Signaling in Primary Human Skin Fibroblasts. J Biol Chem. 2001 Mar 30;276(13):10443–52.

231. Kassis JN, Virador VM, Guancial EA, Kimm D, Ho AS, Mishra M, et al. Genomic and phenotypic analysis reveals a key role for CCN1 (CYR61) in BAG3—modulated adhesion and invasion. J Pathol. 2009;218(4):495–504.

232. Lin B-R, Chang C-C, Chen L-R, Wu M-H, Wang M-Y, Kuo I-H, et al. Cysteine-Rich 61 (CCN1) Enhances Chemotactic Migration, Transendothelial Cell Migration, and Intravasation by Concomitantly Up-Regulating Chemokine Receptor 1 and 2. Mol Cancer Res. 2007 Nov 1;5(11):1111–23.

233. Sun Z-J, Wang Y, Cai Z, Chen P-P, Tong X-J, Xie D. Involvement of Cyr61 in growth, migration, and metastasis of prostate cancer cells. Br J Cancer. 2008 Nov 4;99(10):1656–67.

234. Ho H-H, Chang C-S, Ho W-C, Liao S-Y, Wu C-H, Wang C-J. Anti-metastasis effects of gallic acid on gastric cancer cells involves inhibition of NF-κB activity and downregulation of PI3K/AKT/small GTPase signals. Food Chem Toxicol. 2010 Aug 1;48(8):2508–16.

235. Wang X, Deng Y, Mao Z, Ma X, Fan X, Cui L, et al. CCN1 promotes tumorigenicity through Rac1/Akt/NF-κB signaling pathway in pancreatic cancer. Tumor Biol. 2012 Oct 1;33(5):1745–58.

236. Sanz-Moreno V. Tumour Invasion: A New Twist on Rac-Driven Mesenchymal Migration. Curr Biol. 2012 Jun 5;22(11):R449–51.

237. Sanz-Moreno V, Gadea G, Ahn J, Paterson H, Marra P, Pinner S, et al. Rac Activation and Inactivation Control Plasticity of Tumor Cell Movement. Cell. 2008 Oct 31;135(3):510–23.

238. Babic AM, Kireeva ML, Kolesnikova TV, Lau LF. CYR61, a product of a growth factor-inducible immediate early gene, promotes angiogenesis and tumor growth. Proc Natl Acad Sci U S A. 1998 May 26;95(11):6355–60.

239. Gery S, Xie D, Yin D, Gabra H, Miller C, Wang H, et al. Ovarian Carcinomas: CCN Genes Are Aberrantly Expressed and CCN1 Promotes Proliferation of these Cells. Clin Cancer Res. 2005 Oct 15;11(20):7243–54.

240. Xie D, Miller CW, O'Kelly J, Nakachi K, Sakashita A, Said JW, et al. Breast Cancer Cyr61 IS OVEREXPRESSED, ESTROGEN-INDUCIBLE, AND ASSOCIATED WITH MORE ADVANCED DISEASE. J Biol Chem. 2001 Apr 27;276(17):14187–94.

241. Kok S-H, Chang H-H, Tsai J-Y, Hung H-C, Lin C-Y, Chiang C-P, et al. Expression of Cyr61 (CCN1) in human oral squamous cell carcinoma: An independent marker for poor prognosis. Head Neck. 2010;32(12):1665–73.

242. Haque I, Mehta S, Majumder M, Dhar K, De A, McGregor D, et al. Cyr61/CCN1 signaling is critical for epithelial-mesenchymal transition and stemness and promotes pancreatic carcinogenesis. Mol Cancer. 2011 Jan 13;10:8.

243. Goodwin CR, Lal B, Zhou X, Ho S, Xia S, Taeger A, et al. Cyr61 mediates HGF-dependent tumor cell growth, migration and Akt activation. Cancer Res. 2010 Apr 1;70(7):2932–41.

244. D'Antonio KB, Toubaji A, Albadine R, Mondul AM, Platz EA, Netto GJ, et al. Extracellular Matrix Associated Protein CYR61 is Linked to Prostate Cancer Development. J Urol. 2010 Apr;183(4):1604–10.

245. Tsai M-S, Hornby AE, Lakins J, Lupu R. Expression and Function of CYR61, an Angiogenic Factor, in Breast Cancer Cell Lines and Tumor Biopsies. Cancer Res. 2000 Oct 15;60(20):5603–7.

246. Lin M-T, Chang C-C, Chen S-T, Chang H-L, Su J-L, Chau Y-P, et al. Cyr61 Expression Confers Resistance to Apoptosis in Breast Cancer MCF-7 Cells by a Mechanism of NF-κB-dependent XIAP Up-Regulation. J Biol Chem. 2004 Apr 6;279(23):24015–23.

247. Tsai M-S, Bogart DF, Castañeda JM, Li P, Lupu R. Cyr61 promotes breast tumorigenesis and cancer progression. Oncogene. 2002 Nov;21(53):8178–85.

248. Menendez JA, Vellon L, Mehmi I, Teng PK, Griggs DW, Lupu R. A novel CYR61-triggered 'CYR61-$\alpha_v\beta_3$ integrin loop' regulates breast cancer cell survival and chemosensitivity through activation of ERK1/ERK2 MAPK signaling pathway. Oncogene. 2005 Jan;24(5):761–79.

249. Vellon L, Menendez JA, Lupu R. $\alpha_V\beta_3$ integrin regulates heregulin (HRG)-induced cell proliferation and survival in breast cancer. Oncogene. 2005 May;24(23):3759–73.

250. Todorovicç V, Chen C-C, Hay N, Lau LF. The matrix protein CCN1 (CYR61) induces apoptosis in fibroblasts. J Cell Biol. 2005 Nov 7;171(3):559–68.

251. Schmitt CA. Senescence, apoptosis and therapy — cutting the lifelines of cancer. Nat Rev Cancer. 2003 Apr;3(4):286–95.

252. Franzen CA, Chen C-C, Todorović V, Juric V, Monzon RI, Lau LF. The Matrix Protein CCN1 is Critical for Prostate Carcinoma Cell Proliferation and TRAIL-Induced Apoptosis. Mol Cancer Res MCR. 2009 Jul;7(7):1045–55.

253. Lv H, Fan E, Sun S, Ma X, Zhang X, Han DMK, et al. Cyr61 is up-regulated in prostate cancer and associated with the p53 gene status. J Cell Biochem. 2009;106(4):738–44.

254. Xie D, Yin D, Tong X, O'Kelly J, Mori A, Miller C, et al. Cyr61 Is Overexpressed in Gliomas and Involved in Integrin-Linked Kinase-Mediated Akt and β-Catenin-TCF/Lef Signaling Pathways. Cancer Res. 2004 Mar 15;64(6):1987–96.

255. Shimizu T, Kagawa T, Inoue T, Nonaka A, Takada S, Aburatani H, et al. Stabilized β-Catenin Functions through TCF/LEF Proteins and the Notch/RBP-Jκ Complex To Promote Proliferation and Suppress Differentiation of Neural Precursor Cells. Mol Cell Biol. 2008 Dec 15;28(24):7427–41.

256. Novak A, Hsu S-C, Leung-Hagesteijn C, Radeva G, Papkoff J, Montesano R, et al. Cell adhesion and the integrin-linked kinase regulate the LEF-1 and β-catenin signaling pathways. Proc Natl Acad Sci U S A. 1998 Apr 14;95(8):4374–9.

257. Polakis P. Wnt signaling and cancer. Genes Dev. 2000 Jan 8;14(15):1837–51.

258. He T-C, Sparks AB, Rago C, Hermeking H, Zawel L, Costa LT da, et al. Identification of c-MYC as a Target of the APC Pathway. Science. 1998 Sep 4;281(5382):1509–12.

259. Rimerman RA, Gellert-Randleman A, Diehl JA. Wnt1 and MEK1 Cooperate to Promote Cyclin D1 Accumulation and Cellular Transformation. J Biol Chem. 2000 Dec 5;275(19):14736–42.

260. Mann B, Gelos M, Siedow A, Hanski ML, Gratchev A, Ilyas M, et al. Target genes of β-catenin–T cell-factor/lymphoid-enhancer-factor signaling in human colorectal carcinomas. Proc Natl Acad Sci U S A. 1999 Feb 16;96(4):1603–8.

261. Laterra J, Rosen E, Nam M, Ranganathan S, Fielding K, Johnston P. Scatter Factor/Hepatocyte Growth Factor Expression Enhances Human Glioblastoma Tumorigenicity and Growth. Biochem Biophys Res Commun. 1997 Jun;235(3):743–7.

262. Walter KA, Hossain MA, Luddy C, Goel N, Reznik TE, Laterra J. Scatter Factor/Hepatocyte Growth Factor Stimulation of Glioblastoma Cell Cycle Progression through G1 Is c-Myc Dependent and Independent of p27 Suppression, Cdk2 Activation, or E2F1-Dependent Transcription. Mol Cell Biol. 2002 Apr;22(8):2703–15.

263. Lamszus K, Schmidt NO, Jin L, Laterra J, Zagzag D, Way D, et al. Scatter factor promotes motility of human glioma and neuromicrovascular endothelial cells. Int J Cancer. 1998;75(1):19–28.

264. Lamszus K, Laterra J, Westphal M, Rosen EM. Scatter factor/hepatocyte growth factor (SF/HGF) content and function in human gliomas. Int J Dev Neurosci. 1999 Aug 1;17(5):517–30.

265. Birchmeier C, Birchmeier W, Gherardi E, Vande Woude GF. Met, metastasis, motility and more. Nat Rev Mol Cell Biol. 2003 Dec;4(12):915–25.

266. The Cancer Genome Atlas Home Page [Internet]. The Cancer Genome Atlas - National Cancer Institute. 2011 [cited 2019 Feb 4]. Available from: https://cancergenome.nih.gov/

267. Gusev Y, Bhuvaneshwar K, Song L, Zenklusen J-C, Fine H, Madhavan S. The REMBRANDT study, a large collection of genomic data from brain cancer patients. Sci Data. 2018 Aug 14;5:180158.

268. Haglund C, Aleskog A, Nygren P, Gullbo J, Höglund M, Wickström M, et al. In vitro evaluation of clinical activity and toxicity of anticancer drugs using tumor cells from patients and cells representing normal tissues. Cancer Chemother Pharmacol. 2012 Mar;69(3):697–707.

269. Jardim DL, Groves ES, Breitfeld PP, Kurzrock R. Factors associated with failure of oncology drugs in late-stage clinical development: A systematic review. Cancer Treat Rev. 2017 Jan 1;52:12–21.

270. Baumann K. Moving in 3D. Nat Rev Mol Cell Biol. 2010 Jun 9;11:465.

271. York AG, Chandris P, Nogare DD, Head J, Wawrzusin P, Fischer RS, et al. Instant super-resolution imaging in live cells and embryos via analog image processing. Nat Methods. 2013 Nov;10(11):1122–6.

272. Hell SW, Wichmann J. Breaking the diffraction resolution limit by stimulated emission: stimulated-emission-depletion fluorescence microscopy. Opt Lett. 1994 Jun;19(11):780–782.

273. Gustafsson MGL, Shao L, Carlton PM, Wang CJR, Golubovskaya IN, Cande WZ, et al. Three-Dimensional Resolution Doubling in Wide-Field Fluorescence Microscopy by Structured Illumination. Biophys J. 2008 Jun 15;94(12):4957–70.

274. Curd A, Cleasby A, Makowska K, York A, Shroff H, Peckham M. Construction of an instant structured illumination microscope. Methods San Diego Calif. 2015 Oct 15;88:37–47.

275. York AG, Parekh SH, Nogare DD, Fischer RS, Temprine K, Mione M, et al. Resolution doubling in live, multicellular organisms via multifocal structured illumination microscopy. Nat Methods. 2012 Jul;9(7):749–54.

276. Riss TL, Moravec RA, Niles AL, Duellman S, Benink HA, Worzella TJ, et al. Cell Viability Assays. In: Sittampalam GS, Coussens NP, Brimacombe K, Grossman A, Arkin M, Auld D, et al., editors. Assay Guidance Manual [Internet]. Bethesda (MD): Eli Lilly & Company and the National Center for Advancing Translational Sciences; 2004 [cited 2019 Jan 22]. Available from: http://www.ncbi.nlm.nih.gov/books/NBK144065/

277. Ridley AJ. Rho GTPase signalling in cell migration. Curr Opin Cell Biol. 2015 Oct 1;36:103–12.

278. Tal O, Lim HY, Gurevich I, Milo I, Shipony Z, Ng LG, et al. DC mobilization from the skin requires docking to immobilized CCL21 on lymphatic endothelium and intralymphatic crawling. J Exp Med. 2011 Sep 26;208(10):2141–53.

279. Lawson CD, Burridge K. The on-off relationship of Rho and Rac during integrin-mediated adhesion and cell migration. Small GTPases. 2014 Jan 1;5(1):e27958.

280. Kiosses WB, Shattil SJ, Pampori N, Schwartz MA. Rac recruits high-affinity integrin αvβ3 to lamellipodia in endothelial cell migration. Nat Cell Biol. 2001 Mar;3(3):316–20.

281. Ruprecht V, Wieser S, Callan-Jones A, Smutny M, Morita H, Sako K, et al. Cortical Contractility Triggers a Stochastic Switch to Fast Amoeboid Cell Motility. Cell. 2015 Feb 12;160(4):673–85.

282. Charras G, Paluch E. Blebs lead the way: how to migrate without lamellipodia. Nat Rev Mol Cell Biol. 2008 Jul 16;9:730.

283. Wolf K. Compensation mechanism in tumor cell migration: mesenchymal-amoeboid transition after blocking of pericellular proteolysis. J Cell Biol. 2003 Jan 21;160(2):267–77.

284. Holloway SE, Beck AW, Girard L, Jaber MR, Barnett CC, Brekken RA, et al. Increased expression of Cyr61 (CCN1) identified in peritoneal metastases from human pancreatic cancer. J Am Coll Surg. 2005 Mar 1;200(3):371–7.

285. Rae Buchberger A, DeLaney K, Johnson J, Li L. Mass Spectrometry Imaging: A Review of Emerging Advancements and Future Insights. Anal Chem. 2018 Jan 2;90(1):240–65.

286. Miyamoto S, Hsu C-C, Hamm G, Darshi M, Diamond-Stanic M, Declèves A-E, et al. Mass Spectrometry Imaging Reveals Elevated Glomerular ATP/AMP in Diabetes/obesity and Identifies Sphingomyelin as a Possible Mediator. EBioMedicine. 2016 Mar 28;7:121–34.

287. Bai H, Wang S, Liu J, Gao D, Jiang Y, Liu H, et al. Localization of ginsenosides in Panax ginseng with different age by matrix-assisted laser-desorption/ionization time-of-flight mass spectrometry imaging. J Chromatogr B. 2016 Jul 15;1026:263–71.

288. Chen B, Lietz CB, Li L. In Situ Characterization of Proteins Using Laserspray Ionization on a High-Performance MALDI-LTQ-Orbitrap Mass Spectrometer. J Am Soc Mass Spectrom. 2014 Dec;25(12):2177–80.

289. Gessel M, Spraggins JM, Voziyan P, Hudson BG, Caprioli RM. Decellularization of intact tissue enables MALDI imaging mass spectrometry analysis of the extracellular matrix. J Mass Spectrom JMS. 2015 Nov;50(11):1288–93.

290. Škrášková K, Claude E, Jones EA, Towers M, Ellis SR, Heeren RMA. Enhanced capabilities for imaging gangliosides in murine brain with matrix-assisted laser desorption/ionization and desorption electrospray ionization mass spectrometry coupled to ion mobility separation. Methods. 2016 Jul 15;104:69–78.

291. Hall Z, Chu Y, Griffin JL. Liquid Extraction Surface Analysis Mass Spectrometry Method for Identifying the Presence and Severity of Nonalcoholic Fatty Liver Disease. Anal Chem. 2017 May 2;89(9):5161–70.

292. Oh T, Fakurnejad S, Sayegh ET, Clark AJ, Ivan ME, Sun MZ, et al. Immunocompetent murine models for the study of glioblastoma immunotherapy. J Transl Med. 2014 Apr 29;12:107.

293. Kruse CA, Molleston MC, Parks EP, Schiltz PM, Kleinschmidt-DeMasters BK, Hickey WF. A rat glioma model, CNS-1, with invasive characteristics similar to those of human gliomas: A comparison to 9L gliosarcoma. J Neurooncol. 1994;22(3):191–200.

294. Lin C-M, Yu C-F, Huang H-Y, Chen F-H, Hong J-H, Chiang C-S. Distinct Tumor Microenvironment at Tumor Edge as a Result of Astrocyte Activation Is Associated With Therapeutic Resistance for Brain Tumor. Front Oncol [Internet]. 2019 [cited 2019 Jul 15];9. Available from: https://www.frontiersin.org/articles/10.3389/fonc.2019.00307/full

295. Quiason CM, Shahidi-Latham SK. Imaging MALDI MS of Dosed Brain Tissues Utilizing an Alternative Analyte Pre-extraction Approach. J Am Soc Mass Spectrom. 2015 Jun 1;26(6):967–73.

296. Chughtai K, Jiang L, Greenwood TR, Glunde K, Heeren RMA. Mass spectrometry images acylcarnitines, phosphatidylcholines, and sphingomyelin in MDA-MB-231 breast tumor models. J Lipid Res. 2013 Feb 1;54(2):333–44.

297. Quail D, Joyce J. Microenvironmental regulation of tumor progression and metastasis. Nat Med. 2013 Nov;19(11):1423–37.

298. Denton NL, Chen C-Y, Scott TR, Cripe TP. Tumor-Associated Macrophages in Oncolytic Virotherapy: Friend or Foe? Biomedicines [Internet]. 2016 Jul 7 [cited 2019 Jun 25];4(3). Available from: https://www.ncbi.nlm.nih.gov/pmc/articles/PMC5344259/

299. Alcantara Llaguno SR, Parada LF. Cell of origin of glioma: biological and clinical implications. Br J Cancer. 2016 Dec;115(12):1445–50.

300. Baker M, Robinson SD, Lechertier T, Barber PR, Tavora B, D'Amico G, et al. Use of the mouse aortic ring assay to study angiogenesis. Nat Protoc. 2012 Jan;7(1):89–104.

301. Gau D, Veon W, Capasso TL, Bottcher R, Shroff S, Roman BL, et al. Pharmacological Intervention of MKL/SRF signaling by CCG-1423 impedes Endothelial Cell Migration and Angiogenesis. Angiogenesis. 2017 Nov;20(4):663–72.

302. Tomita M, Matsuzaki Y, Edagawa M, Maeda M, Shimizu T, Hara M, et al. Correlation between tumor angiogenesis and invasiveness in thymic epithelial tumors. J Thorac Cardiovasc Surg. 2002 Sep 1;124(3):493–8.

303. Li Y, Lui KO, Zhou B. Reassessing endothelial-to-mesenchymal transition in cardiovascular diseases. Nat Rev Cardiol. 2018 Aug;15(8):445.

304. Souilhol C, Harmsen MC, Evans PC, Krenning G. Endothelial–mesenchymal transition in atherosclerosis. Cardiovasc Res. 2018 Mar 15;114(4):565–77.

305. Heiss M, Hellström M, Kalén M, May T, Weber H, Hecker M, et al. Endothelial cell spheroids as a versatile tool to study angiogenesis in vitro. FASEB J. 2015 Apr 9;29(7):3076–84.

306. Pardridge WM. Drug transport in brain via the cerebrospinal fluid. Fluids Barriers CNS. 2011 Jan 18;8:7.

307. Stupp R, Mason WP, van den Bent MJ, Weller M, Fisher B, Taphoorn MJB, et al. Radiotherapy plus concomitant and adjuvant temozolomide for glioblastoma. N Engl J Med. 2005 Mar 10;352(10):987–96.

308. Liu C-A, Chang C-Y, Hsueh K-W, Su H-L, Chiou T-W, Lin S-Z, et al. Migration/Invasion of Malignant Gliomas and Implications for Therapeutic Treatment. Int J Mol Sci [Internet]. 2018 Apr 8 [cited 2019 Aug 25];19(4). Available from: https://www.ncbi.nlm.nih.gov/pmc/articles/PMC5979613/

309. Loeffler J, Alexander E III, Hochberg FH, Wen PY, Morris JH, Schoene WC, et al. Clinical patterns of failure following stereotactic interstitial irradiation for malignant gliomas. Int J Radiat Oncol • Biol • Phys. 1990 Dec 1;19(6):1455–62.

310. Kamarudin MNA, Parhar I. Emerging therapeutic potential of anti-psychotic drugs in the management of human glioma: A comprehensive review. Oncotarget. 2019 Jun 11;10(39):3952–77.

311. Sanchez-Rangel E, Inzucchi SE. Metformin: clinical use in type 2 diabetes. Diabetologia. 2017 Sep 1;60(9):1586–93.

312. Al Hassan M, Fakhoury I, El Masri Z, Ghazale N, Dennaoui R, El Atat O, et al. Metformin Treatment Inhibits Motility and Invasion of Glioblastoma Cancer Cells [Internet]. Analytical Cellular Pathology. 2018 [cited 2019 Aug 27]. Available from: https://www.hindawi.com/journals/acp/2018/5917470/

313. Dimitropoulos K, Giannopoulou E, Argyriou AA, Zolota V, Petsas T, Tsiata E, et al. The Effects of Anti-VEGFR and Anti-EGFR Agents on Glioma Cell Migration Through Implication of Growth Factors with Integrins. Anticancer Res. 2010 Jan 12;30(12):4987–92.

314. Thiessen B, Stewart C, Tsao M, Kamel-Reid S, Schaiquevich P, Mason W, et al. A phase I/II trial of GW572016 (lapatinib) in recurrent glioblastoma multiforme: clinical outcomes, pharmacokinetics and molecular correlation. Cancer Chemother Pharmacol. 2010 Jan 1;65(2):353–61.

315. Scott BJ, Quant EC, McNamara MB, Ryg PA, Batchelor TT, Wen PY. Bevacizumab salvage therapy following progression in high-grade glioma patients treated with VEGF receptor tyrosine kinase inhibitors. Neuro-Oncol. 2010 Jun;12(6):603–7.

316. Tan Z, Zhao J, Jiang Y. MiR-634 sensitizes glioma cells to temozolomide by targeting CYR61 through Raf-ERK signaling pathway. Cancer Med. 2018 Feb 23;7(3):913–21.